Gianfranco Piana

Vibrations and Stability of Axially and Transversely Loaded Structures

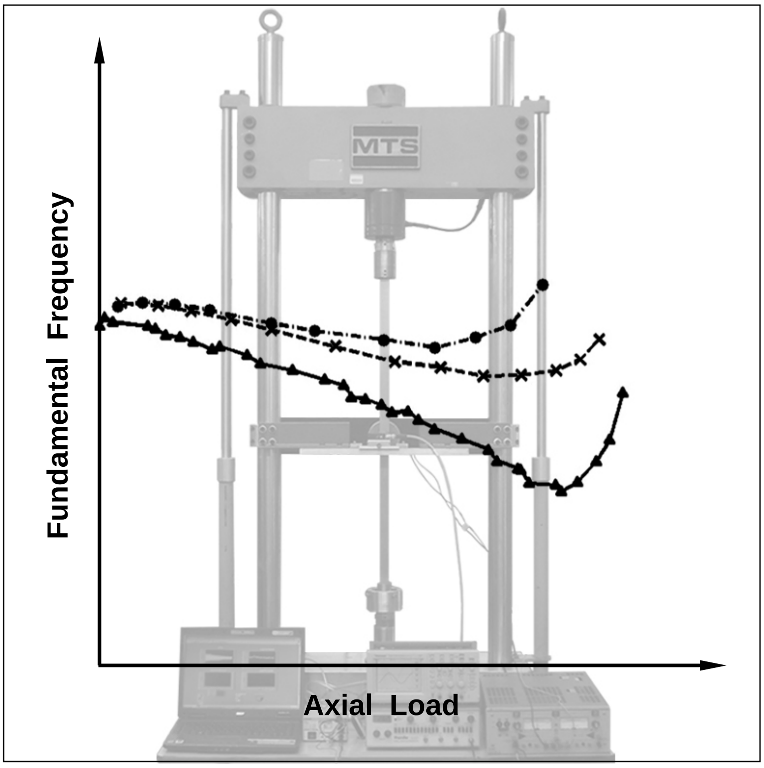

Dottorato di Ricerca in Ingegneria delle Strutture
Politecnico di Torino

Gianfranco Piana

Vibrations and Stability of Axially and Transversely Loaded Structures

Tesi per il conseguimento del titolo di Dottore di Ricerca
XXV Ciclo (2010 - 2011 - 2012)

Dottorato di Ricerca in Ingegneria delle Strutture
Politecnico di Torino

Dicembre 2012

Dottorato di Ricerca in Ingegneria delle Strutture
Politecnico di Torino, Corso Duca degli Abruzzi 24, 10129 Torino, Italy

Tutori: Prof. Alberto Carpinteri, Ing. Riccardo Malvano

Coordinatore: Prof. Alberto Carpinteri

alla mia famiglia
e alla memoria dei miei nonni

Acknowledgements

The research presented in this thesis was carried out at the Department of Structural, Geotechnical and Building Engineering (DISEG) – Politecnico di Torino – in cooperation with the Fluid Dynamics Unit of the National Institute of Metrological Research (INRIM), under the supervision of Prof. Alberto Carpinteri and Eng. Riccardo Malvano.

I would like to thank particularly Eng. Malvano for having introduced me to experimentation and for his constant help and support during the development of the thesis. I am also greatly indebted to Prof. Carpinteri, who always inspired me to do better, for his precious advices and suggestions.

Special thanks are due to Ind. Eng. Franco Alasia for his valuable cooperation during the phases of design and set-up of the experimental tests.

Finally, I would like to reserve a special thank also to Dr. Amedeo Manuello Bertetto, who accompanied and guided me in a continuous process of human and professional growth.

Summary

Modern lightweight and long-span structures are becoming increasingly slender and flexible thanks to continuous improvements in structural analysis techniques, construction methods, and the use of lighter and stronger materials. Modern airplanes, large roofs, and long-span bridges are just some examples of structures for which a design based on vibration and stability is of primary importance.

The thesis aims to investigate into the interplay between vibration and stability phenomena in elastic structures. On the one hand, the concept of stability is intrinsically a dynamic one, and is in general more appropriate to investigate this phenomenon from a dynamic point of view. On the other hand, compressive or compressive-like loads, even if they do not lead to instability, affect the dynamic behaviour of the structure since they influence its natural vibration frequencies.

Three application areas constitute the objective of the present research:

- slender beams subjected to imposed displacements;
- space truss models subjected to dead loads;
- suspension bridges under aerodynamic loads.

Stability and influence of the applied loads on the natural frequencies are studied using analytical, numerical, and experimental tools. The experimental tests were conducted at the Politecnico di Torino in cooperation with the Fluid Dynamics Unit of the National Institute of Metrological Research (INRIM).

The fundamental frequency evolution in slender beams subjected to imposed displacements is analyzed through an experimental study. Different values of geometric imperfections as well as different constraint conditions are investigated, and the natural frequencies are obtained using several methods. The experimental study conducted in the present research leads to recognize two different phases in the bending frequency vs. axial load curves in case of displacement controlled condition, therefore showing a different behaviour with respect to the force

controlled case. After, we show how the experimental results can be interpreted and reproduced through numerical simulations.

The influence of dead loads on the natural frequencies of space truss models is investigated through a modal analysis with second-order effects. In particular, the effects of the direction and magnitude of the acting load are studied, leading to show an interesting aspect of the dynamic behaviour due to different effects of the geometric stiffness. In this case, numerical simulations are accompanied by some experiments.

Finally, the effects of steady aerodynamic loads on stability and natural vibration frequencies of suspension bridge decks are analyzed by means of a simplified analytical model. The single (central) span suspension bridge model is considered, and the linearized integro-differential equations describing the flexural-torsional oscillations of the bridge deck are derived. In conclusion, some address on how this study might be integrated into the flutter analysis of long-span suspension bridges is provided.

The quest for stronger, stiffer, and more lightweight structural systems is making the subject studied in this thesis increasingly important in practical applications in the areas of civil, mechanical, and aerospace engineering.

Sommario

Le moderne strutture leggere e di grande luce diventano via via più snelle e flessibili grazie ai continui avanzamenti nelle tecniche di analisi strutturale, nei metodi di costruzione e all'uso di materiali sempre più resistenti e leggeri. Moderni aeroplani, grandi coperture o ponti di grande luce sono solo alcuni esempi di strutture la cui progettazione richiede di attribuire fondamentale importanza agli aspetti del comportamento dinamico e ai fenomeni di instabilità.

La tesi si propone di indagare sull'interazione tra fenomeni di dinamica e di instabilità in strutture elastiche. Da un lato, il concetto di stabilità è intrinsecamente dinamico, ed è quindi in generale più appropriato affrontarne lo studio da tale punto di vista. D'altra parte, azioni di compressione, o ad esse riconducibili, anche quando non inducano fenomeni di instabilità, influenzano il comportamento dinamico della struttura andando a modificarne le frequenze di vibrazione naturale.

La ricerca è costituita da tre campi di applicazione:

- travi snelle soggette a spostamenti imposti;
- modelli reticolari spaziali soggetti a carichi permanenti;
- ponti sospesi soggetti a carichi aerodinamici.

Si studiano la stabilità e gli effetti dei carichi sulle frequenze di vibrazione naturale attraverso prove sperimentali, simulazioni numeriche o modelli analitici. Le prove sperimentali sono state condotte presso il Politecnico di Torino in collaborazione con l'Unità staccata di fluidodinamica dell'Istituto Nazionale di Ricerca Metrologica (INRIM).

L'evoluzione delle frequenze fondamentali flessionali di travi snelle soggette a spostamenti imposti ad un'estremità viene indagata da un punto di vista sperimentale. In particolare, si analizza l'effetto delle imperfezioni geometriche e delle diverse condizioni di vincolo, ottenendo le frequenze proprie attraverso

l’applicazione di più metodi. Lo studio sperimentale condotto nella presente ricerca porta a riconoscere due fasi distinte nelle curve frequenza fondamentale-carico assiale nel caso di spostamenti imposti, evidenziando un comportamento differente rispetto al caso di carico imposto. Successivamente, si mostra come i risultati sperimentali possano essere interpretati e riprodotti anche attraverso delle simulazioni numeriche.

L’influenza di carichi permanenti sulle frequenze proprie di modelli reticolari spaziali viene studiata attraverso l’analisi modale con effetti del secondo ordine. In particolare, vengono analizzati gli effetti del verso e dell’intensità del carico applicato, consentendo di evidenziare un aspetto interessante del comportamento dinamico dovuto a diversi effetti della rigidezza geometrica. In questo caso, alle simulazioni numeriche vengono affiancate alcune prove sperimentali.

Infine, gli effetti delle azioni aerodinamiche stazionarie sulla stabilità e sulle frequenze di vibrazione naturale della travata dei ponti sospesi vengono analizzati attraverso un modello analitico semplificato. Si considera il modello di ponte sospeso a singola campata (la captata centrale) e si ricavano le equazioni integro-differenziali linearizzate che descrivono le oscillazioni flesso-torsionali dell’impalcato. In conclusione, si accenna a come tale studio potrebbe essere integrato nell’analisi di flutter dei ponti sospesi di grande luce.

La ricerca di sistemi strutturali più resistenti, rigidi e leggeri sta attribuendo all’argomento studiato in questa tesi una rilevanza sempre maggiore per le applicazioni pratiche nei campi dell’ingegneria civile, meccanica e aerospaziale.

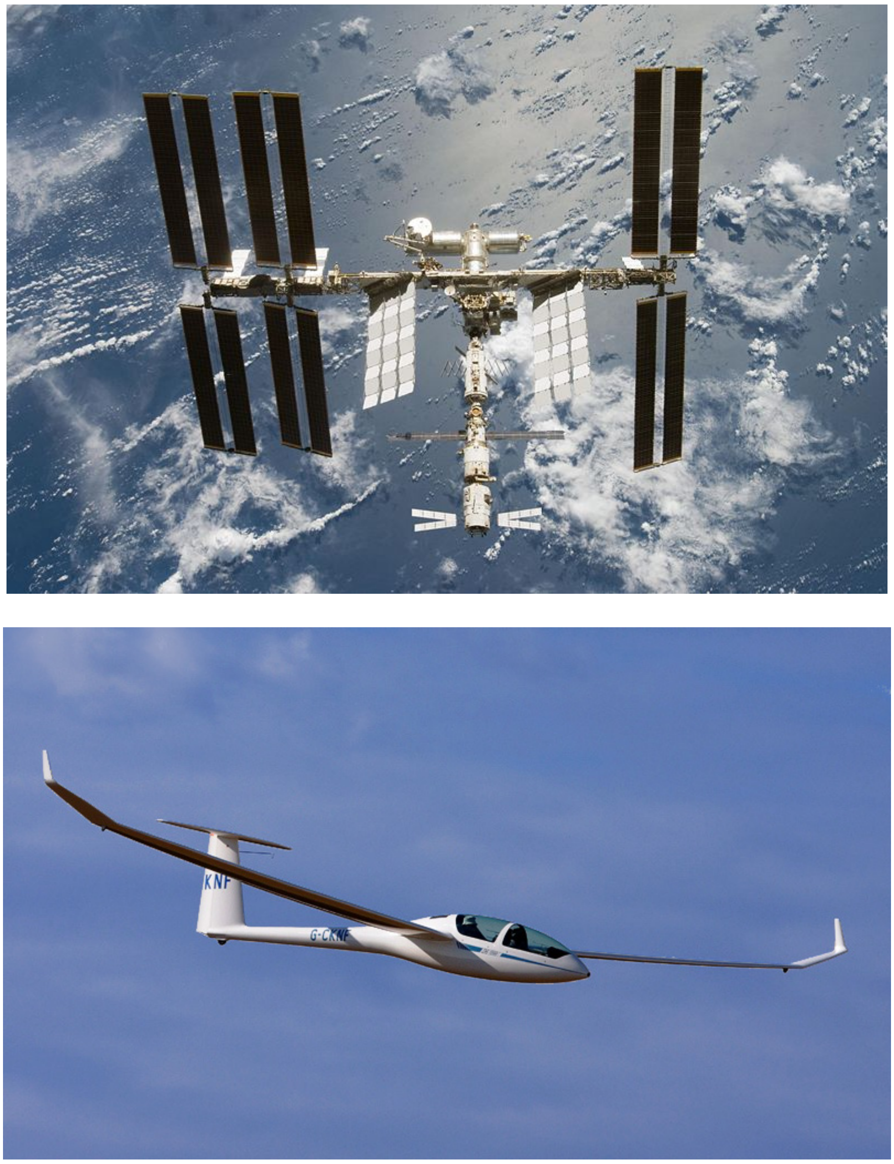

Plate I. Examples of slender structures in an aerospace contest. Top, International Space Station; bottom, DG1000 Glider.

Plate II. Examples of slender structures in a civil contest. Top, Akashi Kaikyo Bridge; bottom, Grid Shell Roof for DZ-Bank.

Plate III. More examples of slender structures. Top, Offshore Wind Turbines; bottom, Offshore Oil Platform.

Contents

Chapter 1

Introduction

Modern long-span and lightweight structures are becoming increasingly slender and flexible thanks to improvements in structural analysis techniques, construction methods, and the use of both light and strong materials. Design based on vibration and stability is a fundamental requirement for such structures.

In this chapter we shall provide some general concepts on the subjects of vibration and stability of structures, including a brief historical review of both fields. Afterwards, we will give the objectives and motivation of the study and, finally, we will discuss the organization of the thesis.

1.1 Vibration Engineering

Vibration is a repetitive, periodic, or oscillatory response of a mechanical system. The rate of the vibration cycles is termed frequency. Repetitive motions that are somewhat clean and regular and occur at relatively low frequencies are commonly called oscillations, while any repetitive motion, even at high frequencies, with low amplitudes, having irregular and random behaviour falls into the general class of vibration. Nevertheless, the terms vibration and oscillation are often used interchangeably, as is done in this thesis.

Vibrations can naturally occur in an engineering system and may be representative of its free and natural dynamic behaviour. Vibrations may also be forced onto a system through some form of excitation. The excitation forces may be either generated internally within the dynamic system, or transmitted to the system through an external source. When the frequency of the forcing excitation coincides with that of the natural motion, the system will respond more vigorously with increased amplitude. This condition is known as resonance, and the associated frequency is called the resonant frequency. There are “good vibrations”, which serve a useful purpose, but there are also “bad vibrations”, which can be unpleasant or harmful. For many engineering systems, operation at resonance would be undesirable and could be destructive. Suppression or elimination of bad vibrations and generation of desired forms and levels of good vibration are general goals of vibration engineering.

Applications of vibration are found in many branches of engineering such as aeronautical and aerospace, civil, manufacturing, mechanical, and even electrical (de Silva, 2000). An analytical or computer model is usually needed to analyze the vibration in an engineering system. Models are also useful in the process of design and development of an engineering system for good performance with respect to vibrations. Vibration monitoring, testing, and experimentation are important as well in the design, implementation, maintenance, and repair of engineering systems.

1.1.1 Study of Vibration

Natural, free vibration is a manifestation of the oscillatory behaviour in mechanical systems, as a result of repetitive interchange of kinetic and potential energies among components in the system. Such natural oscillatory response is not limited, however, to purely mechanical systems, and is found in electrical and fluid systems as well, again due to a repetitive exchange of two types of energy among system components. Yet, purely thermal systems do not undergo free, natural oscillations; this is primarily due to the absence of two forms of reversible energy. Even a system that can hold two reversible forms of energy may not necessarily display free, natural oscillations. The reason for this would be the strong presence of an energy dissipation mechanism that could use up the initial energy of the system before completing a single oscillation cycle (energy interchange). Such dissipation is provided by damping or friction in mechanical systems, and resistance in electrical systems. Any engineering system (even a purely thermal one) is able to undergo forced oscillations, regardless of the degree of energy dissipation. In this case, the energy necessary to sustain the oscillations will come from the excitation source, and will be continuously replenished.

Proper design and control are crucial in maintaining a high performance level and production efficiency, and prolonging the useful life of machinery, structures, and industrial processes. Before designing or controlling an engineering system for good vibratory performance, it is important to understand, represent (model), and analyze the vibratory characteristics of the system. This can be accomplished through purely analytical means, computer analysis of analytical models, testing and analysis of test data, or a combination of these approaches (de Silva, 2000).

The analysis of a vibrating system can be done either in the time domain or in the frequency domain. In the time domain, the independent variable of a vibration signal is time. In this case, the system itself can be modelled as a set of differential equations with respect to time. A model of a vibrating system can be formulated by applying either force-momentum rate relations (Newton's second law) or the concepts of kinetic and potential energies (Lagrangian approach).

In the frequency domain, the independent variable of a vibration signal is frequency. In this case, the system can be modelled by input-output transfer functions which are algebraic, rather than differential, models. Transfer function representations such as mechanical impedance, mobility, receptance and transmissibility can be conveniently analyzed in the frequency domain, and effectively be used in vibration design and evaluation. The two domains are connected by the Fourier transform, which can be treated as a special case of the Laplace transform. In practice, digital electronics and computers are commonly used in signal analysis, sensing, and control. In this situation, one needs to employ concepts of discrete time, sampled data, and digital signal analysis in the time domain. Correspondingly, then, concepts of discrete or digital Fourier transform and techniques of fast Fourier transform (FFT) will be applicable in the frequency domain.

An engineering system, when given an initial disturbance and allowed to execute free vibrations without a subsequent forcing excitation, will tend to do so at a particular "preferred" frequency and maintaining a particular "preferred" geometric shape. This frequency is termed a natural frequency of the system, and the corresponding shape (or motion ratio) of the moving parts of the system is termed a mode shape. Any arbitrary motion of a vibrating system can be represented in terms of its natural frequencies and mode shapes. The subject of modal analysis primarily concerns determination of natural frequencies and mode shapes of a dynamic system. Once the modes are determined, they can be used in understanding the dynamic nature of the systems, and also in design and control. Modal analysis is extremely important in vibration engineering. Natural frequencies and mode shapes of a vibrating system can be determined experimentally through procedures of modal testing. In fact, a dynamic model (an experimental model) of the system can be determined in this manner. The subject of modal testing, experimental modelling (or model identification), and associated analysis and design is known as experimental modal analysis.

Energy dissipation (or damping) is present in any mechanical system. It alters the dynamic response of the system, and has desirable effects such as stability, vibration suppression, power transmission (e.g., in friction drives), and control. It also has obvious undesirable effects such as energy wastage, reduction of the process efficiency, wear and tear, noise, and heat generation. For these reasons, damping is an important topic of study in the area of vibration. In general, energy dissipation is a nonlinear phenomenon. However, in view of well-known difficulties of analyzing nonlinear behaviour and because an equivalent representation of the overall energy dissipation is often adequate in vibration analysis, linear models are primarily used to represent damping.

Properties such as mass (inertia), flexibility (spring-like effect), and damping (energy dissipation) are to a large extent continuously distributed throughout practical mechanical devices and structures. This is the case with distributed components such as cables, shafts, beams, membranes, plates, shells, and various solids, as well as structures made of such components. Representation (i.e., modelling) of these distributed-parameter (or continuous) vibrating systems requires independent variables in space (spatial coordinates) in addition to time; these models are partial differential equations in time and space. The analysis of distributed-parameter models requires complex procedures and special tools. When necessary or more convenient, approximate lumped-parameter models can be developed for continuous systems, using procedures such as modal analysis and energy equivalence.

Vibration testing is useful in a variety of stages in the development and utilization of a product. In the design and development stage, vibration testing can be used to design, develop, and verify the performance of individual components of a complex system before the overall system is built (assembled) and evaluated. In the production stage, vibration testing can be used for screening of selected batches of products for quality control. Another use of vibration testing is in product qualification. In this case, a product of good quality is tested to see whether it can withstand various dynamic environments that it may encounter in a specialized application. An example of a large-scale shaker used for vibration testing of civil engineering structures is shown in Figure 1.1 (de Silva, 2000).

Design is a subject of paramount significance in the practice of vibration. In particular, mechanical and structural design for acceptable vibration characteristics is very important. Modification of existing components and integration of new components and devices, such as vibration dampers, isolators, inertia blocks, and

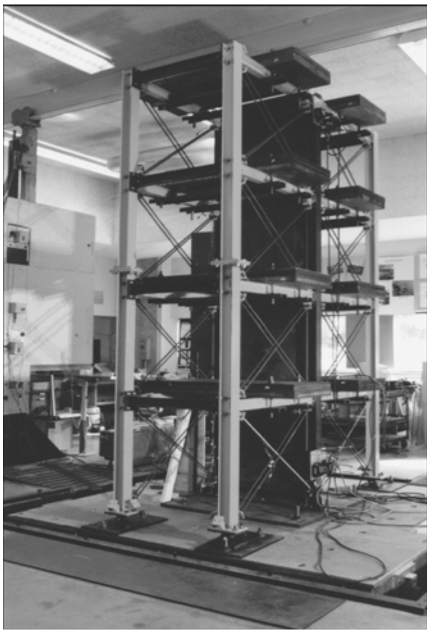

Figure 1.1 – A multi-degree-of-freedom hydraulic shaker used in testing civil engineering structures (University of British Columbia).

dynamic absorbers, can be incorporated into these practices. Furthermore, elimination of sources of vibration –for example, through component alignment and balancing of rotating devices– is a common practice. Both passive and active techniques are used in vibration control (de Silva, 2000). In passive control, actuators that require external power sources are not employed. In active control, vibration is controlled by means of actuators (which need power) to counteract vibration forces. Monitoring, testing, and control of vibration will require devices such as sensors and transducers, signal conditioning and modification hardware (e.g., filters, amplifiers, modulators, demodulators, analog-digital conversion means), and actuators (e.g., vibration exciters or shakers).

The science and engineering of vibration involve two broad categories of applications:

1. elimination or suppression of undesirable vibrations;
2. generation of the necessary forms and quantities of useful vibrations.

Figure 1.2 – The SkyTrain in Vancouver, Canada, a modern automated transit system.

Undesirable and harmful types of vibration include structural motions generated due to earthquakes, dynamic interactions between vehicles and bridges or guideways, noise generated by construction equipment, vibration transmitted from machinery to its supporting structures or environment, as well as damage, malfunction, and failure due to dynamic loading, unacceptable motions, and fatigue caused by vibration. For example, dynamic interactions between an automated transit vehicle and a bridge (see Figure 1.2) can cause structural problems as well as degradation in ride quality. Rigorous analysis and design are needed, particularly with regard to vibration, in the development of these ground transit systems. Lowering the levels of vibration will result in reduced noise and improved work environment, maintenance of a high performance level and production efficiency, reduction in user/operator discomfort, and prolonging the useful life of industrial machinery. Desirable types of vibration include those generated by musical instruments, devices used in physical therapy and medical applications, vibrators used in industrial mixers, part feeders and sorters, and vibratory material removers such as drills and polishers (finishers).

Concepts of vibration have been used for many centuries in practical applications. Recent advances of vibration are quite significant, and the corresponding applications are numerous. Many of the recent developments in the field of vibration were motivated perhaps for two primary reasons:

1. the speeds of operation of machinery have doubled over the past 50 years and, consequently, the vibration loads generated by rotational excitations and unbalances would have quadrupled if proper actions of design and control had not been taken;
2. mass, energy, and efficiency considerations have resulted in lightweight, optimal designs of machinery and structures consisting of thin members with high strength. Associated structural flexibility has made the rigid-structure assumption unsatisfactory, and given rise to the need for sophisticated procedures of analysis and design that govern distributed parameter flexible structures.

A range of applications of vibration can be found in various branches of engineering: particularly civil, mechanical, aeronautical and aerospace, and production and manufacturing. Modal analysis and design of flexible civil engineering structures such as bridges, guideways, tall buildings, and chimneys directly incorporate theory and practice of vibration. A fine example of an elongated building where vibration analysis and design are crucial is the Jefferson Memorial Arch, shown in Figure 1.3.

1.1.2 History of Vibration

The origins of the theory of vibration can be traced back to the design and development of musical instruments (good vibration). It is known that drums, flutes, and stringed instruments existed in China and India for several millennia B.C. Ancient Egyptians and Greeks also explored sound and vibration from both practical and analytical points of view. For example, while Egyptians had known of a harp since at least 3000 B.C., the Greek philosopher, mathematician, and musician Pythagoras (of the Pythagoras theorem fame) who lived during 582 to 502 B.C., experimented on sounds generated by blacksmiths and related them to music and physics. The Chinese developed a mechanical seismograph (an instrument to detect and record earthquake vibrations) in the 2nd century A.D.

The foundation of the modern-day theory of vibration was probably laid by scientists and mathematicians such as Robert Hooke (1635–1703) of the Hooke’s law fame, who experimented on the vibration of strings; Sir Isaac Newton (1642–1727), who gave us calculus and the laws of motion for analyzing vibrations;

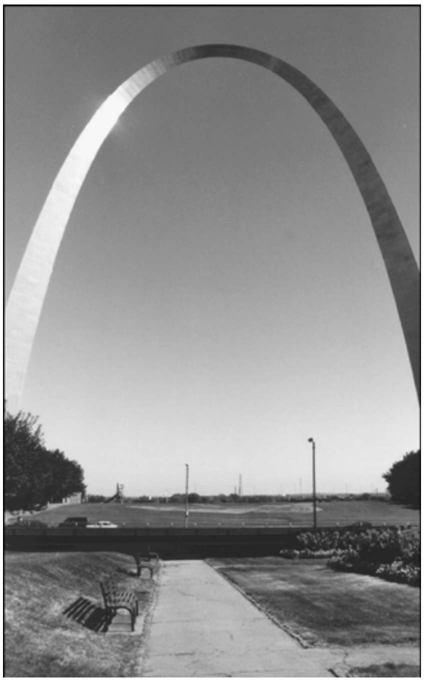

Figure 1.3 – Jefferson Memorial Arch in St. Louis, MO.

Daniel Bernoulli (1700–1782) and Leonard Euler (1707–1783), who studied beam vibrations (Bernoulli-Euler beam) and also explored dynamics and fluid mechanics; Joseph Lagrange (1736–1813), who studied vibration of strings and also explored the energy approach to formulating equations of dynamics; Charles Coulomb (1736–1806), who studied torsional vibrations and friction; Joseph Fourier (1768–1830), who developed the theory of frequency analysis of signals; and Simeon-Dennis Poisson (1781–1840), who analyzed vibration of membranes and also analyzed elasticity (Poisson's ratio). As a result of the industrial revolution and associated developments of steam turbines and other rotating machinery, an urgent need was felt for developments in the analysis, design, measurement, and control of vibration. Motivation for many aspects of the existing techniques of vibration can be traced back to related activities from the industrial revolution.

Much credit should go to scientists and engineers of more recent history, as well. Among the notable contributors are Rankine (1820–1872), who studied critical speeds of shafts; Kirchhoff (1824–1887), who analyzed vibration of plates; Rayleigh (1842–1919), who made contributions to the theory of sound and vibration and developed computational techniques for determining natural vibrations; de Laval (1845–1913), who studied the balancing problem of rotating disks; Poincaré (1854–1912), who analyzed nonlinear vibrations; and Stodola (1859–1943), who studied vibrations of rotors, bearings, and continuous systems. Distinguished engineers who made significant contributions to the published literature and also to the practice of vibration include Timoshenko, Den Hartog, Clough, and Crandall (Weaver et al. 1990; Clough and Penzien, 2003).

1.2 Buckling of Structures

When a slender structure is loaded in compression, for small loads it deforms with hardly any noticeable change in geometry and load-carrying ability. On reaching a critical load value, the structure suddenly experiences a large deformation and it may lose its ability to carry the load. At this stage, the structure is considered to have buckled. For example, when a rod is subjected to an axial compressive force, it first shortens slightly but at a critical load the rod bows out, and we say that the rod has buckled. In the case of a thin circular ring under radial pressure, the ring decreases in size slightly before buckling into a number of circumferential waves. For a cruciform column under axial compression, it shortens and then buckles in torsion. Buckling is also possible under transverse loads or uniform bending: slender beams having narrow and deep cross-section may undergo lateral-torsional buckling when loaded in the plane of maximum flexural rigidity.

Buckling, also known as structural instability, may be classified into two categories (Galambos, 1988; Chen and Lui, 1987): (1) bifurcation buckling and (2) limit load buckling. In bifurcation buckling, the deflection under compressive load changes from one direction to a different direction (e.g., from axial shortening to lateral deflection). The load at which the bifurcation occurs in the load-deflection space is called the critical buckling load or simply critical load. The deflection path that exists prior to bifurcation is known as the primary path, and the deflection path after bifurcation is called the secondary or postbuckling path. Depending on the structure and loading, the secondary path may be symmetric or asymmetric, and it may rise or fall below the critical buckling load (see Figure 1.4) (Wang et al., 2005).

In limit load buckling, the structure attains a maximum load without any previous bifurcation, i.e., with only a single mode of deflection (see Figure 1.5).

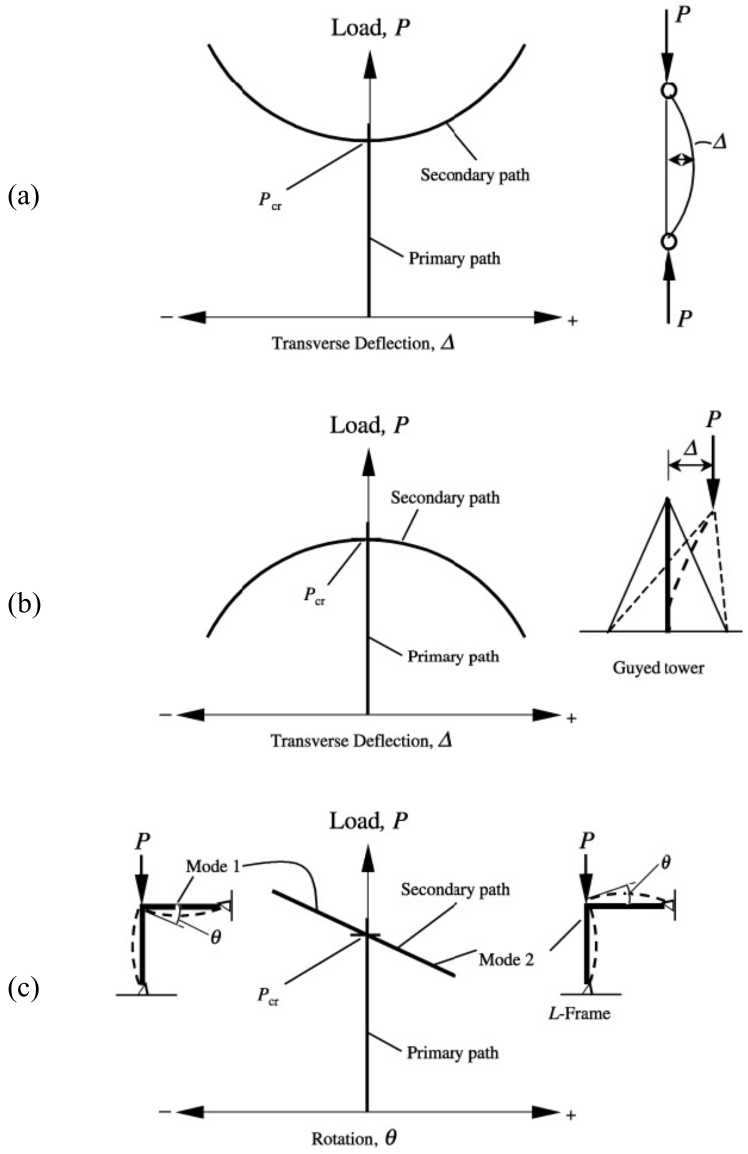

Figure 1.4 – Bifurcation buckling: (a) symmetric bifurcation and stable postbuckling curve; (b) symmetric bifurcation and unstable postbuckling curve; (c) asymmetric bifurcation.

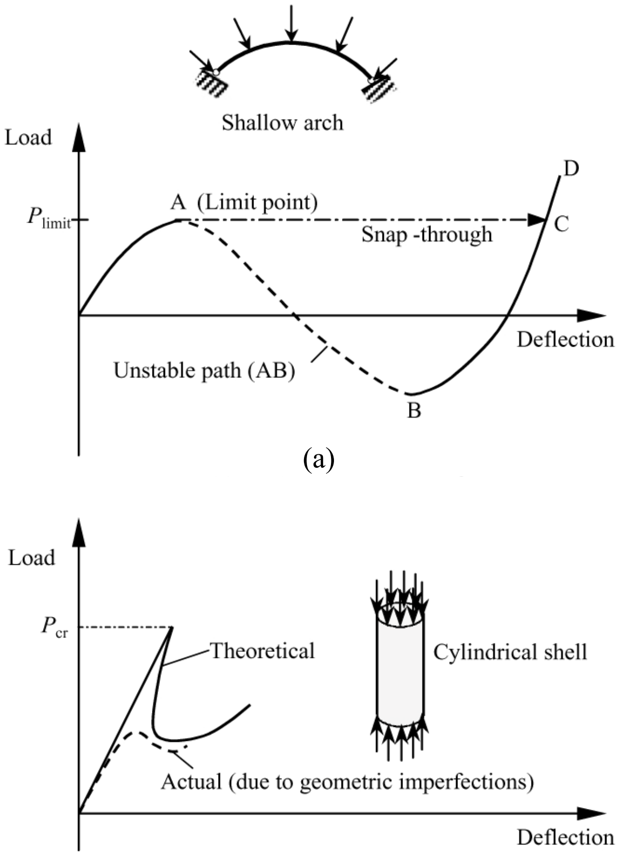

(a)

(b)

Figure 1.5 – Limit load buckling: (a) snap-through buckling; and (b) finite-disturbance buckling.

The snap-through (observed in shallow arches and spherical caps) and finite-disturbance buckling (only unique to shells) are examples of limit load buckling (Wang et al., 2005). Other classifications of buckling are made according to the displacement magnitude (i.e., small or large), or static versus dynamic buckling, or material behaviour such as elastic buckling or inelastic buckling (see El Naschie, 1990).

1.2.1 Buckling Analysis

Design of structures is often based on strength and stiffness considerations. Strength is defined to be the ability of the structure to withstand the applied load, while stiffness is the resistance to deformation (i.e., the structure is sufficiently stiff not to deform beyond permissible limits). However, a structure may become unstable long before the strength and stiffness criteria are violated. For example, one can show that a spherical shell made of concrete and with a thickness-to-radius ratio of $h/R = 1/500$ and modulus of $E = 20\,\mathrm{GPa}$ buckles at a critical stress [$\sigma_{cr} = k(Eh/R)$ and $k \approx 0.25$] of 10 MPa. However, the ultimate strength of the concrete is 21 MPa. Therefore, buckling load governs the design before the strength criterion: buckling is an important consideration in structural design, especially when the structure is slender and lightweight.

Linear elastic buckling of structural members is the most elementary form of buckling, and its study is an essential step towards understanding the buckling behaviour of complex structures, including structures incorporating inelastic behaviour, initial imperfections, residual stresses, etc. (see Bažant, 2000 and Bažant and Cedolin, 2003). The load at which linear elastic buckling occurs is important, because it provides the basis for commonly used buckling formulas used in design codes.

In the open literature and standard text books, buckling loads for different kinds of structures under various loading and boundary conditions are often expressed using approximate simple formulas and design charts to aid designers in estimating the buckling strength of structural members. It is still necessary, however, for designers to perform the buckling analysis if more accurate results are required or if there are no standard solutions available. Apart from a few problems (such as the elastic buckling of perfect and prismatic struts under an axial force or the lateral buckling of simply supported beams under uniform moment and axial force), it is generally rather laborious and in some cases impossible to obtain exact analytical solutions. Thus, it becomes necessary to resort to numerical techniques. In determining the elastic buckling load, there are many techniques. These techniques may be grouped under two general approaches: (a) the vector approach and (b) the energy approach (Reddy, 2002). In the vector approach, Newton's second law is used to obtain the governing equations, whereas in the energy approach the total energy (which is the sum of internal energy and potential energy due to the loads) is minimized to obtain the governing equations. They correspond to the different strategies used in satisfying the state of equilibrium for the deformed member. The governing equations are in the form of an eigenvalue problem in which the eigenvalue represents the buckling load and eigenvector the buckling mode. The smallest buckling load is termed the critical buckling load. Note that the critical buckling load is associated with the state of neutral equilibrium, i.e., characterized by the stationarity condition of the load with respect to the displacement. In order to ascertain whether the equilibrium position is stable or unstable, we use the perturbation technique for the vector approach or by examining the second derivative of the total potential energy.

1.2.2 Historical Review

Buckling is known from ancient times: after early studies by Leonadro Da Vinci (1452–1519), it has been experimentally investigated in a systematic way by Pieter van Musschenbrok (1692–1761) and mathematically solved by Leonhard Euler (1707–783), who used the theory of calculus of variations to obtain the equilibrium equation and buckling load of a compressed elastic column. This work was published in the appendix "De curvis elasticis" of his book titled *Methodus inveniendi lineas curvas maximi minimive proprietate gaudentes*, Lausanne and Geneva, 1744. Joseph-Louis Lagrange (1736–1813) developed the energy approach that is more general than Newton's vector approach for the study of mechanics problems. This led naturally to the fundamental energy theorem of minimum total potential energy being sufficient for stability (Bažant and Cedolin, 2003).

Jules Henry Poincaré (1854–1912) is known as the founder of bifurcation theory and the classification of the singularities. On the other hand, Aleksandr Mikhailovich Liapunov (1857–1918) gave the basic definitions of stability and introduced the generalized energy functions that bear his name, Liapunov functions. Furthermore, Lev Semenovich Pontryagin (1908–1988) introduced, with A. A. Andronov, the important topological concept of structural stability. This work has led to the well known classification theory presented in a treatise, *Stabilite structurelle et morphogenese: Essai d'une theorie generale des modeles (Structural Stability and Morphogenesis: An Outline of General Theory of Models)* by R. Thom.

Theodore von Kármán (1881–1963) began his work on inelastic buckling of columns. He devised a model to explain hysteresis loops and conducted research on plastic deformation of beams. Warner Tjardus Koiter (1914–1997) initiated the classical nonlinear bifurcation theory in his dissertation, "Over de Stabiliteit van het Elastisch Evenwicht", at Delft. Budiansky et al. (1946; 1948) gave a modern account of the nonlinear branching of continuous elastic structures under conservative loads. Furthermore, Hutchinson (1973a; b) made an important contribution to the nonlinear branching theory of structures loaded in the plastic range.

Pioneering research by a number of other individuals is also significant and some of them are: F. Engesser and S. P. Timoshenko on buckling of shear-flexural buckling of columns; A. Considere, F. Engesser and F. R. Shanley on inelastic buckling of columns; G. R. Kirchhoff on buckling of elastica; J. A. Haringx on buckling of springs; V. Vlasov on torsional buckling; L. Prandtl, A. G. M. Michell, S. P. Timoshenko, H. Wagner and N. S. Trahair on flexural-torsional buckling of beams (see Trahair and Bradford, 1991); B. W. James, R. K. Livesly and D. B. Chandler, R. von Mises and J. Ratzersdorfer, and E. Chwalla on buckling of frames; H. Lamb, J. Boussinesq, C. B. Biezeno and J. J. Koch on buckling of rings and arches; E. Hurlbrink, E. Chwalla, E. L. Nicolai, I. J. Steuermann, A. N. Dinnik and K. Federhofer on arches; G. H. Bryan, S. P. Timoshenko, T. von Kármán, E. Trefftz, A. Kromm, K. Marguerre and G. Herrmann on buckling (and postbuckling) of plates; G. H. Handelmann, W. Prager, E. I. Stowell, S. B. Batdorf, F. Bleich and P. P. Bijlaard on plastic buckling of plates; R. Lorentz, R. von Mises, S. P. Timoshenko, R. V. Southwell, T. von Kármán and H. S. Tsien on cylindrical shells under combined axial and lateral pressure; L. H. Donnell, K. M. Marguerre and K. M. Mushtari on the postbuckling of shells; A. Pflüger on buckling of conical shells; and R. Zoelly and E. Schwerin on buckling of spherical shells. Additional references can be found in the book by Timoshenko and Gere (1961) and the survey article by Bažant (2000).

1.2.3 Recent Developments: Tensile Buckling and Constraint's Curvature Effects

Recently Zaccaria et al. (2011) have shown that buckling and instability can also occur in elastic structures subject to tensile dead load. For the first time they have shown that it is possible to design structures (i.e. mechanical systems whose elements are governed by the equation of the elastica) exhibiting bifurcation and instability (buckling) under tensile load of constant direction and point of application (dead). They showed both theoretically and experimentally that the behaviour is possible in elementary structures with a single degree of freedom and in more complex mechanical systems, as related to the presence of a structural junction, called slider, allowing only relative transversal displacement between the connected elements (Zaccaria et al., 2011).

An example of a single-degree-of-freedom structure that buckles in tension is

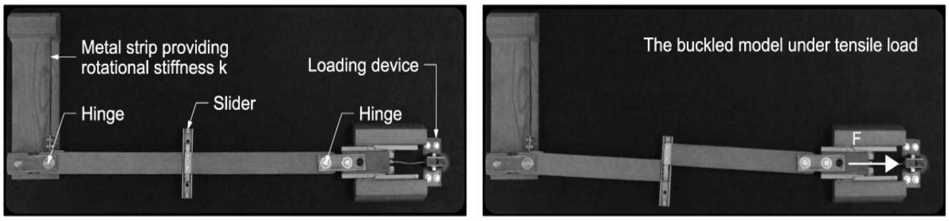

Figure 1.6 – A model of a single-degree-of-freedom elastic structure (in which a metal strip reproduces a rotational spring and the load is given through hanging a load) displaying bifurcation for tensile dead loading (left: undeformed configuration; right: buckled configuration) (Zaccaria et al., 2011).

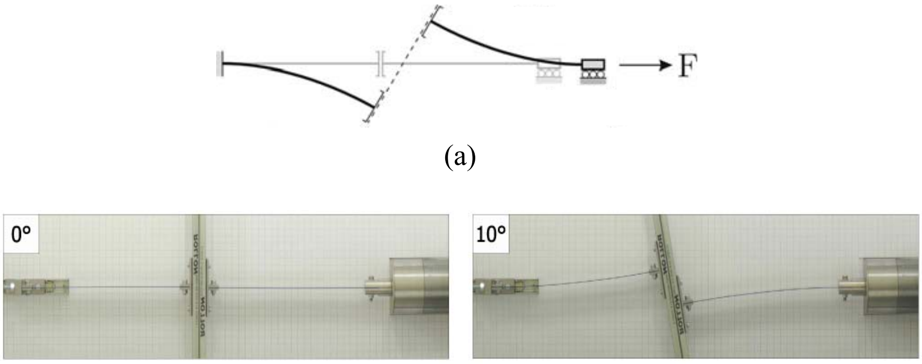

(a)

(b)

Figure 1.7 – Sketch (a) and model (b) of a continuous structure displaying tensile buckling under dead load (left: undeformed configuration; right: buckled configuration in correspondence of a rotation of the slider equal to 10°) (Zaccaria et al., 2011).

shown in Figure 1.6. Another example involving tensile buckling of a structure made up of beam elements governed by the equation of the Euler's elastica is shown in Figure 1.7. In both cases, there are no elements subject to compression. The instability and buckling in tension are related to the presence of the slider.

Even more recently, Bigoni et al. (2012) have shown that bifurcation of an elastic structure crucially depends on the curvature of the constraints against which the ends of the structure are prescribed to move. They showed theoretically and

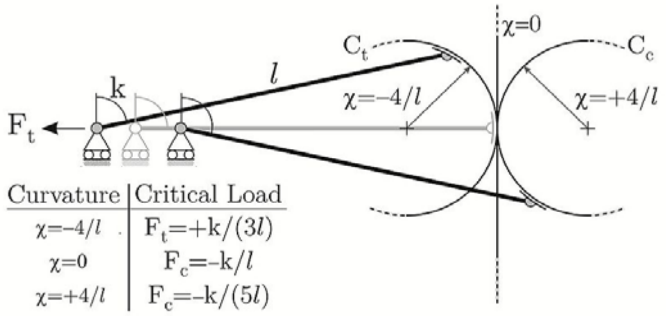

Figure 1.8 – A one-degree-of-freedom structure (with a rotational elastic spring at its left end) evidencing compressive or tensile buckling as a function of the curvature of the constraint (a circular profile with constant curvature, $\chi = \pm 4$) on which the hinge on the right of the structure has to slide (Bigoni et al., 2012).

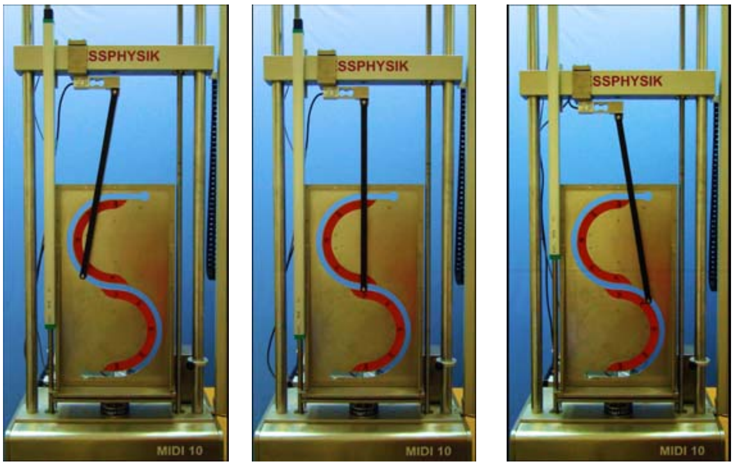

Figure 1.9 – Experimental setup for the S-shaped profile structure with a groove corresponding to two circles: undeformed configuration (centre); elongation after tensile buckling (left); and shortening after compressive buckling (on the right) (Bigoni et al., 2012).

they provided definitive experimental verification that an appropriate curvature of the constraint over which the end of a structure has to slide strongly affects buckling loads and can induce: (1) tensile buckling; (2) decreasing- (softening), increasing- (hardening), or constant-load (null stiffness) postcritical behaviour; (3) multiple bifurcations, determining for instance two bifurcation loads (one tensile and one compressive) in a single-degree-of-freedom elastic system.

In fact, even a single-degree-of-freedom system (see Figure 1.8) may exhibit a tensile (or a compressive) buckling load as related to the fact that one end has to move along the circular profile labelled C_t (labelled C_c). The two circular profiles can be arranged in a S-shaped profile, as shown in Figure 1.9; in that case a discontinuity of the constraint's curvature is introduced, leading to multiple bifurcations. Note that the single-degree-of-freedom structure shown in Figure 1.9 has two buckling loads (one tensile and one compressive).

1.3 Nonconservative Loading and Dynamic Instability

A mechanical system is defined to be conservative when both external and internal forces are derivable from a potential. When considering elastic systems, the internal forces are derivable from a strain (internal) energy potential Φ. Also in the case of dissipative actions (like viscous damping), the internal forces may be deduced from a potential function or a dissipation function. Nonconservative systems in which the nonconservative character is due to mechanical damping are also defined dissipative and their behavior does not differ much from that of conservative systems. Therefore, the conservative/non-conservative character of an elastic system depends on whether the external loads are conservative or nonconservative.

Conservative applied forces $\{f\}$ may be derived from the external loads potential V by differentiating with respect to the state variables $\{u\}$:

$$\{f\} = \frac{\partial V}{\partial \{u\}}. \tag{1.1}$$

However, a force field can be conservative even if it does not have a potential (gyroscopic loads). Nonconservative forces, on the other hand, are never expressible as in Equation (1.1). Examples of sources of nonconservative forces in various branches of engineering are aerodynamic and hydrodynamic forces, aircraft and rocket propulsion forces, frictional forces, and forces in automatic control systems.

The work done by nonconservative forces on a closed path is other than zero.

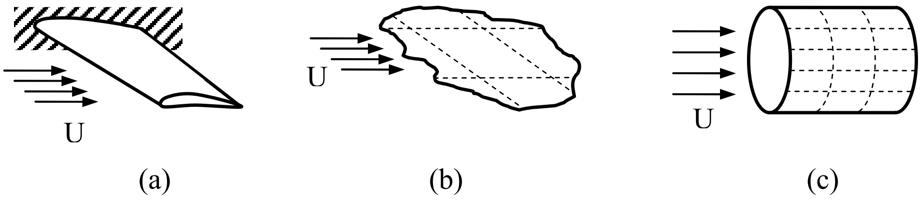

Figure 1.10 – Examples of elastic structures situated in flow of gas. (a) Wing; (b) plate; (c) shell.

Thus, a nonconservative force field gives or subtracts energy. In some cases, a constant (steady) external force can result in pulsating actions if the structure starts accidentally to vibrate. These actions increase with the amplitude of the oscillation, so if the passive resistances are not sufficient to limit the vibration amplitude, the structure may collapse. These actions are therefore generated by the vibration itself, disappearing if the motion ends. Hence, it is possible to have oscillating motions, also of large amplitude, without applying any periodic or variable external force, but simply as a consequence of particular conditions of dynamic instability where the vibration itself generates the forces which maintain and enhance it. Such vibrations are called self-excited, and the eventual resulting instability of the system is called dynamic instability.

Self-excited vibrations may occur, for example, in flexible structures invested by a flow of gas, like in the case of the well-studied wing flutter (Figure 1.10(a)), or in the case of the so-called panel flutter, which regards plates and shells (Figures 1.10(b) and (c)). Similarly, dangerous self-excited vibrations may take place in power transmission lines or in long-span bridges under the action of wind, even if it blows with constant velocity (without gusts).

Self-excited vibrations may also be generated in a moving system in presence of friction between unlubricated parts (dry friction), and they are due to the fact that the friction coefficient decreases with the relative velocity of the two parts. Simple examples are given by a physical pendulum supported by a shaft rotating with constant angular velocity (Figure 1.11(a)), or by a prismatic beam supported by two rollers rotating with the same angular velocity but in opposite sense (Figure 1.11(b)).

For conservative and dissipative systems stability can be determined by energy methods, based on the Principle of Minimum Total Potential Energy. Static analysis, which represents a part of the energy approach, cannot answer the question of stability: statics can only yield equilibrium states, which may be stable

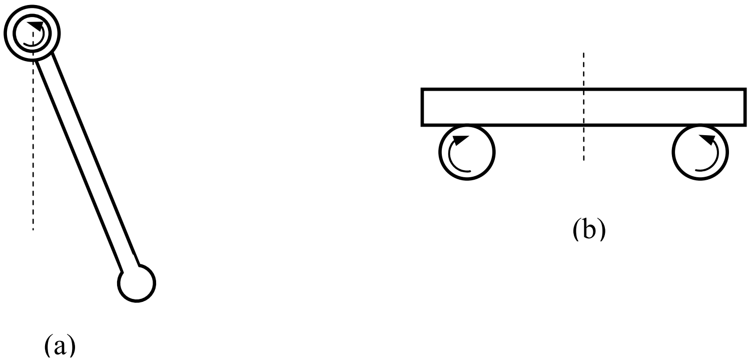

Figure 1.11 – Examples of mechanical systems with dry friction. (a) Pendulum supported by a rotating shaft (Froude pendulum); (b) prismatic beam on rollers.

or unstable. On the other hand, the concept of critical force is extremely useful. The critical force (or, in general, a parameter of the force group) is defined as the smallest value of the force at which, in addition to the initial form of equilibrium, there can exist others which are very close to the initial form. This approach, known as Euler method, enables us to reduce the problem of stability of a form of equilibrium to the simpler problem of finding the minimum characteristic value of certain boundary-value problems.

Although the usefulness of the Euler method in the theory of elastic stability cannot be disputed, it is not universal. The Euler method is applicable to structures that behave linearly on the pre-critical phase if the external forces have a potential (i.e. if they are conservative forces), and in general it is not applicable if they do not. If the loading is nonconservative the loss of stability may not show up by the system going into another equilibrium state but by going into unbounded motion. In using the Euler method, i.e. in considering only a number of forms of equilibrium, we automatically exclude from our analysis any possible forms of motion. To encompass this possibility we must consider the dynamic behavior of the system because stability is essentially a dynamic concept.

Classical examples in which the Euler method cannot be applied are problems of stability of elastic bodies subjected to follower forces, i.e. to forces which during the process of loss of stability follow some particular law other than that of weight forces. Figure 1.12 shows a column under the action of a compressive force which after deformation rotates together with the end section of the column and at

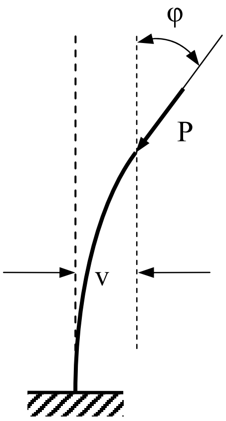

Figure 1.12 – Cantilever subjected to a compressive follower force at the free edge (Beck’s column).

all times remains tangential to its deformed axis (follower force). In this case, the Euler method leads to erroneous results: the rectilinear form of the column for sufficiently large values of the force *P* proves to be unstable, although in this particular problem there cannot exist curvilinear forms of equilibrium close to the initial rectilinear form. The instability of the system is of an oscillatory nature with a definite phase relation between φ and v corresponding to the absorption of energy from outside.

All the nonconservative problems listed above, in spite of their considerable physical disparity, are mathematically very similar, since they all lead to non-self-adjoint boundary-value problems. This is the essential difference between the classical problems considered by the theory of elastic stability, in which, by virtue of the existence of potential in the external forces, all the problems are self-adjoint.

The basic method of investigating nonconservative problems in the theory of elastic stability is the dynamic method, which is based on the investigation of the oscillations of the system close to its position of equilibrium.

1.4 Outline of the Thesis

The present thesis aims to investigate on the interplay between vibration and stability phenomena in elastic structures. On the one hand, stability is essentially a dynamic concept, and is in general more appropriate to investigate this phenomenon from a dynamic point of view; in addition, the loss of stability of a structure is, physically, a dynamic process. On the other hand, compressive or compressive-like loads acting on slender structures, even if they do not lead to instability, affect the dynamic behaviour of the structure since they influence its natural frequencies.

Three application areas constitute the objective of the present research: (1) slender beams subjected to imposed displacements; (2) space truss models subjected to dead loads; and (3) suspension bridges under aerodynamic loads. Stability and influence of the applied loads on the natural frequencies are studied using analytical, numerical, and experimental tools.

The thesis consists of seven chapters. The first three chapters provide the necessary general theoretical framework and the basic references on the subject. The last four chapters are devoted to a specific description of the original contents of the research, and a summary of the main results together with some addresses on possible future developments of the presented work.

The present introductive chapter provides some background material on the subjects of vibration and stability of structures, and sets the course for the following contents.

Chapter 2 presents, in a synthetic and pragmatic way, the general approach for the analysis of the stability of elastic systems, i.e. the dynamic method, and emphasizes that the static and energy methods cannot instead be applied in presence of nonconservative force systems. Dynamic instability (flutter) is then introduced, and some examples of notable and well-known classical problems are presented and discussed in order to familiarize with the main concepts. Some basic references are given for further readings and deepening.

Chapter 3 deals with modal analysis with second-order effects of elastic mechanical systems and structures. It is shown how dead loads influence the natural vibration frequencies. In particular, taking into account the effect of geometric nonlinearity in the equations of motion through the geometric stiffness matrix, the study is reduced to a generalized eigenproblem where both the load multiplier and the natural frequency of the system are unknown. According to this approach, all the configurations intermediate between those of pure buckling and pure free vibrations can be investigated. Several examples are presented, including discrete or continuous systems subjected to axial load or uniform bending. A general finite element procedure is also outlined.

Chapter 4 is devoted to an experimental study conducted on the fundamental frequency evolution in slender beams subjected to imposed displacements.

Different values of geometric imperfections as well as different constraint conditions are investigated, and the natural frequencies are obtained using several methods. It is shown that, in case of displacement-controlled condition, a different evolution of the fundamental frequency vs. the axial load is obtained respect to the force-controlled case. The chapter provides a detailed description of the whole experimental setup. In particular, specimen preparation, experimental apparatus, experimental equipment and instrumentation, testing procedure, and data acquisition and analysis are discusses. Experimental results are then presented and commented. Although the chapter primarily exposes experimental tests, in conclusion, numerical simulations reproducing the experiments in a multibody dynamic modelling framework are presented, showing results which are in perfect accordance with those obtained in the laboratory.

Chapter 5 exclusively deals with a numerical and experimental study on natural frequencies and stability of simple space truss models loaded by dead loads. Numerical simulations are performed using a finite element software which runs modal analysis with second-order effects. Different constraint and load conditions are analyzed. In particular, the effects of the direction and magnitude of the acting load are studied, leading to show an interesting behaviour due to the asymmetry characterizing the considered models. In fact, while in some cases the frequencies exhibit a monotonic evolution as the load increases, in other cases there is a reversal in the tendency (e.g., a stiffening followed by a softening) due to different effects of the geometric stiffness. Also the buckling loads, of course, vary. In addition to the numerical models, experimental tests on a physical model are presented, in which the behaviour found in the numerical simulations is experimentally confirmed.

Chapter 6 investigates on dynamics and stability of suspension bridges under aerodynamic loads. In particular, the effects of steady aerodynamic loads on natural frequencies and static stability are studied using an analytical model. The single (central) span suspension bridge model is considered, and the linearized integro-differential equations describing the flexural and torsional deformations of the bridge deck are adopted as starting point. A generalized eigenvalue problem is then derived, in which, considering the steady aerodynamic drag force and pitching moment, all configurations intermediate between those of pure instability and pure free vibrations can be investigated. In the final part of the chapter, some address on how this study might be integrated into the aeroelastic dynamic stability analysis of very long-span suspension bridges is provided.

Chapter 7 contains a short review of the objective and contents of the developed study, and draws the main conclusions based on the original results found in the present research. Some addresses for further development of the presented work are also given.

Chapter 2

Dynamic Analysis of Stability

If the loading is nonconservative, the loss of stability may not show up by the system going into another equilibrium state but by exhibiting oscillations of increasing amplitude. To encompass this possibility we must consider the dynamic behaviour of the system because stability is essentially a dynamic concept.

In this chapter we will introduce the concept of dynamic instability and the general method to analyze the stability of elastic equilibrium: the dynamic method. A few classical examples of systems loaded by nonconservative forces will be presented in order to highlight the fundamental concepts. It will be shown that static analysis (Euler method) is in general not applicable to determine stability of an elastic structure subjected to nonconservative loads.

2.1 Introduction

The theory of elastic stability, which originated in the works of Euler, is now a very well-developed branch of applied mechanics employing many effective techniques and possessing a large number of problems already solved, as well as a very large body of literature. One of the major factors which contributed to the rapid accumulation of material in the field of elastic stability was undoubtedly the extremely successful concept of stability and critical force. In the theory of elastic stability it is assumed that for sufficiently small loads the equilibrium of an elastic system is stable, and that it remains so up to the first point of bifurcation of equilibrium forms; thereafter, the initial form of equilibrium becomes unstable.

The critical force (or, in general, a parameter of the force group) is then defined as the smallest value of the force at which, in addition to the initial form of equilibrium, there can exist others which are very close to the initial form. This concept is to be found as far as back as the works of Euler, who defined the critical force as “the force required to cause the smallest inclination of a column”. This approach, known as the Euler method or the static method, has enabled us to reduce the problem of the stability of a form of equilibrium to the simpler problem of finding the minimum characteristic value of certain boundary-value problems.

The usefulness of the Euler method in the theory of elastic stability cannot be disputed. Is has been also extended to problems of non-elastic stability, expressed in the concept of a “reduced modulus” introduced by Von Kármán. However, the Euler method is not universal, and its range of application can be clearly defined. The category of Eulerian problems in the theory of elastic stability is constituted by conservative systems that behave linearly in the pre-critical phase. In this case, the instability corresponds to a bifurcation, when a deformation mode not directly induced by the load has completely lost its stiffness. On the other hand in a real structure, where imperfections cannot be avoided, it is impossible to approach the critical load maintaining the structure close to its fundamental configuration. As a consequence, the Euler’s critical load is not by itself a reliable indication of the actual ultimate capacity of the structure and the result must be integrated by information about the post-critical behaviour.

As far back as the thirties of the last century it was established that in the case of shells a systematic and very significant divergence existed in the values of critical loads given by the classical theory and by experimental results. It was found that for thin shells initial inaccuracies and nonlinear effects assume considerable importance, and that the critical force corresponding to the points of bifurcation of equilibrium are in fact the upper limit of the critical forces, which are difficult to realize even under the most ideal experimental conditions. This fact led to the nonlinear theory of thin elastic shells.

A second factor is associated with the development of the theory of plastic stability. In 1946 Shanley pointed out that the concept of a reduced modulus corresponds only to a particular assumption concerning the behaviour of the load, and that in the plastic range the critical load should be determined by a different method from that used in the elastic range. Further investigations have clearly established the important part played by the behaviour of the load during the process of loss of stability and, in general, the part played by the time factor, which in the classical theory is not taken into account at all.

Conservative systems may exhibit a nonlinear behaviour from the beginning of the loading process, this is due to the large influence of displacements on the way the equilibrium is established. The critical threshold may therefore correspond to a limit point, rather than a bifurcation point, in the equilibrium path. In this case there not exist other configurations of equilibrium close to the initial one at the critical load. This is the case of the snap-through phenomenon shown by shallow arches, shells and trusses when loaded by transverse forces. This class of problems is obviously outside the range of applicability of the Euler method.

Anyway, a conservative structure reaches its limit of stability when it completely loses its stiffness, or with respect to the fundamental configuration (snap-through), or with respect to an adjacent configuration of equilibrium not directly activated by loads (buckling).

The loss of stability has, however, a dynamic nature and a static interpretation, admissible in conservative systems, is not always permissible outside this range. The loss of stability of elastic systems subjected to nonconservative forces is not due to a loss of stiffness. On the contrary, they lose stability when still possess a considerable stiffness, making the applicability of the static criterion impossible. As far back as near 1928-1929 Nikolai, while investigating one of the problems of elastic stability of a bar under follower axial load and torque moment, discovered that the Euler method led to a paradoxical result (Nikolai, 1928; 1929; 1955). In the problem he was investigating there were, in general, no forms of equilibrium close to the undisturbed (rectilinear) form, and it appeared that the rectilinear form of the bar would remain stable for all values of the torque. This result was, however, interpreted correctly as an indication that the Euler method was inapplicable to that particular problem, and that it should be replaced by the more general method of investigating stability –the method of small oscillations–. It was later discovered that an important part is played here by the existence of a potential of the external forces. The Euler method is applicable if the external forces have a potential (i.e. they are conservative forces), and in general is not applicable if they do not.

The basic method of investigating non-conservative problems in the theory of elastic stability is the dynamic method, which is based on the investigation of the oscillations of the system close to its position of equilibrium. This draws the theory of elastic stability closer to the general theory of stability of motion (Liapunov, 1892; Huseyin, 1986; Seyranian and Mailybaev, 2003). The Euler method, which reduces the problem to an analysis of the bifurcation of the forms of equilibrium of the system, can be looked upon as a particular case of the dynamic method.

Nonconservative problems of the theory of elastic stability were widely investigated during the second half of the last century mainly by Ziegler, Bolotin, and Herrmann. The sections that follow will be devoted to an elementary introduction to the fundamentals of the subject.

2.2 Massless Column Under Vertical Force

2.2.1 Euler's Method

To explain the reason why in a number of cases the formulation of the stability problem differs from the classical Euler formulation, we shall start by considering the well-known problem of a column compressed by a force with a fixed line of action (Figure 2.1).

We shall find the minimum value of the compressive force *P* for which, in addition to the rectilinear form of equilibrium, a slightly curved form first become possible. Having chosen the axes of coordinates as shown in Figure 2.1, we can derive a differential equation for the elastic line of the slightly bent column:

$$EI\frac{\mathrm{d}^2 v}{\mathrm{d}z^2} = P\left(f - v\right), \tag{2.1}$$

where EI is the bending stiffness of the column, f is the deflection at the end of the column. Making use of the following designation:

$$\frac{P}{EI} = \alpha^2, \tag{2.2}$$

we can write Equation (1) in the form:

$$\frac{\mathrm{d}^2 v}{\mathrm{d}z^2} + \alpha^2 v = \alpha^2 f. \tag{2.3}$$

Its general solution is:

$$v = C_1 \sin\alpha z + C_2 \cos\alpha z + f. \tag{2.4}$$

In order to find the three constants C_1, C_2 and f we have the three boundary conditions: $v\left(0\right) = 0,\ v'\left(0\right) = 0$ and $v\left(l\right) = f$. Substituting Expression (2.4) into the boundary conditions, we obtain the three relations:

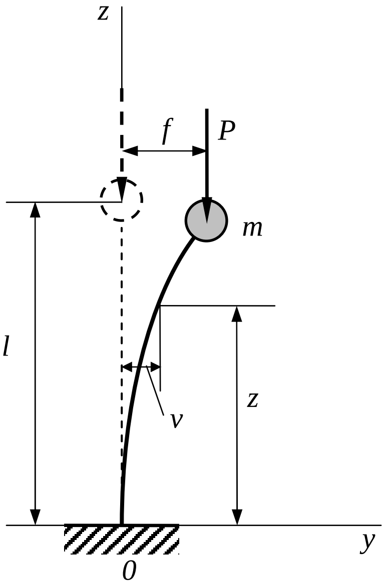

Figure 2.1 – Massless column with a point mass at the end compressed by a force acting in a fixed direction.

$$\begin{cases} C_2 + f = 0, \\ \alpha C_1 = 0, \\ C_1 \sin \alpha l + C_2 \cos \alpha l = 0, \end{cases} \tag{2.5}$$

which constitute a system of three linear algebraic equations in the three constants C_1, C_2 and f. The trivial solution of this system $C_1 = C_2 = C_3 = f = 0$ corresponds to the rectilinear form of equilibrium of the compressed column. Following the procedure adopted by Euler, we shall try to find the conditions under which, in addition to the rectilinear form of equilibrium, slightly curved forms close to the rectilinear form are possible. In order that the homogeneous system (2.5) has a non-trivial solution its determinant must vanish, i.e.:

$$\det\begin{bmatrix} 0 & 1 & 1 \\ \alpha & 0 & 0 \\ \sin\alpha l & \cos\alpha l & 0 \end{bmatrix} = 0. \tag{2.6}$$

It follows that $\cos\alpha l = 0$, and the minimum value of the force corresponding to this condition is:

$$P_c = \frac{\pi^2 EI}{4l^2}, \tag{2.7}$$

i.e., it is equal to the Euler value of the compressive force.

In the classical theory of elastic stability it is considered to be self-evident that when the force P reaches the minimum value at which, in addition to the undisturbed (rectilinear) form of the column, other very close curvilinear forms become possible, this value is the critical value. This definition of the critical force is not only the basis of methods which employ directly the differential equations of equilibrium, but is also the basis of a number of other methods.

2.2.2 Dynamic Method

We shall derive the equation of small oscillations of the column about its rectilinear position, assuming for simplicity that the distributed mass of the column is negligible compared with the mass m concentrated at the end (see Figure 2.1), and that the resistance forces can be ignored.

The equation of small oscillations is of the form:

$$EI\frac{\partial^2 v}{\partial z^2} = P\left(f - v\right) - m\left(l - z\right)\frac{\mathrm{d}^2 f}{\mathrm{d}t^2}, \tag{2.8}$$

where $v\left(z,t\right)$ is the dynamic deflection at each point and $f\left(t\right)$ is the deflection at the end. Equation (2.8) is satisfied by the expressions:

$$v\left(z,t\right) = V\left(z\right)\mathrm{e}^{\mathrm{i}\omega t}, \tag{2.9a}$$

$$f\left(t\right) = F\,\mathrm{e}^{\mathrm{i}\omega t}, \tag{2.9b}$$

where ω is some constant to be found. If this constant is real, then the column performs harmonic oscillations with frequency[1] ω about its rectilinear position. In this case we can assume (although we shall see later that this is not quite so) that the rectilinear form of the column is stable. If ω proves to be a complex number and if its imaginary part is negative, then this would correspond to disturbances which become infinitely large (as a result of linearizing the problem) with time. If $\omega = a + \mathrm{i}b,$ then:

$$v(z,t) = V(z)\mathrm{e}^{(\mathrm{i}a-b)t}, \tag{2.10}$$

and if $b < 0$ an exponentially increasing term appears in the expression for $v(z,t)$.

If we now substitute Expressions (2.9a) and (2.9b) into Equation (2.8) and use the definition (2.2),we obtain:

$$\frac{\mathrm{d}^2V}{\mathrm{d}z^2} + \alpha^2 V = \alpha^2 F + \frac{m\omega^2 F}{EI}(l - z). \tag{2.11}$$

The general solution of Equation (2.11) is:

$$V(z) = C_1 \sin\alpha z + C_2 \cos\alpha z + F + \frac{m\omega^2 F}{\alpha^2 EI}(l - z), \tag{2.12}$$

for which the boundary conditions remain as before: $V(0) = 0, V'(0) = 0$ and $V(l) = F.$ Making use of these conditions, we obtain a system of three linear algebraic equations in C_1, C_2 and $F,$ and if we equate to zero its determinant we obtain the frequency equation:

$$\det\begin{bmatrix} 0 & 1 & 1 + \dfrac{m\omega^2 l}{\alpha^2 EI} \\ \alpha & 0 & -\dfrac{m\omega^2}{\alpha^2 EI} \\ \sin\alpha l & \cos\alpha l & 0 \end{bmatrix} = 0. \tag{2.13}$$

---

[1] Angular frequency (rad/sec).

Whence:

$$\omega = \pm\sqrt{\frac{P}{ml}\frac{\cos\alpha l}{\dfrac{\sin\alpha l}{\alpha l}-\cos\alpha l}}. \tag{2.14}$$

Provided the expression under the root is positive, both frequencies are real, i.e. the rectilinear form of the column is stable (in the sense indicated above). The frequencies vanish when $\cos\alpha l = 0$ and become purely imaginary with further increase in the force *P*, when one of them has a negative imaginary part. The condition $\cos\alpha l = 0$ corresponds to a transition from the stable rectilinear form to an unstable form, and the critical value of the force *P* apparently coincides with the Euler value (2.7).

Thus, in the problem of the stability of a column compressed by a force acting in a fixed direction, the Euler method and the dynamic method give identical results.

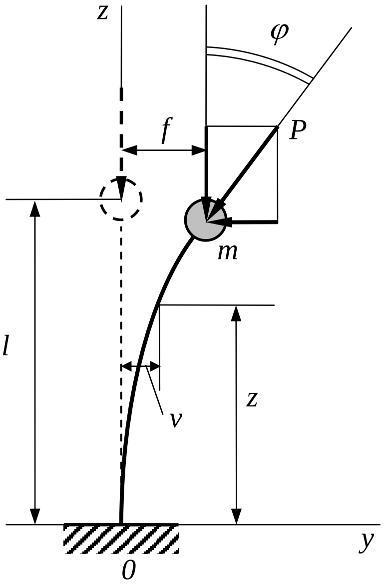

Figure 2.2 – Massless column with a point mass at the end loaded by a follower force.

2.3 Massless Column Under Follower Force

2.3.1 Euler’s Method

We can extend the Euler method to the problem of the stability of a column under the action of a compressive force which after deformation rotates together with the end section of the column and at all times remains tangential to its deformed axis (Figure 2.2). We shall leave open the question of how such a follower force is realized.

By virtue of the assumed smallness of the deflection, $P_x \cong P,\ \ P_y \cong P\varphi,$ where φ is the angle of rotation of the end section and $\varphi \cong v'(l)$.

The equation of the elastic line of the slightly bent column is given by:

$$EI\frac{\mathrm{d}^2 v}{\mathrm{d}z^2} = P(f - v) - P\varphi(l - z), \tag{2.15}$$

and its general solution, making use of the definition (2.2), can be written in the form:

$$v = C_1 \sin\alpha z + C_2 \cos\alpha z + f - \varphi(l - z). \tag{2.16}$$

There are four boundary conditions in this particular problem: $v(0) = 0,$ $v'(0) = 0,$ $v(l) = f,$ $v'(l) = \varphi.$ If we substitute Expression (2.16) into these conditions we obtain the system:

$$\begin{cases} C_1 \cos\alpha l - C_2 \sin\alpha l = 0, \\ C_2 + f - \varphi l = 0, \\ \alpha C_1 + \varphi = 0, \\ C_1 \sin\alpha l + C_2 \cos\alpha l = 0, \end{cases} \tag{2.17}$$

the determinant of which is:

$$\Delta = \det\begin{bmatrix} 0 & 1 & 1 & -l \\ \alpha & 0 & 0 & 1 \\ \sin\alpha l & \cos\alpha l & 0 & 0 \\ \cos\alpha l & -\sin\alpha l & 0 & 0 \end{bmatrix} = -1, \tag{2.18}$$

i.e. is non-zero for all values of P. This means that there are no values of P under which there can exist curvilinear forms of equilibrium of the column close to the undisturbed (rectilinear) form.

Pflüger and Feodos'ev, who were first to investigate this problem, came to the conclusion that a column compressed by a follower force cannot in general lose stability (Pflüger, 1950; Feodos'ev, 1953). In order to establish whether such a conclusion is correct, we must take a closer look at the fundamental concept underlying the Euler method, which relates it to the generally accepted concepts of stability of equilibrium (and motion).

Expressed in technical terms the concept of stability may be stated as follows. The form of equilibrium is said to be stable if a slight disturbance causes a small deviation of the system from the considered configuration of equilibrium, but by decreasing the magnitude of the disturbance the deviation can be made as small as required. On the other hand, the equilibrium is said to be unstable if a disturbance, however small, causes a finite deviation of the system from the considered form of equilibrium.

It will be readily seen that the concept of stability is not in effect implicit in the Euler method of the theory of elastic stability. It is possible, of course, that if there is a form of equilibrium close to the initial (undisturbed) form, the latter might become unstable by being replaced by another form of equilibrium. However, the existence of a branch point is neither a necessary nor a sufficient condition for loss of stability. The initial form of equilibrium may cease to be stable not only at branch points, but also at so-called limit points. On the other hand, cases are known where the existence of branch points does not lead to instability of the initial form of equilibrium (Ishlinskii et al., 1958). The most essential fact to bear in mind is that in using the Euler method, i.e. in considering only a number of forms of equilibrium, we automatically exclude from our analysis any possible forms of motion. The initial form of equilibrium may remain unstable, having been replaced by some form of motion, whereas if we use the Euler method we consider only the possible forms of equilibrium close to the initial form.

The complete solution can be obtained by assuming that a disturbance depends on time and by deriving equations which will enable the variation of the disturbance with time to be taken into account. Roughly speaking the form of equilibrium under investigation will be stable if all the disturbances are limited in time.

2.3.2 Dynamic Method

We shall now apply the dynamic method to the problem of the stability of the column loaded by a follower force reported in Figure 2.2. The equation of small oscillations of the column about its position of equilibrium in this case is:

$$EI\frac{\partial^2 v}{\partial z^2}=P\left(f-v\right)-P\varphi\left(l-z\right)-m\left(l-z\right)\frac{\mathrm{d}^2 f}{\mathrm{d}t^2}. \tag{2.19}$$

By making the substitutions:

$$v\left(z,t\right)=V\left(z\right)\mathrm{e}^{\mathrm{i}\omega t}, \tag{2.20a}$$

$$f\left(t\right)=F\,\mathrm{e}^{\mathrm{i}\omega t}, \tag{2.20b}$$

$$\varphi\left(t\right)=\Phi\,\mathrm{e}^{\mathrm{i}\omega t}, \tag{2.20c}$$

we reduce Equation (2.19) to the form:

$$\frac{\mathrm{d}^2 V}{\mathrm{d}z^2}+\alpha^2 V=\alpha^2 F-\alpha^2\Phi\left(l-z\right)+\frac{m\omega^2 F}{EI}\left(l-z\right). \tag{2.21}$$

Its solution:

$$V\left(z\right)=C_1\sin\alpha z+C_2\cos\alpha z+F-\Phi\left(l-z\right)+\frac{m\omega^2 F}{\alpha^2 EI}\left(l-z\right) \tag{2.22}$$

must satisfy the boundary conditions $V\left(0\right)=0,\ V'\left(0\right)=0,\ V\left(l\right)=F,\ V'\left(l\right)=\Phi.$ from this we obtain the frequency equation:

$$\det\begin{bmatrix} 0 & 1 & 1+\dfrac{m\omega^2 l}{\alpha^2 EI} & -l \\ \alpha & 0 & -\dfrac{m\omega^2}{\alpha^2 EI} & 1 \\ \sin\alpha l & \cos\alpha l & 0 & 0 \\ \alpha\cos\alpha l & -\alpha\sin\alpha l & -\dfrac{m\omega^2}{\alpha^2 EI} & 0 \end{bmatrix}=0, \tag{2.23}$$

the solution of which gives the formula:

$$\omega = \pm \sqrt{\frac{P}{ml} \frac{1}{\frac{\sin \alpha l}{\alpha l} - \cos \alpha l}}. \tag{2.24}$$

As the force P increases from zero, the natural frequencies increase in magnitude; when:

$$\tan \alpha l = \alpha l \tag{2.25}$$

they become infinite, and with further increase in P they become purely imaginary, their signs remaining opposite. The smallest root of Equation (2.25) is $\alpha l = 4.493$, which, from Expression (2.2), gives a critical value of the follower force of:

$$P_c = \frac{20.19\, EI}{l^2}. \tag{2.26}$$

Thus, in the case of a column under the action of a follower force, the Euler method leads to erroneous results: the rectilinear form of the column for sufficiently large values of the force P proves to be unstable, although in this particular problem there cannot exist curvilinear forms of equilibrium close to the initial rectilinear form. The loss of stability in which the structure is oscillating at the critical load is called oscillatory instability or flutter, and the critical load is called the flutter load. The present example is a limiting case of flutter in which the frequency tends to infinity at the loss of stability[2].

2.3.3 System with Two Degrees of Freedom

The features of the problem considered in Section 2.3.2, become even more apparent if we consider a system with two degrees of freedom. We can take, for such a system, a column with two concentrated masses as an example.

Let m_1 and m_2 be the masses, $f_1(t)$ and $f_2(t)$ their displacements in the direction of the y-axis (Figure 2.3). To obtain the frequency equations we choose a procedure slightly different from the one employed in Section 2.3.2. Using D'Alembert's principle we form the equations of the small oscillations of the

---

[2] The infinite value of the frequency is due to our neglect of the mass between the column ends.

column about the undisturbed equilibrium configuration:

$$f_1 = -\delta_{11} m_1 \frac{\mathrm{d}^2 f_1}{\mathrm{d}t^2} - \delta_{12} m_2 \frac{\mathrm{d}^2 f_2}{\mathrm{d}t^2}, \tag{2.27a}$$

$$f_2 = -\delta_{21} m_1 \frac{\mathrm{d}^2 f_1}{\mathrm{d}t^2} - \delta_{22} m_2 \frac{\mathrm{d}^2 f_2}{\mathrm{d}t^2}, \tag{2.27b}$$

where $\delta_{11}(P)$, $\delta_{12}(P)$, $\delta_{21}(P)$ and $\delta_{22}(P)$ are the corresponding displacements produced by unit transverse forces applied to the column. These displacements are determined, obviously, taking into account the force P.

The unit displacements are easily found from elementary considerations. For this purpose we use the equation of static bending:

$$EI \frac{\mathrm{d}^4 v}{\mathrm{d}z^4} + P \frac{\mathrm{d}^2 v}{\mathrm{d}z^2} = 0, \tag{2.28}$$

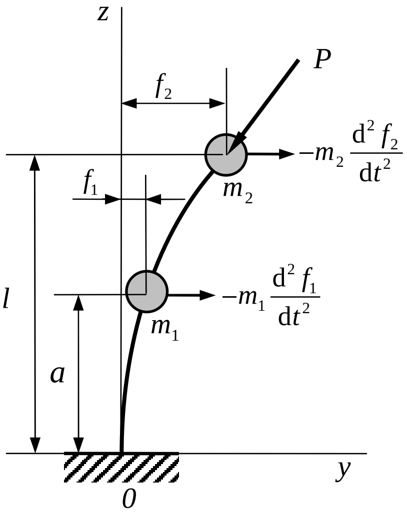

Figure 2.3 – Column with two point masses loaded by a follower force.

which is obtained from Equation (2.8) as a result of a repeated termwise differentiation. The equation possesses a general integral:

$$v(z) = C_1 \sin\alpha z + C_2 \cos\alpha z + C_3 z + C_4, \tag{2.29}$$

where, as before, the notation (2.2) is used. Considering in succession the cases of the effect of a unit force applied to the masses m_1 and m_2, and subjecting the solution to boundary conditions we obtain:

$$\begin{aligned}
\delta_{11} &= \frac{1}{\alpha P}\left(\sin\alpha h - \alpha h \cos\alpha h\right),\\
\delta_{12} &= \frac{1}{\alpha P}\left[\sin\alpha l - \alpha h \cos\alpha l - \sin\alpha\left(l-h\right)\right],\\
\delta_{21} &= \frac{1}{\alpha P}\left[\sin\alpha l - \alpha l \cos\alpha l + \sin\alpha\left(l-h\right)\right],\\
\delta_{22} &= \frac{1}{\alpha P}\left(\sin\alpha l - \alpha l \cos\alpha l\right).
\end{aligned} \tag{2.30}$$

Let us note that, in general, $\delta_{11} \neq \delta_{21}$, i.e. the reciprocity principle for displacements is not valid. We shall return to this remark in the sequel. Analogous to (2.9.a) and (2.9.b) we set in this case:

$$f_1(t) = F_1 \, \mathrm{e}^{\mathrm{i}\omega t}, \tag{2.31a}$$

$$f_2(t) = F_2 \, \mathrm{e}^{\mathrm{i}\omega t}. \tag{2.31b}$$

As a results we obtain the frequency equation:

$$\det\begin{bmatrix} m_1\delta_{11}\omega^2 - 1 & m_2\delta_{12}\omega^2 \\ m_1\delta_{21}\omega^2 & m_1\delta_{22}\omega^2 - 1 \end{bmatrix} = 0. \tag{2.32}$$

Expanding the determinant and solving the equation, we arrive at the formula:

$$\omega^2 = \frac{m_1\delta_{11} + m_2\delta_{22} \pm \sqrt{\left[\left(m_1\delta_{11} - m_2\delta_{22}\right)^2 + 4 m_1 m_2 \delta_{12}\delta_{21}\right]}}{2 m_1 m_2 \left(\delta_{11}\delta_{22} - \delta_{12}\delta_{21}\right)}. \tag{2.33}$$

For sufficiently small values of the force P Formula (2.33) gives real values for the frequency of vibrations. However, as the force P reaches a certain critical value P_c, the expression underneath the radical becomes equal to zero and the frequency equation will have a double root. With further increase of the force P among the natural frequencies there will be a frequency which has a negative imaginary part. As may be seen from Formulas (2.31a) and (2.31b), this corresponds to unbounded increase of disturbances in time, i.e. instability of the rectilinear form of the equilibrium of the column.

The formula for critical forces may be expressed in the form:

$$P_c = \frac{\beta EI}{l^2}. \tag{2.34}$$

For $m_1 = 0$ we obtain $\beta \cong 20.19,$ i.e. we are led to Formula (2.26). With $m_2 = 0$ and $h = l/2$ the critical value, as should have been expected, becomes exactly four time as large.

2.4 Discussion of Previous Results

In connection with the problems we have just examined, the following questions arise. Why is it that the Euler method is acceptable in one case, but not in the other? What is the physical meaning of the instability discovered in the second problem?

To find the answer to these questions let us examine once again the behaviour of the column in both problems after the occurrence of small deviations from the rectilinear form. Instead of the frequencies $\omega,$ we introduce the characteristic exponents connected to the frequencies by the simple relations $s = \mathrm{i}\omega.$ The expressions for the dynamic deflection of the column then assumes the form:

$$v(z,t) = V(z)\mathrm{e}^{st}. \tag{2.35}$$

The rectilinear form of the column becomes unstable if one of the characteristic exponents has a positive real part.

The behaviour of the characteristic exponents can conveniently be represented graphically, their real parts being taken as abscissas and their imaginary parts as ordinates; points corresponding to various values of P are then joined to give a continuous curve.

Figure 2.4 shows the variation of the characteristic exponents for the first case

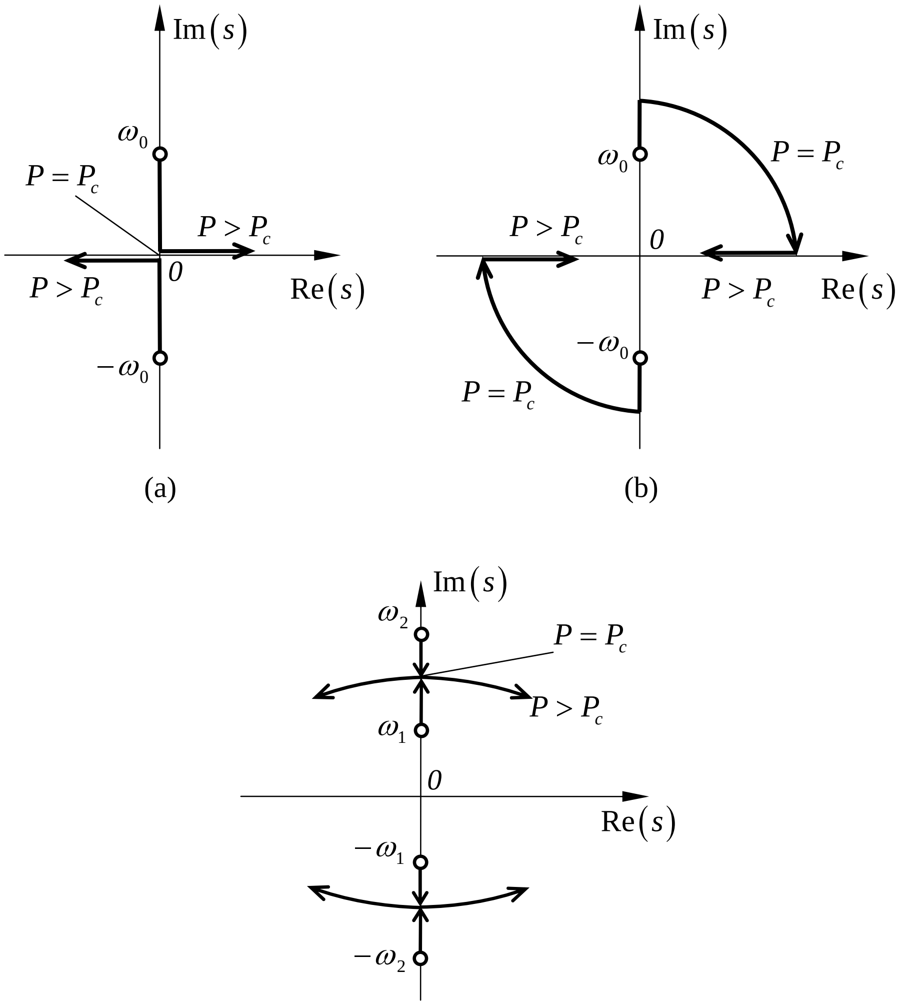

(a) (b)

(c)

Figure 2.4 – Variation of the characteristic exponents with the load P in the three analyzed cases: (a) column with a point mass loaded by a force acting in a fixed direction (column in Figure 2.1); (b) column with a point mass loaded by a follower force (column in Figure 2.2); (c) column with two point masses loaded by a follower force (column in Figure 2.3).

(a force acting in a fixed direction). When $P = 0$ we have $s = \pm \mathrm{i}\omega_0$, where ω_0 is the natural frequency of the unloaded column. With increase in P the characteristic exponents, while remaining purely imaginary, decrease in modulus until when $P = P_c$ they vanish. The vanishing of the characteristic exponents corresponds to neutral equilibrium –to the existence, in addition to the initial form of equilibrium, of other infinitely close forms of equilibrium. If $P > P_c$ one of the characteristic exponents is real and positive, which corresponds to instability of the rectilinear form of equilibrium of the column

Whereas in the case of a force acting in a fixed direction the characteristic exponent enters the right-hand half-plane of the complex variable, passing through the value of $s = 0,$ in the case of a follower force (Figures 2.4(b), 2.4(c)) it enters this half-plane without passing through this value. In the first case the Euler method can be used to establish the point of transition from stability to instability; in the second case it cannot.

The Euler method is applicable in cases when the external forces acting on the body are conservative, i.e. when they have a potential (since we are dealing with ideally elastic bodies, the internal forces in our problems do have a potential). It can be easily shown that when the external forces have a potential, transition from stability to instability takes place only through the value of $s = 0,$ i.e. in this case the Euler method gives correct results. But if the external forces are not conservative, then, although in a number of problems it may give the correct solution, the Euler method in order to avoid errors, should be replaced by the more general dynamic method based on considerations of the oscillations of the system about the equilibrium position under investigation.

It is not difficult to see that in the problem under consideration the follower force has no potential. The indication of whether a potential of the external forces exists is provided by the independence of the work done by these forces on the manner in which the system attains its final state. Figure 2.5 shows three ways in which the column can reach a state defined by a transverse deflection f and an angle of rotation φ of the end section. In case (a) (rotation through an angle φ with a subsequent displacement) the work done by the force P is obviously negative; in case (b) (displacement with a subsequent rotation) it is zero, and in case (c) (rotation through an angle $-\varphi,$ a displacement and a final rotation through an angle 2φ) the work done it positive[3].

In contrast to the well-known and thoroughly studied self-excited oscillating systems, the non-conservative nature of which depends on negative friction, in the problem considered here the coupled interaction of the degrees of freedom plays a significant part. The supply of energy to a column subjected to a follower force (Figure 2.5) is possible only for a particular change with time of the angle of rotation φ and of the linear displacement f. This coupled interaction becomes more obvious if we consider the small oscillations of the bar as a system with two degrees of freedom (see Section 2.3.3). The instability of the system is of an oscillatory nature with a definite phase relation between φ and f corresponding to the absorption of energy form outside. The case of a mass concentrated at a point considered in Section 2.3.3 should be treated as the limiting case of a system with two degrees of freedom in which the second partial frequency tends to infinity.

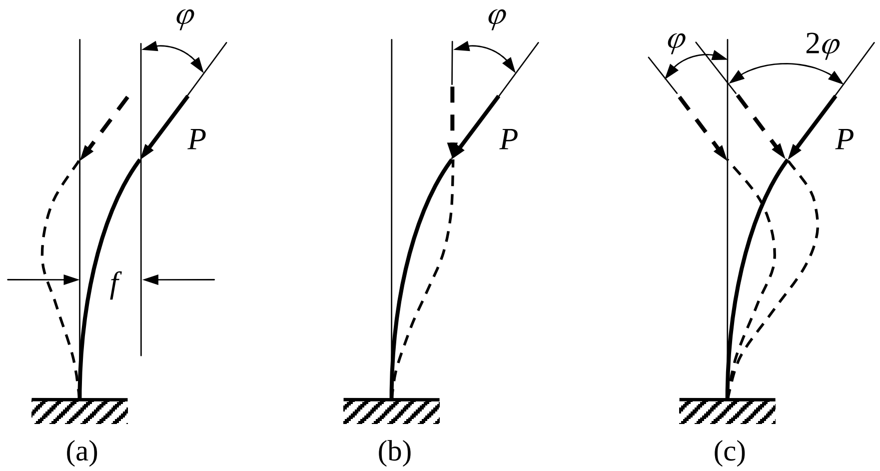

Figure 2.5 – Three different ways to reach a state defined by a transverse displacement f and an angle of rotation φ: (a) rotation through an angle φ with a subsequent displacement; (b) displacement with a subsequent rotation; (c) rotation through an angle $-\varphi$, a displacement and a final rotation through an angle 2φ.

---

[3] We call attention also to the fact that the reciprocity relations for displacements are not satisfied, as indicated in discussing Formulas (2.30).

2.5 Dynamic Analysis of Stability

The basic method of investigating nonconservative problems in the theory of elastic stability is therefore the dynamic method, in which the local stability is studied by applying a small perturbation to the equilibrium state being tested, and then investigating the motion that results in order to infer or deny stability. The practicality of this approach depends crucially on the linearization of the equations of motion of the perturbation.

Let $[M]$ be the symmetric mass matrix, which is assumed positive definite, and $[K]$ the tangent stiffness matrix, which is real but generally unsymmetric because of load nonconservativeness. The perturbation motion is denoted as:

$$\{\delta(t)\} = \{u(t)\} - \{u(0)\}, \qquad t \geq 0^+ \tag{2.36}$$

where $\{u\}$ is the displacement vector, $\{\delta\}$ is the perturbed displacement vector, and t is the time.

The discrete, unforced, undamped governing equations of motion are:

$$[M]\{\ddot{\delta}\} + [K]\{\delta\} = \{0\}. \tag{2.37}$$

The ordinary differential equations (2.37) express the linearized dynamic equilibrium between stiffness and inertial forces. The stiffness forces generally include nonconservative loading effects.

The linear ordinary differential equation system (2.37) can be treated by assuming the eigenmodal expansion:

$$\{\delta(t)\} = \sum_i \{\delta_i(t)\} = \sum_i \{\delta_{0i}\}\,\mathrm{e}^{s_i t}, \tag{2.38}$$

where i ranges over the number of degrees of freedom (number of state parameters). The s_i are generally complex numbers called characteristic exponents whereas the corresponding column vectors $\{\delta_{0i}\}$ are the characteristic modes or characteristic vectors. Introducing Expression (2.38) into Equation (2.37) yields:

$$\left([K] + s_i^2 [M]\right)\{\delta_{0i}\} = \{0\}, \tag{2.39}$$

which is the characteristic problem or eigenproblem that governs dynamic stability. A nontrivial solution to the system (2.39) exists if and only if the determinant of the coefficient matrix of the vector $\{\delta_{0i}\}$ is equal to zero. This yields the following generalized eigenvalue problem:

$$\det\left(\left[K\right]+s_i^2\left[M\right]\right)=0, \tag{2.40}$$

in which s_i^2 are the eigenvalues. The square root of these eigenvalues yield the characteristic exponents s_i of the eigenmodal expansion (2.38). The characteristic exponents may be expressed in the form:

$$s_i=\alpha_i+\mathrm{i}\omega_i, \tag{2.41}$$

where α_i and ω_i are real numbers, and $\mathrm{i}=\sqrt{-1}$. The component representation of the square of s_i is:

$$s_i^2=\left(\alpha_i^2-\omega_i^2\right)+2\mathrm{i}\alpha_i\omega_i, \tag{2.42}$$

while recalling the component representation of the exponential of a complex number, we have:

$$\mathrm{e}^{s_i t}=\mathrm{e}^{(\alpha_i+\mathrm{i}\omega_i)t}=\mathrm{e}^{\alpha_i t}\left(\cos\omega_i t+\mathrm{i}\sin\omega_i t\right). \tag{2.43}$$

On the basis of the representation (2.43) we can classify the growth behaviour of the subsequent motion and consequently the stability of the system.

If s_i^2 is negative real, its square root is a purely imaginary number:

$$s_i=\pm\mathrm{i}\omega_i, \tag{2.44}$$

and the motion $\{\delta_i\}$ associated with $\mathrm{i}\omega_i$ is harmonic and bounded, as illustrated in Figure 2.6. The system is dynamically stable for this individual eigenvalue. If all eigenvalues are negative real and distinct, the system is dynamically stable because any superposition of harmonic motion of different periods is also a harmonic motion. If two or more eigenvalues coalesce the analysis become more complicated because of the appearance of secular terms that grow linearly in time. These effects can be studied in more detail in treatises in mechanical vibrations. The presence of positive damping will of course damp out these oscillations and the system eventually returns to the static equilibrium position.

If s_i^2 is positive real, we have:

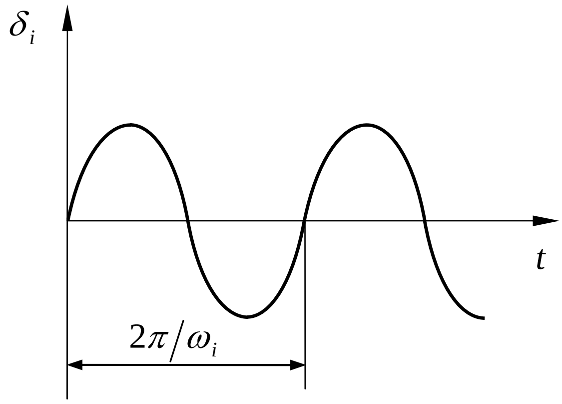

Figure 2.6 – Harmonic oscillatory motion (stable case).

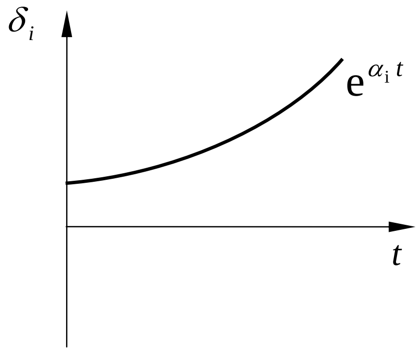

Figure 2.7 – Aperiodic, exponentially growing motion (divergence instability).

$$s_i = \pm\alpha_i . \tag{2.45}$$

The $+\alpha_i$ square root will give rise to an aperiodic, exponentially growing motion. The other root will give rise to an exponentially decaying motion. When the two solutions are combined, the exponentially growing one will dominate for sufficiently large t as sketched in Figure 2.7, and the system is exponentially unstable.

In practical studies, the characteristic exponents are function of a control parameter, say λ. The transition from stability (in which all roots are negative real) to this type of instability necessarily occurs when a eigenvalue $s_i^2(\lambda)$, moving from left to right as λ varies, passes through the origin $s^2 = 0$ of the s^2 complex plane. This type of instability is called divergence and it represents a static instability, since the structure when loses stability is incapable of vibrating, and simply diverges. Figure 2.8 illustrates loss of stability by divergence in the so-called root locus plots. As λ is varied in the s^2-plane, eigenvalue s_i^2 passes from the left-hand plane to the right-hand plane through the origin $s_i^2 = 0$ (Figure 2.8(a)). Figure 2.8(b) depicts the same phenomenon on the s-plane, for the root pair $\pm s_i$. In this case, the critical load may be obtained by static analysis (Euler method) because the motion is at constant velocity ($\omega_i = 0$) and the inertia forces at incipient instability vanish (after instability the motion is accelerated). Such motion implies the existence of neutral equilibrium when $\{\delta_i(0)\} = \{0\}$ and $\{\dot{\delta}_i(0)\} = \{0\}$, and this explains why the static analysis gives the right critical load. Every conservative system (with forces derivable from a potential) exhibits static instability (divergence).

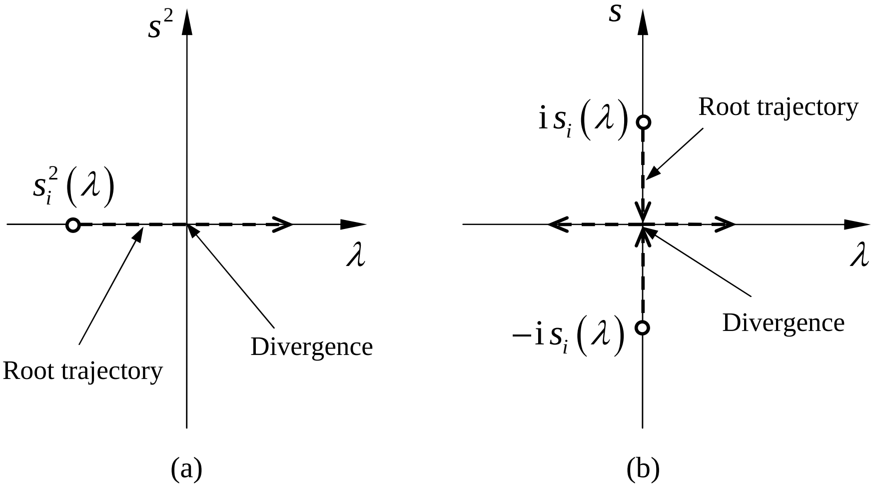

Figure 2.8 – Root locus plots on the complex s^2-plane (a) and s-plane (b) for divergence instability.

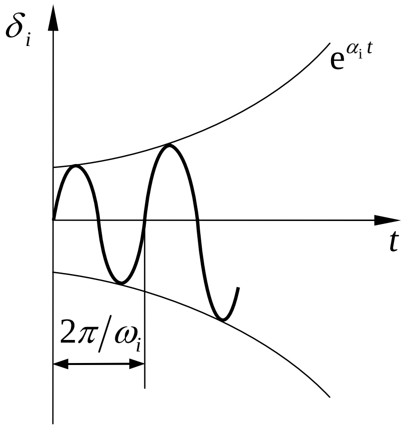

Figure 2.9 – Periodic, exponentially growing motion (flutter instability).

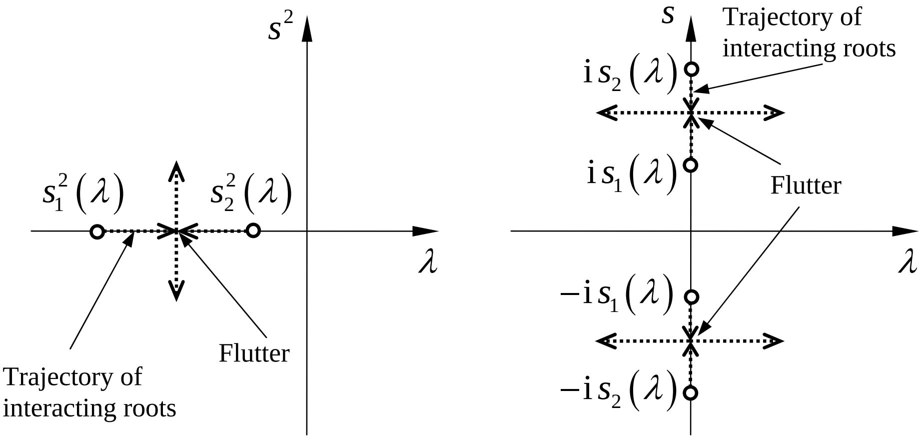

(a) (b)

Figure 2.10 – Root locus plots on the complex s^2-plane (a) and s-plane (b) for flutter instability.

If s_i^2 is complex, solutions of the eigenproblem (2.39) occur in conjugate pairs because both matrices $\left[M\right]$ and $\left[K\right]$ are real. Consequently, if $s_i^2=\left(\alpha_i^2-\omega_i^2\right)+\mathrm{i}\left(2\alpha_i\omega_i\right)$ is a complex eigenvalue, its conjugate is $\overline{s_i^2}=\left(\alpha_i^2-\omega_i^2\right)-\mathrm{i}\left(2\alpha_i\omega_i\right)$. Tacking the square root of these pair we found four characteristic exponents:

$$\pm\alpha_i\pm\mathrm{i}\omega_i. \tag{2.46}$$

Two of these square roots will have positive real parts $\left(+\alpha_i\right)$ and for sufficiently large t they will eventually dominate the other pair, yielding exponentially growing oscillations (see Figure 2.9). This periodic exponential instability is called oscillatory instability or flutter, and it represents a dynamic instability. If the system is initially stable (i.e., all roots are negative real), then transition to this type of instability occurs when at a certain value of λ two real roots coalesce on the real axis and branch out into the complex s^2-plane. Figure 2.10 illustrates loss of stability by flutter in the root locus plots. As λ is varied, two interacting eigenvalues, labelled as s_1^2 and s_2^2 coalesce on the negative real axis of the s^2-plane and branch out into the unstable region (Figure 2.10(a)). Figure 2.10(b) depicts the same phenomenon on the s-plane for the interacting roots, which appears in complex-conjugate pairs. In this case the loss of stability is characterized by a motion at a circular frequency $\omega_1=\omega_2=\omega$ other than zero, called the flutter frequency. When stability is lost by flutter, static analysis of the critical load is generally inapplicable.

From the preceding study it follows that the only stable region in the complex s^2-plane is the negative real axis:

$$\mathrm{Re}\left(s^2\right)<0, \qquad \mathrm{Im}\left(s^2\right)=0. \tag{2.47}$$

The rest of the s^2-plane is unstable (see Figure 2.11(a)). On the complex s-plane, the stable region is the left-hand plane:

$$\alpha=\mathrm{Re}\left(s\right)<0, \tag{2.48}$$

while the imaginary axis $\alpha=0$ can be stable or unstable. The right-hand s-plane $\alpha>0$ is unstable (see Figure 2.11(b)).

Another commonly used visualization technique is the root amplitude plots. These plots show the magnitude of $s_i(\lambda)$, that is $|s_i(\lambda)|$, on the vertical axis against the control parameter λ on the horizontal axis. If the eigenvalue is real, $|s_i|$ is simply its absolute value whereas if it is complex $|s_i|$ is its modulus. Figures 2.12(a) and 2.12(b) illustrate typical root amplitude plots in loss of stability by divergence and flutter, respectively.

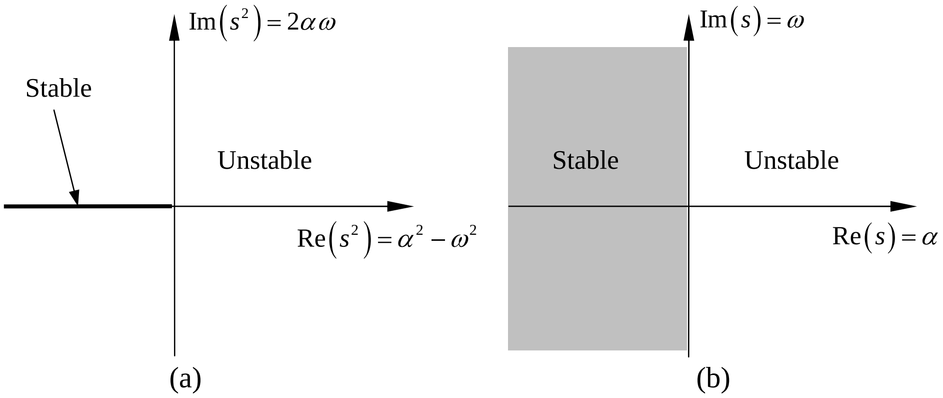

Figure 2.11 – Stable and unstable regions in the complex s^2-plane (a) and s-plane (b).

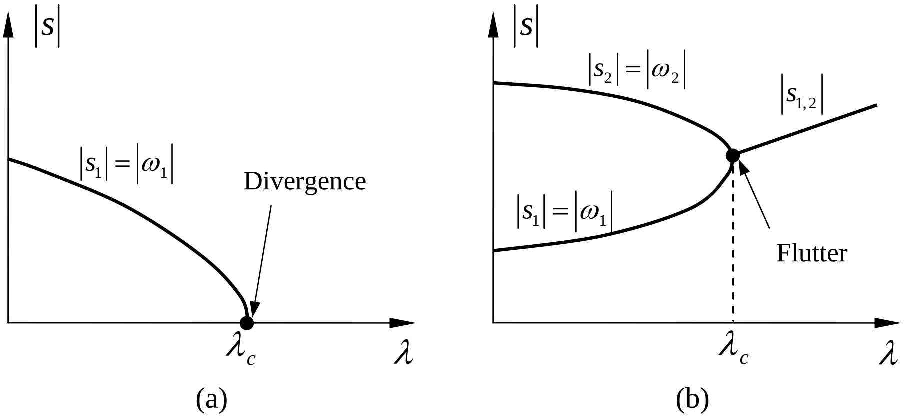

Figure 2.12 – Root amplitude plots illustrating loss of stability by divergence (a) and flutter (b).

2.6 Elastically Supported Rigid Plate Under Aerodynamic Forces

Let us consider the stability of a massive rigid plate of unit width and specific mass μ per unit length , suspended on springs of stiffness C_1 and C_2 as shown in Figure 2.13. The plate, initially in a horizontal position of static equilibrium, is loaded by wind of velocity v, characterized by wind force resultant $F = kv^2\vartheta$ acting at a distance a ahead of the downwind end of the plate; k is a constant, ϑ is the rotation of the plate. (The foregoing definition of F in valid only for very slow steady oscillations, such that $\omega b / v \ll 1$; see Bisplinghoff et al., 1996). The location of the resultant of the aerodynamic forces on the plate is called in aeroelasticity the aerodynamic center. Its location does not depend on angle ϑ. For two-dimensional incompressibile flow this center is located at $a = 3b/4$, while for supersonic flow it is located at $a = b/2$ (see Dowell, 2004). Denoting the deflection from the static equilibrium position at midpoint as w (Figure 2.13), the inertia effects are characterized by vertical inertia force $\mu b\ddot{w}$, applied at the center of the plate, and inertia moment $\mu b^3\ddot{\vartheta}/12$. The equations of motion may be obtained as the equations of dynamic equilibrium of vertical forces and moments about the center of the plate, and they yield the following system of two linear ordinary differential equations for w and ϑ:

$$\begin{aligned} &\ddot{w} + a_{11} w + a_{12} \vartheta = 0, \\ &\ddot{\vartheta} + a_{21} w + a_{22} \vartheta = 0, \end{aligned} \tag{2.49}$$

in which:

$$\begin{aligned} &a_{11} = \frac{C_1 + C_2}{\mu b}, \qquad a_{12} = \frac{C_1 - C_2}{2\mu} - \frac{kv^2}{\mu b}, \\ &a_{21} = \frac{6}{b^2\mu}\left(C_1 - C_2\right), \qquad a_{22} = \frac{3}{b\mu}\left(C_1 + C_2\right) - \frac{12kv^2}{\mu b^3}\left(a - \frac{b}{2}\right). \end{aligned} \tag{2.50}$$

The loss of stability due to divergence (equivalent to static buckling) may be determined by setting $\ddot{w} = \ddot{\vartheta} = 0$. Equations (2.49) then become a system of two linear algebraic homogeneous equations, and so the loss of stability occurs when

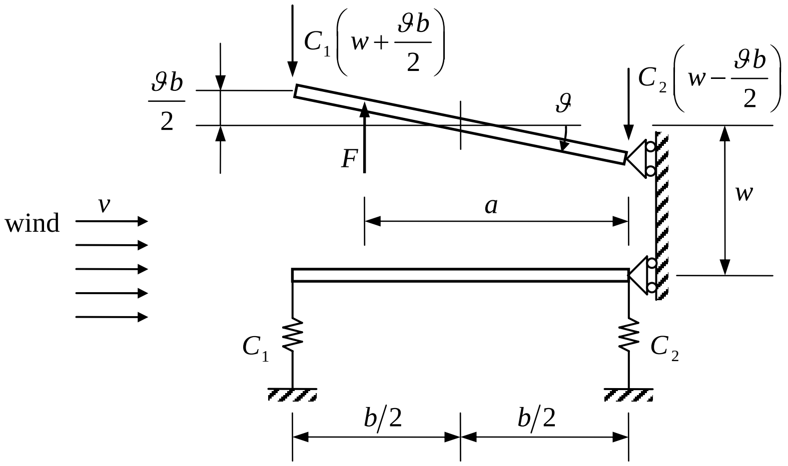

Figure 2.13 – Rigid plate suspended on springs and loaded by wind of constant velocity *v*.

$\det a_{ij} = 0.$ From this condition, the critical wind velocity for divergence may be solved, and it is found that (since v is real) divergence is possible only if $C_2 > C_1(b/a - 1).$

The dynamic solutions are found by substituting $w = q_1 \mathrm{e}^{\mathrm{i}\omega t}$ and $\vartheta = q_2 \mathrm{e}^{\mathrm{i}\omega t}$. This reduces Equations (2.49) to the following homogeneous linear algebraic equation for the amplitudes q_1 e q_2:

$$\begin{bmatrix} a_{11} - \omega & a_{12} \\ a_{21} & a_{22} - \omega^2 \end{bmatrix} \begin{Bmatrix} q_1 \\ q_2 \end{Bmatrix} = \begin{Bmatrix} 0 \\ 0 \end{Bmatrix}. \tag{2.51}$$

Nonzero amplitudes are possible only if the determinant of this equation system vanishes, which yields the condition:

$$\omega^2 = \frac{a_{11} + a_{22}}{2} \pm \sqrt{\left(\frac{a_{11} + a_{22}}{2}\right)^2 - a_{11}a_{22} + a_{12}a_{21}}. \tag{2.52}$$

Assuming that $a_{11} + a_{22} > 0,$ the condition that ω^2 be real and positive requires that:

$$0 < a_{11} a_{22} - a_{12} a_{21} < \left(\frac{a_{11} + a_{22}}{2} \right)^2 . \tag{2.53}$$

The second of these inequalities reduces to $(a_{11} - a_{22})^2 + 4 a_{12} a_{21} > 0,$ and it is found that the condition (2.53) is always satisfied if $C_1 < C_2$ (because $a_{12} a_{21} > 0$); in this case no flutter is possible. If $C_1 > C_2,$ then this condition can be violated and flutter is possible for a sufficiently high wind speed $v,$ which is solved by the foregoing condition.

The condition $a_{11} a_{22} - a_{12} a_{21} = 0$ yields the critical velocities for divergence $(\omega = 0)$, that is, static buckling, the case we have already solved.

It may be noted that the condition for critical velocity is not changed if the initial angle of attack of the plate is other than zero. In this case ϑ and w must be interpreted as incremental generalized displacements due to elastic deformations of the springs; the problem is analogous to that of lateral deflection of an imperfect column (see Bisplinghoff et al., 1996).

The last problem illustrates some but not all of the essential aspects of instability of aircraft wings as well as suspension bridges. In wings design it is desirable to make flutter impossible at any velocity. This is achieved with $C_2 > C_1.$ It can be shown that, more generally, stability of a plate whose center of gravity is not at midlength is achieved if the center of the spring stiffness of the links is behind the center of gravity.

In relation to the suspension bridge problem, the plate in our example may be imagined as a section of the roadway and the springs model the suspension cables. A realistic analysis of a suspension bridge, however, must also take into account the effect of motions $\vartheta(t)$ and $w(t)$ on the aerodynamic forces, as well as the inertia of the added mass of air that is forced to move with the plate.

The understanding of dynamic stability of suspension bridges was greatly advanced by the collapse of the first Tacoma Narrows Bridge near Seattle in 1940 (Bowers, 1940; Simiu and Scanlan, 1986). Shortly after the erection of the bridge, which was of a much lighter design than the preceding large suspension bridges (the Golden Gate Bridge in San Francisco, opened in 1937, and the George Washington Bridge over the Hudson River in New York, opened in 1931), a strong gale caused large torsional oscillations of the center span that produced collapse within a few hours. These oscillations as well as the subsequent collapse

Figure 2.14 – Oscillations and collapse of the first Tacoma Narrows Bridge.

were recorded on a film (Figure 2.14). Analysis of this disaster (e.g., von Kármán, 1940; Farquarson, 1954; Simiu and Scanlan, 1986) eventually led to a much better understanding of the behavior of suspension bridges and made it possible to design light large-span suspension bridges that are safe from aerodynamic instability. An example is the Humber Bridge over the mouth of the Humber River in England, whose span (in 1990 a world record) is 1410 m (compared with 853 m for the Tacoma Narrows Bridge and 1280 m for the Golden Gate Bridge, which held the world record until the Verrazzano Narrows Bridge in New York, also of classical design, surpassed it in the 1960s; see, e.g., Leonhardt, 1982, which gives a good discussion of practical design aspects). The current world record for suspension bridges is held by the Akashi Kaikyo Bridge, located over the Akashi Strait in Japan, whose central span is 1991 m.

2.7 Equations Governing Flutter of Suspension Bridges

To supplement the preceding discussion of the behaviour of suspension bridges, let us state the full equations that are adequate for most practical purposes. The equations of motion of the bridge deck beam (Figure 2.15) that vibrates flexurally and torsionally in a steady flow of air and does not exhibit significant warping torsion or cross-section distortion are partially differential equations of the form:

$$\begin{aligned} &\left(EI\,w_{,xx}\right)_{,xx} + \mu w_{,tt} + \mu y_e \vartheta_{,tt} + C_w w_{,t} + L = 0, \\ -&\left(GJ\,\vartheta_{,xx}\right)_{,x} + \mu y_e w_{,tt} + I_\mu \vartheta_{,tt} + C_\vartheta \vartheta_{,t} + M = 0, \end{aligned} \tag{2.54}$$

in which subscripts following a comma denote partial derivatives (e.g., $w_{,tt} = \ddot{w} = \partial^2 t / \partial t^2$); ϑ is the rotation about beam axis; EI is the flexural stiffness; GJ is the torsional stiffness (for simple or Saint Venant's torsion); μ is the beam mass per unit length; I_μ is the mass moment of inertia about the elastic axis; y_e is the distance of the elastic axis from the inertia axis, C_w, C_ϑ are the damping coefficients for bending and torsional motions, respectively; and L, M are the aerodynamic lift force and moment per unit length. According to Simiu and Scanlan (Simiu and Scanlan, 1996):

$$\begin{aligned} L &= -\frac{1}{2}\rho v^2\, 2b\left[KH_1(K)\left(\frac{\dot{w}}{v}\right) + KH_2(K)\left(\frac{b\dot{\vartheta}}{v}\right) + K^2 H_3(K)\vartheta\right], \\ M &= -\frac{1}{2}\rho v^2 (2b)^2\left[KA_1(K)\left(\frac{\dot{w}}{v}\right) + KA_2(K)\left(\frac{b\dot{\vartheta}}{v}\right) + K^2 A_3(K)\vartheta\right], \end{aligned} \tag{2.55}$$

in which b is the width of the deck; $K = b\omega/v$ is the so-called reduced frequency of oscillation; ω is the angular frequency of oscillation; v is the undisturbed wind velocity; and $H_1, H_2, H_3, A_1, A_2, A_3$ are aerodynamic coefficients depending on $K,$ known as flutter derivatives. Further one must add the boundary condition of the beam; for example, $w = w_{,x} = \vartheta = 0$ at $x = 0$ and $x = l$ for fixed ends.

2.8 Conservative and Nonconservative Forces

Let us now consider the nature of forces that produce dynamic instability. When a structure oscillates, its amplitude as well as its kinetic energy increases beyond any bound. This energy must come from somewhere. Clearly, it is extracted from the load. However, if the loads are conservative and have a potential, the energy supplied to the structure cannot exceed the potential-energy loss of the applied loads due to deflection, and it is therefore bounded. Hence, dynamic instability (flutter) can be caused only by nonconservative forces.

The loads on a structure are generally defined as a force field $\mathbf{P} = \mathbf{P}(\mathbf{x}),$ where $\mathbf{x} = (x, y, z)$ is the position vector in Cartesian coordinates $x, y, z.$ During the deflection of the structure, the load vector $\mathbf{P}$ moves along path s consisting of displacement vector $d\mathbf{s}$. A load is said to be conservative if the work $W=\int_A^B \mathbf{P}\, d\mathbf{s}$ from position *A* to position *B* is independent of the path taken and depends only on these final positions. An equivalent condition is that the closed path integral $\oint \mathbf{P}\, d\mathbf{s} = \oint \left(P_x\, d_x + P_y\, d_y + P_z\, d_z\right)$ must be zero for all closed paths. This is always true if a potential-energy function $\Pi = \Pi\left(x, y, z\right)$ exists such that:

$$P_x = \frac{\partial \Pi}{\partial_x}, \qquad P_y = \frac{\partial \Pi}{\partial_y}, \qquad P_z = \frac{\partial \Pi}{\partial_z}. \tag{2.56}$$

The potential-energy function always exists if the following integrability conditions are satisfied:

$$\frac{\partial P_x}{\partial_y} = \frac{\partial P_y}{\partial_x}, \qquad \frac{\partial P_x}{\partial_z} = \frac{\partial P_z}{\partial_x}, \qquad \frac{\partial P_y}{\partial_z} = \frac{\partial P_z}{\partial_y}. \tag{2.57}$$

The force field is conservative if it possesses a potential. However, it can be conservative even it does not have a potential (see, for example, Bažant and Cedolin, 2003, Sect. 3.4).

For the follower loads on a column, as well as the wind force on the plate in the preceding examples, a potential cannot be defined and does not exist because the load direction depends on the deformation of the structure and different amounts of work are done for different paths leading to the same final state. We should remark, however, that the dependence of the load direction on the structure deformation does not in itself cause the load to be nonconservative. Furthermore, the fact that the loads are constant in magnitude and keep constant direction does not in itself guarantee that they are conservative (Bažant and Cedolin, 2003, p. 159).

As is apparent from the preceding discussion, it is important to distinguish various types of forces. Following Ziegler (1968), the forces on dynamic systems may be classified as follows:

1. *Nonstationary* (or *heteronomous*) loads, which are specified functions of time. They are obviously nonconservative and always require a kinetic approach. Pulsating loads are an example.
2. *Stationary* loads, which do not depend directly on time.
    a. *Velocity-dependent* loads.

    - (1) *Dissipative* load, which are nonconservative; they do work (dissipate energy) as the structure moves.
    - (2) *Gyroscopic* loads (such as the Coriolis force or gyroscopic moments), which are *conservative* but have no potential since they do no work.
- b. *Velocity-independent* loads.
    - (1) Loads having *no potential*, which may be termed *circulatory* (borrowing this expression from hydrodynamics). They are *nonconservative*.
    - (2) Loads having a *potential*, which may be termed *noncirculatory*. They are *conservative*.

Note that the class of conservative loads includes two categories: (1) velocity-independent loads having a potential; (2) velocity-dependent gyroscopic loads. All other loads are non conservative. The last class of loads occurs in the classical stability problems, in which static (as well as energy method) are always applicable.

Among *reactions*, one may distinguish (1) *nonworking* reactions (i.e., reactions of rigid supports) and (2) *dissipative* reactions (e.g., reaction of a viscous dashpot or frictional slider). The work of reactions can never be positive in scleronomic systems. *Scleronomic* systems are systems in which the constraints do not depend explicitly on time (Gantmacher, 1970, p. 11), that is, the position vector of the reaction point may depend on a set of Lagrangian coordinates but not explicitly on time (Ziegler, 1968, p. 27).

The basic lesson from our preceding discussions is that examination of equilibrium states (i.e., static analysis) is in general insufficient to determine stability of an elastic structure subjected to nonconservative loads.

2.9 Concluding Remarks

In this chapter we gave an introduction to dynamic stability of elastic systems and to dynamic stability analysis. We dealt with elementary examples like columns subjected to a follower force, and we also outlined some of the main aspects related to aeroelastic flutter. A survey on dynamic stability of columns subjected to follower loads may be found in (Langthjem and Sugiyama, 2000). Problems related to aeroelastic stability may be studied in classical books like those by Bisplinghoff et al. (1996), Dowell (2004), Fung (2002), and Simiu and Scanlan

(1996).

Dynamic stability has been here only mentioned with respect to structures that possess a configuration of static equilibrium, in which instability typically occurs by flutter. The danger is, however, also present in purely dynamic situations, when the fundamental response is itself a function of the time: if the system is perturbed, it is possible that spurious vibrations combine together with the main solution, or that the response diverges from this solution. This problem is relevant, for example, in mechanical engineering. Another particular problem connected to dynamic stability is parametric resonance, in which a structure subjected to a pulsating load may lose stability at a frequency other than the natural ones, stability being governed by further parameters. Solutions of particular problems may be found, for example, in (Bažant and Cedolin, 2003; Bolotin, 1963; Huseyin, 1986; Seyranian and Mailybaev, 2003). A recent book entirely devoted to dynamic stability of structures, which deals with both deterministic and stochastic loads, is that by Xie (2006).

An aspect that must be remarked is that in this chapter we systematically neglected mechanical damping in all the discussed examples. When stability is lost by divergence, linear mechanical damping has no stabilizing (or destabilizing) influence. This is generally true for linear systems with conservative loads, but not always true for systems with nonconservative loads. In a nonconservative system a small internal (viscous) damping can have a destabilizing influence, that is, it can lower the critical load, as corroborated by certain examples (Bažant and Cedolin, 2003).

All these problems find their systematization within the general theory of stability of motion, which finds applications in all fields of theoretical and applied science (Leipholz, 1987; Liapunov, 1892; Pignataro et al., 1991).

Chapter 3

Modal Analysis with Second-Order Effects

In this chapter we will discuss the dependence of the natural frequencies of a structure on the applied loads.

Restricting our analysis to structures subjected to conservative loads (such as gravity loads), we will derive a generalized eigenvalue problem where both the buckling loads and the natural frequencies of the system are unknown and represent the eigenvalues. In particular, we will consider discrete mechanical systems with one or two degrees of freedom subjected to compressive forces, as well as continuous mechanical systems such as slender beams subjected to compressive axial loads or to bending moments. Finally, a general finite element formulation will be outlined, with the possibility to be applied to any general two- or three-dimensional framed structure.

3.1 Introduction

From Structural Dynamics it is well known how to determine the natural frequencies of a linear elastic structure according to modal analysis, as it is also known the importance of keeping the vibration frequencies of an external periodic excitation as far as possible from such natural frequencies, in order to avoid resonance loading (Clough and Penzien, 2003). On the other hand, it is well known from Structural Mechanics how to obtain the buckling loads of a structure according to a linearized approach to the elastic stability analysis (Bažant and Cedolin, 2003). The smallest one among these loads (or load multipliers) corresponds to the critical load, associated to the condition of neutral equilibrium that separates the region of stability (load smaller than the critical load) from that of instability (load greater than the critical load).

From a mathematical point of view, both modal analysis and buckling analysis are treated as eigenvalue problems: they both lead to two formally identical equations written in symbolic form, each one having, of course, different physical meanings. In this chapter we will focus our analysis on structures subjected to loads that may cause static instability. Thus, taking into account the effect of geometric nonlinearity in the equations of motion through the geometric stiffness matrix, the problem can be reduced to a generalized eigenproblem where both the load multiplier and the natural frequency of the system are unknown. According to this approach, all the configurations intermediate between those of pure buckling and pure free vibrations can be investigated (Carpinteri and Paggi, 2013).

3.2 Influence of the Load on the Natural Frequency

In engineering applications there are a lot of situations where structures that undergo flexural vibrations are also loaded by a static axial load. Very common examples are structural members as columns, struts, and towers. In other cases, for example, beams carrying transverse loads may undergo lateral-torsional vibrations.

As anticipated in the previous section, in the case of a slender elastic structure, the applied static load, even if it does not lead to instability, has an influence on the natural vibration frequencies of the structure. In other words, the resonance frequencies result changed, in the sense that they are no longer those of the unloaded structure: in general they depend also on the kind and magnitude of the applied load. As a consequence, for example, an external harmonic excitation to produce resonance should have a frequency that matches one of the natural frequencies of the loaded structure, and not of the unloaded one. This fact requires a very careful analysis of the natural vibration frequencies, which must take into account the second order effects induced by the applied loads, in line with the modal analysis with second-order effects.

One example is given by the transverse vibrations of a cable in tension: if the tension is increased, the geometric contribution to the elastic stiffness makes the cable more rigid, and so its natural frequencies increase. Similarly, a tension on a beam will increase its natural frequencies of bending, while a compression will decrease them. In general, as we will better see later on, there are more complicated cases in which a load increases certain frequencies while others are reduced. The fact that the natural frequencies of a structure depend upon the applied load do not have to be necessarily regarded as negative: it could also become a powerful tool. For instance, one way to avoid the excitation of a particular natural frequency (and mode) of bending vibration of a beam could be to use a suitable tension or compression in the axial direction.

The described influence of the load on the natural frequencies appears in general, not only in the case of slender structures, but in this last case it has a larger influence, while in the other cases it is normally negligible because no important second order effects take place.

3.3 Discrete Mechanical Systems

3.3.1 Discrete Mechanical Systems with One Degree of Freedom

Let us consider the mechanical system shown in Figure 3.1, consisting of two rigid rods connected by an elastic hinge of rotational rigidity *k* and constrained at one end by a pinned support and at the other by a roller support. A mass *m* is placed in correspondence of the intermediate elastic hinge and the system is loaded by a horizontal axial force *N*. Considering the absolute rotation φ of the two arms as the generalized coordinate, the total potential energy, *W*, and the kinetic energy, *T*, of the whole system are:

$$\begin{aligned} W(\varphi) &= \frac{1}{2}k(2\varphi)^2 - 2Nl(1-\cos\varphi), \\ T(\dot{\varphi}) &= \frac{1}{2}m\left[\frac{\mathrm{d}}{\mathrm{d}t}(l\sin\varphi)\right]^2 + \frac{1}{2}m\left[\frac{\mathrm{d}}{\mathrm{d}t}(l-l\cos\varphi)\right]^2 = \frac{1}{2}ml^2\dot{\varphi}^2. \end{aligned} \tag{3.1}$$

The equation of motion can be determined by writing Lagrange’s equation:

$$\frac{\partial}{\partial t}\left(\frac{\partial T}{\partial\dot{\varphi}}\right) - \frac{\partial T}{\partial\varphi} = -\frac{\partial W}{\partial\varphi}. \tag{3.2}$$

In the present case, this yields:

$$ml^2\ddot{\varphi} = -4k\varphi + 2Nl\sin\varphi, \tag{3.3}$$

which can be suitably linearized in correspondence of $\varphi = 0$:

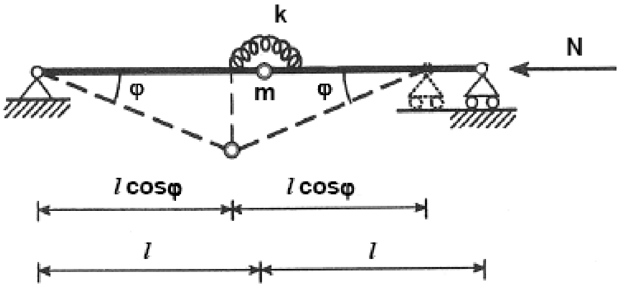

Figure 3.1 – Scheme of the first one-degree of freedom system analyzed.

$$ml^2\ddot{\varphi} = -4k\varphi + 2Nl\varphi. \tag{3.4}$$

Looking for the solution to Equation (3.4) in the general form $\varphi = \varphi_0 \mathrm{e}^{\mathrm{i}\omega t}$, where ω denotes the natural angular frequency of the system, we obtain the following equation which provides the conditions of equilibrium of the system:

$$\left(4k - 2Nl - \omega^2 ml^2\right)\varphi_0 = 0. \tag{3.5}$$

A nontrivial solution to Equation (3.5) exists if and only if the term in brackets is equal to zero. This critical condition corresponding to the bifurcation of the equilibrium establishes a one-to-one relationship between the applied axial force, N, and the angular frequency, φ:

$$N = \frac{2k}{l} - \frac{ml}{2}\omega^2. \tag{3.6}$$

Moreover, Equation (3.6) admits two important limit conditions for (respectively) $N = 0$ and $m = 0$. In the former case, Equation (3.6) gives the natural angular frequency of the system according to pure modal analysis, i.e. $\omega_1 = \sqrt{4k/ml^2}$. In the latter, the pure critical Eulerian load is obtained, i.e. $N_1 = 2k/l$.

Dividing Equation (3.6) by N_1, we obtain the following relationship between N and φ in a nondimensional form:

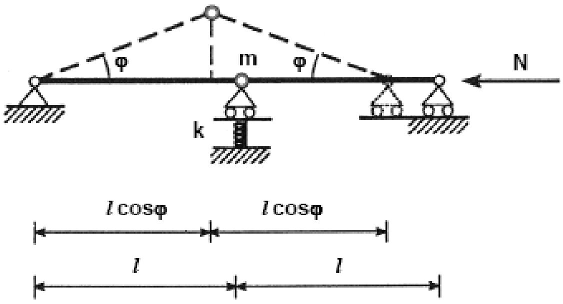

Figure 3.2 – Scheme of the second one-degree of freedom system analyzed.

$$\left(\frac{\omega}{\omega_1}\right)^2+\left(\frac{N}{N_1}\right)=1. \tag{3.7}$$

As a second example, let us consider the mechanical system shown in Figure 3.2, consisting of two rigid rods on three supports, of which the intermediate one is assumed to be elastically compliant with rigidity *k*. As in the previous case, a mass *m* is placed in correspondence of the intermediate hinge and the system is loaded by a horizontal axial force *N*. Considering the absolute rotation φ of the two arms as the generalized coordinate, the total potential energy, *W*, and the kinetic energy, *T*, of the whole system are:

$$\begin{aligned} W(\varphi)&=\frac{1}{2}k\left(l\sin\varphi\right)^2-2Nl\left(1-\cos\varphi\right),\\ T(\dot{\varphi})&=\frac{1}{2}ml^2\dot{\varphi}^2. \end{aligned} \tag{3.8}$$

Following the procedure discussed above, we determine the equation of motion by employing Lagrange’s equation (3.2):

$$ml^2\ddot{\varphi}=-l\sin\varphi\left(kl\cos\varphi-2N\right), \tag{3.9}$$

which can be suitably linearized in correspondence of $\varphi=0$:

$$ml^2\ddot{\varphi}=-l\varphi\left(kl-2N\right). \tag{3.10}$$

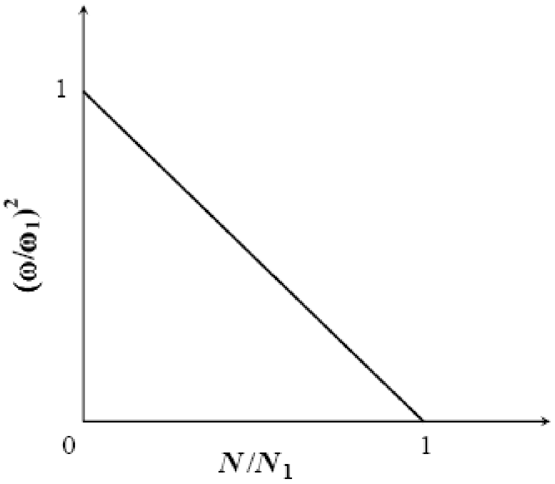

Figure 3.3 – Nondimensional frequency squared vs. nondimensional axial force for the single degree of freedom systems analyzed.

Looking for the solution to Equation (3.10) in the general form $\varphi=\varphi_0 \mathrm{e}^{\mathrm{i}\omega t}$, where ω denotes the natural angular frequency of the system, we obtain the following condition of equilibrium of the system:

$$\left(kl^2-2Nl-\omega^2 ml^2\right)\varphi_0=0. \tag{3.11}$$

As in the previous example, by setting the term in brackets equal to zero, we obtain a one-to-one relationship between the applied axial force, N, and the angular frequency, φ:

$$N=\frac{kl}{2}-\frac{ml}{2}\omega^2. \tag{3.12}$$

This equation admits two important limit conditions for (respectively) $N=0$ and $m=0$. In the former case, Equation (3.12) gives the natural angular frequency of the system according to pure modal analysis, i.e $\omega_1=\sqrt{k/m}$. In the latter, the pure critical Eulerian load for buckling instability is obtained, i.e. $N_1=kl/2$. Dividing Equation (3.12) by N_1, we obtain the same relationship between the nondimensional terms N/N_1 and $(\omega/\omega_1)^2$ as in the previous example (see Equation (3.7)).

A graphical representation of the condition (3.7) in Figure 3.3 shows that the resonance frequency is a decreasing function of the compressive axial load. This demonstrates, for the analyzed mechanical systems with a single degree of freedom, that resonance can take place for $\omega < \omega_1$, provided that the system is loaded by an axial force *N* given by Equation (3.7).

In addition, for the static case, the issue of stability or instability of the mechanical system in the correspondence of the bifurcation point, can be discussed by evaluating the higher order derivatives of the total potential energy *W* (Carpinteri, 1997).

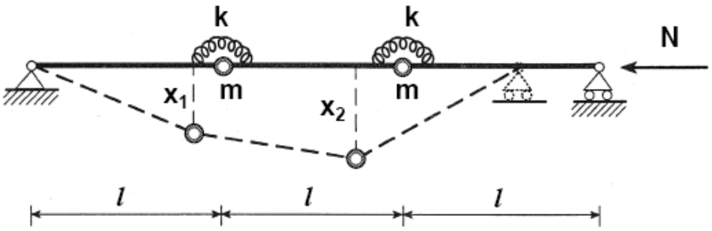

Figure 3.4 – Scheme of the first two-degrees of freedom system analyzed.

3.3.2 Discrete Mechanical Systems with Two Degrees of Freedom

Let us now consider the mechanical system with two degrees of freedom shown in Figure 3.4, consisting of three rigid rods connected by two elastic hinges of rotational rigidity *k*, and constrained at one end by a pinned support and at the other by a roller support. A mass *m* is placed in correspondence of the intermediate elastic hinges and the system is loaded by a horizontal axial force *N*. Assuming the vertical displacements x_1 and x_2 of the elastic hinges as the generalized coordinates, the total potential energy, *W*, and the kinetic energy, *T*, of the whole system are given by:

$$\begin{aligned}
W\left(x_1,x_2\right) = \frac{1}{2}k\Bigg[&\left(\arcsin\frac{x_1}{l}-\arcsin\frac{x_2-x_1}{l}\right)^2 \\
&+\left(\arcsin\frac{x_2}{l}+\arcsin\frac{x_2-x_1}{l}\right)^2\Bigg] \\
&-Nl\Bigg[3-\cos\left(\arcsin\frac{x_1}{l}\right)-\cos\left(\arcsin\frac{x_2}{l}\right) \\
&-\cos\left(\arcsin\frac{x_2-x_1}{l}\right)\Bigg], \\
T\left(\dot{x}_1,\dot{x}_2\right) = \frac{1}{2}m\dot{x}_1^2&+\frac{1}{2}m\dot{x}_1^2x_1^2+\frac{1}{2}m\dot{x}_2^2 \\
&+\frac{1}{2}m\left(\frac{2x_1\dot{x}_1}{l}+\frac{x_2\dot{x}_2}{l}-\frac{x_2\dot{x}_1}{l}-\frac{x_1\dot{x}_2}{l}\right)^2.
\end{aligned} \tag{3.13}$$

Performing a Taylor series expansion of Equation (3.13) about the origin, and assuming $x_1/l<1/10$ and $x_2/l<1/10$, we obtain:

$$\begin{aligned}
W\left(x_1,x_2\right) &\cong \frac{k}{2l^2}\left(5x_1^2+5x_2^2-8x_1x_2\right)-\frac{N}{l}\left(x_1^2+x_2^2-x_1x_2\right), \\
T\left(\dot{x}_1,\dot{x}_2\right) &\cong \frac{1}{2}m\dot{x}_1^2+\frac{1}{2}m\dot{x}_2^2.
\end{aligned} \tag{3.14}$$

The equations of motion are identified by considering Lagrange’s equations:

$$\frac{\partial}{\partial t}\left(\frac{\partial T}{\partial \dot{x}_i}\right)-\frac{\partial T}{\partial x_i}=-\frac{\partial W}{\partial x_i}, \qquad i=1,2. \tag{3.15}$$

In matrix form, they are:

$$\begin{bmatrix} m & 0 \\ 0 & m \end{bmatrix}\begin{Bmatrix} \ddot{x}_1 \\ \ddot{x}_2 \end{Bmatrix}+\begin{bmatrix} \frac{5k}{l^2} & -\frac{4k}{l^2} \\ -\frac{4k}{l^2} & \frac{5k}{l^2} \end{bmatrix}\begin{Bmatrix} x_1 \\ x_2 \end{Bmatrix}-N\begin{bmatrix} \frac{2}{l} & -\frac{1}{l} \\ -\frac{1}{l} & \frac{2}{l} \end{bmatrix}\begin{Bmatrix} x_1 \\ x_2 \end{Bmatrix}=\begin{Bmatrix} 0 \\ 0 \end{Bmatrix}. \tag{3.16}$$

Looking for the solution to Equation (3.16) in the general form $\{q\}=\{q_0\}\mathrm{e}^{\mathrm{i}\omega t}$, where ω denotes the natural angular frequency of the system, we obtain the following equation, written in symbolic form:

$$\left(-\omega^2\left[M\right]+\left[K\right]-N\left[K_g\right]\right)\left\{q_0\right\}=\left\{0\right\}, \tag{3.17}$$

where $\left[M\right]$, $\left[K\right]$ and $\left[K_g\right]$ denote (respectively) the mass matrix, the elastic stiffness matrix and the geometric stiffness matrix of the mechanical system. Their expressions can be simply obtained by comparing Equation (3.17) with Equation (3.16).

A nontrivial solution to Equation (3.17) exists if and only if the determinant of the resultant coefficient matrix of the vector $\left\{q_0\right\}$ vanishes. This yields the following generalized eigenvalue problem:

$$\det\left(\left[K\right]-N\left[K_g\right]-\omega^2\left[M\right]\right)=0, \tag{3.18}$$

where N and ω^2 represent the eigenvalues. For this example, Equation (3.18) provides the following relationships between the eigenvalues ω^2 and N :

$$\omega^2=\frac{k}{ml^2}-\frac{N}{ml}, \tag{3.19a}$$

$$\omega^2=\frac{3k}{ml^2}-\frac{3N}{ml}. \tag{3.19b}$$

As limit cases, if $m=0$, then we obtain the Eulerian buckling loads:

$$N_1=\frac{k}{l}, \tag{3.20a}$$

$$N_2=\frac{3k}{l}, \tag{3.20b}$$

whereas, if $N=0$, we obtain the natural frequencies of the system:

$$\omega_1=\sqrt{\frac{k}{ml^2}}, \tag{3.21a}$$

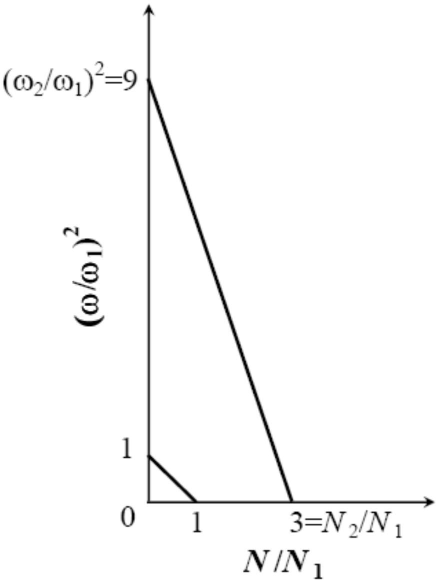

Figure 3.5 – Nondimensional frequencies squared vs. nondimensional axial forces for the two-degrees of freedom system in Figure 3.4.

$$\omega_2=\sqrt{\frac{9k}{ml^2}}. \tag{3.21b}$$

As far as the eigenvectors are concerned, the system (3.17) yields the eigenvectors corresponding (respectively) to the eigenfrequencies (3.19a) and (3.19b) as functions of N:

$$x_1=\frac{4k/l-N}{6k/l-3N}x_2, \tag{3.22a}$$

$$x_1=\frac{4k/l-N}{14k/l-5N}x_2. \tag{3.22b}$$

Dividing Equations (3.19a) and (3.19b) by ω_1^2, we derive the following nondimensional relationships between the eigenvalues:

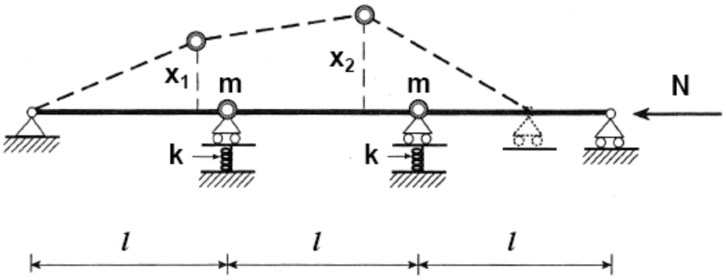

Figure 3.6 – Scheme of the second two-degrees of freedom system analyzed.

$$\left(\frac{\omega}{\omega_1}\right)^2 = 1 - \left(\frac{N}{N_1}\right), \tag{3.23a}$$

$$\left(\frac{\omega}{\omega_1}\right)^2 = \left(\frac{\omega_2}{\omega_1}\right)^2 - \frac{N_2}{N_1}\left(\frac{N}{N_1}\right). \tag{3.23b}$$

In analogy with the results for the single degree of freedom systems, a graphical representation of Equations (3.23a) and (3.23b) is provided in Figure 3.5. We notice that both the eigenfrequencies are decreasing functions of the compressive axial load. Entering the diagram with a value of the nondimensional compressive axial force in the range $0 < N/N_1 < 1$, the coordinates of the points of the two curves provide the two modified resonance frequencies of the mechanical system. Axial forces larger than N_1 in the range $1 < N/N_1 < N_2/N_1$ can only be experienced if an additional constraint is introduced into the system in order to prevent the vertical displacement of the midpoint, allowing at the same time the rotation and the horizontal displacement. Moreover, we observe that the applied compressive load influences all the eigenfrequencies, and not just the first one. In particular, in the present example, the influence of the axial load is greater on the highest frequency than on the lower one.

As a second example of a system with two degrees of freedom, let us examine that of Figure 3.6, which consists of three rigid rods on four supports, of which the central ones are assumed to be elastically compliant with rigidity *k*. A mass *m* is placed in correspondence of the intermediate hinges and the system is loaded by a horizontal axial force *N*. Assuming the vertical displacements x_1 and x_2 of the elastic hinges as the generalized coordinates, the total potential energy, *W*, and the kinetic energy, *T*, of the whole system are given by ($x_1/l < 1/10$ and $x_2/l < 1/10$):

$$\begin{aligned} W(x_1, x_2) &= \frac{1}{2}k\left(x_1^2 + x_2^2\right) - Nl\left[3 - \cos\left(\arcsin\frac{x_1}{l}\right)\right. \\ &\quad \left. - \cos\left(\arcsin\frac{x_2}{l}\right) - \cos\left(\arcsin\frac{x_2 - x_1}{l}\right)\right] \\ &\cong \frac{1}{2}k\left(x_1^2 + x_2^2\right) - \frac{N}{l}\left(x_1^2 + x_2^2 - x_1 x_2\right), \\ T(\dot{x}_1, \dot{x}_2) &\cong \frac{1}{2}m\dot{x}_1^2 + \frac{1}{2}m\dot{x}_2^2. \end{aligned} \tag{3.24}$$

In this case, Lagrange's equations (3.5) yield the following matrix form:

$$\begin{bmatrix} m & 0 \\ 0 & m \end{bmatrix}\begin{Bmatrix} \ddot{x}_1 \\ \ddot{x}_2 \end{Bmatrix} + \begin{bmatrix} k & 0 \\ 0 & k \end{bmatrix}\begin{Bmatrix} x_1 \\ x_2 \end{Bmatrix} - N\begin{bmatrix} \frac{2}{l} & -\frac{1}{l} \\ -\frac{1}{l} & \frac{2}{l} \end{bmatrix}\begin{Bmatrix} x_1 \\ x_2 \end{Bmatrix} = \begin{Bmatrix} 0 \\ 0 \end{Bmatrix}. \tag{3.25}$$

Looking for the solution to Equation (3.25) in the general form $\{q\} = \{q_0\}\mathrm{e}^{\mathrm{i}\omega t}$, where ω denotes the natural angular frequency of the system, we obtain the following equation, written in symbolic form:

$$\left(-\omega^2[M] + [K] - N\left[K_g\right]\right)\{q_0\} = \{0\}, \tag{3.26}$$

where $[M]$, $[K]$ and $\left[K_g\right]$ denote (respectively) the mass matrix, the elastic stiffness matrix and the geometric stiffness matrix of the mechanical system. As it can be readily seen, the geometric stiffness matrix for this problem is the same as that of the previous example.

A nontrivial solution to Equation (3.26) exists if and only if the determinant of the resultant coefficient matrix of the vector $\{q_0\}$ is equal to zero. This yields the following generalized eigenvalue problem:

$$\det\left([K] - N\left[K_g\right] - \omega^2[M]\right) = 0, \tag{3.27}$$

where N and ω^2 are the eigenvalues of the system. For this example, Equation (3.27) provides the following relationships between the eigenvalues:

$$\omega^2 = \frac{k}{m} - 3\frac{N}{ml}, \tag{3.28a}$$

$$\omega^2 = \frac{k}{m} - \frac{N}{ml}. \tag{3.28b}$$

As limit cases, if $m = 0$, we obtain the Eulerian buckling loads:

$$N_1 = \frac{1}{3}kl, \tag{3.29a}$$

$$N_2 = kl, \tag{3.29b}$$

whereas, if $N = 0$, then we obtain the natural frequencies of the system:

$$\omega_1 = \omega_2 = \sqrt{\frac{k}{m}}. \tag{3.30}$$

As far as the eigenvectors are concerned, the system (3.26) yields the eigenvectors corresponding (respectively) to the eigenfrequencies (3.28a) and (3.28b), as functions of the axial force, *N*:

$$x_1 = \frac{N/l}{5N/l - 2k} x_2, \tag{3.31a}$$

$$x_1 = \frac{N/l}{3N/l - 2k} x_2. \tag{3.31b}$$

Dividing Equations (3.28a) and (3.28b) by ω_1^2, we derive the following nondimensional relationships between the eigenvalues:

$$\left(\frac{\omega}{\omega_1}\right)^2 = 1 - \left(\frac{N}{N_1}\right), \tag{3.32a}$$

$$\left(\frac{\omega}{\omega_1}\right)^2 = 1 - \frac{N_1}{N_2}\left(\frac{N}{N_1}\right). \tag{3.32b}$$

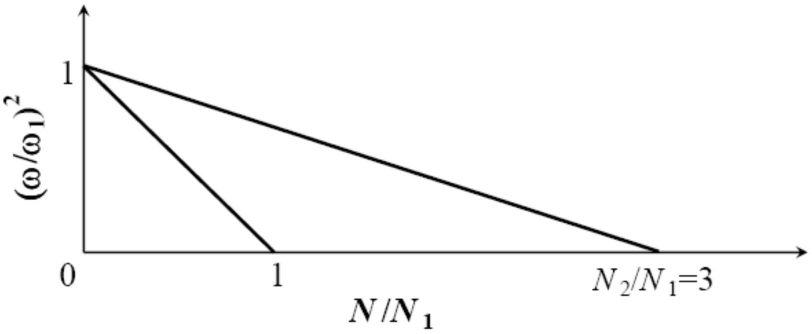

Figure 3.7 – Nondimensional frequencies squared vs. nondimensional axial forces for the two-degrees of freedom system in Figure 3.6.

A graphical representation of Equations (3.32a) and (3.32b) is provided in Figure 3.7. Also in this case, both the frequencies are decreasing functions of the compressive axial load. However, in the present example, the influence of the axial load is greater on the lower frequency of the system than on the higher one.

3.4 Continuous Mechanical Systems

3.4.1 Slender Beam Under Compressive Axial Load

Let us consider a slender elastic beam of constant cross-section, inextensible and not deformable in shear, through deformable in bending, constrained at one end by a pinned support and at the other by a roller support, loaded by an axial force, N (see Figure 3.8). In this case, with the purpose of analyzing the free flexural oscillations of the beam, the differential equation of the elastic line with second-order effects can be written by replacing the distributed load with the force of inertia:

$$EI\frac{\partial^4 v}{\partial z^4} + N\frac{\partial^2 v}{\partial z^2} = -\mu\frac{\partial^2 v}{\partial t^2}, \tag{3.33}$$

where EI denotes the flexural rigidity of the beam and μ is its linear density (mass per unit length). Equation (3.33) can be rewritten in the following form:

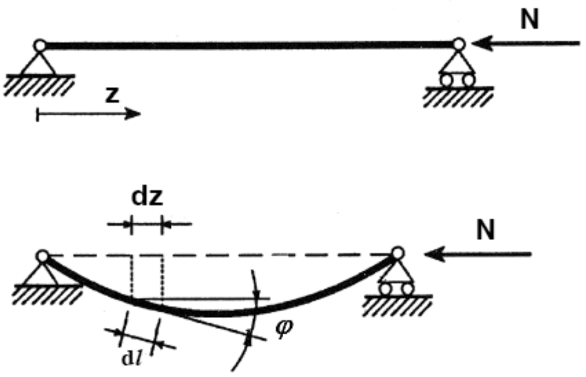

Figure 3.8 – Undeformed and deformed configurations of a deflected beam under compressive axial force.

$$\frac{\partial^4 v}{\partial z^4} + \alpha^2 \frac{\partial^2 v}{\partial z^2} = -\frac{\mu}{EI}\frac{\partial^2 v}{\partial t^2} \tag{3.34}$$

where we have set $\alpha^2 = N/EI$.

Equation (3.34) is an equation with separable variables, the solution being represented as the product of two different functions, each one depending on a single variable:

$$v(z,t) = \eta(z)\, f(t). \tag{3.35}$$

Introducing Equation (3.35) into Equation (3.34), leads:

$$\frac{\mathrm{d}^4\eta}{\mathrm{d}z^4} f + \alpha^2 \frac{\mathrm{d}^2\eta}{\mathrm{d}z^2} f + \frac{\mu}{EI}\eta \frac{\mathrm{d}^2 f}{\mathrm{d}t^2} = 0. \tag{3.36}$$

Dividing Equation (3.36) by the product ηf, we find:

$$-\frac{\dfrac{\mathrm{d}^2 f}{\mathrm{d}t^2}}{f} = \frac{EI}{\mu}\frac{\dfrac{\mathrm{d}^4\eta}{\mathrm{d}z^4} + \alpha^2 \dfrac{\mathrm{d}^2\eta}{\mathrm{d}z^2}}{\eta} = \omega^2, \tag{3.37}$$

where ω^2 represents a positive constant, the left and the right hand-sides of Equation (3.37) being at most functions of the time t and the coordinate z, respectively. From Equation (3.37) there follow two ordinary differential equations:

$$\frac{\mathrm{d}^2 f}{\mathrm{d}t^2} + \omega^2 f = 0, \tag{3.38a}$$

$$\frac{\mathrm{d}^4\eta}{\mathrm{d}z^4} + \alpha^2 \frac{\mathrm{d}^2\eta}{\mathrm{d}z^2} - \beta^4\eta = 0, \tag{3.38b}$$

with

$$\beta = \sqrt[4]{\frac{\mu\omega^2}{EI}}. \tag{3.39}$$

Whereas Equation (3.38a) is the equation of the harmonic oscillator, with the well-known complete integral

$$f\left(t\right) = A\cos\omega t + B\sin\omega t, \tag{3.40}$$

Equation (3.38b) admits the following complete integral

$$\eta\left(t\right) = C\mathrm{e}^{\lambda_1 z} + D\mathrm{e}^{\lambda_2 z} + E\mathrm{e}^{-\lambda_1 z} + F\mathrm{e}^{-\lambda_2 z}, \tag{3.41}$$

where λ_1 and λ_2 are functions of α and β :

$$\lambda_{1,2} = \sqrt{\frac{-\alpha^2 \pm \sqrt{\alpha^4 + 4\beta^4}}{2}}. \tag{3.42}$$

As in the modal analysis, the constants A and B can be determined on the basis of the initial conditions, while the constants C, D, E and F can be determined by imposing the boundary conditions. As it will be shown in the sequel, for a given value of α , the parameters ω and β can be determined by solving a generalized eigenvalue problem resulting from the imposition of the boundary conditions. From the mathematical point of view, this eigenvalue problem is analogous to that shown for the discrete systems. On the other hand, since we are considering a continuous mechanical system which has infinite degrees of freedom, we shall obtain an infinite number of eigenvalues ω_i and β_i, just as there will be an infinite number of eigenfunctions f_i and η_i. The complete integral of the differential Equation (3.33) may therefore be given the following form, according to the Principle of Superposition:

$$v(z,t) = \sum_{i=1}^{\infty} \eta_i(z) \, f_i(t), \tag{3.43}$$

with:

$$f_i(t) = A_i \cos \omega_i t + B_i \sin \omega_i t, \tag{3.44a}$$

$$\eta_i(t) = C_i \mathrm{e}^{\lambda_{1i} z} + D_i \mathrm{e}^{\lambda_{2i} z} + E_i \mathrm{e}^{-\lambda_{1i} z} + F_i \mathrm{e}^{-\lambda_{2i} z}. \tag{3.44b}$$

It is important to remark that the eigenfunctions η_i are still orthonormal functions, as in the classical modal analysis (Carpinteri and Paggi, 2013). We may in fact write Equation (3.38b) for two different eigensolutions:

$$\eta_j^{IV} + \alpha^2 \eta_j^{II} = \beta_j^4 \eta_j, \tag{3.45a}$$

$$\eta_k^{IV} + \alpha^2 \eta_k^{II} = \beta_k^4 \eta_k. \tag{3.45b}$$

Multiplying Equation (3.45a) by η_k and Equation (3.45b) by η_j, and integrating over the beam length, we obtain:

$$\int_0^l \eta_k \eta_j^{IV} \mathrm{dz} + \alpha^2 \int_0^l \eta_k \eta_j^{II} \mathrm{dz} = \beta_j^4 \int_0^l \eta_k \eta_j \mathrm{dz}, \tag{3.46a}$$

$$\int_0^l \eta_j \eta_k^{IV} \mathrm{dz} + \alpha^2 \int_0^l \eta_j \eta_k^{II} \mathrm{dz} = \beta_k^4 \int_0^l \eta_j \eta_k \mathrm{dz}. \tag{3.46b}$$

Integrating by parts the left-hand sides, the foregoing equations transform as follows:

$$\begin{gathered} \left[\eta_k \eta_j^{III}\right]_0^l - \left[\eta_k^I \eta_j^{II}\right]_0^l + \int_0^l \eta_k^{II} \eta_j^{II} \mathrm{dz} + \alpha^2 \left[\eta_k \eta_j\right]_0^l \\ -\alpha^2 \int_0^l \eta_k^I \eta_j^I \mathrm{dz} = \beta_j^4 \int_0^l \eta_k \eta_j \mathrm{dz}, \end{gathered} \tag{3.47a}$$

$$\begin{aligned}&\left[\eta_j\eta_k^{III}\right]_0^l-\left[\eta_j^I\eta_k^{II}\right]_0^l+\int_0^l\eta_j^{II}\eta_k^{II}\mathrm{dz}+\alpha^2\left[\eta_j\eta_k\right]_0^l\\&-\alpha^2\int_0^l\eta_j^I\eta_k^I\mathrm{dz}=\beta_k^4\int_0^l\eta_j\eta_k\mathrm{dz}.\end{aligned}\tag{3.47b}$$

When each of the two ends of the beam is constrained by a built-in support ($\eta=\eta^I=0$), or by a pinned support ($\eta=\eta^{II}=0$), the quantities in square brackets vanish. On the other hand, when the end in $z=0$ is either unconstrained ($\eta^{III}=\eta^{II}=0$), or constrained by a double rod ($\eta^{III}=\eta^I=0$), the remaining end of the beam has to be constrained either by a built-in support ($\eta=\eta^I=0$), or by a simple support ($\eta=\eta^{II}=0$). For both configurations, only the terms $[\eta_i\eta_k]_0^l$ are different from zero.

In any case, subtracting member by member, these quantities are cancelled and we have:

$$\left(\beta_j^4-\beta_k^4\right)\int_0^l\eta_j\eta_k=0,\tag{3.48}$$

which leads to the orthonormality condition:

$$\int_0^l\eta_j\eta_k=\delta_{ij},\tag{3.49}$$

where δ_{ij} is the Kronecker delta. Thus, when the eigenvalues are distinct, the integral of the product of the corresponding eigenfunctions vanishes. When, instead, the indices *j* and *k* coincide, the condition of normality reminds us that the eigenfunctions are defined up to a factor of proportionality.

The orthonormality of the eigenfunctions η_i permits us to determine the constants A_i and B_i in Equation (3.44a) via the initial conditions:

$$v\left(t=0\right)=v_0\left(z\right),\tag{3.50a}$$

$$\frac{\partial v}{\partial t}\left(t=0\right)=\dot{v}_0\left(z\right).\tag{3.50b}$$

As regards to the boundary conditions, let us consider as an example a beam supported at both ends, of length l:

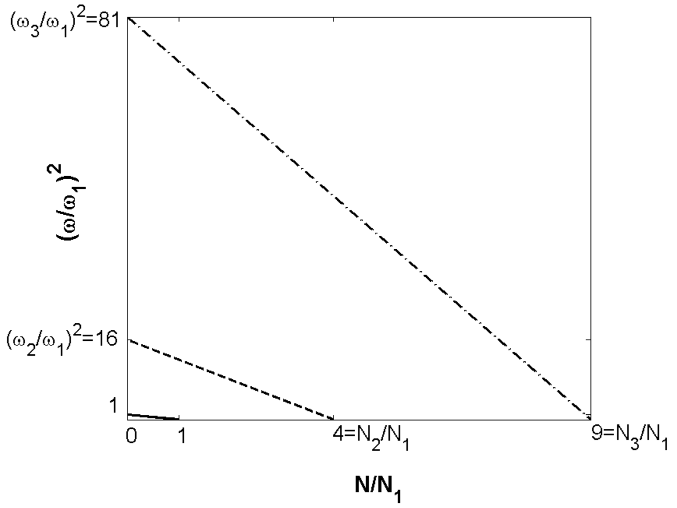

Figure 3.9 – Nondimensional frequencies squared vs. nondimensional axial force for the continuous system in Figure 3.8.

$$\left\{\begin{array}{l}\eta(0)=0,\\ \eta''(0)=0,\\ \eta(l)=0,\\ \eta''(l)=0,\end{array}\right. \Rightarrow \begin{bmatrix}1 & 1 & 1 & 1\\ \lambda_1^2 & \lambda_2^2 & \lambda_1^2 & \lambda_2^2\\ \mathrm{e}^{\lambda_1 l} & \mathrm{e}^{\lambda_2 l} & \mathrm{e}^{-\lambda_1 l} & \mathrm{e}^{-\lambda_2 l}\\ \lambda_1^2\mathrm{e}^{\lambda_1 l} & \lambda_2^2\mathrm{e}^{\lambda_2 l} & \lambda_1^2\mathrm{e}^{-\lambda_1 l} & \lambda_2^2\mathrm{e}^{-\lambda_2 l}\end{bmatrix}\begin{Bmatrix}C\\ D\\ E\\ F\end{Bmatrix}=\begin{Bmatrix}0\\ 0\\ 0\\ 0\end{Bmatrix}, \tag{3.51}$$

For a nontrivial solution to the system in Equation (3.51), the determinant of the coefficient matrix must vanish. The resulting eigenequation permits, for each given value of the parameter α, to determine the eigenvalues β_i of the system. Finally, the corresponding natural eigenfrequencies ω_i can be obtained by inverting Equation (3.39).

As an illustrative example, the first three nondimensional frequencies of the simply supported beam shown in Figure 3.8 are reported in Figure 3.9 as functions of the applied nondimensional axial force. Parameters ω_i and N_i denote (respectively) the *i*-th frequency of the system determined according to modal analysis and the *i*-th buckling load determined according to Euler's formula. In close analogy with the discrete mechanical systems, the curves in the $(\omega/\omega_1)^2$ vs. N/N_1 plane are represented by straight lines. Also in this case, the coordinates of the points along these lines provide the natural vibration frequencies as functions of the applied compressive axial force.

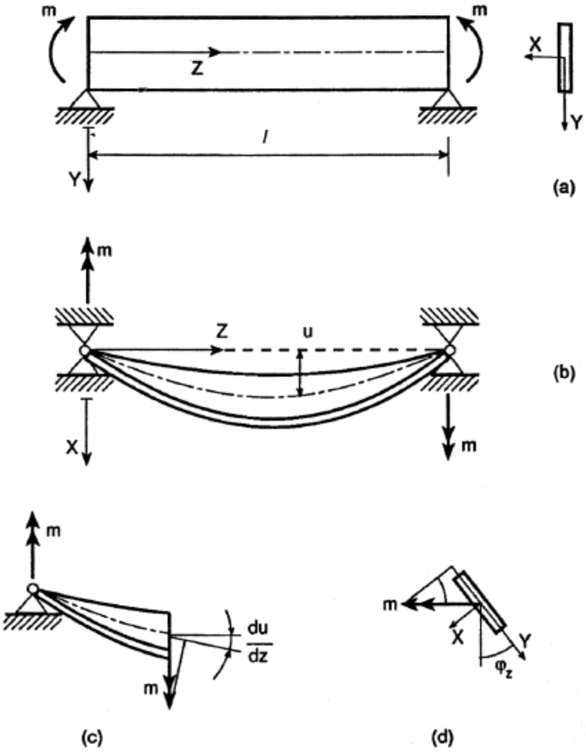

Figure 3.10 – Scheme of a beam subjected to lateral-torsional buckling.

3.4.2 Rectangular Narrow Beam Under End Bending Moments

Let us consider an elastic beam of uniform, narrow, rectangular cross-section, constrained at the ends so that rotation about the longitudinal axis *Z* is prevented. Let this beam be subjected to uniform bending by means of the application at the ends of two moments *m* contained in the plane *YZ* of greater flexural rigidity (see

Figure 3.10).

Considering a deformed configuration of the beam, with deflection thereof in the *XZ* plane of smaller flexural rigidity, and simultaneous torsion about the *Z* axis (see Figure 3.10), bending-torsional out-of-plane vibrations of the beam are described by the following partial differential equations:

$$\begin{aligned} &EI_y \frac{\partial^4 u}{\partial z^4} + m\frac{\partial^2 \varphi_z}{\partial z^2} = -\mu \frac{\partial^2 u}{\partial t^2}, \\ &-GI_t \frac{\partial^2 \varphi_z}{\partial z^2} + m\frac{\partial^2 u}{\partial z^2} = -\mu\rho^2 \frac{\partial^2 \varphi_z}{\partial t^2}, \end{aligned} \tag{3.52}$$

where $u(z,t)$ and $\varphi_z(z,t)$ are, respectively, the out-of-plane deflection and the twist angle of the beam cross-section; EI_y and GI_t are the bending and torsional rigidities; μ is the mass of the beam per unit length, and $\rho = \sqrt{I_P/A}$ is the polar radius of inertia of the beam cross-section.

A solution to the system (3.52) can be found in the following variable-separable form:

$$\begin{aligned} &u(z,t) = U(t)\eta(z), \\ &\varphi_z(z,t) = \Phi(t)\psi(z), \end{aligned} \tag{3.53}$$

where the functions $\eta(z)$ and $\psi(z)$ are such that the boundary conditions $\eta(0) = \eta(l) = \eta''(0) = \eta''(l) = 0$ and $\psi(0) = \psi(l) = 0$ are satisfied. According to Bolotin (Bolotin, 1995) we can assume $\eta(z) = \psi(z) = \sin\frac{n\pi z}{l}$, with *n* being a natural number. In this case, we obtain the following matrix form:

$$\begin{bmatrix} \mu & 0 \\ 0 & \mu\rho^2 \end{bmatrix} \begin{Bmatrix} \ddot{U} \\ \ddot{\Phi} \end{Bmatrix} + \begin{bmatrix} EI_y \dfrac{n^4\pi^4}{l^4} & 0 \\ 0 & GI_t \dfrac{n^2\pi^2}{l^2} \end{bmatrix} \begin{Bmatrix} U \\ \Phi \end{Bmatrix} - m \begin{bmatrix} 0 & \dfrac{n^2\pi^2}{l^2} \\ \dfrac{n^2\pi^2}{l^2} & 0 \end{bmatrix} \begin{Bmatrix} U \\ \Phi \end{Bmatrix} = \begin{Bmatrix} 0 \\ 0 \end{Bmatrix}, \tag{3.54}$$

which can be symbolically rewritten as:

$$[M]\{\ddot{q}\}+[K]\{q\}-m\left[K_g\right]\{q\}=\{0\}, \tag{3.55}$$

where $\{q\}=(U,\Phi)^T$. The mass matrix, $[M]$, the elastic stiffness matrix $[K]$, and the geometric stiffness matrix $\left[K_g\right]$ in Equation (3.55) can be defined in comparison with Equation (3.54). Looking for a general solution in the form $\{q\}=\{q_0\}\mathrm{e}^{\mathrm{i}\omega t}$, we obtain:

$$\left([K]-m\left[K_g\right]-\omega^2[M]\right)\{q_0\}=\{0\}. \tag{3.56}$$

A nontrivial solution to Equation (3.56) exists if and only if the determinant of the resultant coefficient matrix of the vector $\{q_0\}$ vanishes. This yield the following generalized eigenvalue problem:

$$\det\left([K]-m\left[K_g\right]-\omega^2[M]\right)=0, \tag{3.57}$$

where m and ω^2 are the eigenvalues of the system.
As limit cases, if $\mu=0$, then we obtain the critical bending moments given by Prandtl's formula:

$$m_{nc}=\frac{n\pi}{l}\sqrt{EI_yGI_t}, \tag{3.58}$$

whereas, if $m=0$, then we obtain the natural flexural and torsional eigenfrequencies of the beam:

$$\begin{aligned}\omega_n^{\text{flex}}&=\left(\frac{n\pi}{l}\right)^2\sqrt{\frac{EI_y}{\mu}},\\ \omega_n^{\text{tors}}&=\frac{n\pi}{\rho l}\sqrt{\frac{GI_t}{\mu}}.\end{aligned} \tag{3.59}$$

Considering a rectangular beam with a depth to span ratio of 1/3 and with a thickness to depth ratio of 1/10, the evolution of the first two flexural and torsional eigenfrequencies of the system are shown in Figure 3.11 as functions of the applied bending moment. In this case, the curves in the nondimensional plane $(\omega/\omega_1^{\text{flex}})^2$ vs. m/m_{1c} are no longer straight lines. This fact can be ascribed to the

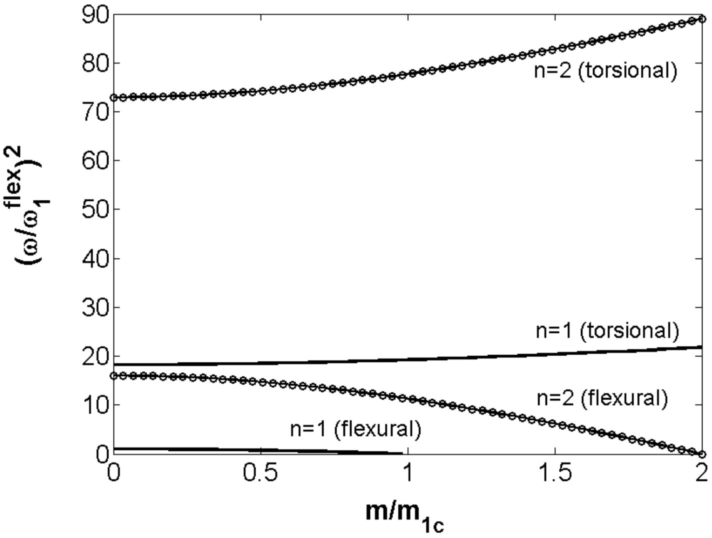

Figure 3.11 – Nondimensional flexural and torsional frequencies squared vs. nondimensional bending moments for the continuous system in Figure 3.10.

coupling between torsional and flexural vibrations of the beam. Moreover, when *m* is increased from zero (pure free vibrations) up to the critical bending moment computed according to Parandtl's formula (pure buckling instability), m_{1c}, we note that the resonance frequencies related to flexural oscillations progressively decrease from ω_1^{flex} down to zero in correspondence of the critical bending moments given by Prandtl's formula. Conversely, the resonance frequencies related to torsional oscillations increase. From the mathematical point of view, this is the result of the fact that the sum of the squares of the two eigenfrequencies for a given value of *n* is constant when the applied moment *m* is varied.

3.5 Finite Element Procedure

When the mechanical system cannot be reduced to the schemes previously analyzed, it is possible to apply the Finite Element Method (Bathe, 1982; Zienkiewicz and Taylor, 2005). According to this approach, the equations of motion for an elastic system with a finite number of degrees of freedom can be expressed in matrix form, also taking into account the effect of the geometric nonlinearity through the geometric stiffness matrix (Carpinteri and Paggi, 2013).

For the sake of generality, let the elastic domain *V* be divided into subdomains V_e, and let each element contain *m* nodal points, each one having *g* degrees of freedom. In compact form, the displacement vector field defined on the element V_e may be represented as:

$$\underset{(g\times 1)}{\{\eta_e\}} = \underset{g\times(g\times m)}{[\eta_e]}\ \underset{(g\times m)\times 1}{\{\delta_e\}}\ , \tag{3.60}$$

where $[\eta_e]$ is the matrix collecting the shape functions and $\{\delta_e\}$ is the nodal displacement vector.

The deformation characteristic vector is obtained by derivation:

$$\underset{(d\times 1)}{\{q_e\}} = \underset{(d\times g)}{[\partial]}\ \underset{(g\times 1)}{\{\eta_e\}}, \tag{3.61}$$

where $[\partial]$ is the kinematic operator relating strains to displacements, whereas d denotes the dimension of the strain characteristic vector, e.g. $d=3$ for a beam in plane or $d=6$ for a beam in space. Hence, introducing Equation (3.60) into Equation (3.61), we obtain:

$$\underset{(d\times 1)}{\{q_e\}} = \underset{(d\times g)}{[\partial]}\ \underset{g\times(g\times m)}{[\eta_e]}\ \underset{(g\times m)\times 1}{\{\delta_e\}} = \underset{d\times(g\times m)}{[B_e]}\ \underset{(g\times m)\times 1}{\{\delta_e\}}\ , \tag{3.62}$$

where the matrix $[B_e]$ is calculated by derivation of the shape functions.

According with these definitions, we can obtain the following matrix equation for each finite element:

$$[M_e]\{\ddot{\delta}_e\} + \left([K_e] - \lambda\left[K_{ge}\right]\right)\{\delta_e\} = \{0\}, \tag{3.63}$$

where $[M_e]$, $[K_e]$ and $\left[K_{ge}\right]$ denote, respectively, the local mass matrix, the local elastic stiffness matrix and the local geometric stiffness matrix of the finite element.

As usual, the local mass and elastic stiffness matrices are given by:

$$\left[M_e\right]=\int_{V_e}\left[\eta_e\right]^T\left[\mu\right]\left[\eta_e\right]dV, \tag{3.64a}$$

$$\left[K_e\right]=\int_{V_e}\left[B_e\right]^T\left[H\right]\left[B_e\right]dV. \tag{3.64b}$$

The local geometric stiffness matrix can be computed as follows:

$$\left[K_{ge}\right]=\int_{V_e}\left[G_e\right]^T\left[S_e\right]\left[G_e\right]dV, \tag{3.65}$$

where the matrix $\left[S_e\right]$ is related to the components of the stress field:

$$\left[S_e\right]=\begin{bmatrix}\sigma_x\left[I_3\right] & \tau_{xy}\left[I_3\right] & \tau_{xz}\left[I_3\right]\\ \tau_{xy}\left[I_3\right] & \sigma_y\left[I_3\right] & \tau_{yz}\left[I_3\right]\\ \tau_{xz}\left[I_3\right] & \tau_{yz}\left[I_3\right] & \sigma_z\left[I_3\right]\end{bmatrix}, \tag{3.66}$$

where $\left[I_3\right]$ denotes a unit matrix with dimensions $\left(3\times3\right)$. The matrix $\left[G_e\right]$ is related to the first derivative of the shape functions through the differential operator $\left[\bar{\partial}\right]$:

$$\underset{(g\times g)\times(g\times m)}{\left[G_e\right]}=\underset{(g\times g)\times g}{\left[\bar{\partial}\right]}\;\underset{g\times(g\times m)}{\left[\eta_e\right]}, \tag{3.67}$$

where

$$\left[\bar{\partial}\right]=\begin{bmatrix}\dfrac{\partial}{\partial x}\left[I_3\right]\\ \dfrac{\partial}{\partial y}\left[I_3\right]\\ \dfrac{\partial}{\partial z}\left[I_3\right]\end{bmatrix}. \tag{3.68}$$

According with this formulation, we note that the geometric stiffness matrix is a function of the stress components through the matrix $\left[S_e\right]$. In the case of a compressive stress field, the geometric stiffness terms become negative and reduce the corresponding elements of the local elastic stiffness matrix, as shown for the discrete mechanical systems. We also remark that this formulation is quite general, since the information related to the finite element topology is simply included in the matrix $\left[\eta_e\right]$ which collects the shape functions and in the differential operator $\left[\partial\right]$.

By performing the usual operations of rotation, expansion and assemblage of the mass, elastic stiffness and geometric stiffness matrices of the element, Equation (3.63) can be written in global form:

$$\left[M\right]\left\{\ddot{\delta}\right\}+\left(\left[K\right]-\lambda\left[K_g\right]\right)\left\{\delta\right\}=\left\{0\right\}. \tag{3.69}$$

Looking for the solution to Equation (3.69) in the general form $\left\{\delta\right\}=\left\{\delta_0\right\}\mathrm{e}^{\mathrm{i}\omega t}$, where ω is the natural frequency of the system, we can formulate the generalized eigenproblem as in the cases discussed above:

$$\det\left(\left[K\right]-\lambda\left[K_g\right]-\omega^2\left[M\right]\right)=0. \tag{3.70}$$

Therefore, the numerical procedure for the determination of the frequency-loading multiplier diagram consists in the following steps:

1. for a given loading configuration defined by the loading multiplier λ, determine the stress field according to a linear elastic stress analysis;
2. compute the local mass matrix, the local elastic stiffness matrix and the local geometric stiffness matrix for each finite element;
3. perform the rotation, expansion and assemblage operations to obtain the global matrices;
4. solve the generalized eigenvalue problem of Equation (3.70) and find the eigenfrequencies of the system, ω_i^2, with $i=1,\ldots,g\times n$;
5. iterate the above-described procedure for different values of λ.

3.6 Concluding Remarks

The examples considered in this chapter represent an introduction to the subject, they are obviously not exhaustive. Nevertheless, they have the advantage of showing the essential aspects of the dependence of vibration frequencies on dead loads.

For example, we have not treated curved beams, cables, two-dimensional structural elements, or thin-walled structures, or composite structures. Even particular loading conditions and other special effects such as those of impact loads and of temperature variations have not been analyzed. Most importantly, our analysis has been restricted to linear vibrations. The literature on the subject is very vast, and any attempt to list would remain incomplete. We will only give some basic references.

Solutions in terms of eigenvalues and eigenfunctions for non-classical problems of free vibrations of arches, beams and frames can be found in the books by Karnovsky and Lebed (Karnovsky and Lebed, 2001; 2004). A detailed presentation of free and forced vibration of axially loaded structures, including practical applications and experimental verifications, can be found in the book by Virgin (Virgin, 2007). Solutions regarding thin-walled composite beams can be found in the book by Librescu and Song (Librescu and Song, 2006).

Chapter 4

Slender Beams Subjected to Imposed Displacements

In this chapter we shall present an experimental study on the fundamental frequency evolution in slender elastic beams subjected to displacements imposed to one end. Different geometrical imperfections as well as different constraint conditions will be analyzed.

The proposed study leads to recognise two different phases in the bending frequency vs. axial load curves under different imposed axial displacements. In the final part of the chapter it will be shown how the behaviours observed during the experiments can be reproduced by numerical simulations.

4.1 Introduction

A very large number of engineering problems in structural dynamics, both in linear and nonlinear ranges, have been studied during the last decades, and powerful methods have been developed for different structural elements subjected to different loading conditions (Clough and Penzien, 2003; Karnovsky and Lebed, 2001; Weaver et al., 1990). In addition, the influence of the applied loads on the natural frequencies is one of the most investigated problems (Virgin, 2007). Early studies were focused on transverse vibrations of elastic beams under constant axial loads (Abramovich, 1992; Belluzzi, 1951a; Bokaian, 1988; 1990; Matsunaga, 1996), these were then followed by more and more refined analyses, regarding beams, arches, plates and shells (Addessi et al., 2005a; 2005b; Arboleda-Monsalvea, 2007; Batra et al. 2002; Carrera, 1999; Chen and Shen, 1998; Cortinez and Piovan, 2002; Fridman and Abramovich, 2008; Hallauer and Ma, 2011; Jun and Hongxing, 2011; Kim, 2005; Lacarbonara et al., 2004; Li et al., 2011; Matsunaga, 1999; Vo et al., 2010; Yang et al., 2008; Zhang et al., 2008). As we have seen in the previous chapters, the problem of the influence of applied loads on the natural vibration frequencies is strictly connected with the analysis of the stability of the elastic equilibrium of mechanical systems and structures. In particular, the zero-frequency condition corresponds to the loss of stability by divergence (static instability), and it furnishes the critical buckling load (or load group multiplier). On this basis, the experimental determination of instability loads of columns and structures by non-destructive vibration tests have been performed, by different authors, for different structural configurations, such as column-type and thin-walled structures (Anik'ev et al., 1994; Anik'ev and Sushchenko, 2002; Belluzzi, 1951b; Virgin, 2007). The unifying approach of these studies is to consider the influence of applied loads on natural vibration frequencies of slender structures. On the other hand, reduced attention is usually given to the influence of imposed displacements and structural subsidence on natural frequencies of slender structures. These effects –less infrequent than we might think– may appear when slender structures are subjected to external moving constraints. For example, for bridges and large structures the reduction in bearing capacity and the sudden collapse of compressed elements can be the result of constraint settlements or structural subsidence due to seismic events.

In the present chapter we will present the results of an experimental investigation on the fundamental flexural frequency evolution of slender beams under imposed displacements. The tests have been carried out using steel elements characterized by a constant rectangular cross-section, with different constraint conditions. Different geometrical imperfections were also considered, in order to understand their influence on natural frequency evolution. The tests were conducted using a servo-controlled testing machine under displacement-controlled condition, and the natural flexural vibration frequencies were extracted in both the pre- and post-buckled configurations using different procedures. Free and forced vibrations were investigated, by means of a measuring device acting without any contact with the specimens (laser sensor). The dynamic forcing was realized through an electromagnet, imposing transverse displacements to the middle of the monitored beam. The experimental apparatus was realized according to metrological requirements and was fine tuned at the National Institute of Metrological Research (INRIM), while the experiments were carried out at the Experimental Laboratory of Materials and Structures of the Politecnico di Torino (MASTRLAB). The fundamental frequencies of rectified and deformed elements were carried out for different imposed vertical displacements, corresponding to different axial loads. The possibility to recognise a transition between a pseudo-linear and a nonlinear behaviour in the frequency vs. axial load curve is used to describe the behaviour of simple elements subjected to vertical displacements at one of the two end joints. This transition may be used to discriminate between two different phases and to evaluate the instability of structures subjected to imposed external conditions such as structural subsidence. The achievement of particular values of the natural frequency just before the final instability collapse may be used to provide an indication of the impending collapse and could be used as a monitoring indicator of instability condition for existing structures. Lastly, numerical simulations were performed offering a valid interpretation of the experimental results and contributing to recognize the fundamental frequency evolution of slender structures subjected to imposed displacements.

4.2 Experimental Setup

Figure 4.1 shows a general view of the experimental setup. The experimental tests were conducted using a servo-controlled machine (MTS) with a closed-loop electronic control, having a maximum capacity of 100 kN. The specimen is positioned vertically and connected to the testing machine by two end joints, realizing the external constraints. Two horizontal transverses which support the measuring device (displacement transducer) and an electromagnet, that realizes the forcing, are positioned at the mid-height of each tested beam. Both the electromagnet and the measuring device act without any contact with the specimen.

The complete experimental apparatus is constituted by a wave generator, a signal amplifier, an oscilloscope, and a data acquisition device (see Figure 4.1).

4.2.1 Specimens

The specimens used during the experimental tests consisted of three slender steel beams. All these elements present a rectangular cross-section 15 mm deep and 30 mm thick, and a length (l) equal to 1000 mm (Figure 4.2). In order to evaluate the fundamental vibration frequency under different values of the imposed displacement, considering different initial imperfections, these specimens were subjected to a preliminary phase where different geometrical imperfections were introduced.

The geometrical defects are obtained imposing a prescribed offset from the

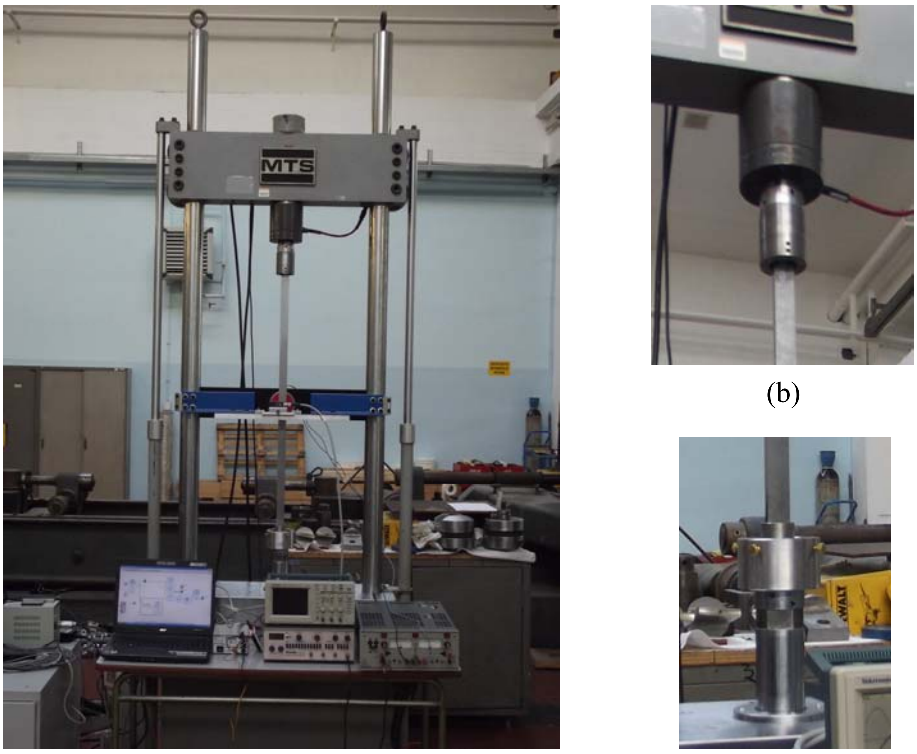

(b)

(a) (c)

Figure 4.1 – General view of the experimental setup showing (a) the testing machine, a specimen, the experimental equipment, and the data acquisition system, (b) and (c) the upper and lower end joints in the case of the hinged-hinged constraint condition.

rectilinear configuration. The first specimen, i.e. B1, is a rectified beam, with a maximum offset (e_0) from the ideal rectilinear condition no larger than 0.2 mm (i.e. a ratio $e_0 / l \leq 0.2/1000$) (Figure 4.2(a)). This configuration is assumed as the rectilinear one and will be used to compare the results given by the other beams presenting larger imposed geometrical deviations. For the other two cases, different maximum offsets at mid-length equal to 1 mm ($e_0 / l = 1/1000$) and 2 mm ($e_0 / l = 2/1000$) respectively for specimens B2 and B3 were considered (Figure

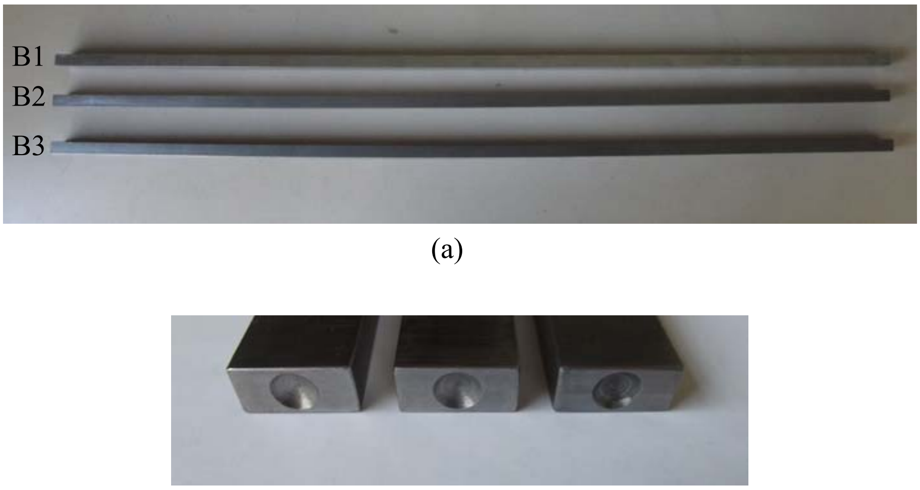

(a)

(b)

Figure 4.2 – Specimens with different geometrical deviations from the rectilinear condition, i.e., different ratios between the maximum offset at midlength e_0 and the specimen length l. (a) Rectified beam B1, with $e_0/l \leq 0.2/1000$, curved beam B2, with $e_0/l=1/1000$, and curved beam B3, with $e_0/l=2/1000$. (b) End cross-sections with spherical cavities of the three considered specimens.

4.2(a)). At both the ends of all beams a spherical cavity was created, with a radius of 8 mm and a maximum depth of 2.5 mm, centred with a tolerance of ± 0.1 mm (see Figure 4.2(b)). During the tests, in each one of these cavities an end sphere was positioned in order to realize the external constraints in the form of spherical hinges that react only in compression.

4.2.2 End Connections

Two aluminium end joints were specially designed and realized in order to create the end restraints of the specimens and, at the same time, to connect them the testing machine.

Figure 4.3 shows a schematic representation of the upper and lower end joints, with an indication of the main dimensions in mm. These joints are rigidly connected through a double-threaded pin to the testing machine, with steel rings that guarantee a correct transmission of the load (see Figures 4.1(b), (c)). The

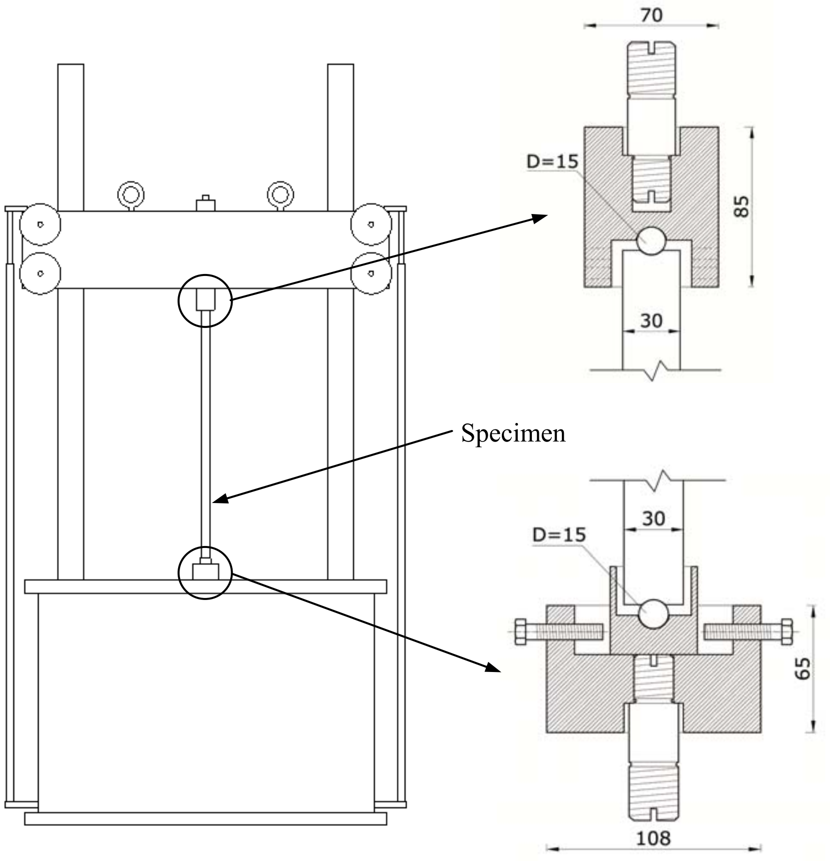

Figure 4.3 – Schematic representation of the upper and lower end joints with indication of the main dimensions in mm.

lower joint has a part that can be adjusted in the horizontal plane to allow the required alignment with the upper one. Figure 4.4 shows a rendering of the lower joint, in the assembled (a) and disassembled (b) configurations.

The contact surfaces between the sphere, the beam and the joint have been spherically shaped in order to realize a self-centring system, at the same time obtaining a reduction of the contact pressure with respect to the case of a contact between non-spherical surfaces. The diameters of these spherical cavities are equal

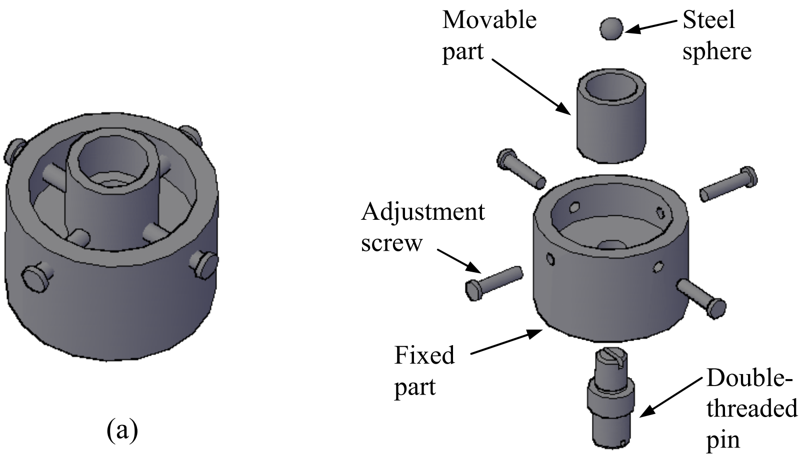

(a)

(b)

Figure 4.4 – Renderings of the lower connection in assembled (a) and disassembled (b) visualizations.

(a)

(b)

Figure 4.5 – Lower (a) and upper (b) connection joints.

to 16 mm. During the tests, two steel spheres having a diameter of 15 mm were interposed to facilitate the self-centring of the specimen. Pictures of the lower and upper joints are shown in Figure 4.5.

4.2.3 Experimental Equipment

The experimental equipment, supporting the forcing and the measuring devices, is shown in Figure 4.6. It consists basically of two transversal elements supporting the forcing actuator (electromagnet) and the measuring device (laser sensor), connected to two circular joints made of aluminium. The aluminium joints, having an external diameter of 120 mm and an internal one of 76.5 mm, serve for the connection of the experimental equipment to the testing machine frame (see Figure 4.1).

On the transversal element presenting a C-shaped cross-section the electromagnet is fastened with a bolt in middle position, while the second transversal element is used to allocate the laser sensor (see Figure 4.6). During the tests, the specimen is positioned between the electromagnet and the laser sensor. The laser sensor is allocated on an adjustable sled, mounted on a sliding plate, in order to allow the regulation of the distance between the measuring point and the reflection surface. In particular, the inferior plate and the superior slide are used to regulate larger and smaller displacements respectively (see Figure 4.7).

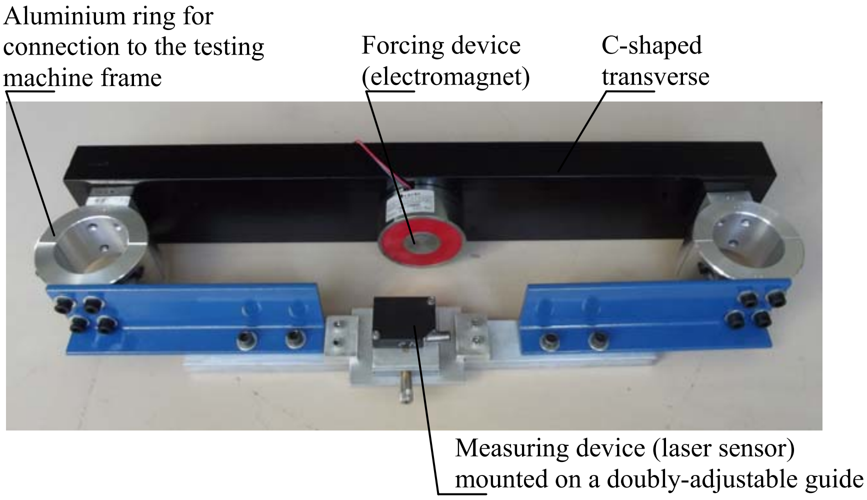

Figure 4.6 – Experimental equipment.

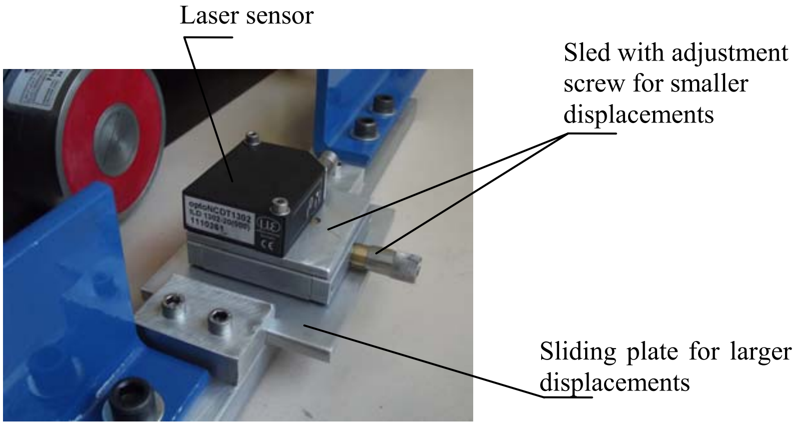

Figure 4.7 – Laser sensor mounted on an adjustment sled connected to a sliding plate for regulation of the distance.

Forcing Device (Electromagnet)

The forcing device is constituted by an electromagnet for industrial applications, of cylindrical shape. We adopted the type T100 produced by C.E.I. srl. A picture of the device together with the corresponding characteristic curve, reporting the force vs. magnetic gap diagram, are shown in Figure 4.8. The curve reported in Figure 4.8(b) is related to experiments on a ferromagnetic object at least 12 mm thick and with the electromagnet powered by direct current at a voltage of 24 V.

The electromagnetic force may also be controlled by changing the voltage powering of the device. The result of a calibration of the electromagnet made on a ferromagnetic object 10 mm thick, powering the electromagnet at different voltages for different magnetic gaps is shown in Figure 4.9.

Measuring Device (Laser Sensor)

The measuring device is constituted by a laser triangulation displacement sensor. The adopted type of sensor has the advantages of being a non-contact device, therefore enabling high speed measurement with high precision.

Among the models available, we selected the one having characteristic parameters which were suitable for the purposes of our application. The adopted

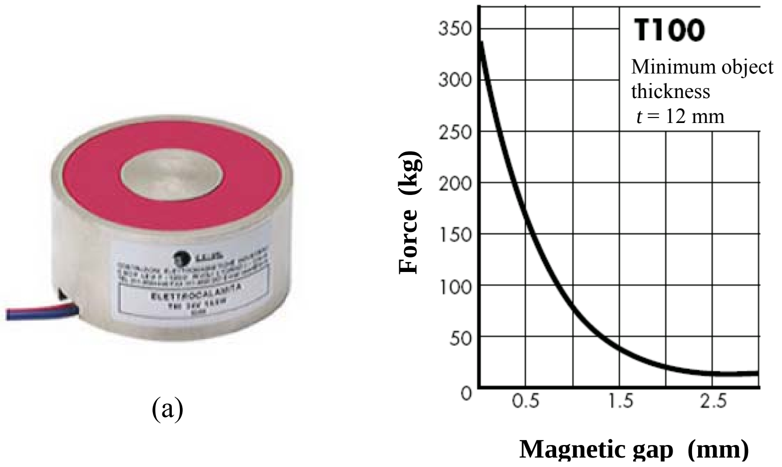

(a)

(b)

Figure 4.8 – Adopted electromagnet (a) and corresponding characteristic curve (b).

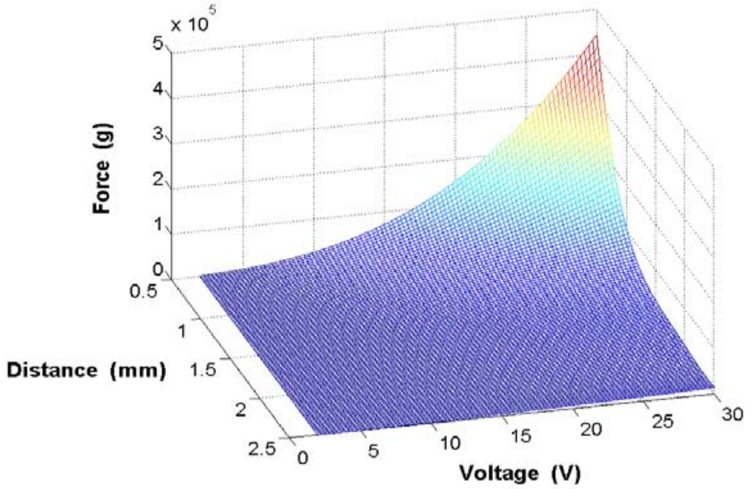

Figure 4.9 – Result of calibration of the electromagnet on a ferromagnetic object 10 mm thick.

sensor is the optoNCDT 1302-20 produced by Micro-Epsilon. Figure 4.10 shows a scheme of the laser sensor and reports the corresponding characteristic curve, with indication of Start and End of Measuring Range. The measuring range is equal to 20 mm, while the resolution is equal to 10 µm, and the measuring rate is equal to 750 Hz. The main characteristics of the laser sensor are collected in Table 4.1. The measuring range may be narrowed to improve the accuracy of the measurement using the sample frequency of 750 Hz on a smaller range. During the experiments the default parameters were adopted.

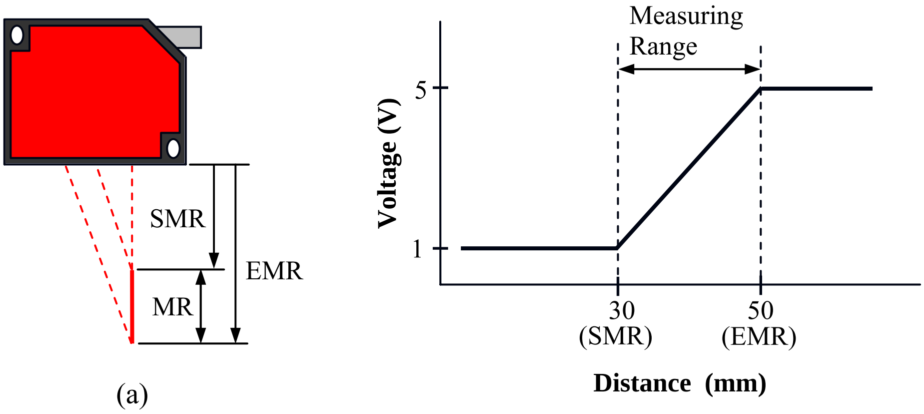

(a)

(b)

Figure 4.10 – Scheme of the adopted laser triangulating displacement sensor (a) and corresponding characteristic curve (b) with indication of Start of Measuring Range (SMR) and End of Measuring Range (EMR).

Table 4.1 – Main characteristics of the laser sensor.

Measuring Range (MR)	Start of Measuring Range (SMR)	Midrange (MR)	End of Measuring Range (EMR)	Resolution (Dynamic 750 Hz)
20 mm	30 mm	40 mm	50 mm	10 µm

4.2.4 Specimen Centring and Testing Procedure

Figure 4.11 shows the upper and lower joints connected to the testing machine.

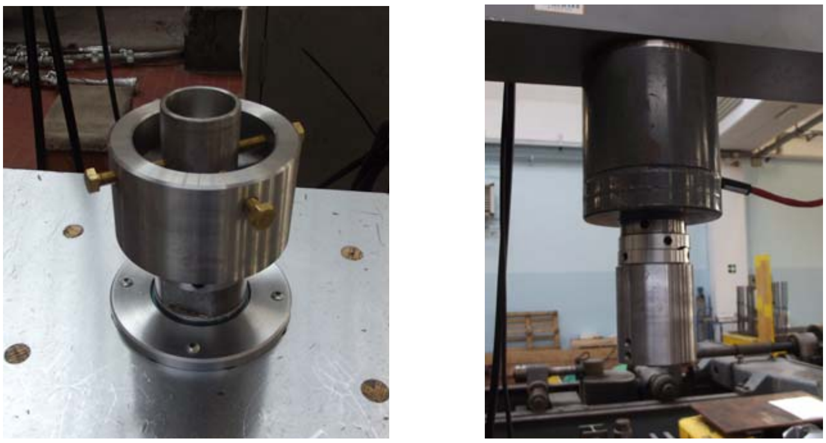

(a) (b)

Figure 4.11 – Lower (a) and upper (b) end joints connected to the testing machine.

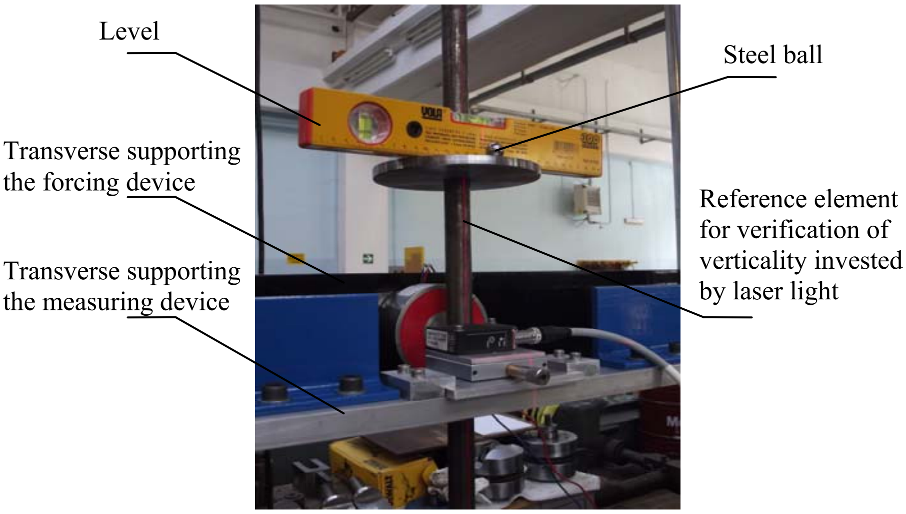

Figure 4.12 – Verification of the vertical alignment of the upper and lower end joints through a reference device coupled with a level and a self-levelling laser to guarantee the vertical positioning of the specimens and the correct transmission of the forces.

While the upper joint, once mounted, remains in a fixed position, the lower one may be adjusted in the horizontal plane to allow the correct positioning therefore ensuring the vertical alignment.

To ensure the required verticality, a steel element was created *ad hoc* for the verification of the alignment of the two joints and the correct assembly of the apparatus (Figure 4.12). It consists of a straight bar of full-round circular cross-section, welded to a circular disk which, by construction, was made orthogonal to the bar longitudinal axis. The assessment was done using a level positioned along different orientations, and a self-levelling laser as shown in Figure 4.12. The alignment is important to transmit displacements (and therefore, forces) along a direction as vertical as possible at the same time allowing the positioning of the specimen with its longitudinal axis in the vertical position. The adjustment of the position of the movable part of the lower joint may be controlled by the regulation of the four threaded screws, positioned at 90° from each other in the horizontal plane (see Figure 4.11(a)).

The tests were performed controlling the vertical displacement transmitted to the beam by the linear actuator (hydraulic jack) (see Figure 4.1(c)). To each value of the imposed displacement corresponds an internal axial load. For each imposed

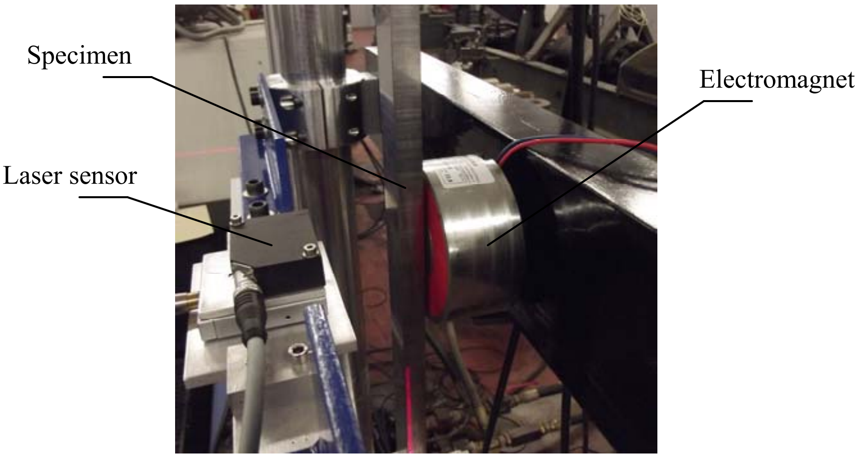

Figure 4.13 – Testing configuration with rectified beam (specimen B1) undergoing post-critical deflections.

displacement, the fundamental vibration frequency was obtained analyzing the time history of the transversal displacement of the beam, measured by the laser sensor disposed as shown in Figure 4.13. Both conditions of forced and free vibrations were analyzed. In both cases, an external forcing was obtained by the electromagnet disposed as shown in Figure 4.13. In the first case (forced vibrations), the electromagnet transmitted to the beam a sinusoidal force, controlled in frequency and amplitude by a wave generator, so that the forced response could be measured under different conditions. In the second case (free vibrations), the electromagnet was turned off after 10 s and the free response was measured. A total of three independent methods were used to analyze the response, as will be described in the sequel. Figure 4.14 shows a test on the rectified beam (specimen B1) for the evaluation of the natural fundamental frequencies under imposed displacements.

Figure 4.14 – A test on the rectified beam (specimen B1) for the evaluation of the natural fundamental frequencies under different imposed displacements.

4.2.5 Data Acquisition and Analysis

The laser sensor was coupled with a data acquisition device NI USB-6009 produced by National Instruments^{TM}. Acquisition and analysis of the measured signals were carried out through computer programs that were specially developed using the software LabVIEW®.

LabVIEW (Laboratory Virtual Instrument Engineering Workbench) is a powerful instrumentation and analysis programming language for PCs, produced by National Instruments. It is a graphical programming language that has been widely adopted throughout industry, academia, and research labs as the standard for data acquisition and instrument control software. LabVIEW integrates data acquisition, analysis, and presentation in one system.

LabVIEW program development environment is different from other programming systems which use text-based languages to create lines of code. LabVIEW uses a graphical programming language (called G) to create programs in a pictorial form called a block diagram, eliminating a lot of the syntactical details. LabVIEW programs are called virtual instruments (VIs) because their appearance and operation imitate actual instruments.

The graphical interface which allows to create and use LabVIEW programs has two distinct work planes:

- the *front panel*, which is the interactive user interface of a VI, so named because it simulates the front panel of a physical instrument. The front panel can contain knobs, push buttons, graphs, and many other controls (which are user inputs) and indicators (which are program outputs);
- the *block diagram* is the VI's source code, constructed in LabVIEW's graphical programming language, G. The block diagram is the actual executable program. The components of a block diagram are lower-level VIs, built-in functions, constants, and program execution control structures. Wires must be drawn to connect the appropriate objects together to indicate the flow of data between them. Front panel objects have corresponding terminals on the block diagram so data can pass from the user to the program and back to the user. In order to use a VI as a subroutine in the block diagram of another VI, it must have an icon and a connector. A VI that is used within another VI is called a *subVI* and is analogous to a subroutine. The icon is a VI's pictorial representation and is used as an object in the block diagram of another VI. A VI's connector is the mechanism used to wire data into the VI from other block diagrams

when the VI is used as a subVI. Much like parameters of a subroutine, the connector defines the inputs and outputs of the VI.

Four LabVIEW programs were developed for the acquisition and analysis of the measured time histories of the mid-point displacement of each specimen in all the testing configurations.

Long-Time Acquisition

A first program was developed for long-time acquisition of non-oscillating displacements. It was used to register the transversal displacement (as a voltage signal) of the mid-point of each specimen to get the transversal displacement vs. time and vertical load vs. transversal displacement curves. Figures 4.15(a) and (b) show the block diagram and front panel worktops, respectively, for the long-time acquisition program.

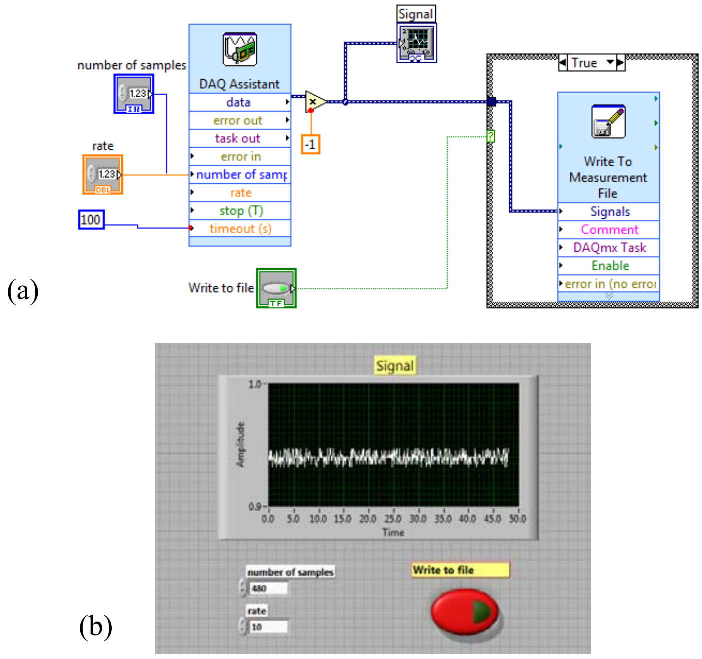

Figure 4.15 – Block diagram (a) and front panel (b) of the LabVIEW program for long-time acquisition.

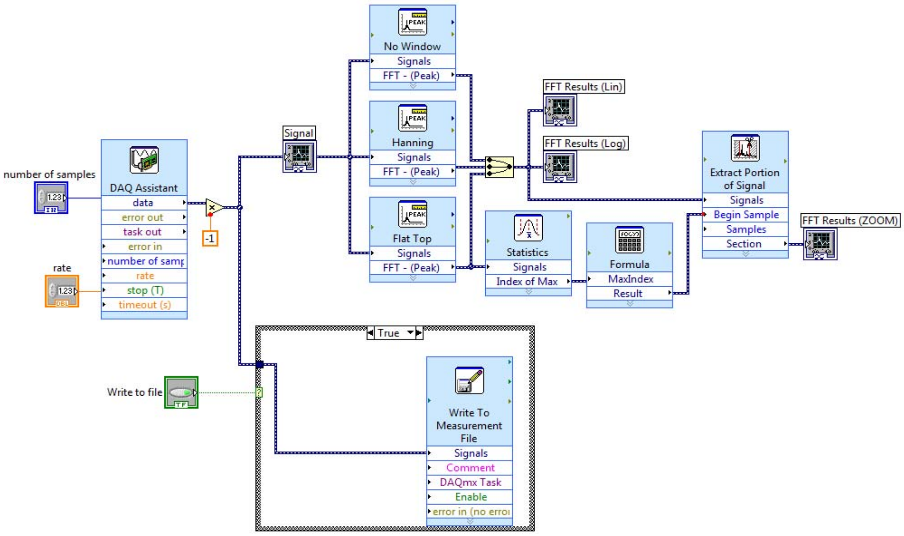

Figure 4.16 – Block diagram of the LabVIEW program for short-time acquisition.

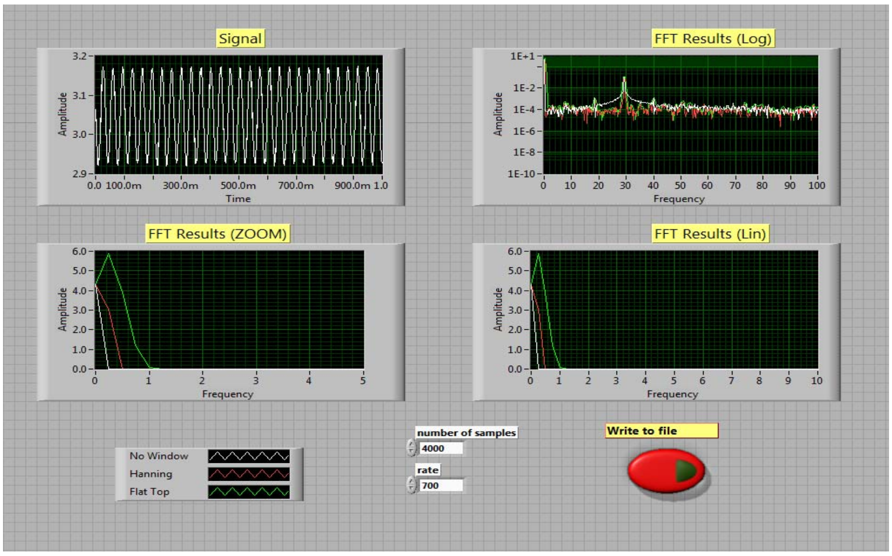

number of samples 4000

rate 700

Figure 4.17 – Front panel of the LabVIEW program for short-time acquisition.

Short-Time Acquisition

A specific program for short-time acquisition was also developed. It was used to acquire the time histories of the mid-point displacement during all the dynamic tests. On the basis of these data, the free and forced responses were consequently analyzed, in a second phase, to carry out the natural frequencies and detect the resonance conditions. Figures 4.16 and 4.17 show the block diagram and front panel worktops, respectively, for the short-time acquisition program.

This program, in addition, makes the Fast Fourier Transform (FFT) of the acquired signal (see Figure 4.17).

Reading and Writing to a File

The acquired signals are then read and written to a file by another program, which transforms the data into a form that could conveniently be analyzed by the last program. This reading and writing program therefore reads the values saved by the acquisition program and creates a .txt file containing two column vectors whose elements are the time and voltage values. The block diagram of the read and write to a file program is shown in Figure 4.18, while the front panel of the same program is shown in Figure 4.19.

Data Analysis

The last program analyzes the measured signal to extract the modal parameters like natural frequencies and damping ratios. Basically, it applies the Logarithmic Decrement Method to the free response signal.

The program allows the user to select the interval of values to be analyzed, and within that interval the range of values to be considered in calculations may be chosen. Among the selected values, the program applies the Logarithmic Decrement Method several times to different couples of values, running all the possible combinations of values. At the end, the mean values of the quantities of interest are calculated, and some statistics to judge the goodness of the estimate are given.

The program code is composed by sixteen block diagrams. As an example, one of them is shown in Figure 4.20. Figure 4.21 shows the front panel of the LabVIEW program for data analysis.

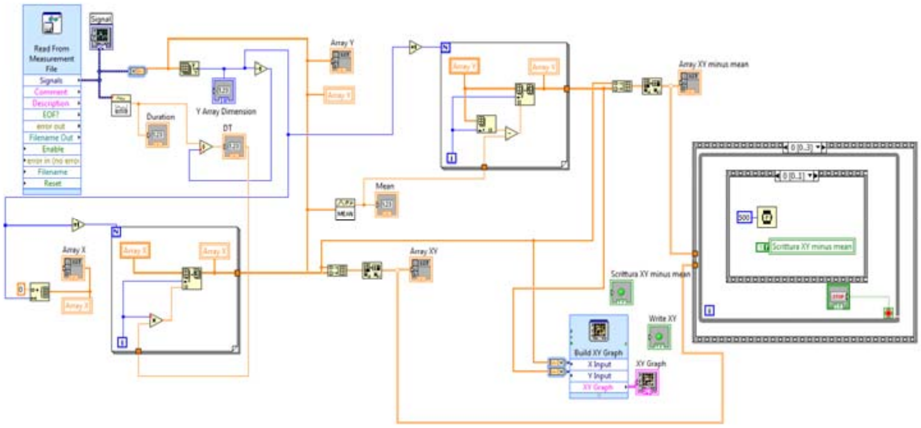

Figure 4.18 – Block diagram of the LabVIEW program for reading and writing to a file.

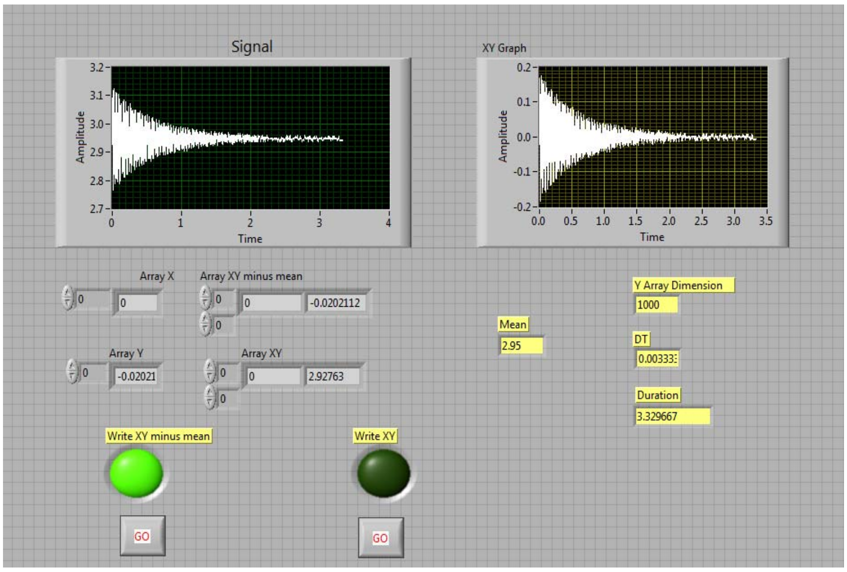

Array X: 0 | 0
Array XY minus mean: 0 | 0 | 0 | -0.0202112
Array Y: 0 | -0.02021
Array XY: 0 | 0 | 0 | 2.92763
Mean: 2.95
Y Array Dimension: 1000
DT: 0.00333
Duration: 3.329667
Write XY minus mean
Write XY

Figure 4.19 – Front panel of the LabVIEW program for reading and writing to a file.

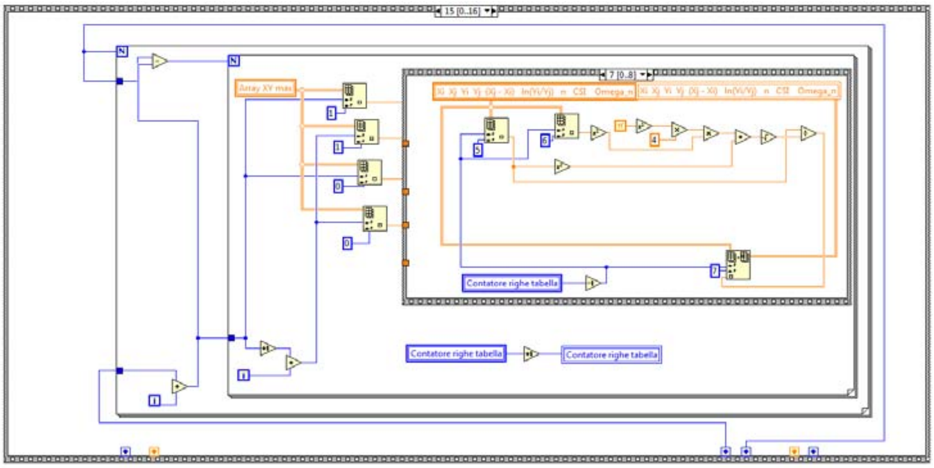

Figure 4.20 – One of the sixteen block diagrams constituting the LabVIEW program for data analysis.

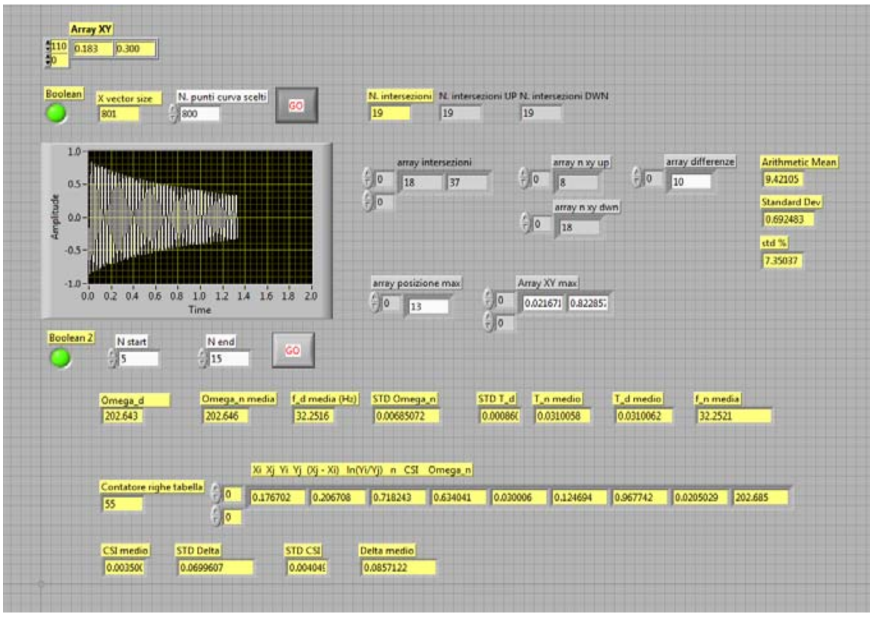

Array XY
110 0.183 0.300
0

Boolean
X vector size 801
N. punti curva scelti 800
N. intersezioni 19
N. intersezioni UP 19
N. intersezioni DWN 19

array intersezioni
0 18 37
0

array n xy up
0 8

array n xy dwn
0 18

array differenze
0 10

Arithmetic Mean 9.42105
Standard Dev 0.692483
std % 7.35037

array posizione max
0 13

Array XY max
0 0.021671 0.82285
0

Boolean 2
N start 5
N end 15

Omega_d 202.643
Omega_n media 202.646
f_d media (Hz) 32.2516
STD Omega_n 0.00685072
STD T_d 0.00086
T_n medio 0.0310058
T_d medio 0.0310062
f_n media 32.2521

Contatore righe tabella 55

Xi Xj Yi Yj (Xj - Xi) ln(Yi/Yj) n CSI Omega_n
0 0.176702 0.206708 0.718243 0.634041 0.030006 0.124694 0.967742 0.0205029 202.685
0

CSI medio 0.00350
STD Delta 0.0699607
STD CSI 0.00404
Delta medio 0.0857122

Figure 4.21 – Front panel of the LabVIEW program for data analysis.

4.3 Experimental Results

A total of six testing configurations were performed changing the constraint conditions for each specimen (see Table 4.2). For each configuration, the fundamental vibration frequency was determined under different values of the mean axial force obtained imposing different vertical displacements to the beam end. The testing configurations are also schematically represented in Figure 4.22 and reported in Table 4.2 according to their initial imperfection and considering the different constraints adopted.

Testing configurations 1 and 2 in Table 4.2, shown in Figures 4.22(a) and (b) respectively, represent the cases in which the rectified beam is hinged at both ends (case 1) and the case in which the upper end is clamped and the lower one is hinged (case 2). The same constraint configurations are replicated for specimen B2, having a geometrical imperfection $e_0 / l = 1/1000$ (testing configurations 3 and 4 in Table 4.2), and for specimen B3, were $e_0 / l = 2/1000$ (testing configurations 5 and 6 in Table 4.2).

Table 4.2 – Testing configurations.

Testing configuration	**Specimen**	**Geometrical deviation (e_0/l)**	**Upper-constraint condition***
1	B1	≤0.2/1000	Hinged
2	B1	≤0.2/1000	Clamped
3	B2	1/1000	Hinged
4	B2	1/1000	Clamped
5	B3	2/1000	Hinged
6	B3	2/1000	Clamped

* The lower joint is always a hinge in all the testing configurations.

In the case of double-hinged beam the theoretical buckling load calculated according to the Euler’s formula (Bažant and Cedolin, 2003) is about 17.5 kN, while the theoretical fundamental flexural frequency according to linear dynamics (Clough and Penzien, 2003; Weaver et al., 1990) is about 35.2 Hz. On the other hand, in the case of hinged-clamped beam, the Euler’s critical load is about 37.2 kN, while the fundamental frequency is 55 Hz. The previous theoretical values are not affected by imperfections and so they hold for all specimens B1, B2, and B3. First, the load vs. transversal displacement measured at the midpoint of the beam

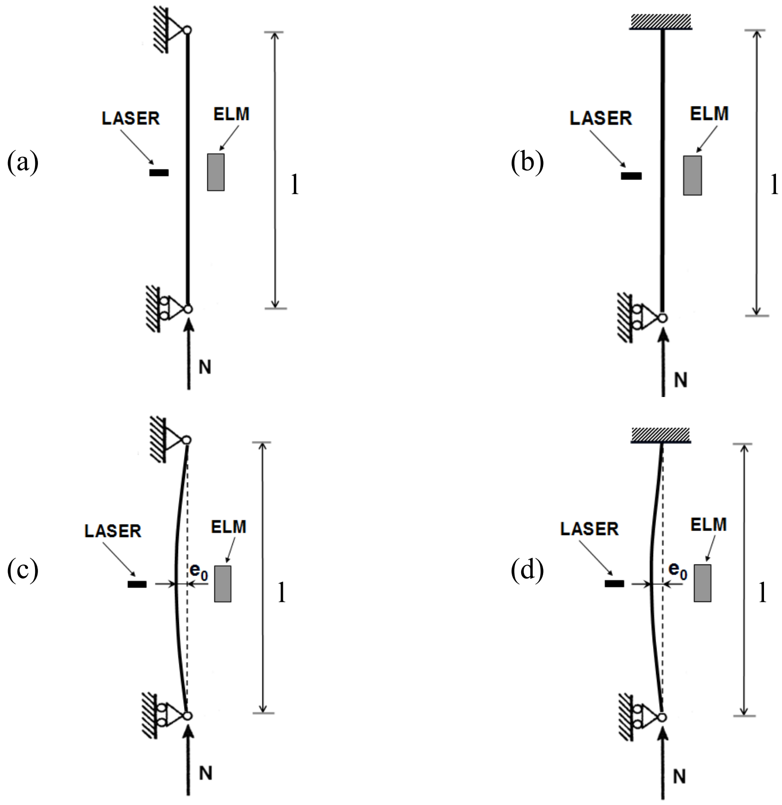

Figure 4.22 – Schematic representation of the testing configurations. (a) Double-hinged rectified beam (configuration 1 in Table 4.2), (b) hinged-clamped rectified beam (configuration 2 in Table 4.2), (c) double-hinged imperfect beam (configurations 3 and 5 in Table 4.2), and (d) hinged-clamped imperfect beam (configurations 4 and 6 in Table 4.2).

was obtained in all the tested configurations (Figure 4.23). The axial load was measured by the testing machine, while the transversal displacement was measured by the laser sensor. The axial load is intended to be the value which corresponds to the vertical displacement imposed by the actuator of the testing machine. The curves reported in Figure 4.23 are obtained by applying a ramp to the displacement of the lower actuator with an imposed velocity of 25×10^{-6} m/s.

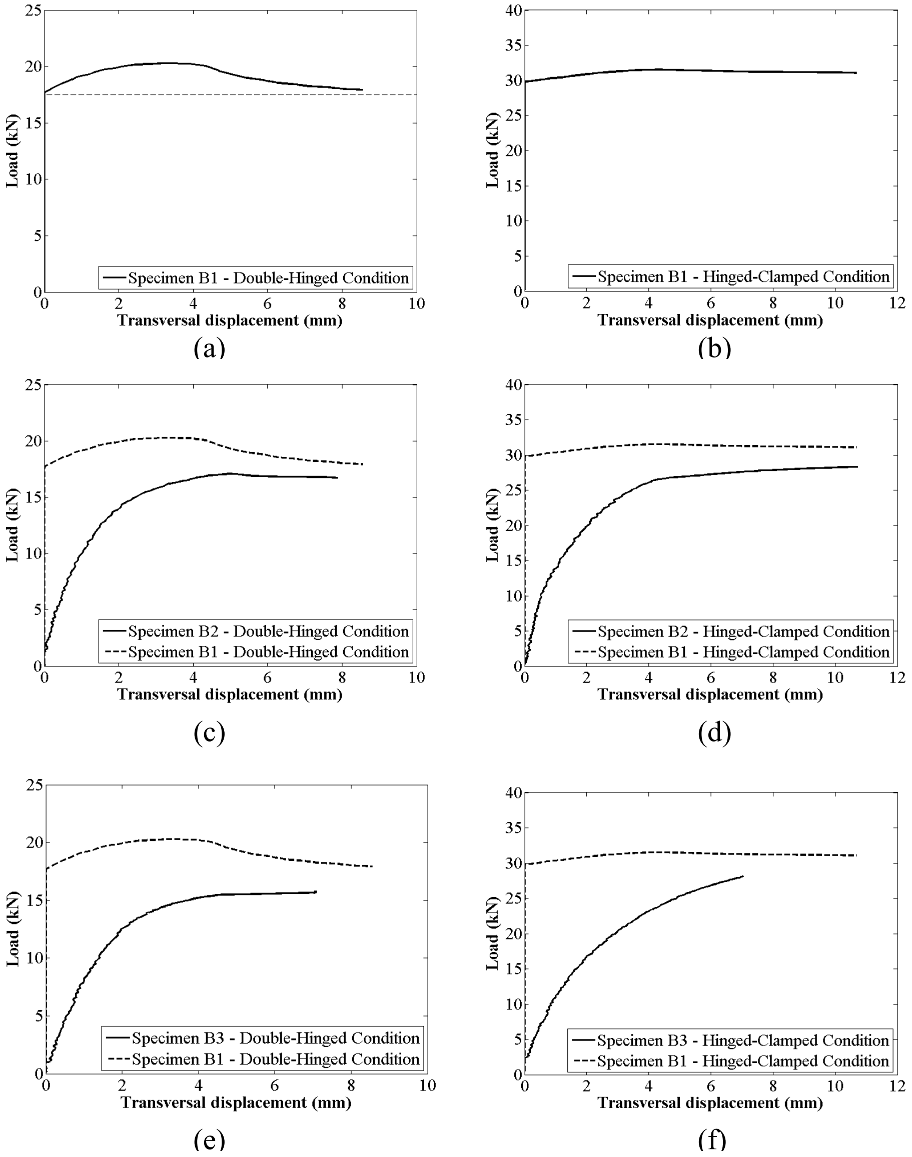

(a) (b)

(c) (d)

(e) (f)

Figure 4.23 – Load vs. transversal displacement curves for specimens B1-3 under different constraint conditions. (a) Specimen B1 (rectified beam) in the double-hinged constraint condition, (b) specimen B1 in the hinged-clamped constraint condition, (c) specimen B2

(1/1000) compared with specimen B1 in the double-hinged constraint condition, (d) specimen B2 compared with specimen B1 in the hinged-clamped constraint condition, (e) specimen B3 (2/1000) compared with specimen B1 in the double-hinged constraint condition, and (f) specimen B3 compared with specimen B1 in the hinged-clamped constraint condition.

Figure 4.23(a) shows the load vs. transversal displacement for the double-hinged rectified beam (case 1 in Table 4.2). This graph represents the typical response of a perfect beam, showing a bifurcation point almost equal to the theoretical Euler's buckling load (17.5 kN). The post-critical response is also reported, showing a stable post-critical branch, exhibiting a hardening phase and then a softening behaviour which asymptotically reaches the critical load.

Figure 4.23(b) shows the load vs. transversal displacement of the same beam but considered in the case of hinged-clamped constraint condition (case 2 in Table 4.2). In this case larger differences between the expected and the measured results are obtained. In fact, the graph shows a bifurcation in correspondence of a load equal to about 30 kN, while the theoretical Euler's load is equal to 37.2 kN. This behaviour can be interpreted as an inefficiency of the constraint condition at the upper end with a condition of not-perfectly-clamped joint.

Figures 4.23(c) and (d) show in solid line the load vs. displacement curves for the first curved beam (cases 3 and 4 in Table 4.2, respectively). In both the double-hinged (Figure 4.23(c)) and hinged-clamped (Figure 4.23(d)) cases the response is the typical one of beams with initial imperfections. Transversal displacements appear from the beginning and increase more than proportionally with the load due to second-order effects that reduce the flexural stiffness. When the flexural stiffness approaches zero, the maximum loading capacity is reached.

The load vs. displacement curves for specimen B3, under testing conditions 5 and 6 in Table 4.2, are reported in Figures 4.23(e) and (f), respectively. In these cases, responses analogous to those observed for specimen B2, reported in Figures 4.23(c) and (d), were observed. For specimen B3 the effects of the initial imperfection are larger respect to specimen B2, although the behaviour is similar.

In all the cases presenting initial deformation, the maximum load never reaches the equivalent value of the rectified beam (testing configurations 1 and 2 of Table 4.2). In order to appreciate these differences, in Figures 4.23(c)-(f) the corresponding curves of the rectified beam are also reported (dashed lines).

Figure 4.24 shows the curves fundamental frequency vs. axial load for the case 1 listed in Table 4.2. Natural fundamental frequencies were obtained by three different and independent procedures. Lines marked with solid triangles are

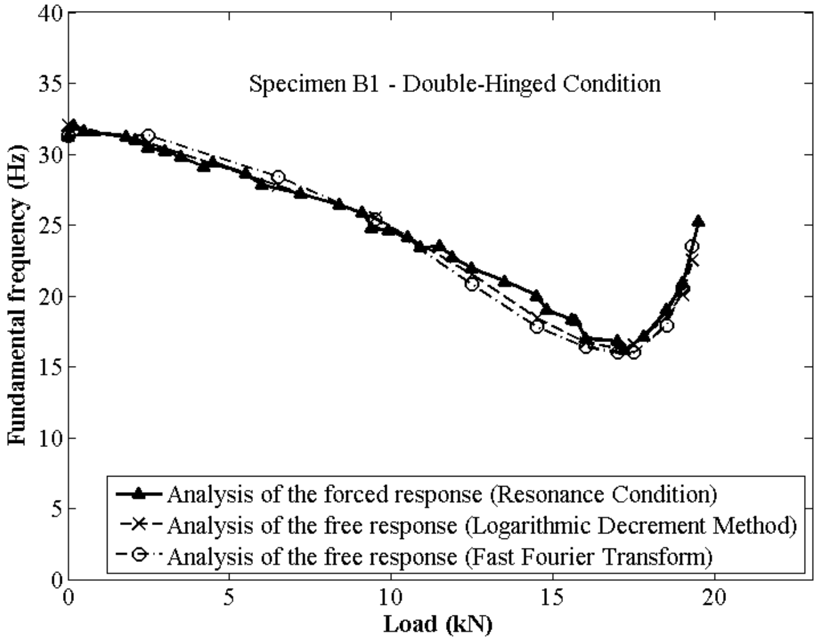

Figure 4.24 – Fundamental frequency vs. axial load curves for the testing configuration 1 in Table 4.2 (specimen B1, double-hinged condition) obtained applying three different procedures: the analysis of the forced response to different frequencies of the harmonic excitation, through which resonance condition may be detected; the analysis of the free response applying the Logarithmic Decrement Method; and the analysis of the free response using the Fast Fourier Transform.

related to the fundamental frequencies obtained analyzing the forced response to different frequencies of the acting electromagnetic sinusoidal force, i.e. identifying the resonance condition. Lines marked with crosses are related to the fundamental frequencies obtained by the analysis of the free response using the Logarithmic Decrement Method (Clough and Penzien, 2003). Lines marked with white circles are referred to the signal analysis of the free response through the Fast Fourier Transform. In all the analyzed cases (1 to 6 in Table 4.2), there is a perfect correspondence between the results given by the three adopted methods.

Even though in a displacement-controlled test the zero-frequency condition is never reached, due to the fact that the structural response is always stable, a

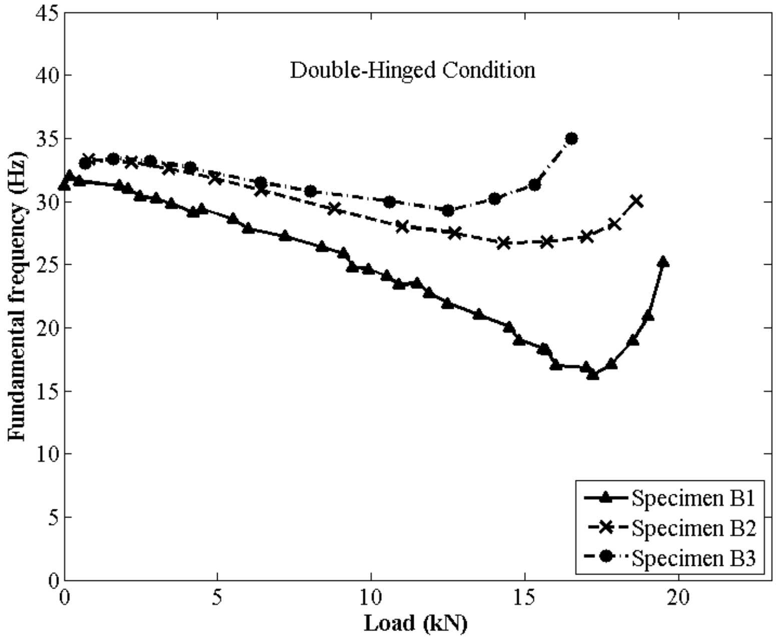

Figure 4.25 – Fundamental frequency vs. axial load curves for specimens B1-3 in the double-hinged constraint condition (only the values obtained by the analysis of the forced response are reported).

distinction between the pre- and the post-buckled phases is possible. In fact, two different trends of the frequencies with respect to the axial load were observed. It is possible to observe that the transition from the first phase to the second is particularly sharp for the rectified beam, while it becomes smoother in the cases of beams presenting initial curvature (geometrical imperfection). Moreover, an important influence of the initial imperfections on the natural frequency evolution can be observed.

Figure 4.25 shows the variations of the fundamental frequency vs. the axial load for specimens B1-3 in the double-hinged constraint condition (cases 1, 2, and 3 in Table 4.2), while the same curves for specimens B1-3 in the hinged-clamped constraint condition are reported in Figure 4.26 (cases 2, 4, and 6 in Table 4.2). For all these tests the qualitative trend of the fundamental frequency shows a decrease down to the minimum of the curve, after which the natural frequency

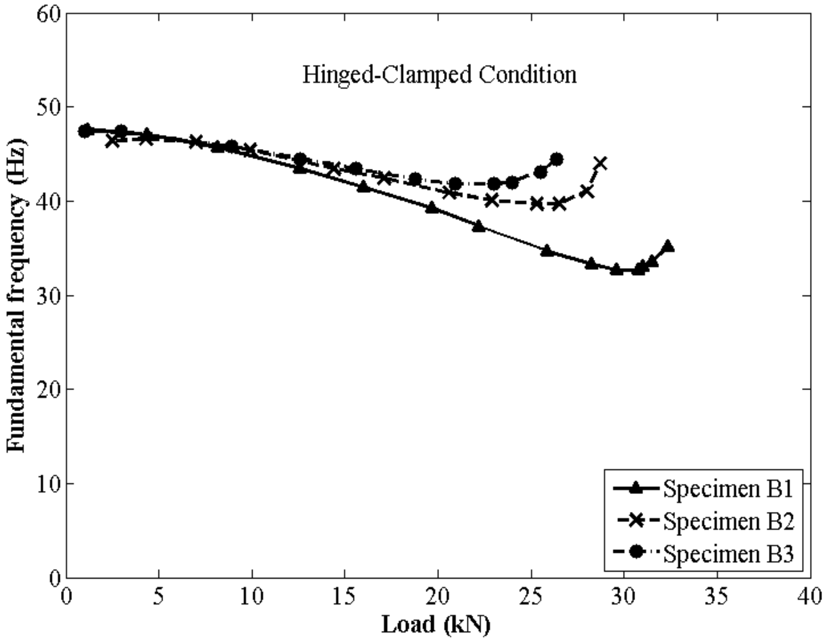

Figure 4.26 – Fundamental frequency vs. axial load curves for specimens B1-3 in the hinged-clamped constraint condition (only the values obtained by the analysis of the forced response are reported).

starts to increase sharply, showing a stiffening behaviour. In this case of displacement controlled experiments the response is always stable, but after a certain value of the transversal displacement the tendency is reversed. In the first phase, the specimens show a decrease in the fundamental frequency as the axial load increases (softening behaviour), while during the second phase the fundamental frequency increases with the displacement (hardening behaviour). This effect may be ascribed to the control of the axial displacement and it can not be observed if the load is imposed and the sliding of one end is allowed.

The behaviour observed for specimen B1 in the double-hinged condition (case 1 in Table 4.2) is characterized by two well distinguishable phases. In this case, the transition between a pseudo-linear branch and a pseudo-exponential one is particularly marked (see Figures 4.24 and 4.25). From this point of view the transition is sharp and the values corresponding to 17.2 kN and 16.2 Hz of the curve are unpredictable. Under the same constraint condition, specimens B2 and B3 (cases 3, and 5 in Table 4.2) show a wider transition interval with respect to specimen B1. The greater the geometrical deviations the smoother the transition phase (see Figure 4.25). The possibility to foresee the beginning of the second phase when the acting load is far from the ultimate load could be used in analogous measurements performed on slender elements subjected to subsidence imposed in situ. Analogous considerations could be done in the case of hinged-clamped configurations (see Figure 4.26).

4.4 Numerical Simulations

Numerical models were implemented in order to reproduce the experimental tests conducted on specimens B1, B2, and B3 in the case of double-hinged condition (testing configurations 1, 3, and 5 in Table 4.2). The simulations were conducted using Working Model 2D 5.0, a multibody dynamic simulator based on the numerical solution of the equations of motion.

4.4.1 Numerical Models

Figure 4.27(a) shows a general view of the model reproducing the rectified beam (specimen B1), hinged at both the ends, in the undeformed configuration. The model is constituted by nine elements where the mass is concentrated, ten massless connection units, ten axial springs, eighteen torsional springs, two end constraints, and, lastly, a rod element simulating the effect of the hydraulic jack.

The model concentrates the mass of the specimen, uniformly distributed, into nine squared masses, each one being two centimetres long. Each of these elements has the mass of one ninth of the total mass of the specimen, and, in particular, the value was set up equal to 3.09×10^{-3} kg. The masses are connected to each other through connection units that are massless and infinitely rigid in flexure, but at the same time they allow axial displacements (see Figure 4.27(b)). The axial stiffness of the specimen is concentrated in ten axial springs, placed inside the connection units. These springs present a relaxed length of two centimetres and a linear stiffness equal to 9.45×10^{8} N/m. The flexural stiffness of the specimen is concentrated into the torsional springs connecting the masses to the rigid massless elements (see Figure 4.27(b)). Each torsional spring has a linear stiffness equal to 6.0×10^{4} Nm/rad.

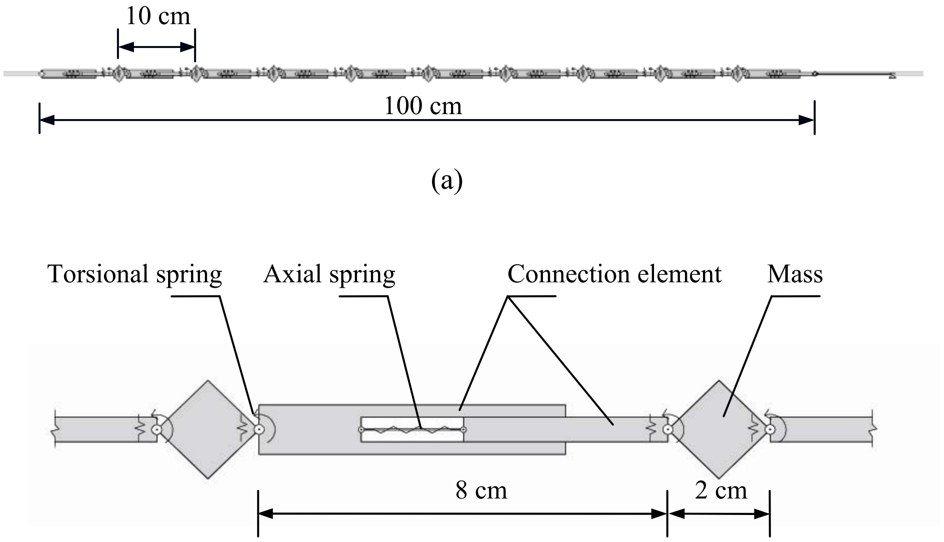

(a)

(b)

Figure 4.27 – Multibody model of a specimen obtained with Working Model 2D 5.0. (a) General view of the complete model showing nine masses (squares) and the connecting elements. (b) Detail of a portion showing masses, a massless connection element, axial and torsional springs that simulate the axial and flexural elastic stiffness of the entire beam.

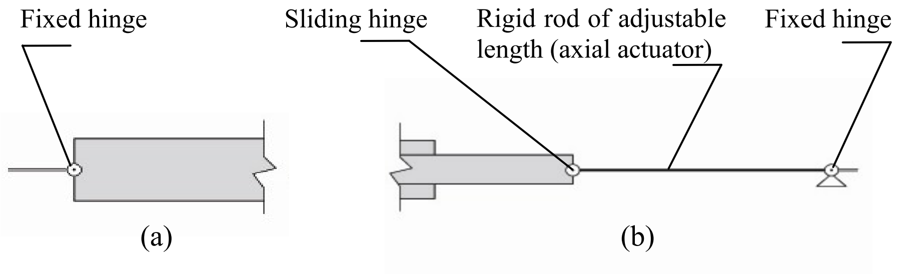

(a) (b)

Figure 4.28 – External constraints simulating the end connections (upper and lower joints) of the experimental tests. (a) Fixed hinge simulating the upper joint. (b) Sliding hinge simulating the lower joint connected to a rod element that simulates the linear actuator of the testing machine (hydraulic jack).

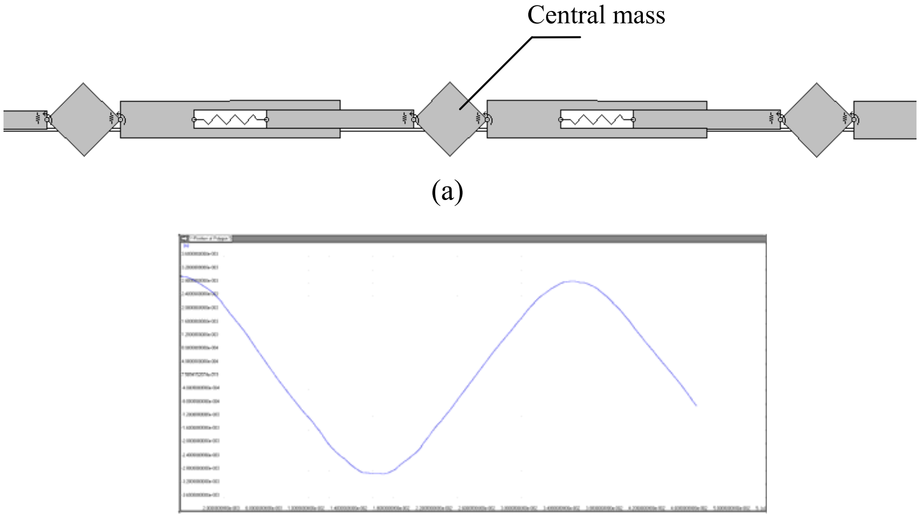

(a)

(b)

Figure 4.29 – Procedure adopted for the evaluation of the fundamental natural frequency. (a) Initial condition represented by a deformed shape similar to the first vibration mode of the beam with zero-velocity. (b) Transversal displacement of the central mass vs. time.

The external constraints are represented by two hinges, one of which is fixed and simulates the upper joint, while the other one can slide on a guide in order to simulate the lower joint (see Figures 4.1 and 4.28). The hydraulic jack is simulated by means of an infinitely rigid rod element, whose length can be adjusted in order to reproduce the imposed displacements obtained experimentally.

Under each imposed displacement, the fundamental vibration frequency was obtained by analyzing the time history of the transversal displacement of the central mass. The initial condition was represented by a deformed shape similar to the first vibration mode of the beam, with zero-velocity (Figure 4.29). The maximum displacement imposed in the initial condition was equal to 2 mm (deflection of the central mass), in all the simulations.

The numerical models allowed the simulation of the response of the three specimens B1, B2, and B3, with their geometrical imperfections. Specimen B1 (rectified beam) was considered perfectly straight, and its initial configuration was

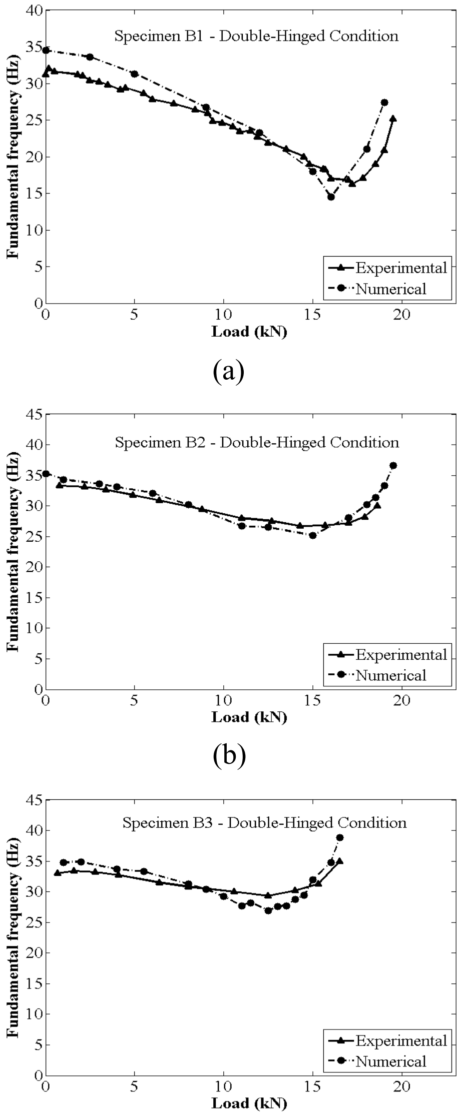

(a)

(b)

(c)

Figure 4.30 – Comparison between experimental and numerical fundamental frequency vs. axial load curves for specimens B1 (a), B2 (b), and B3 (c) in the double-hinged constraint condition.

assumed rectilinear. For specimens B2 and B3 an originally curved shape was generated to reproduce the imperfect geometry of the two specimens. This approximation was very close to the experimental conditions realized in the laboratory and it allowed us to obtain a good numerical reproduction of the experimental results.

4.4.2 Numerical Results and Discussion

Figure 4.30 shows the comparison between the experimental results and those obtained by the numerical simulations. It is possible to observe that fundamental frequency vs. load behaviours obtained during the tests are well reproduced by the numerical model. In the case of specimen B1 (rectified beam), in particular, the frequency trend obtained by increasing the imposed displacement is well reproduced showing an abrupt transition from the first to the second phase. The cusp localized approximately in correspondence of 16 kN is even more evident than in the experimental plot (see Figure 4.30(a)), consistently with the model of a perfectly straight element.

The different behaviour shown by specimen B1 during the first and the second phase can be explained by the numerical model. In fact, while during the first phase the beam oscillates about the original rectilinear configuration (Figure 4.31), in the second one it oscillates about a curved configuration (Figure 4.32). In reality, some imperfections are present and the consequence is that the transition is smoother. In particular, in the cases of specimens B2 and B3, the beams never oscillate about a rectilinear configuration; starting from their originally curved configurations, they oscillate about a more and more curved configuration. In any case, a distinction between a first and a second phase is always possible. The results obtained by the simulations reproducing the tests on specimens B2 and B3 are reported in Figures 4.30(b) and (c), respectively.

Figure 4.33 collects all the fundamental frequency vs. load curves obtained by the numerical simulations. From these graphs it is possible to observe that for specimens B2 and B3, the transition between the first and the second phase (which can be identified also in these cases) appears in advance with respect to the case of specimen B1: this transition is favoured by the presence of the geometrical imperfection. Moreover, from Figure 4.33 it can also be seen that the greater the initial geometrical deviation the smaller the slope in the first branch of the frequency trend. These aspects, originally observed from the experimental results, are both confirmed and reproduced by the numerical simulations.

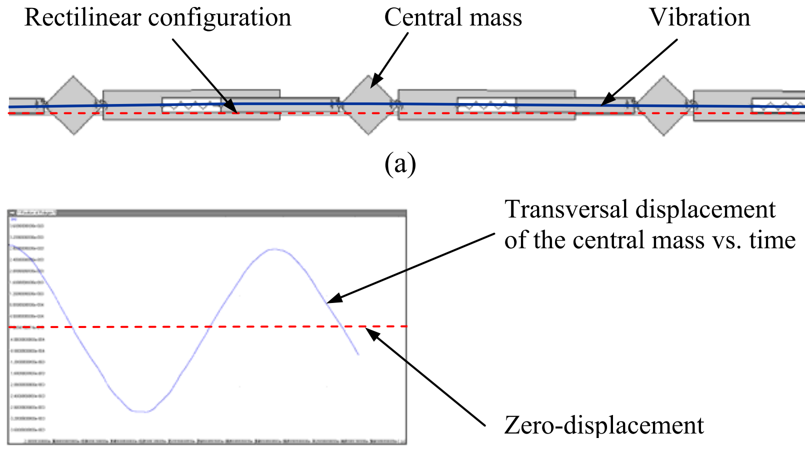

(a)

(b)

Figure 4.31 – Behaviour of specimen B1 during the first phase predicted by the numerical model. (a) Oscillations about the rectilinear configuration. (b) Transversal displacement of the central mass vs. time.

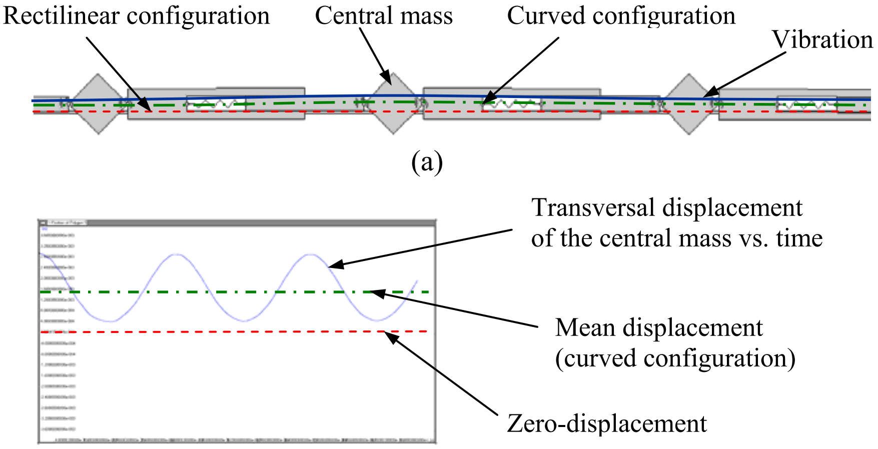

(a)

(b)

Figure 4.32 – Behaviour of specimen B1 during the second phase predicted by the numerical model. (a) Oscillations about a curved configuration. (b) Transversal displacement of the central mass vs. time.

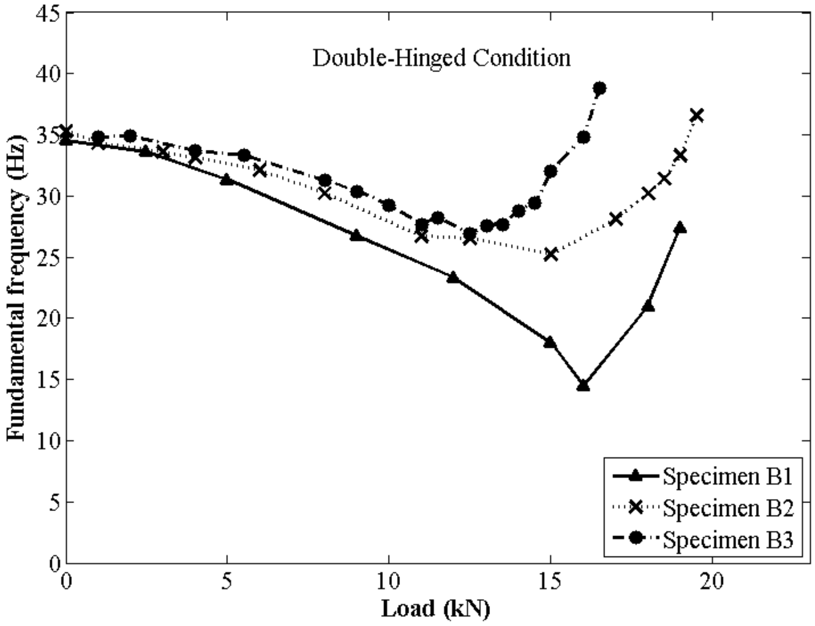

Figure 4.33 – Comparison between numerical fundamental frequency vs. axial load curves for specimens B1-3 in the double-hinged constraint condition.

In conclusion, the implemented numerical models are able to describe the most important features characterizing the frequency vs. load evolution in slender elements subjected to imposed displacements, showing a good agreement with the experiments. An improvement of the closeness of the numerical values to the experimental ones could be obtained by refining the models. A larger number of elements, as well as a better fitting of the numerical values attributed to mass and stiffness of each component should induce a better reproduction of the experiments. Finally, models like those implemented in the present study may be useful to predict, by simulating laboratory tests, the behaviour of structural elements to obtain indications in designing new structures and components or to offer a valid interpretation to experimental measurements carried out on existing structures subjected to imposed displacements or constraint settlements.

4.5 Concluding Remarks

In the present chapter, the evolution of the fundamental flexural frequency vs. the axial load in the case of imposed displacements has been analyzed for different beams and different constraint conditions. We observed that the presence of an initial curvature favours the transition from a softening behaviour to a hardening behaviour. In both the considered constraint conditions, the initial imperfections produce the effect of reducing the negative slope of the fundamental frequency vs. axial load curve, at the same time anticipating the stiffening behaviour of the final branch. The proposed study could find application in designing new structures as well as in monitoring existing ones. The possibility to foresee the beginning of the second phase could be used in analogous measurements performed on in-service structures and components. In addition, the different behaviour encountered for the rectified beam compared to those of beams presenting geometrical deviations can be reproduced by numerical simulations. This approach could be used to interpret the evolution of more complicated structural systems subjected to imposed displacements or affected by the subsidence of the external constraints.

Chapter 5

Space Truss Models Under Dead Loads

In this chapter we shall apply the modal analysis with second-order effects to simple space truss models subjected to dead loads. In particular, we will investigate the effects of direction and magnitude of the acting force on the natural vibration frequencies through finite element modelling. Some experimental results will be presented in the final part of the chapter.

5.1 Introduction

Trusses represent a class of structures whose elements are mainly subjected to normal forces, providing they are loaded strictly in correspondence of the nodes[1]. On the other hand, vibration modes that only involve axial deformations require a much higher energy to be activated than modes that involve flexural deformations of the members. As a consequence, the internal normal forces influence the natural vibration frequencies of slender trusses, since they affect the flexural stiffness of the members. In other words, the natural frequencies of the unloaded structure differ from those of the loaded one if we take into account the geometric nonlinearities.

By taking into account the geometric nonlinearities in the equations of motion

---

[1] In the ideal case of perfectly hinged connections, only the normal forces are other than zero.

through the geometric stiffness matrix, we arrive to a generalized eigenproblem like those in Chapter 3, in which the natural frequencies of the structure depend upon the applied loads. Curves describing the dependence of the natural frequencies on the applied loads may be obtained, considering the load multiplier as a free parameter and determining at each step the corresponding eigenvalue of the problem, i.e., the frequency of natural vibration. In this way, all the cases intermediate between those of pure free vibrations and pure buckling may be investigated.

In general, trusses have elements under tension and elements under compression. Compressive forces in members will act to reduce the stiffness of the system, while tensile forces will act to increase it. Therefore, when assembling the geometric stiffness matrices of each element to obtain the one of the whole structure, contributions of different weight and opposite sign are summed up. It results that the global geometric stiffness matrix may represent a positive as well as a negative contribution to the elastic stiffness matrix; so the natural frequencies may increase or decrease, depending on the relative influence of compressive and tensile internal forces in the members composing the structure. In addition, as will be shown later on, in some cases the frequencies always follow the same trend (e.g., decrease) as the external load increases; in other cases a reversal in the frequency evolutions is possible.

In this chapter we will analyze the behaviour of elementary systems in which, due to the particular load condition, some elements will be in tension, while others will be in compression. Then, changing the direction of the acting load, the analogous but opposite situation is obtained. This will lead to reveal an interesting aspect in the dynamic behaviour. The simplicity of the analyzed examples is intentional in order to emphasize the conceptual aspects, in the belief that this is better achieved considering elementary models.

5.2 Natural Vibrations of a Space Truss with Three Elements

5.2.1 Fundamental Case

Let us consider a tripod-shaped structure, made of three steel bars (S235) having a hollow circular cross-section with external diameter equal to 51 mm and thickness equal to 5 mm (Figure 5.1). These three bars are rigidly connected to each other in correspondence of the vertex (top node), while they are connected to the ground by spherical hinges (see Figure 5.1). The geometry is indicated in the same figure, while Table 5.1 reports the main material and section properties.

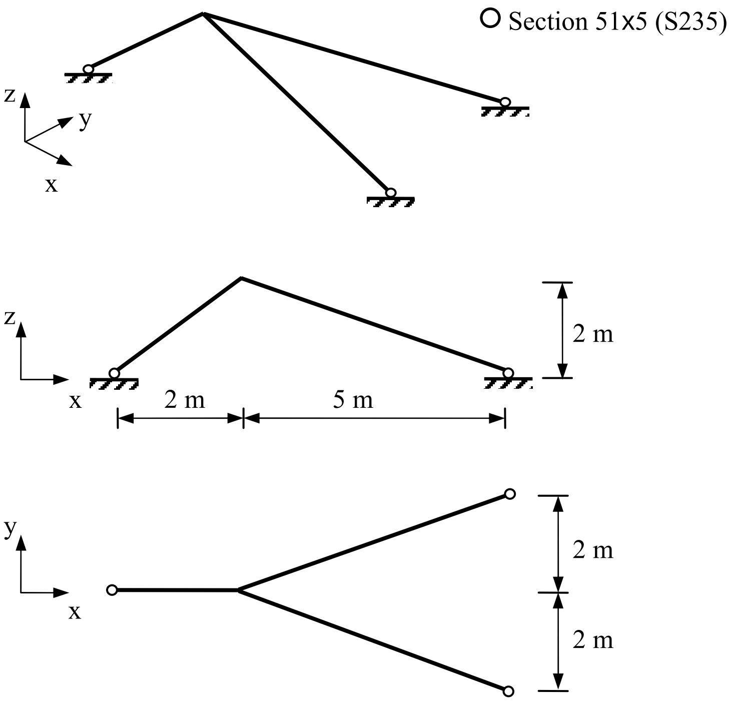

Figure 5.1 – Tripod-shaped structure made of three steel bars having a circular hollow cross-section. The bars are rigidly connected to each other at the top node and are connected to the ground by spherical hinges.

Table 5.1 – Main material and section properties for the structure in Figure 5.1.

Material properties (steel S235)	**Section properties (circular hollow section)**
Young modulus E (N/mm^2): 210000	External diameter d_e (mm): 51
Specific mass ρ (kg/m^3): 7850	Wall thickness t_w (mm): 5
Ultimate tensile strength f_{tk} (N/mm^2): 360	Area A (mm^2): 721.65
Tensile yield strength f_{yk} (N/mm^2): 235	Second moment of area I (mm^4): 192886.5

In order to analyze the free dynamic response under the action of a dead load, let the structure be loaded by a force applied at the top node, that always maintains the same line of action (Figure 5.2). If the acting force were vertical (parallel to the

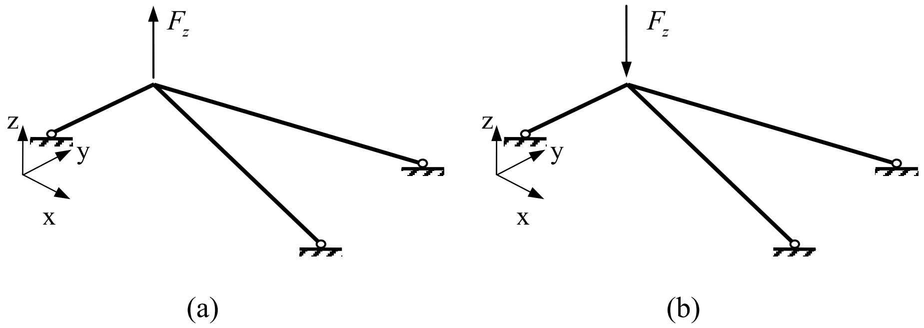

Figure 5.2 – Space truss model in Figure 5.1 loaded by a vertical force directed (a) upwards and (b) downwards.

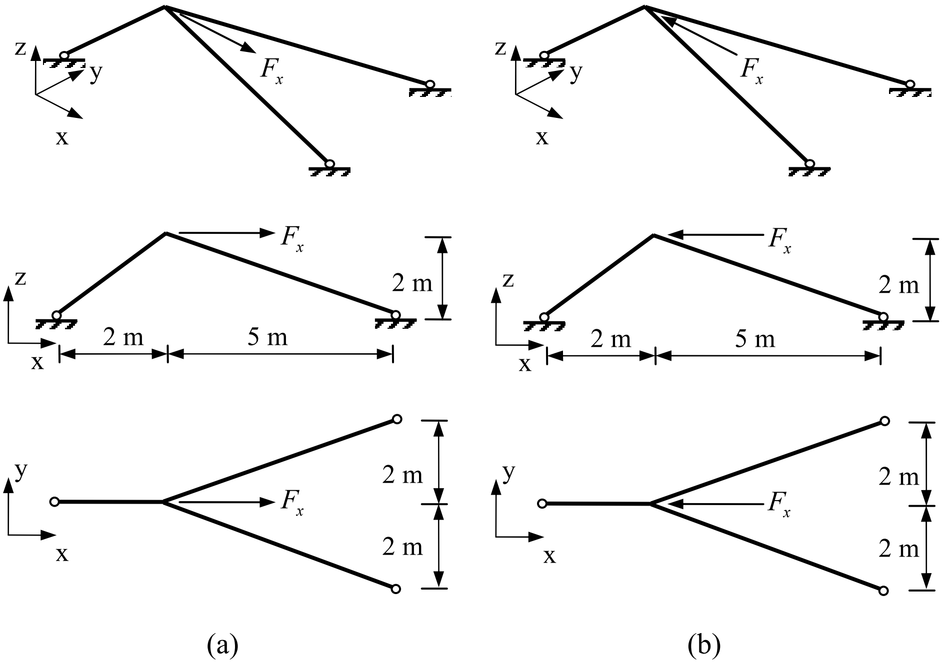

Figure 5.3 – Space truss model in Figure 5.1 loaded by a horizontal force directed (a) along the positive x-axis and (b) along the negative x-axis (fundamental case).

z-axis) the normal forces in all the elements would have the same sign. For instance, if the force were vertical and directed upwards, all the elements would be under tension (Figure 5.2(a)). As a consequence, the natural frequencies of the structure would increase with respect to those of the unloaded one. On the contrary, if the acting force were vertical but directed downwards, all the elements would be compressed, with a consequent decreasing in the natural frequencies (Figure 5.2(b)). In both the previous cases, the qualitative evolution of the frequencies with the load is rather obvious. A more interesting case is obtained when the nodal force acts in horizontal direction (in the plane parallel to the xy-plane).

Let us consider the case in which a force acting along the x-axis is applied at the top node (Figure 5.3). If the force acts in the same direction of the positive x-axis, the longer elements will be in compression, while the shorter one will be under tension (Figure 5.3(a)). On the contrary, if the force acts in the direction opposite to the x-axis, the shorter element will be compressed, while the longer ones will be in tension (Figure 5.3(b)). In the latter cases, the effects of the force on the natural frequencies of vibration are no longer obvious and will be analyzed in more details in the following sections.

5.2.2 Numerical Model

A numerical model of the structure reported in Figure 5.1 was implemented using the finite element software AxisVM©. This software allows to perform the modal analysis with second-order effects, in addition to the classical one. In the former case, the software takes into account the effects of the axial load on the flexural stiffness of the element through the geometric stiffness matrix. The structure is modelled using Euler-Bernoulli beam elements and the mesh is built adopting eight subdivisions per element.

Figure 5.4 shows the finite element model of the structure reported in Figure 5.1, under the load conditions shown in Figure 5.3. In the same figure, the deformed configurations are superposed to the undeformed ones. For example, under the action of a force $F_x = 15\,\text{kN}$ directed along the positive x-axis, the displacements of the top node are $u_x = 0.237\,\text{mm}$ and $u_z = -0.093\,\text{mm}$ (see Figure 5.4(a)). On the contrary, under the action of a force $F_x = 15\,\text{kN}$ directed along the negative x-axis, the displacements of the top node have, of course, the same magnitude but opposite signs (see Figure 5.4(b)).

For the case in Figure 5.4(a), the buckling load is $F_{xc} = 29.5\,\text{kN},$ while for the

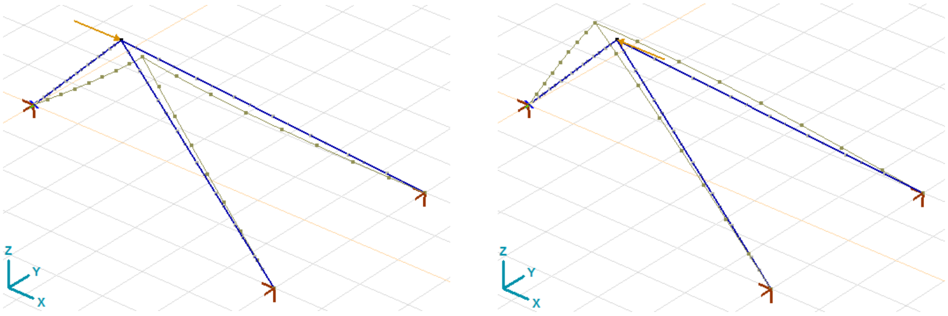

(a) (b)

Figure 5.4 – Finite element model of the structure reported in Figure 5.3. (a) Case in Figure 5.3(a) and (b) case in Figure 5.3(b).

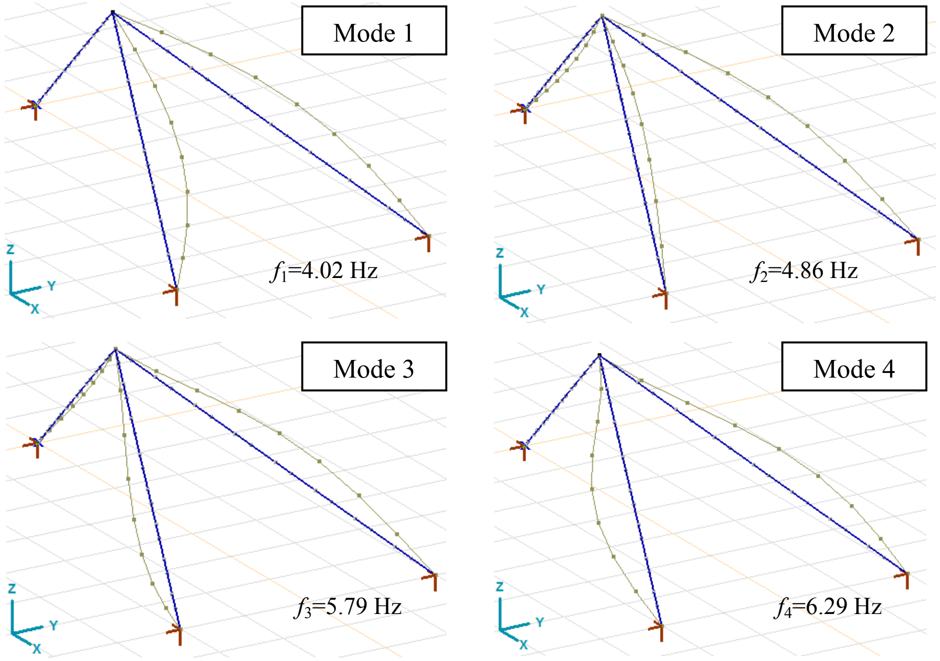

Figure 5.5 – First four modal shapes and corresponding frequencies for the structure in Figure 5.1 obtained through a classical modal analysis.

case in Figure 5.4(b) the buckling load is much larger, and corresponds to $F_{xc} = 147.7\,\text{kN}$. The associated critical pressures are $\sigma_c = 17\,\text{MPa}$ and $\sigma_c = 84.7\,\text{MPa}$, respectively, therefore buckling occurs in both cases within the elastic range.

5.2.3 Numerical Results

Figure 5.5 shows the first four modal shapes for the structure in Figure 5.1 obtained through a classical modal analysis (i.e., neglecting the effects of the applied loads). The corresponding natural frequencies are also reported in the same figure. Notice that the first mode does not activate any flexural oscillation of the shorter element.

When the same structure is loaded by a force acting along the x-axis as shown in Figure 5.3, modal shapes and natural frequencies may be calculated by means of a modal analysis with-second order effects. The first four modal shapes and corresponding frequencies for the case in Figure 5.3(a) with $F_x = 15\,\text{kN}$, obtained by the second-order modal analysis, are reported in Figure 5.6. In order to make a comparison, the frequencies obtained by the classical modal analysis (subscript (I)) are reported below the analogous values obtained by the second-order modal analysis (subscript (II)). It can be rapidly seen that all the first four frequencies decrease with respect to those corresponding to the unloaded case. For example, the first frequency drops from 4.02 Hz for the unloaded case to 2.82 Hz, the second one drops from 4.86 to 3.97, and so on. Despite this fact, the effect of the load on the mode shapes is almost negligible, at least for the first four modes and for the considered load.

Figure 5.7 reports the first four modal shapes and corresponding frequencies for the case in Figure 5.3(b) with $F_x = 15\,\text{kN}$, obtained by the second-order modal analysis. Also in this case, to make a comparison, the first four frequencies obtained by the classical modal analysis are reported in addition to those obtained by the second-order analysis. In this case, the first four frequencies increase under the action of the force F_x with respect to the unloaded case. For example, the lowest natural frequency increases from 4.02 Hz for the unloaded case to 4.94, the second one increases from 4.86 to 5.60, and so on. Also in this case the influence of the load on the mode shapes is almost negligible. In general, despite the relatively strong effect of axial loads on the natural frequencies of slender beam systems, the effect on mode shapes is relatively minor. As we have seen in section 3.4.1, for example, for simply supported beams the mode shapes (sine waves) are

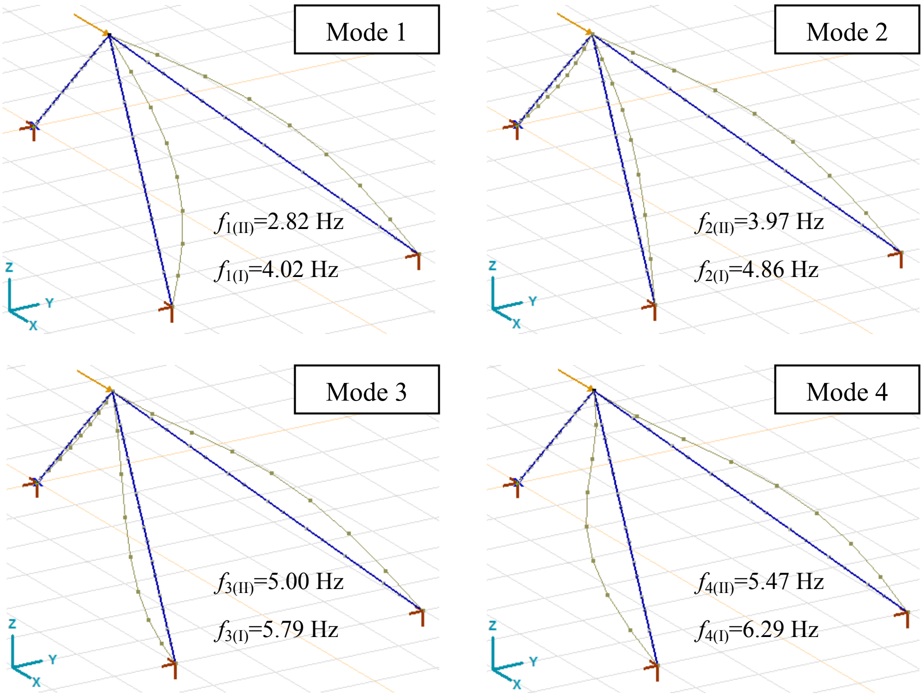

Figure 5.6 – First four modal shapes and corresponding frequencies for the structure in Figure 5.3(a) with F_x = 15 kN, obtained through a modal analysis with second-order effects (subscript (II)). The corresponding frequencies obtained through the classical modal analysis are also reported (subscript (I)).

not affected at all. Nevertheless, it must be pointed out that this is not necessarily always the case, as for example, for plated structures (see Virgin, 2007). We shall see later that also for the structure considered in this section, relatively considerable effects of the load on mode shapes are possible. Table 5.2 collects the first four natural frequencies for the structure in Figure 5.3 obtained by the classical modal analysis (first-order) and by the second-order modal analysis with $F_x = 15\,\text{kN}$ (i.e., along the positive x-axis) and $F_x = -15\,\text{kN}$ (i.e., along the negative x-axis).

At this point, it is of some interest to analyze the evolution of the natural frequencies with the load in the two cases reported in Figure 5.3, for values of the

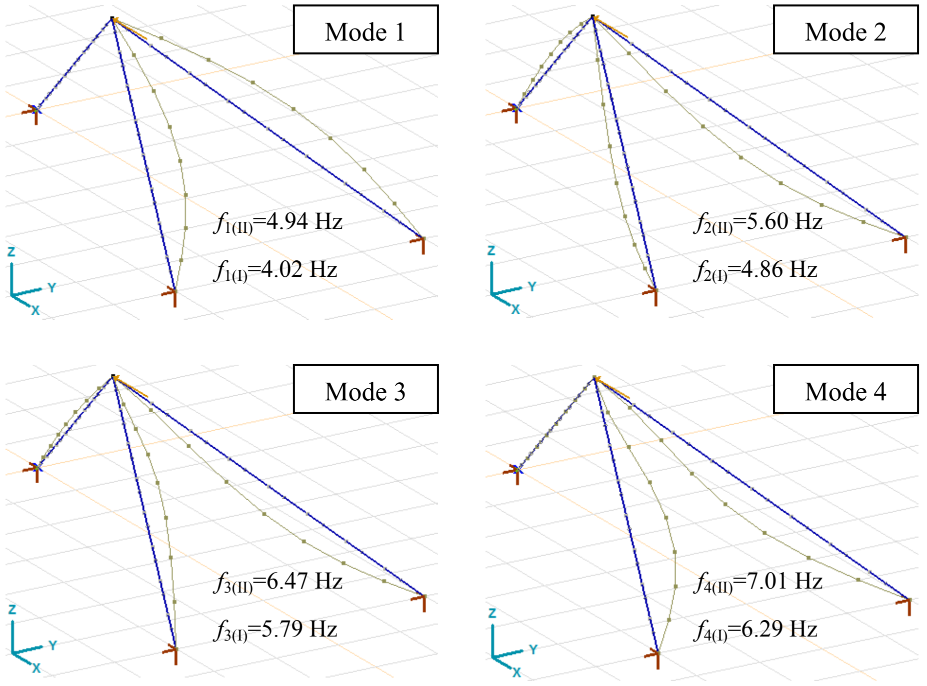

Figure 5.7 – First four modal shapes and corresponding frequencies for the structure in Figure 5.3(b) with F_x = 15 kN, obtained through a modal analysis with second-order effects (subscript (II)). The corresponding frequencies obtained through the classical modal analysis are also reported (subscript (I)).

Table 5.2 – First four natural frequencies for the structure in Figure 5.3 with F_x= ±15 kN, obtained through first- and second-order modal analyses.

Modal Analysis	**Mode 1**	**Mode 2**	**Mode 3**	**Mode 4**
I-order (classical)	4.02 Hz	4.86 Hz	5.79 Hz	6.29 Hz
II-order with F_x=15 kN	2.82 Hz	3.97 Hz	5.00 Hz	5.47 Hz
II-order with F_x=−15 kN	4.94 Hz	5.60 Hz	6.47 Hz	7.01 Hz

forces F_x between zero and the relative buckling loads. For the structure in Figure 5.3(a), performing a modal analysis with second-order effects for different values of the force F_x between zero and the buckling load F_{xc} leads to obtain the curves

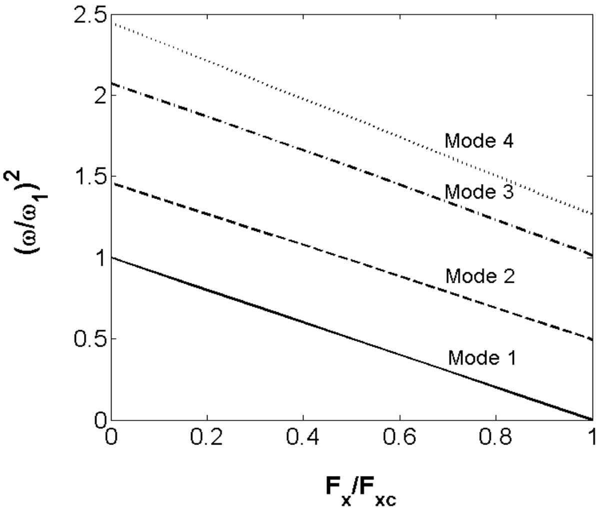

Figure 5.8 – First four nondimensional circular frequencies squared vs. nondimensional force for the structure in Figure 5.3(a).

in Figure 5.8. This figure shows the square of the nondimensional circular frequencies vs. nondimensional force, for the first four modes. The circular frequencies are nondimensionalized with respect to the fundamental circular frequency of the unloaded structure $\omega_1 = 25.28\,\text{rad/sec}$,[2] while the force is nondimensionalized with respect to the critical force $F_{xc} = 29.5\,\text{kN}$. As is easily seen, in this case, the first four frequencies are all decreasing functions of the applied load. The load for which the fundamental frequency vanishes, corresponds to the buckling load.

Similarly, in case of the structure in Figure 5.3(b), a second-order modal analysis performed for different values of the force F_x between zero and the buckling load F_{xc} leads to the curves shown in Figure 5.9. Also in this case, the first four nondimensional circular frequencies vs. nondimensional force curves are

---

[2] $\omega_1 = 2\pi f_1$ with $f_1 = 4.02$ Hz.

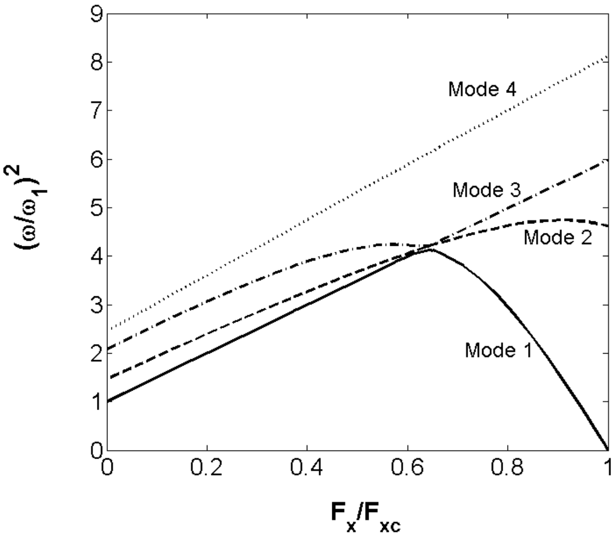

Figure 5.9 – First four nondimensional circular frequencies squared vs. nondimensional force for the structure in Figure 5.3(b).

reported. The circular frequencies are nondimensionalized again with respect to the fundamental circular frequency $\omega_1 = 25.28\,\text{rad/sec}$,[3] while the force is nondimensionalized with respect to the critical value $F_{xc} = 147.7\,\text{kN}$. In this case, unlike the previous one, the natural frequencies are no longer monotonic functions of the applied force. In particular, as it can be easily seen, the fundamental frequency increases at first with the load, but after a certain point the trend is reversed and it decreases down to zero in correspondence of the buckling load. In this particular case, the load that produces the inversion in the fundamental frequency evolution is about the 65 percent of the buckling load. Thus, an initial stiffening behaviour, during which the fundamental frequency increases, is then followed by a softening branch, which brings the first frequency down to zero. Moreover, again in Figure 5.9 it can be seen that in correspondence of the turning point of the curve related to the first frequency, the third natural frequency

---

[3] The fundamental frequency of the unloaded structure is, obviously, the same as before.

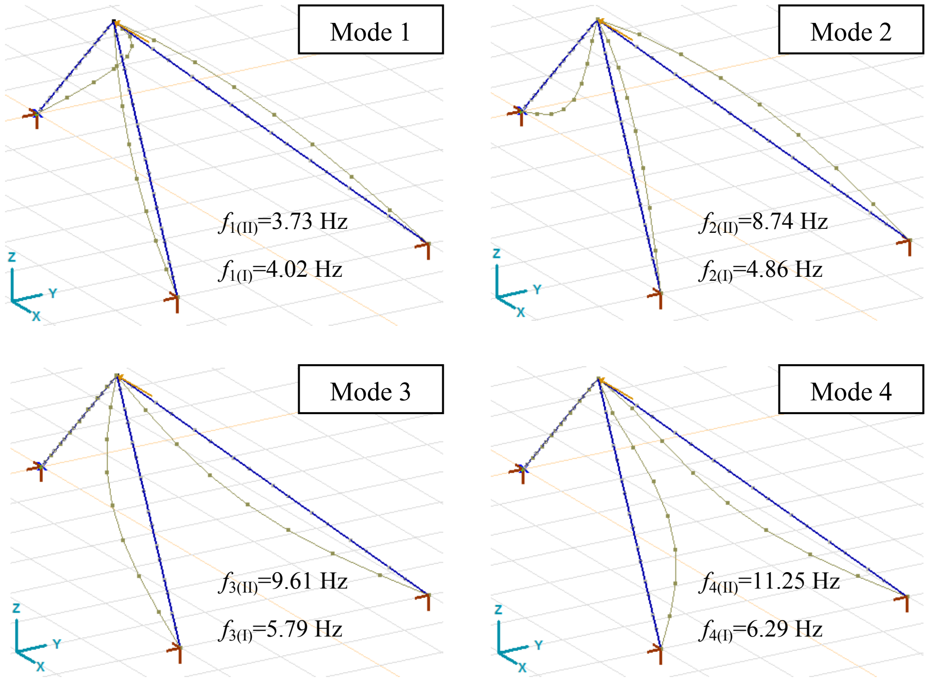

Figure 5.10 – First four modal shapes and corresponding frequencies for the structure in Figure 5.3(b) with F_x = 140 kN, obtained through a modal analysis with second-order effects (subscript (II)). The corresponding frequencies obtained through the classical modal analysis are also reported (subscript (I)).

shows an abrupt change in the trend. This could be better understood looking at the modal shapes of the structure in both the stiffening and softening phases.

Figure 5.10 reports the first four modal shapes and the corresponding frequencies for the structure in Figure 5.3(b) with $F_x = 140\,\text{kN}$. As usual, to make a comparison with the unloaded case, the frequencies obtained by the classical modal analysis are reported below the analogous values obtained by the second-order modal analysis. It must be pointed out that the first modal shape is characterized by a flexural oscillation of the shorter element, oscillation which has disappeared in the third modal shape (compare Figure 5.10 with Figure 5.7). This apparent exchange of modal shapes seems to have a sort of confirmation in the plots shown in Figure 5.9. Furthermore, larger effects of the force on the modal

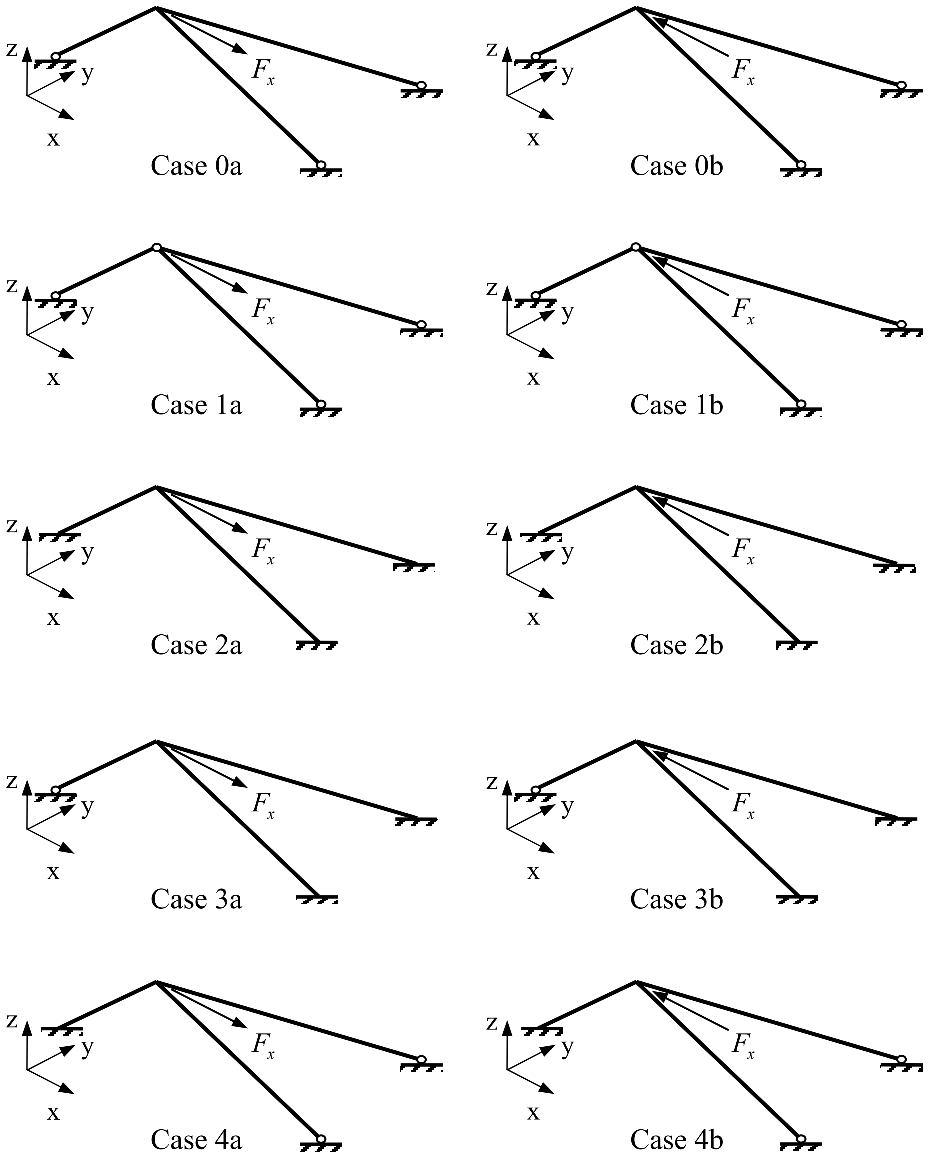

Case 0a
Case 0b
Case 1a
Case 1b
Case 2a
Case 2b
Case 3a
Case 3b
Case 4a
Case 4b

Figure 5.11 – Tripod shaped structure with different constraint conditions loaded by a horizontal force directed along the positive or the negative x-axis.

shapes are also observed for modes two and four. Thus, for sufficiently large values of the force, also the modal shapes, in addition to the frequencies, are considerably affected by the acting force.

Actually, all the frequencies, sooner or later, must decrease down to zero: the loads corresponding to the vanishing of higher frequencies are nothing but the higher buckling loads. The reversal in the trend of the second frequency is visible in Figure 5.9. Of course, only the first buckling load is of practical interest, unless additional restraints are provided to the structure. On the contrary, more frequencies are usually needed in dynamic analyses, but their variations must be evaluated for loads lower than the critical one.

5.2.4 Comparison with Different Constraint Conditions

The results presented in the previous section will be compared with those obtained for the same structure when the constraint condition are changed. Figure 5.11 collects all the configurations examined. The dimensions, as well as the material and section properties, are the same indicated in Section 5.2.1. Four constraint configurations will be compared with the fundamental case already studied (see Figure 5.3), considering the same two opposite loading conditions: a force directed along the positive (Cases a in Figure 5.11) and the negative (Cases b in Figure 5.11) x-axis. Cases 0a and 0b in Figure 5.11 recall the fundamental cases in Figure 5.3(a) and (b), respectively. Cases 1a and 1b in Figure 5.11 represent the case in which all the elements are connected to each other and to the ground by spherical hinges. In Cases 2a and 2b, all the elements are rigidly fixed at each end. In Cases 3a and 3b, the elements are rigidly connected to each other at the top node, while the shorter element is hinged to the ground and the longer ones are externally clamped. Finally, in Cases 4a and 4b, the elements are rigidly connected to each other, but, while the shorted element is fixed to the ground, the longer ones are now connected to it by hinges.

A view of the finite element models of the structures in Figure 5.11 is reported in Figure 5.12. The models were built adopting the same criteria used for the fundamental case, as described in Section 5.2.2. Opportune differences in the deformed configurations may be observed in Figure 5.11, according to the different constraint conditions. Figure 5.13 shows the modal shapes and the corresponding natural frequencies of the structures in Figure 5.11, in the unloaded configuration (classical modal analysis). Also in this case, differences in the modal shapes may be observed, according to the different constraint conditions.

In order to make a first comparison among the different cases in Figure 5.11,

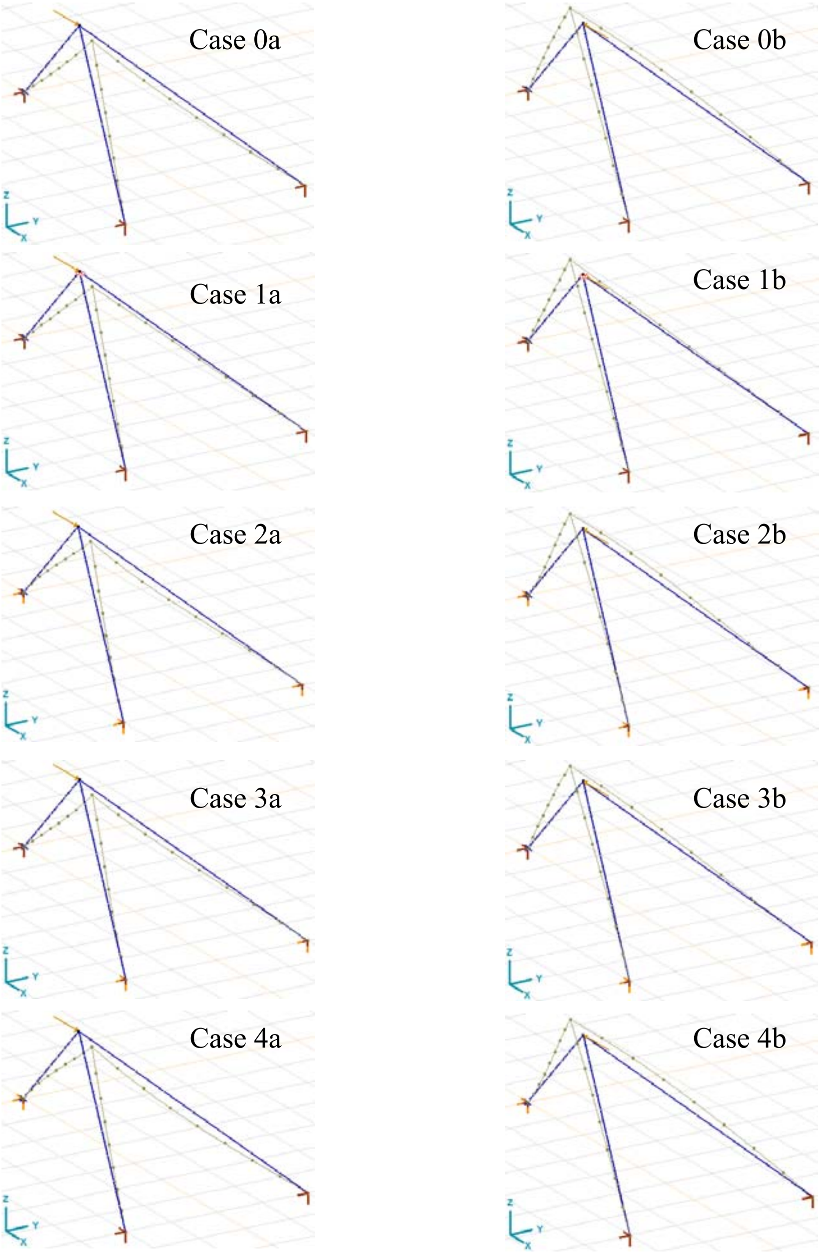

Figure 5.12 – Finite element models of the structures reported in Figure 5.11.

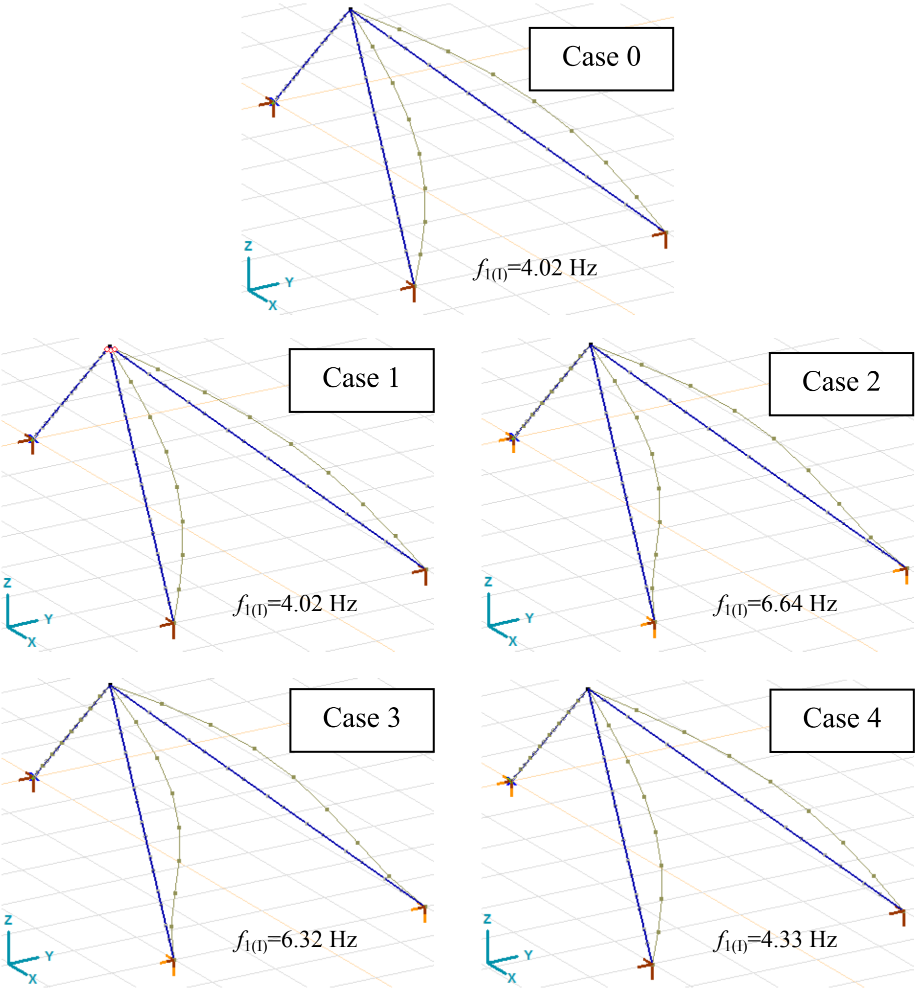

Figure 5.13 – Fundamental frequencies and corresponding modal shapes, in the unloaded configuration, for the constraint conditions reported in Figure 5.11.

in Table 5.3 the fundamental frequencies in the unloaded case and the critical loads are reported. As could have been expected, the stiffest case is Case 2, while the most flexible is Case 1, followed by Case 0; the others represent intermediate situations. As is easy to see, the influence of the change in the constraint conditions is smaller on the fundamental frequencies than on the critical loads. The fundamental frequencies of the unloaded structure are equal in Cases 0 and 1, as well as the critical loads in Case 0a and Case 1a, while they are different in Cases 0b and 1b. It must be noted that the buckling loads in Cases 2b and 4b correspond to stresses outside the elastic range, and therefore they do not represent the actual critical loads.

Table 5.3 – Comparison among the different constraint conditions indicated in Figure 5.11.

	Case 0	**Case 1**	**Case 2**	**Case 3**	**Case 4**
Fundamental frequency - unloaded case (Hz)	4.02	4.02	6.64	6.32	4.33
Critical load - case a (kN)	29.5	29.5	68.4	61.3	34.2
Critical load - case b (kN)	147.7	123.7	326.0*	160.8	306.5*

* Value outside the elastic range.

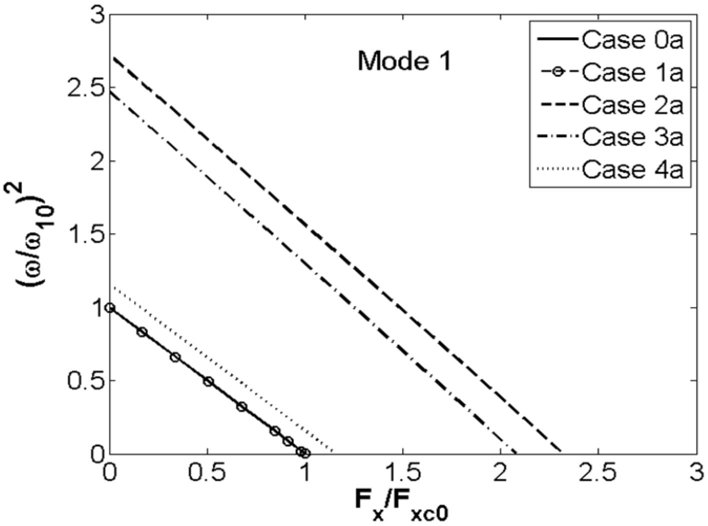

Figure 5.14 – Nondimensional fundamental frequency squared vs. nondimensional force for the structures in Figure 5.11 (Cases a).

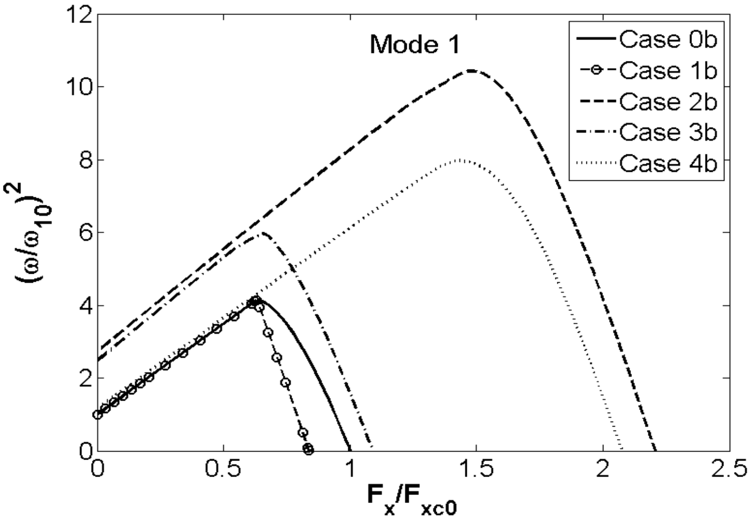

Figure 5.15 – Nondimensional fundamental frequency squared vs. nondimensional force for the structures in Figure 5.11 (Cases b).

The evolution of the natural frequencies with the load may be plotted into graphs analogous to those presented in Section 5.2.3. Our comparison will be restricted to the evolution of the fundamental frequencies, thus only the first modes will be considered. Figure 5.14 shows the nondimensional fundamental circular frequency vs. the nondimensional force for Cases a in Figure 5.11. The circular frequencies are nondimensionalized with respect to the fundamental frequency of Case 0a, $\omega_{10} = 25.28\,\text{rad/sec}$, obtained for the unloaded structure, while the forces are nondimensionalized with respect to the critical force of the same case, $F_{xc0} = 29.5\,\text{kN}$. As could be seen in Figure 5.14, in this case, the effect of the change in the constraint conditions is just a sort of translation (the curves are almost parallel) of the previous case (Case 0a), being the qualitative behaviour perfectly preserved. In fact, all the natural frequencies are still decreasing functions of the applied load, and the dependence is described by straight lines, although differences due to the various stiffnesses may be appreciated. In this case in particular, there are no differences between Case 0a and Case 1a, being that the two curves are exactly superposed (see Figure 5.14). This is a consequence of the fact that these cases have the same fundamental frequencies and the same critical loads, as pointed out before. In addition, they represent the most flexible configurations, as clearly appears in Figure 5.14. However, still in this case, in general, the higher the fundamental frequency the higher the critical load.

The evolutions of the fundamental frequencies with the load for Cases b in Figure 5.11, are reported in nondimensional form in Figure 5.15. In this case, Case 0b is chosen as the reference case: the fundamental circular frequencies are nondimensionalized with respect to the fundamental frequency corresponding to Case 0b in the unloaded condition, $\omega_{10} = 25.28\,\text{rad/sec}$, while the forces are nondimensionalized with respect to the critical force of the same case, $F_{xc0} = 147.7\,\text{kN}$. Also in this case, the qualitative behaviour of the fundamental frequency shown by the system already analyzed (Case 0) is confirmed (see Figure 5.15). In particular, all the fundamental frequencies show a stiffening phase followed by a softening branch, according to the behaviour described in Section 5.2.3.

Now, compared to Cases a, the evolution curves of Cases 0b and 1b are superposed only in the stiffening branch, while in the softening phase they follow different paths. In fact, as we pointed out before, Cases 0b and 1b have different critical loads, although the fundamental frequencies are the same. In particular, the critical load corresponding to Case 1b is lower than the one corresponding to Case 0b. Furthermore, with respect to the previous case, now the fact that the higher the fundamental frequency the higher the critical load is not always true. In fact, in addition to Cases 0b and 1b, which have the same fundamental frequency but different critical loads, the fundamental frequency in Case 3b is higher than in Case 4b, while the critical load is lower. This inversion, not present in Case a (see Figure 5.14), is due to a combined effect of load direction and constraint conditions. Nevertheless, for the stiffest case, Case 2b, we have, at the same time, the highest fundamental frequency and the highest critical load. As we will see in the next section, this is not necessarily always the case.

5.2.5 Comparison with Different Geometric Configurations

In this section, we shall compare the results discussed in Section 5.2.3 with those analogous corresponding to different geometric configurations. Four new cases, obtained by changing the geometry of the structure in Figure 5.3, will be compared with the fundamental case.

Figure 5.16 shows the structural schemes under consideration, where, once again, Case 0 recalls the fundamental case, chosen as the reference case. Case 5 is obtained doubling the internal angle α corresponding to Case 0, while Case 6 is obtained halving the same angle (see Figure 5.16). In Case 7, one of the longer

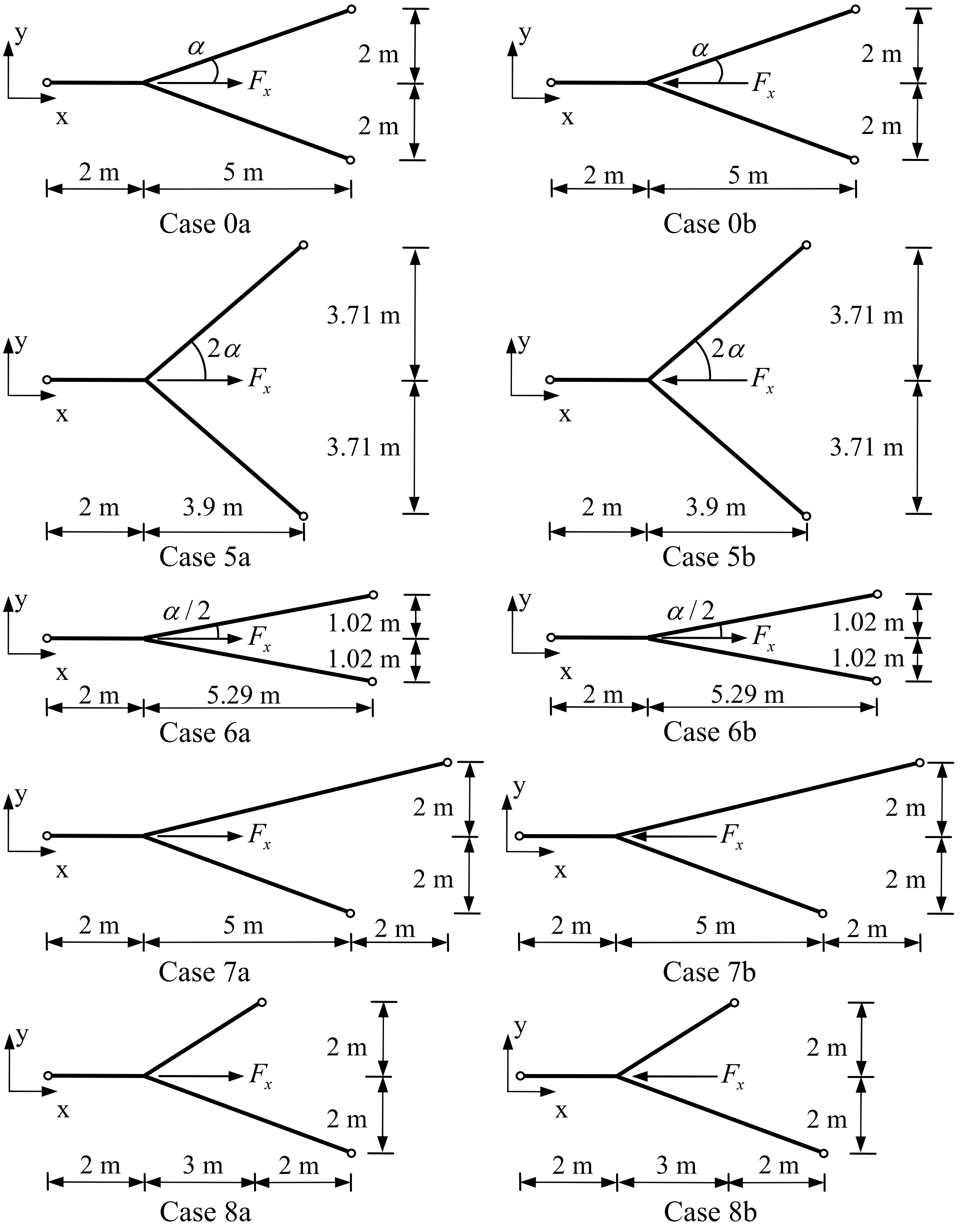

Case 0a

Case 0b

Case 5a

Case 5b

Case 6a

Case 6b

Case 7a

Case 7b

Case 8a

Case 8b

Figure 5.16 – Different geometric configurations for the structure in Figure 5.3.

elements is stretched, increasing the *x*-coordinate of one base node and maintaining unvaried its *y*-coordinate. Finally, in Case 8, one of the longer elements is shortened, reducing the *x*-coordinate of one base node and maintaining unvaried its *y*-coordinate. In Cases 7 and 8 we lose the geometric symmetry present in all the previous cases. In all the considered configurations, the *z*-coordinate of the top node is maintained equal to 2 m.

Two-node Euler-Bernoulli beam elements were adopted in the finite element modelization, and a mesh with eight subdivisions per element was created in all the analyzed cases. Figure 5.17 shows the finite element models of the structures reported in Figure 5.16. In addition to the original configuration, the static deformed configuration, obtained by a linear elastic analysis, is reported for all the considered cases.

Table 5.4 reports a comparison among the different geometric configurations illustrated in Figure 5.16, in terms of fundamental frequencies of the unloaded structure and critical loads. If we take into consideration the comparison proposed in Section 5.2.4, the situation appears more complicated. First, we may observe that Cases 0, 5, and 6 have almost the same fundamental frequency, due to the fact that the elements conserve the same length. At the same time, the influence of the change in the internal angle (see Figure 5.16) on the critical loads is larger. For Cases 7 and 8, the effects of the change of geometry are more important on both the fundamental frequency and the critical loads. Most important of all, we can see that in this case, it is no longer true that the highest frequency always corresponds to the highest buckling load (see Table 5.4). Moreover, the structure which has the highest critical load is not the same for Cases a and b, as was the case in the comparison made in Section 5.2.4. This discussion will be completed later on, when the dependence of the fundamental frequency upon the load will be discussed.

Table 5.4 – Comparison among the different geometric configurations indicated in Figure 5.16.

	Case 0	**Case 5**	**Case 6**	**Case 7**	**Case 8**
Fundamental frequency - unloaded case (Hz)	4.02	4.03	4.01	2.76	4.86
Critical load - case a (kN)	29.5	24.9	30.7	19.8	35.0
Critical load - case b (kN)	147.7	154.1	135.9	165.6	133.2

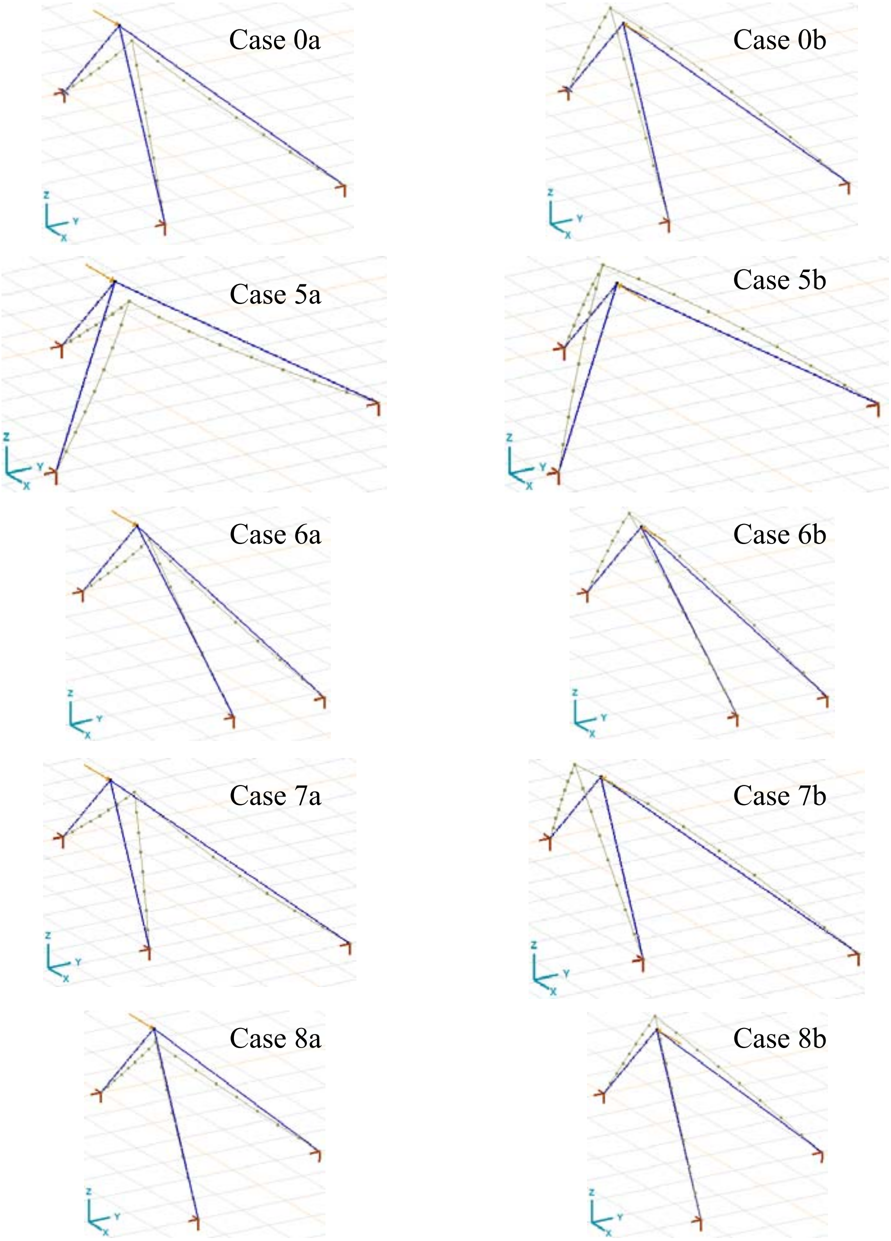

Case 0a

Case 0b

Case 5a

Case 5b

Case 6a

Case 6b

Case 7a

Case 7b

Case 8a

Case 8b

Figure 5.17 – Finite element models of the structures reported in Figure 5.16.

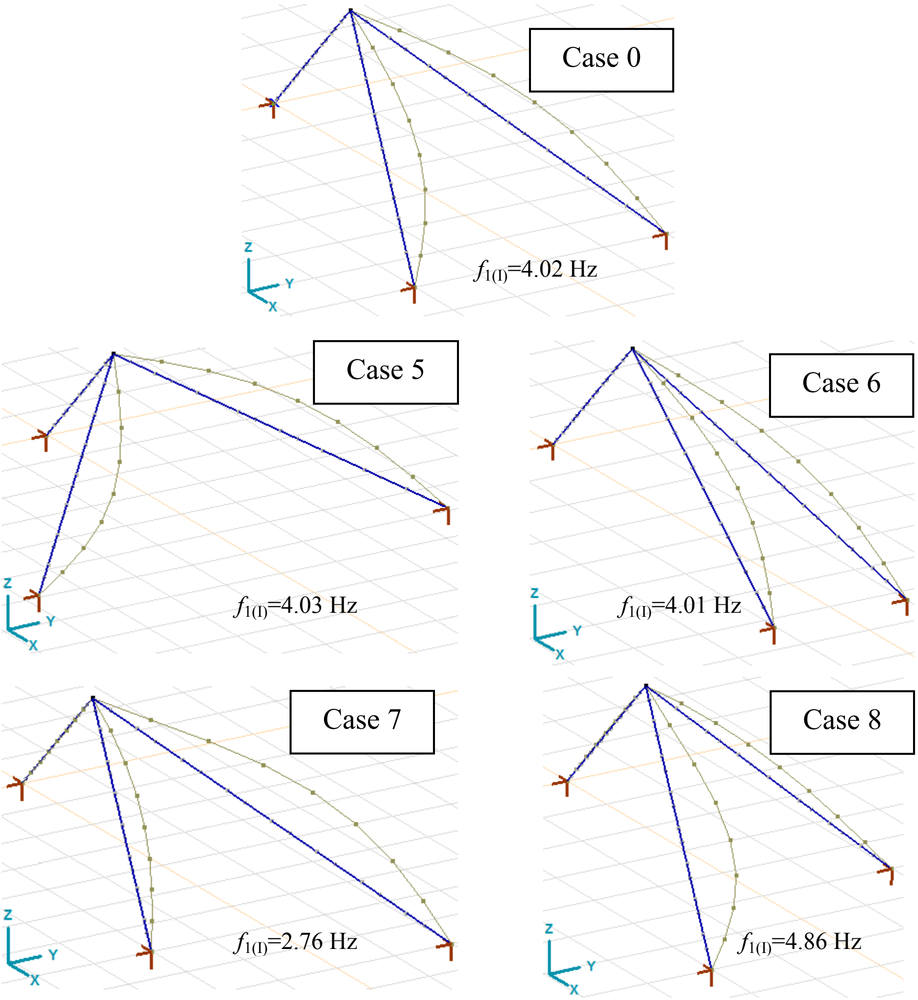

Figure 5.18 – Fundamental frequencies and corresponding modal shapes, in the unloaded configuration, for the geometric configurations reported in Figure 5.16.

Figure 5.18 shows the fundamental modal shapes, with the associated frequencies, which correspond to the different geometric configurations in Figure 5.16. These modal shapes and natural frequencies are related to the unloaded configuration. For each case under investigation, the evolution of the fundamental

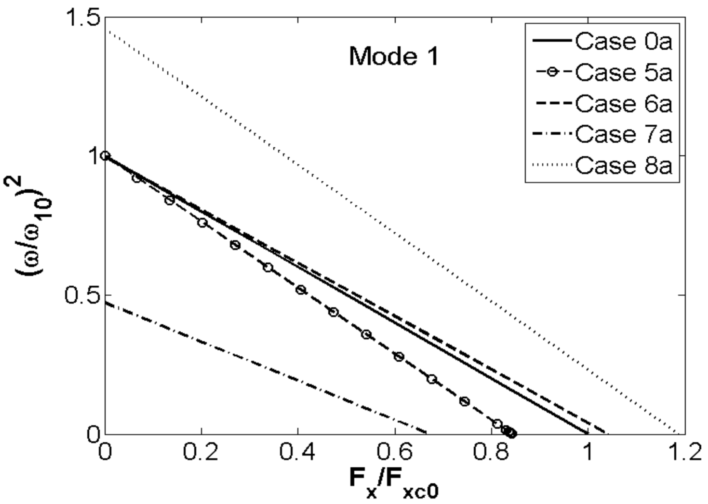

Figure 5.19 – Nondimensional fundamental frequency squared vs. nondimensional force for the structures in Figure 5.16 (Cases a).

frequency with the load, comprised between zero and the corresponding critical value, is studied through a modal analysis with second-order effects. The results are collected in Figures 5.19 and 5.20. Figure 5.19 shows the nondimensional fundamental frequency vs. nondimensional force curves, for Cases a in Figure 5.16. The frequencies are nondimensionalized with respect to the fundamental frequency of Case 0a, $\omega_{10} = 25.28\,\text{rad/sec}$, corresponding to the unloaded structure, while the forces are nondimensionalized with respect to the critical force of the same case, $F_{xc0} = 29.5\,\text{kN}$. As it can easily be seen, the fundamental frequencies are still all decreasing functions of the applied load; the evolutions are represented by straight lines, which have different slopes. Now, the stiffest structure is that of Case 8a, while the most flexible is that represented by Case 7a; the other cases represent intermediate situations. Notice that, in this case, Case 7a has at the same time the lowest fundamental frequency and the lowest critical load. On the contrary, Case 8a has the highest fundamental frequency and the highest critical load.

The evolution of the fundamental frequencies with the load for Cases b in Figure 5.16, are reported in Figure 5.20 in nondimensional form. The frequencies are nondimensionalized with respect to the fundamental frequency of Case 0b,

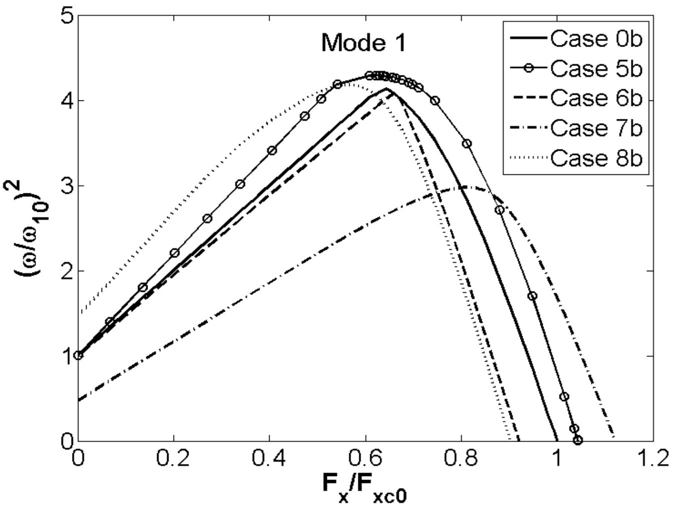

Figure 5.20 – Nondimensional fundamental frequency squared vs. nondimensional force for the structures in Figure 5.16 (Cases b).

$\omega_{10} = 25.28$ rad/sec, corresponding to the unloaded structure, while the forces are nondimensionalized with respect to the critical force of the same case, $F_{xc0} = 147.7$ kN. Also in this case, the qualitative behaviour shown by the reference case (Case 0b) is preserved in all cases, however some new aspects arise. First, it is interesting to note that, compared with the previous case summarized in Figure 5.19, the highest frequency is now associated to the lowest critical load, and vice versa. In fact, Case 8b is the case which has both the highest fundamental frequency and the lowest critical load at the same time. On the contrary, Case 7b is the one with the lowest fundamental frequency and the highest critical load. Furthermore, we notice that the sequences in which the critical loads are ordered in Cases a and b are exactly opposite, although the order of the frequencies is obviously the same (see Figures 5.19 and 5.20).

5.3 Experimental Tests

To complete the study presented in this chapter, experimental tests were conducted on a physical model realizing a structural scheme analogous to that reported in

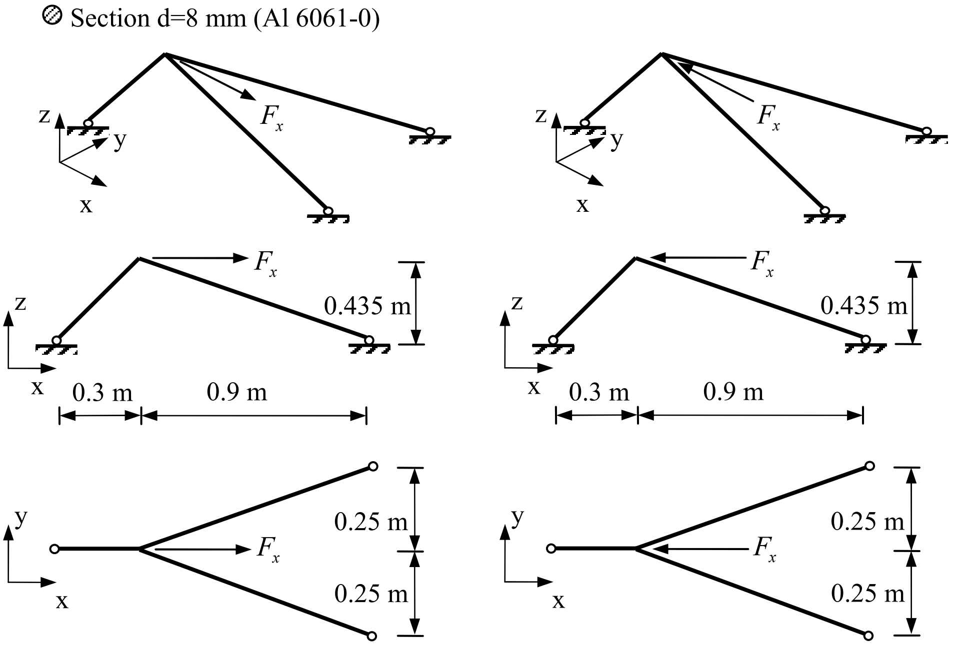

(a) (b)

Figure 5.21 – Structural configurations adopted for the experimental tests.

Table 5.5 – Main material and section properties for the structure in Figure 5.21.

Material properties (aluminium 6061-0)	**Section properties (full round section)**
Young modulus E (N/mm^2): 68900	Diameter d (mm): 8
Specific mass ρ (kg/m^3): 2700	Area A (mm^2): 50.27
Ultimate tensile strength f_{tk} (N/mm^2): 124	Second moment of area I (mm^4): 201.1
Tensile yield strength f_{yk} (N/mm^2): 55.2	

Figure 5.3. Figure 5.21 shows the structural configurations adopted for the experimental tests. The constraint conditions, as well as the loading conditions, are the same as in Figure 5.3, while the geometric dimensions and the material constituting the structure are different. In this case, in fact, the structure is made of aluminium (Al 6061-0), and the elements composing the truss present a full round

section with a diameter equal to 8 mm. The measurements defining the geometry of the structure are those reported in Figure 5.21, while the main material and section properties are collected in Table 5.5.

A numerical model of the structure reported in Figure 5.21 was built using the software AxisVM©. The structure is modelled using two-node Euler-Bernoulli beam elements, and the mesh is constructed dividing each element into ten parts. Also in this case, modal analyses with second-order effects were performed under different loading levels. The structural response is perfectly analogous to that described in Section 5.2.3, with differences regarding only the numerical values. For the case in Figure 5.21(a), the buckling load corresponds to $F_{xc} = 0.3\,\text{kN}$, while for the case in Figure 5.21(b) the buckling load is given by $F_{xc} = 1.21\,\text{kN}$. Since the associated critical pressures are $\sigma_c = 2.6\,\text{MPa}$ and $\sigma_c = 10.8\,\text{MPa}$, respectively, buckling occurs in both cases within the elastic range (see Table 5.5). The fundamental frequency of the unloaded structure in this case is equal to 14.93 Hz.

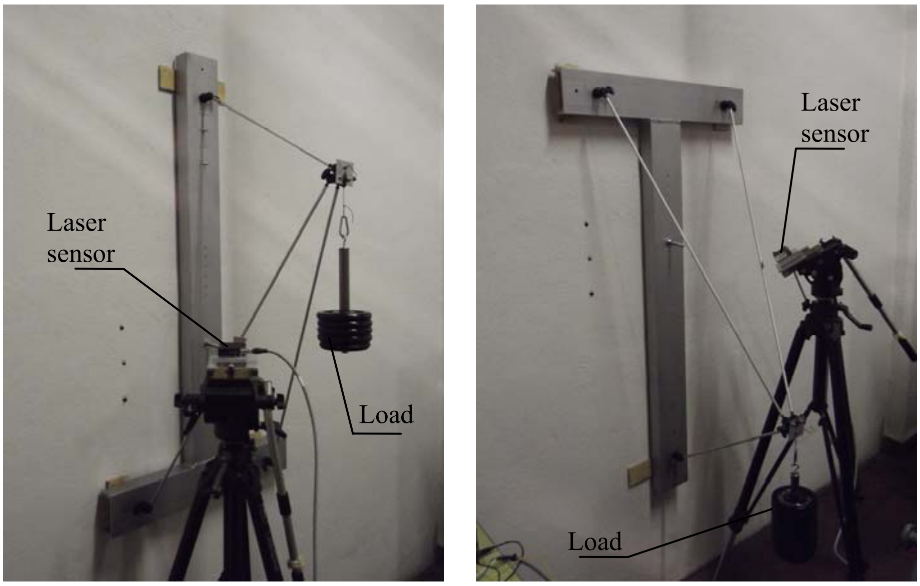

Case a Case b

Figure 5.22 – Experimental setup realizing the structural configurations in Figure 5.21.

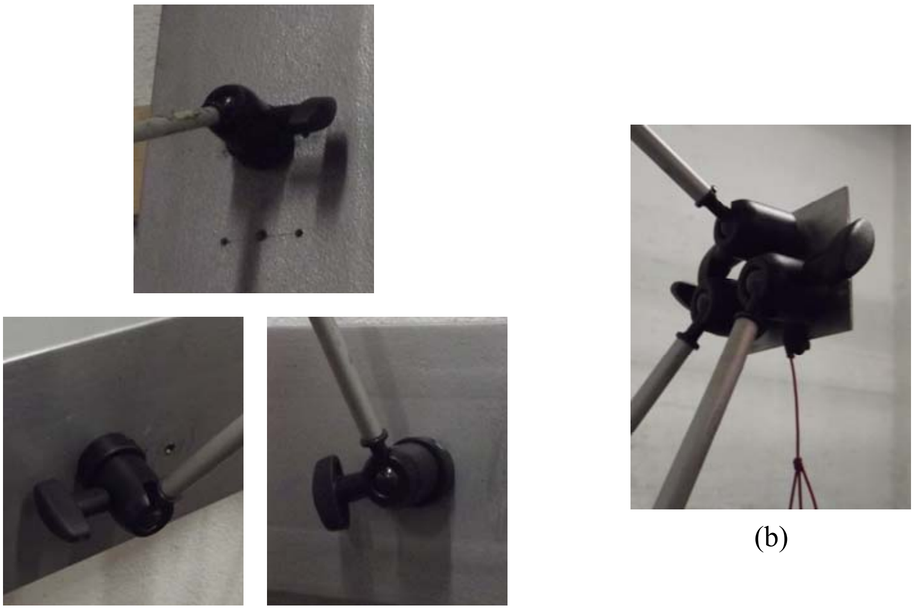

(a)

(b)

Figure 5.23 – Details of (a) external constraints (free spherical joints) and (b) internal constraints in correspondence of the vertex (fixed spherical joints) for the structure in Figure 5.22.

5.3.1 Experimental Setup

Figure 5.22 shows the experimental setup realizing the structural configurations indicated in Figure 5.21. The external force (dead load) was realized by means of suspended masses, varying in number according to the required load magnitude. In this way the force always keeps the same line of action, as required by the original hypothesis, the force being generated by gravitational loads. The same model was mounted in two opposite positions realizing the configurations in Figure 5.21. Case a in Figure 5.22 is related to the scheme in Figure 5.21(a), in which the two longer bars are compressed and the shorter one is under tensile, while Case b realizes the scheme in Figure 5.21(b), where the two longer bars are under tensile and the shorter one is in compression. A displacement transducer (laser sensor) was mounted near one of the longer bars, as shown in Figure 5.22, to measure the time history of the midpoint displacement. The laser sensor is the same used in the experimental campaign conducted on the slender bars, described in Chapter 3. The main features related to the laser sensor are described in Section 4.2.3.

Figure 5.23 shows the connections realizing the external and internal constraints in detail. The external constraints are constituted by spherical joints allowing the rotation, apart from a small friction due to contact (Figure 5.23(a)). These constraints want to simulate the base spherical hinges shown in Figure 5.21. The internal constraints are constituted by spherical joints, fixed, in this case, by the closing of the screws in order to prevent the end rotation for all the bars (Figure 5.23(b)). They want to simulate the internal node shown in Figure 5.21.

Under each loading level, the fundamental vibration frequency was evaluated analyzing the free response of the system, i.e. the time history of the displacement measured with the laser sensor. The fundamental frequencies were estimated applying the Logarithmic Decrement Method and the Fast Fourier Transform to the measured signal. The initial condition from which the free response was measured was realized inducing a deformed shape as close as possible to the first mode shape. The adopted data acquisition and analysis procedures were analogous to those described in Section 4.2.5.

5.3.2 Experimental Results

In this section we present the experimental results related to the evolution of the fundamental frequency under different loading values for the structural schemes shown in Figure 5.22. The experimental values will be compared with those obtained by the finite element analyses performed using AxisVM©. Given the simplicity of the way adopted to apply the loads, only the first part of the fundamental frequency vs. load curves were investigated during the laboratory tests. Nevertheless, the values obtained are sufficient to confirm the essential aspects concerning the phenomenon under investigation. In both Cases a and b in Figure 5.22, the fundamental frequencies were measured in correspondence of different values of the force ranging between 0 and about 0.2 kN.

Figure 5.24 shows the evolution of the fundamental frequency with the load for Case a in Figure 5.22, while Figure 5.25 shows the same evolution for Case b in Figure 5.22. As can be easily seen, the qualitative trends are perfectly confirmed, showing a decrease of the frequency in the first case and an increase in the second, as was expected. In both cases there is a good agreement between the measured frequencies and the corresponding values obtained by the numerical simulations. The small differences are due to the inevitable discrepancies between the

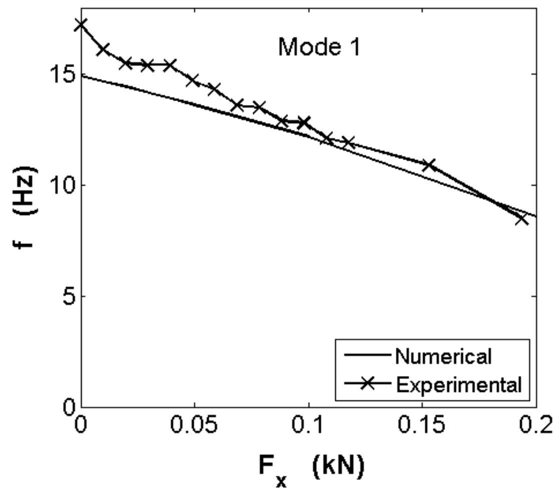

Figure 5.24 – Evolution of the fundamental frequency with the load for the structure in Figure 5.22 (Case a).

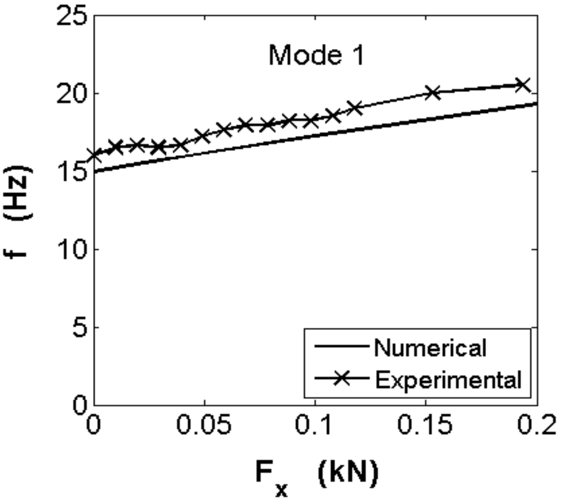

Figure 5.25 – Evolution of the fundamental frequency with the load for the structure in Figure 5.22 (Case b).

numerical models and the actual physical models realized in the laboratory.

5.4 Concluding Remarks

In this chapter, we analyzed the influence of dead loads on the natural vibration frequencies and mode shapes of slender space trusses made of three elements. Firstly, we showed how the evolution of the natural frequencies with the load is not necessarily monotonic, having a stiffening or a softening structural behaviour governed by the magnitude and direction of the applied load. In some cases and for sufficiently large loads, also the modal shapes, and not only the natural frequencies, are strongly affected by the applied loading. Afterwards, different constraint conditions and different geometric configurations were compared, therefore showing how the structure having the highest fundamental frequency does not necessarily have the highest buckling load at the same time.

The models analyzed in this chapter may be considered as basic structural schemes, as well as elementary moduli, of large space truss roofs, for which a design based on dynamics and stability is of primary importance. Nevertheless, it must be highlighted that we referred to non-shallow structural schemes. Hence, the loss of stability considered in this chapter is of the Euler's type, and therefore corresponds to the vanishing of the fundamental frequency. On the other hand, when analyzing shallow structural schemes, snap-through instability must be considered. In this case, the interplay between the frequencies evolution and the loss of stability needs to be reconsidered.

Chapter 6

Suspension Bridges Under Aerodynamic Loads

In this chapter we will investigate the effects of steady aerodynamic loads on stability and natural frequencies of suspension bridges through a simplified analytical model. We will present a generalized eigenvalue problem in which all configurations intermediate between those of pure lateral-torsional buckling, pure torsional divergence, and pure free vibrations can be analyzed. Finally, possible implications for the flutter analysis of suspension bridges will be discussed.

6.1 Preliminary Remarks

The inherent flexibility of suspension bridges makes their design particularly sensitive to the effects of the natural wind, which may induce instability and excessive vibrations. Instability is the onset of an infinite displacement granted by a linear solution technique. Actually, displacement is limited by different kind of nonlinearities. Design against instability requires that the maximum wind velocity at the bridge site is sufficiently lower than the critical wind velocity associated to the occurrence of a certain phenomenon. Vibration is a cyclic movement induced by dynamic effects and it may cause fatigue or serviceability problems. In this case, the design requires the analysis of the structural response in presence of the dynamic forcing, in order to check if it is satisfactory or not. Since both instability and vibration failures in reality occur at finite displacement, it is often hard to judge whether a structure failed due to instability or excessive vibration-induced damage to some key elements.

Instability caused by the interaction between moving air and an elastic structure is termed aeroelastic or aerodynamic instability. Aeroelastic instability of bridges include torsional divergence, galloping, and flutter. Typical wind-induced vibrations consist of vortex shedding and buffeting. These types of instability and vibration may occur alone or in combination. For example, a structure must experience vibration to some extent before flutter instability starts. A detailed consideration of these effects is beyond the scope of this chapter and reference must be made to the extensive specialist literature on this subject (e.g., Dyrbye and Hansen, 1997; Jurado et al., 2011; Larsen, 1992; Larsen and Esdahl, 1998; Simiu and Scanlan, 1996).

The interaction between the bridge vibration and wind is usually treated as consisting of two kinds of forces (Cai and Montens, 2000): motion-dependent and motion-independent. The former vanishes if the structures are rigidly fixed. The latter, being purely dependent on the wind characteristics and section geometry, exists whether or not the bridge is moving. The equation of motion in presence of the aerodynamic forces is then expressed in the following general form:

$$\left[M\right]\left\{\ddot{\delta}\right\}+\left[C\right]\left\{\dot{\delta}\right\}+\left[K\right]\left\{\delta\right\}=\left\{F\left(\delta\right)\right\}_{md}+\left\{F\right\}_{mi}, \tag{6.1}$$

where $\left[M\right]$ is the mass matrix, $\left[C\right]$ is the damping matrix, $\left[K\right]$ is the stiffness matrix, $\left\{\delta\right\}$ is the displacement vector, $\left\{F\left(\delta\right)\right\}_{md}$ is the motion-dependent aerodynamic force vector, and $\left\{F\right\}_{mi}$ is the motion-independent wind force vector.

While the motion-independent part together with the motion-dependent part causes deformation, aeroelastic instability is only due to the motion-dependent force. The difference between short-span and long-span bridges lies in the motion-dependent part. For the short-span bridges, the motion-dependent part is insignificant and there is no concern about aeroelastic instability. For flexible structures like long-span bridges, however, both instability and vibration need to be carefully investigated.

The prediction of the critical speed for a dynamic aeroelastic instability requires the knowledge of the natural frequencies and mode shapes of the structure, in addition to the aerodynamic properties of the suspended structure cross-section. Modal analysis is therefore used to determine natural frequencies and mode shapes for input to an aeroelastic stability analysis. Mode shapes and natural frequencies of the structure are generally determined by a linear eigenvalue analysis technique, using the structure equilibrium geometry and stiffness derived from the non-linear large deflection analysis of the structure under permanent loads.

In this chapter we will show that the natural frequencies of a suspended deck depend on the mean (quasi-static) wind loading. As a consequence, the input parameters to the aeroelastic stability analysis result affected by that dependence, suggesting the possibility of modifying the dynamic stability analysis in order to take into account the mentioned influence.

6.2 Elements of Statics of Suspension Bridges

The problem of the static equilibrium of suspension bridges against vertical loads is governed, in general, by two non-linear integro-differential equations, coupled together: one related to the flexure and the other related to the torsion of the bridge. These equations, if we accept their linearization, result uncoupled so that the flexural and the torsional behaviours may be treated separately.

6.2.1 Two-Dimensional Model

The basic model of suspension bridge is bidimensional and is constituted by a flexible cable, hanging between two points on the same level, connected through a dense sequence of vertical elements (the hangers) to a stiffening girder, which is simply supported at the ends aligned on the same vertical of the cable supports (Figure 6.1).

The elements constituting the model are therefore the cable, the hangers, and the stiffening girder. In practice the cables slide in saddles located on the tops of the towers. The supports, *O* and *P*, on the tops of the towers may be represented by two rollers, to which the cable ends are connected, subjected to opportune horizontal forces that equilibrate the tension in the cable itself. The cable considered in the model represents the two cables that suspend the bridge deck by the hangers connected to the edges of the stiffening girder.

The two-dimensional model introduced is sufficient to describe the vertical flexure, basically due to the dead loads (self weight of the whole structure) plus any live load symmetric with respect to the vertical midplane[1]. The consideration of eccentric loads inducing a torsion of the stiffening girder implies the substitution of this model with the three-dimensional model of suspension bridge.

---

[1] The vertical plane containing the stiffening girder axis.

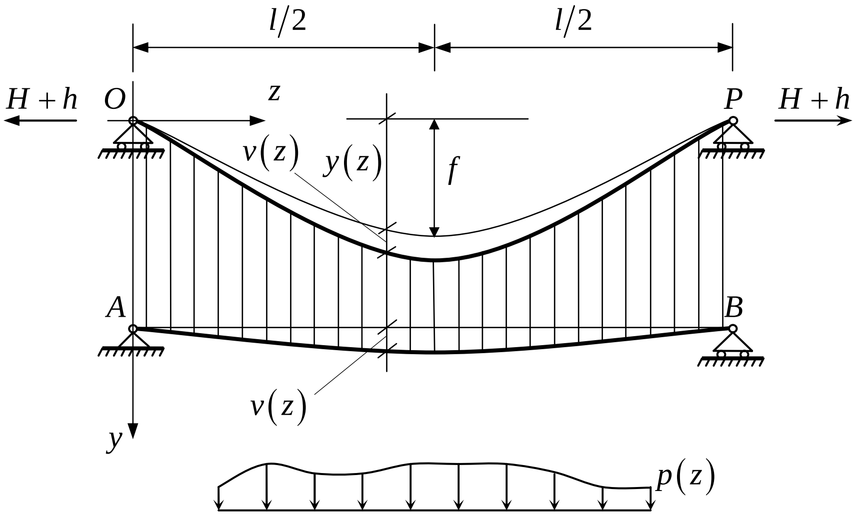

Figure 6.1 – Two-dimensional model of suspension bridge.

Considering the scheme of the single-span suspension bridge in Figure 6.1, let us call:

l	the stiffening girder/main cable span;
f	the main cable sag;
q_g	the bridge weight per unit length (along the z-axis), inclusive of the weight of cables, hangers, deck and its associated stiffening girder, constant by assumption;
μ_g	the bridge mass per unit length, obtained as $\mu_g = q_g / g$, being g the gravitational acceleration;
S	the main cable length under the bridge weight q_g;
H	the horizontal component of the tension in the main cable due to the bridge weight q_g;
EI	the flexural stiffness of the girder, constant by assumption;
$E_c A_c$	the extensional stiffness of the main cable, constant by assumption;
$p(z)$	an additional vertical load applied to the bridge;

h the additional horizontal component of the main cable tension due to the application of the additional load p;

$y(z)$ the deflected shape of the cable under the action of the bridge weight q_g;

$v(z)$ the additional deflection of the cable due to the additional load p.

The governing equation for the deflected shape of the cable $y(z)$ under the action of the bridge weight q_g is:

$$H\frac{\mathrm{d}^2 y}{\mathrm{d}z^2} = -q_g. \tag{6.2}$$

Integrating Equation (6.2) and considering $y(l/2) = f$ leads to the well known formula $H = q_g\, l^2 / 8f$.

If we apply the additional load p to the girder, a certain amount, p_1, will be supported by the cable, while the remaining part, $p - p_1$, will be supported by the stiffening girder. The horizontal component H of the cable tension will therefore become $H + h$, and to the original cable deflection $y(z)$ will be summed the additional deflection $v(z)$. Neglecting both hangers deformation and horizontal displacements of the cable, the vertical deflection of the girder will be equal to the additional deflection of the cable in correspondence of the same abscissa z, $v(z)$. Hence, the equations governing the deflection of the cable and the girder[2] are, respectively:

$$(H + h)\frac{\mathrm{d}^2}{\mathrm{d}z^2}(y + v) = -q_g - p_1, \tag{6.3}$$

$$EI\frac{\mathrm{d}^4 v}{\mathrm{d}z^4} = p - p_1. \tag{6.4}$$

Equations (6.3) and (6.4) contain three unknown quantities: the two functions $y(z)$ and $v(z)$, and the additional horizontal component of the cable tension h.

---

[2] The girder is assumed to be not deformable in shear.

We will need another equation to determine *h*.

Let us suppose, at first, that the additional horizontal component *h* is known. Substituting for p_1 from Equation (6.4) in Equation (6.3) gives:

$$\left(H+h\right)\frac{\mathrm{d}^2}{\mathrm{d}z^2}\left(y+v\right)=-q_g-p+EI\frac{\mathrm{d}^4 v}{\mathrm{d}z^4}, \tag{6.5}$$

and then, considering Equation (6.2):

$$EI\frac{\mathrm{d}^4 v}{\mathrm{d}z^4}-\left(H+h\right)\frac{\mathrm{d}^2 v}{\mathrm{d}z^2}=p+h\frac{\mathrm{d}^2 y}{\mathrm{d}z^2}. \tag{6.6}$$

Hence, substituting for $\mathrm{d}^2 y/\mathrm{d}z^2$ from Equation (6.2) in Equation (6.6), we obtain the following non-linear differential equation representing the first fundamental equation governing the statics of suspension bridges (Melan, 1888):

$$EI\frac{\mathrm{d}^4 v}{\mathrm{d}z^4}-\left(H+h\right)\frac{\mathrm{d}^2 v}{\mathrm{d}z^2}=p-\frac{h}{H}q_g. \tag{6.7}$$

An exam of Equation (6.7) shows that when the girder is loaded by the additional load *p*, thanks to the presence of the cable, we have: (1) the girder is stiffened by the action $\left(H+h\right)\left(\mathrm{d}^2 v/\mathrm{d}z^2\right)$, and (2) the load applied to the girder is reduced by the quantity $\left(h/H\right)q_g$, proportional to the percent increment in the horizontal component of the cable tension.

Equation (6.7) contains the unknown quantity *h*, i.e., the horizontal component of the cable tension increment. The second fundamental equation governing the statics of suspension bridges, from which we can obtain *h*, is given by the following compatibility condition (Melan, 1888):

$$\frac{h\,S}{E_c A_c}=\frac{q_g}{H}\int_0^l v\,\mathrm{d}z, \tag{6.8}$$

where *S*, as we said before, is the cable length in the actual configuration under the bridge weight q_g. In case of shallow cable[3], we may assume $S \cong l$.

---

[3] Sag/span ratio not larger than 1/8.

Substituting the solution to Equation (6.7), which contains the parameter *h*, into Equation (6.8) gives an equation whose solution furnishes the sought value of the additional force *h*. On the other hand, if we regard the cable as inextensible, it results:

$$\int_0^l v\,\mathrm{d}z = 0, \tag{6.9}$$

so that the increase *h* of the horizontal component vanishes.

In case of a suspension bridge with short cable end portions[4], the horizontal displacements of the main cable in correspondence of the tops of the towers are rather small. In this case, the additional force *h* given by Equation (6.8) can be completely developed and the support effect offered by the cable is fully efficient. Conversely, the presence of long cable end portions reduces the cable extensional stiffness in the central span. As a consequence, the additional horizontal component *h* will be sensibly reduced as well as the load lowering provided by the cable to the girder, $(h/H)q_g$. The girder deflection, on the contrary, increases. These effects may be taken into account by considering the main cable suspended between two fixed supports (in correspondence of the tops of the towers) and adopting a fictitious modulus E_c^*, conveniently smaller than the actual modulus E_c.

The Linearized Theory

When the resultant, *P*, of the additional load *p* applied to the girder is small compared to the resultant, *G*, of the distributed weight of the bridge q_g, then the force increment *h* is small compared to the force *H*. Equation (6.7) then becomes (Bleich, 1935):

$$EI\frac{\mathrm{d}^4 v}{\mathrm{d}z^4} - H\frac{\mathrm{d}^2 v}{\mathrm{d}z^2} = p - \frac{h}{H}q_g. \tag{6.10}$$

The first fundamental equation of suspension bridges thus becomes linear. The second fundamental equation keeps the same aspect of Equation (6.8):

---

[4] I.e., the portions between the tops of the towers and the anchor blocks.

$$\frac{h\,l}{E_c A_c} = \frac{q_g}{H}\int_0^l v\,\mathrm{d}z, \tag{6.11}$$

where we have set $S \cong l$.

Integrating Equation (6.10) and imposing the boundary conditions we obtain the function $v(z)$ up to the unknown parameter *h*. Equation (6.11) allows the determination of the additional force *h* by solving a compatibility equation linear in *h*. In practice, using Equation (6.10) instead of Equation (6.7) we neglect the gradual stiffening of the bridge as *p* increases. For small values of the ratio P/G, as is usually the case for long-span suspension bridges, the two solutions overlap.

The integral of Equation (6.10) assumes the form:

$$v(z) = A + B\,z + C\,\mathrm{e}^{\beta z} + D\,\mathrm{e}^{-\beta z} + v_p(z), \tag{6.12}$$

where we have set:

$$\beta^2 = \frac{H}{EI}, \tag{6.13}$$

and where $v_p(z)$ represents a particular solution, depending on the loading condition. The constants *A*, *B*, *C*, and *D* that appear in Equation (6.12) are to be identified via the boundary conditions.

6.2.2 Three-Dimensional Model

Let us now consider the case in which the girder is subjected to an additional distributed vertical load $p(z)$ and an additional distributed torque moment $m(z)$ caused, for example, by an eccentricity of the vertical load (Figure 6.2). In this case, the tensions in the left and right cables will no longer be equal, and the girder deformation will be characterized by a vertical deflection $v(z)$ and a simultaneous torsion $\vartheta(z)$ (Bleich, 1935).

Neglecting the axial deformability of the hangers, the additional vertical deflections of the right (R) and left (L) cables, $v_R(z)$ and $v_L(z)$ respectively, are equal to the vertical deflections of the girder in correspondence of the same vertical lines (Figure 6.2):

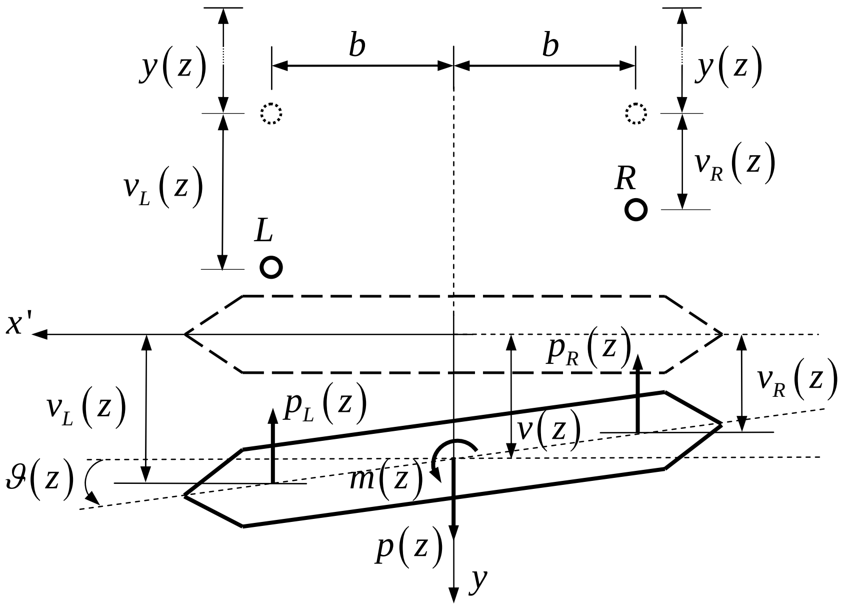

Figure 6.2 – Flexural-torsional deformation of a suspension bridge deck section.

$$v_R(z) = v(z) - b\,\vartheta(z), \tag{6.14a}$$

$$v_L(z) = v(z) + b\,\vartheta(z). \tag{6.14b}$$

Indicating with $p_R(z)$ and $p_L(z)$ the parts of the additional load $p(z)$ supported by right and left cables, respectively, we have the following equations governing the equilibrium of the cables:

$$\left(\frac{H}{2} + h_R\right)\frac{\mathrm{d}^2}{\mathrm{d}z^2}(y + v_R) = -\frac{q_g}{2} - p_R, \tag{6.15a}$$

$$\left(\frac{H}{2} + h_L\right)\frac{\mathrm{d}^2}{\mathrm{d}z^2}(y + v_L) = -\frac{q_g}{2} - p_L, \tag{6.15b}$$

where h_R and h_L are the increasing in the horizontal component of the cables tension due to the application of the additional loads $p(z)$ and $m(z)$. Therefore, the cables support a part of the additional vertical load $p(z)$ globally equal to $p_R + p_L$. Bearing in mind that the equilibrium of each cable is initially expressed by:

$$\frac{H}{2}\frac{\mathrm{d}^2 y}{\mathrm{d}z^2} = -\frac{q_g}{2}, \tag{6.16}$$

and considering only the terms linear in the displacement $v(z)$, we obtain the following linearized equations for the cables:

$$\frac{H}{2}\frac{\mathrm{d}^2 v_R}{\mathrm{d}z^2} + h_R\frac{\mathrm{d}^2 y}{\mathrm{d}z^2} = -p_R, \tag{6.17a}$$

$$\frac{H}{2}\frac{\mathrm{d}^2 v_L}{\mathrm{d}z^2} + h_L\frac{\mathrm{d}^2 y}{\mathrm{d}z^2} = -p_L. \tag{6.17b}$$

Neglecting the shear deformability and taking into account the effects of warping torsion, we have the following flexural and torsional equilibrium equations:

$$EI\frac{\mathrm{d}^4 v}{\mathrm{d}z^4} = p - \left(p_R + p_L\right), \tag{6.18}$$

$$EI_\omega\frac{\mathrm{d}^4 \vartheta}{\mathrm{d}z^4} - GI_t\frac{\mathrm{d}^2 \vartheta}{\mathrm{d}z^2} = m + b\left(p_R - p_L\right), \tag{6.19}$$

where E and G are the Young's modulus and the shear modulus, respectively, I is the area moment of inertia with respect to the x'-axis (see Figure 6.2), I_ω is the warping constant, and I_t is the torsion constant of the girder cross-section[5].

Adding and subtracting side by side Equations (6.17a) and (6.17b) we find the

---

[5] All these quantities are assumed to be constant.

quantities $\left(p_R + p_L\right)$ and $\left(p_R - p_L\right)$, and considering the relations[6]

$$\frac{\mathrm{d}^2 v_R}{\mathrm{d}z^2} + \frac{\mathrm{d}^2 v_L}{\mathrm{d}z^2} = 2\frac{\mathrm{d}^2 v}{\mathrm{d}z^2}, \tag{6.20a}$$

$$\frac{\mathrm{d}^2 v_R}{\mathrm{d}z^2} - \frac{\mathrm{d}^2 v_L}{\mathrm{d}z^2} = -2b\frac{\mathrm{d}^2 \vartheta}{\mathrm{d}z^2}, \tag{6.20b}$$

Equations (6.18) and (6.19) can be rewritten as follows:

$$EI\frac{\mathrm{d}^4 v}{\mathrm{d}z^4} - H\frac{\mathrm{d}^2 v}{\mathrm{d}z^2} = p + \frac{\mathrm{d}^2 y}{\mathrm{d}z^2}\left(h_R + h_L\right), \tag{6.21}$$

$$EI_\omega\frac{\mathrm{d}^4 \vartheta}{\mathrm{d}z^4} - GI_t\frac{\mathrm{d}^2 \vartheta}{\mathrm{d}z^2} = m + Hb^2\frac{\mathrm{d}^2 \vartheta}{\mathrm{d}z^2} - b\frac{\mathrm{d}^2 y}{\mathrm{d}z^2}\left(h_R - h_L\right). \tag{6.22}$$

The additional horizontal forces h_R and h_L, still unknowns in the previous Equations (6.21) and (6.22), are to be determined by means of compatibility equations similar to Equation (6.11). Therefore, recalling Equations (6.14a) and (6.14b), we have the following conditions to be associated to Equations (6.21) and (6.22):

$$h_R = \frac{E_c\left(A_c/2\right)}{l}\frac{q_g/2}{H/2}\int_0^l\left(v - b\,\vartheta\right)\mathrm{d}z, \tag{6.23a}$$

$$h_L = \frac{E_c\left(A_c/2\right)}{l}\frac{q_g/2}{H/2}\int_0^l\left(v + b\,\vartheta\right)\mathrm{d}z. \tag{6.23b}$$

Hence, adding and subtracting Equation (6.23b) to Equation (6.23a), substituting into Equations (6.21) and (6.22), and taking into account Equation (6.16), we derive the integro-differential equations governing the flexure and torsion of suspension bridges subjected to a vertical load $p(z)$ and to a torque moment $m(z)$:

---

[6] From Figure 6.2 is easy to find:
$v_R + v_L = 2v, \quad v_R - v_L = -2b\,\vartheta.$

$$EI\frac{\mathrm{d}^4 v}{\mathrm{d}z^4} - H\frac{\mathrm{d}^2 v}{\mathrm{d}z^2} = p - \left(\frac{q_g}{H}\right)^2 \frac{E_c A_c}{l}\int_0^l v\,\mathrm{d}z, \tag{6.24}$$

$$EI_\omega \frac{\mathrm{d}^4 \vartheta}{\mathrm{d}z^4} - \left(GI_t + Hb^2\right)\frac{\mathrm{d}^2 \vartheta}{\mathrm{d}z^2} = m - b^2\left(\frac{q_g}{H}\right)^2 \frac{E_c A_c}{l}\int_0^l \vartheta\,\mathrm{d}z. \tag{6.25}$$

The equations governing the vertical deflection and the torsion of suspension bridges, in their linearized formulation, are therefore uncoupled. This fact leads to significant simplifications in the analysis of small flexural and torsional oscillations of the bridge deck.

6.3 Free Vibrations and Stability Under Steady Aerodynamic Drag and Moment

In this section, we will study the free oscillations of a suspension bridge girder subjected to a transverse constant wind (mean wind). We will analyze the small flexural and torsional oscillations about the original undeformed configuration, taking into account the second-order effects induced by the aerodynamic loads into the equations of motion of the bridge girder.

As is well known, the mean wind loading consists of the quasi-static load arising from the wind flow past the bridge, and is determined by its size and shape, the air density, the square of the mean wind speed, and its angle of inclination to the structure (angle of attack) (Dyrbye and Hansen, 1997; Holms, 2007). The mean wind flow can produce horizontal (drag), vertical (lift), and torsional (moment) forces on the bridge deck, with their relative magnitudes depending on the geometry of the cross-section. Relatively to static stability, the torsional moment on the deck can by itself induce torsional divergence. In fact, the aerodynamic moment usually increases with increase in the incident angle of the wind. If this increase in applied torsional moment exceeds the resisting moment from the elasticity of the structure, the total stiffness against rotation can become zero, and torsional deformations will increase without limit to the point of failure. On the other hand, given the slenderness of the stiffening girder, the drag force can induce lateral-torsional buckling. In fact, due to the presence of the drag force, the linearized equations governing bending and torsion of suspension bridges result coupled. Conversely, considering the large bridge weight involved, the lift force has no relevance on static stability of suspension bridges, and will be neglected in

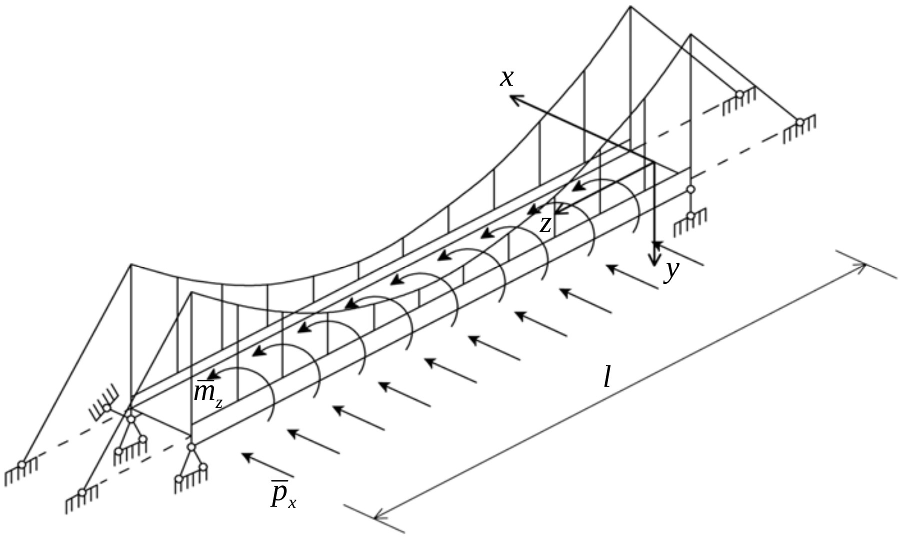

Figure 6.3 – Central span of a suspension bridge subjected to steady aerodynamic drag and moment.

the following analysis.

As will be shown later, the aerodynamic drag and moment have an influence on the transverse (vertical) bending and torsional natural frequencies of the bridge deck.

6.3.1 Governing Equations of Motion

Let us consider the central span of a suspension bridge, of length *l*, shown in Figure 6.3. Let EI be the vertical bending stiffness of the stiffening girder, GI_t its torsional stiffness, EI_ω its warping stiffness. All these quantities are constant by assumption. Moreover, let *H* be the total horizontal force in the main cables under the bridge self weight.

The mean wind, blowing with velocity *U*, induces the aerodynamic loads of lift, drag, and moment on the stiffening girder. The lift force will not be considered in the following analysis for the reasons pointed out before. We assume that the girder is horizontal in its original configuration and that the wind, constant in space and time, invests the girder with zero angle of attack (i.e., has horizontal direction). Under these assumptions, we have the following expressions for the steady aerodynamic drag and moment, uniformly distributed along the girder axis (Figure 6.3):

$$\bar{p}_x = D_s(0) = \frac{1}{2}\rho U^2 B C_D(0), \tag{6.26a}$$

$$\bar{m}_z = M_s(0) = \frac{1}{2}\rho U^2 B^2 C_M(0), \tag{6.26b}$$

where ρ is the air density, U is the mean wind velocity, B is the deck width, and $C_D(0)$ and $C_M(0)$ are the aerodynamic coefficient of drag and moment, respectively, evaluated for zero angle of attack.

The distributed drag, $\bar{p}_x$, induces a bending of the girder in the horizontal plane (*xz*-plane), and therefore produces the bending moment $\bar{m}_y$ about the vertical axis defined by:

$$\bar{m}_y = \bar{p}_x \frac{z}{2}(l - z). \tag{6.27}$$

Hence, considering a deformed configuration characterized by a vertical deflection $v(z)$ and a simultaneous torsion $\vartheta(z)$, the destabilizing distributed vertical load $(\bar{m}_y \vartheta)''$ and torque moment $\bar{m}_y v''$ are generated[7].

At the same time, due to the steady torsion $\vartheta(z)$, an additional distributed aerodynamic moment arises. This can be expressed in the following form, linearized in a neighbour of $\vartheta = 0$:

$$\Delta\bar{m}_z(z) = \frac{1}{2}\rho U^2 B^2 C'_M(0)\vartheta(z) = \bar{\mu}_s \vartheta(z), \tag{6.28}$$

being $C'_M(0) = (\mathrm{d}C_M/\mathrm{d}\vartheta)_{\vartheta=0}$, and where we have set:

---

[7] $(\cdot)'' = \mathrm{d}^2(\cdot)/\mathrm{d}z^2$.

$$\bar{\mu}_s = \frac{1}{2}\rho U^2 B^2 C_M'(0). \tag{6.29}$$

Now, with the aim of analyzing the free bending-torsional oscillations of the bridge, let us replace the distributed vertical load p and torque moment m considered in Section 6.2.2 with the forces of inertia:

$$p = -\mu_g \frac{\mathrm{d}^2 v}{\mathrm{d}t^2}, \tag{6.30a}$$

$$m = -I_\vartheta \frac{\mathrm{d}^2 \vartheta}{\mathrm{d}t^2}, \tag{6.30b}$$

where μ_g is the bridge mass per unit length and I_ϑ denotes the bridge polar mass moment of inertia per unit length, about the z-axis, given by the following formula:

$$I_\vartheta = I_{\vartheta G} + \mu_C b^2. \tag{6.31}$$

In the formula (6.31), $I_{\vartheta G}$ is the girder polar mass moment of inertia[8], while $\mu_C b^2$ is the cables (including the hangers) mass moment of inertia, being μ_C their mass per unit length and b the half-distance between the right and left cables (see Figure 6.2).

Then, taking into account the second-order effects induced by the aerodynamic drag and moment, the bending-torsional oscillations of the bridge are governed by the following partial differential equations, (see Equations (6.21) and (6.22)):

$$EI\frac{\partial^4 v}{\partial z^4} - H\frac{\partial^2 v}{\partial z^2} + \frac{\partial^2\left(\bar{m}_y \vartheta\right)}{\partial z^2} = -\mu_g \frac{\partial^2 v}{\partial t^2} + \frac{\partial^2 y}{\partial z^2}\left[h_R(t) + h_L(t)\right], \tag{6.32a}$$

$$EI_\omega \frac{\partial^4 \vartheta}{\partial z^4} - \left(GI_t + Hb^2\right)\frac{\partial^2 \vartheta}{\partial z^2} + \bar{m}_y \frac{\partial^2 v}{\partial z^2} - \bar{\mu}_s \vartheta = -I_\vartheta \frac{\partial^2 \vartheta}{\partial t^2} - b\frac{\partial^2 y}{\partial z^2}\left[h_R(t) - h_L(t)\right], \tag{6.32b}$$

---

[8] $I_{\vartheta G} = \mu_g \left(I_P / A\right)$, where I_P is the polar area moment of inertia and A is the area of the girder cross-section.

where the increments h_R and h_L in the horizontal forces in the main cables are now functions of the time t [9] (see Equations (6.23a) and (6.23b)):

$$h_R(t) = \frac{E_c(A_c/2)}{l}\frac{q_g}{H}\int_0^l \left[v(z,t) - b\vartheta(z,t)\right]\mathrm{d}z, \tag{6.33a}$$

$$h_L(t) = \frac{E_c(A_c/2)}{l}\frac{q_g}{H}\int_0^l \left[v(z,t) + b\vartheta(z,t)\right]\mathrm{d}z. \tag{6.33b}$$

Notice that Equations (6.32a) and (6.32b) are coupled due to the presence of the bending moment $\overline{m}_y$ induced by the drag $\overline{p}_x$. Then, introducing Equations (6.33a) and (6.33b) into Equations (6.32a) and (6.32b), we may write the system of integro-differential equations describing the small bending-torsional oscillations of the suspension bridge about its original rectilinear configuration of static equilibrium.

In the next section, we will study the antisymmetric oscillations of the bridge girder. This study is of particular interest in the case of suspension bridges with relatively short side spans, for which, thanks to the short and stiff lateral portions of the main cables, antisymmetric modes are activated more easily than symmetric ones.

6.3.2 Antisymmetric Oscillations

In the case of antisymmetric oscillations of the girder, the functions $v(z,t)$ and $\vartheta(z,t)$ describing the flexural and torsional deformations are such that the definite integrals $\int_0^l v(z,t)\,\mathrm{d}z$ and $\int_0^l \vartheta(z,t)\,\mathrm{d}z$ vanish. Consequently, the additional forces in the right and left cables, defined by Equations (6.33a) and (6.33b), are identically zero. Equations (6.32a) and (6.32b) are therefore reduced to the following coupled equations:

$$EI\frac{\partial^4 v}{\partial z^4} - H\frac{\partial^2 v}{\partial z^2} + \frac{\partial^2\left(\overline{m}_y\vartheta\right)}{\partial z^2} = -\mu_g\frac{\partial^2 v}{\partial t^2}, \tag{6.34a}$$

---

[9] With the assumption of small oscillations, the horizontal forces in the main cables may be regarded as constant along the z-axis.

$$EI_\omega \frac{\partial^4 \vartheta}{\partial z^4} - \left(GI_t + Hb^2\right)\frac{\partial^2 \vartheta}{\partial z^2} + \bar{m}_y \frac{\partial^2 v}{\partial z^2} - \bar{\mu}_s \vartheta = -I_\vartheta \frac{\partial^2 \vartheta}{\partial t^2}, \tag{6.34b}$$

and, recalling the expression of $\bar{m}_y$ given by Equation (6.27), we obtain:

$$E_1(z,t) = EI\frac{\partial^4 v}{\partial z^4} - H\frac{\partial^2 v}{\partial z^2} + \bar{p}_x\left[-\vartheta + (l-2z)\frac{\partial \vartheta}{\partial z} + \frac{z}{2}\frac{\partial^2 \vartheta}{\partial z^2}\right] + \mu_g \frac{\partial^2 v}{\partial t^2} = 0, \tag{6.35a}$$

$$E_2(z,t) = EI_\omega \frac{\partial^4 \vartheta}{\partial z^4} - \left(GI_t + Hb^2\right)\frac{\partial^2 \vartheta}{\partial z^2} + \bar{p}_x \frac{z}{2}(l-z)\frac{\partial^2 v}{\partial z^2} - \bar{\mu}_s \vartheta + I_\vartheta \frac{\partial^2 \vartheta}{\partial t^2} = 0. \tag{6.35b}$$

The solution to the system defined by Equations (6.35a) and (6.35b) can be found in the following variable-separable form:

$$v(z,t) = V(t)\,\eta(z), \tag{6.36a}$$

$$\vartheta(z,t) = \Theta(t)\,\psi(z), \tag{6.36b}$$

where the functions $\eta(z)$ e $\psi(z)$ are such that the boundary conditions $\eta(0)=\eta(l)=\eta''(0)=\eta''(l)=\psi(0)=\psi(l)=0$ are satisfied. We can assume the following expression for the functions $\eta(z)$ e $\psi(z)$:

$$\eta(z) = \psi(z) = \sin\frac{2n\pi z}{l}, \tag{6.37}$$

with n being a natural number, and where the factor 2 is necessary in order to select only the antisymmetric deformations. An approximate solution to the system defined by Equations (6.35a) and (6.35b), which contains nonconstant coefficients, can be obtained by applying the Galerkin method of weighted residuals[10]. Thus, introducing Equations (6.36a) and (6.36b), with $\eta(z)$ e $\psi(z)$ expressed by Equation (6.37), into Equations (6.35a) and (6.35b), and imposing the integral conditions:

---

[10] See, for example, pages 116-123 in (Bathe, 1982).

$$\int_0^l E_i\left(z,t\right)\sin\left(\frac{2n\pi z}{l}\right)\mathrm{d}z = 0, \qquad i = 1, 2, \tag{6.38}$$

we obtain the following differential system in matrix form:

$$\begin{bmatrix} \mu_g & 0 \\ 0 & I_g \end{bmatrix} \begin{Bmatrix} \ddot{V} \\ \ddot{\Theta} \end{Bmatrix} + \\ + \begin{bmatrix} \frac{4n^2\pi^2}{l^2}\left(\frac{4n^2\pi^2}{l^2}EI + H\right) & 0 \\ 0 & \frac{4n^2\pi^2}{l^2}\left(\frac{4n^2\pi^2}{l^2}EI_\omega + GI_t + Hb^2\right) \end{bmatrix} \begin{Bmatrix} V \\ \Theta \end{Bmatrix} + \\ - \bar{p}_x \begin{bmatrix} 0 & \frac{1}{12}\left(3+4n^2\pi^2\right) \\ \frac{1}{12}\left(3+4n^2\pi^2\right) & 0 \end{bmatrix} \begin{Bmatrix} V \\ \Theta \end{Bmatrix} - \bar{\mu}_s \begin{bmatrix} 0 & 0 \\ 0 & 1 \end{bmatrix} \begin{Bmatrix} V \\ \Theta \end{Bmatrix} = \begin{Bmatrix} 0 \\ 0 \end{Bmatrix}, \tag{6.39}$$

which can be symbolically rewritten as:

$$\left[M\right]\left\{\ddot{q}\right\} + \left[K\right]\left\{q\right\} - \bar{p}_x\left[K_g^p\right]\left\{q\right\} - \bar{\mu}_s\left[K_g^\mu\right]\left\{q\right\} = \left\{0\right\}, \tag{6.40}$$

where $\left\{q\right\} = \left(V, \Theta\right)^{\mathrm{T}}$. The mass matrix, $\left[M\right]$, the elastic stiffness matrix, $\left[K\right]$, and the geometric stiffness matrices, $\left[K_g^p\right]$ and $\left[K_g^\mu\right]$, in Equation (6.40) can be defined in comparison with Equation (6.39). Looking for a general solution in the form $\left\{q\right\} = \left\{q_0\right\}\mathrm{e}^{\mathrm{i}\omega t}$, where ω represents the angular frequency of free oscillation, we obtain:

$$\left(\left[K\right] - \bar{p}_x\left[K_g^p\right] - \bar{\mu}_s\left[K_g^\mu\right] - \omega^2\left[M\right]\right)\left\{q_0\right\} = \left\{0\right\}. \tag{6.41}$$

A nontrivial solution to Equation (6.41) exists if and only if the determinant of the resultant coefficient matrix of the vector $\left\{q_0\right\}$ vanishes. This yields the following generalized eigenvalue problem:

$$\det\left(\left[K\right] - \bar{p}_x\left[K_g^p\right] - \bar{\mu}_s\left[K_g^\mu\right] - \omega^2\left[M\right]\right) = 0, \tag{6.42}$$

where $\overline{p}_x$, $\overline{\mu}_s$ and ω^2 are the eigenvalues of the system.

For each value of *n*, knowing the values of $\overline{p}_x$ and $\overline{\mu}_s$, the condition (6.42) gives a second order algebraic equation in ω^2 whose solutions are the squares of the n^{th} flexural and torsional angular frequencies of the bridge.

Before considering the general case, let us analyze some special cases. If $\overline{p}_x = \overline{\mu}_s = 0,$ then we fall into the purely dynamic problem. In this case, Equation (6.41) becomes:

$$\begin{bmatrix} \frac{4n^2\pi^2}{l^2}\left(\frac{4n^2\pi^2}{l^2}EI + H\right) - \omega^2\mu_g & 0 \\ 0 & \frac{4n^2\pi^2}{l^2}\left(\frac{4n^2\pi^2}{l^2}EI_\omega + GI_t + Hb^2\right) - \omega^2 I_\vartheta \end{bmatrix} \begin{Bmatrix} V \\ \Theta \end{Bmatrix} = \begin{Bmatrix} 0 \\ 0 \end{Bmatrix}, \tag{6.43}$$

showing that the equations governing the free flexural and torsional oscillations are uncoupled: this is a direct consequence of the linearized deflection theory of suspension bridges presented in Section 6.2.2. From the first equation of System (6.43) we obtain the natural flexural frequencies:

$$\omega_{vn} = \frac{2n\pi}{l}\sqrt{\frac{4n^2\pi^2}{l^2}\frac{EI}{\mu_g} + \frac{H}{\mu_g}}, \tag{6.44}$$

whereas from the second one we obtain the natural torsional frequencies:

$$\omega_{\vartheta n} = \frac{2n\pi}{l}\sqrt{\frac{1}{I_\vartheta}\left(\frac{4n^2\pi^2}{l^2}EI_\omega + GI_t + Hb^2\right)}. \tag{6.45}$$

For $n = 1$ we get the fundamental antisymmetric flexural and torsional frequencies of the bridge:

$$\omega_{v1} = \frac{2\pi}{l}\sqrt{\frac{4\pi^2}{l^2}\frac{EI}{\mu_g} + \frac{H}{\mu_g}}, \tag{6.46}$$

$$\omega_{\vartheta 1} = \frac{2\pi}{l}\sqrt{\frac{1}{I_\vartheta}\left(\frac{4\pi^2}{l^2}EI_\omega + GI_t + Hb^2\right)}. \tag{6.47}$$

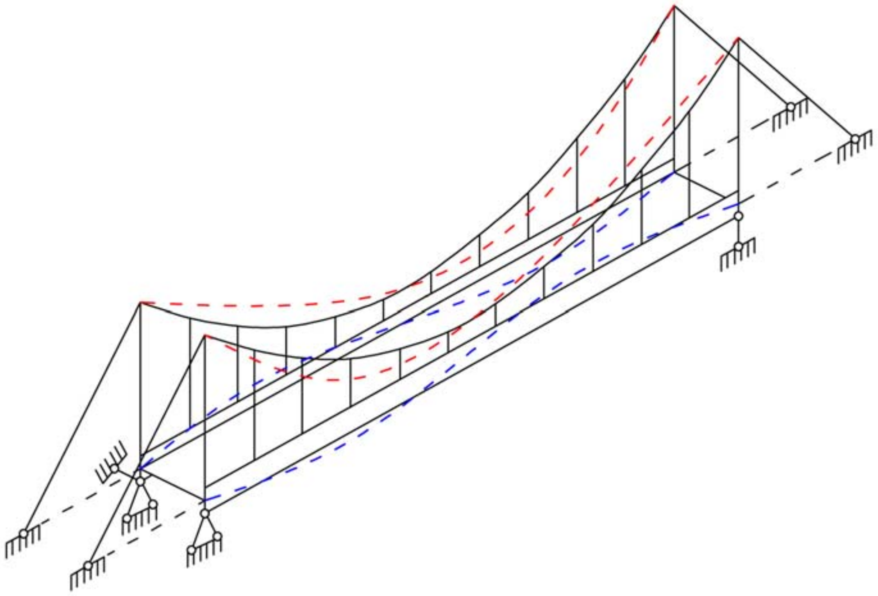

Figure 6.4 – First antisymmetric torsional mode shape.

The first antisymmetric torsional mode shape is schematically shown in Figure 6.4.

Equivalently, the same conclusions about the free dynamic response of the bridge could have been drawn by setting $\overline{p}_x = \overline{\mu}_s = 0$ directly into Equation (6.42).

As second special case, let us analyze the purely static problem. Thus, setting $\mu_g = I_\vartheta = 0,$ Equation (6.42) yields:

$$\det\begin{bmatrix} \frac{4n^2\pi^2}{l^2}\left(\frac{4n^2\pi^2}{l^2}EI + H\right) & -\frac{\overline{p}_x}{12}\left(3+4n^2\pi^2\right) \\ -\frac{\overline{p}_x}{12}\left(3+4n^2\pi^2\right) & \frac{4n^2\pi^2}{l^2}\left(\frac{4n^2\pi^2}{l^2}EI_\omega + GI_t + Hb^2\right) - \overline{\mu}_s \end{bmatrix} = 0. \quad (6.48)$$

First of all we analyze the two limit cases which derive from Equation (6.48). If $\overline{p}_x = 0,$ then we obtain the critical condition for torsional divergence. The n^{th} critical coefficient for torsional divergence (see Equation (6.28)) is therefore given by:

$$\bar{\mu}_{scn} = \frac{4n^2\pi^2}{l^2}\left(\frac{4n^2\pi^2}{l^2}EI_\omega + GI_t + Hb^2\right), \tag{6.49}$$

from which, for $n = 1$, we obtain its smallest value:

$$\bar{\mu}_{sc1} = \frac{4\pi^2}{l^2}\left(\frac{4\pi^2}{l^2}EI_\omega + GI_t + Hb^2\right). \tag{6.50}$$

Recalling the expression of the n^{th} torsional eigenfrequency given by Equation (6.45), Equation (6.50) may be written in the following alternative form:

$$\bar{\mu}_{scn} = \omega_{\vartheta n}^2 I_\vartheta. \tag{6.51}$$

Knowing $\bar{\mu}_{sc1}$, the critical wind velocity for torsional divergence may be obtained from Equation (6.29).

The second limit case of Equation (6.48) is obtained for $\bar{\mu}_s = 0$: in this case we have the critical condition for lateral-torsional buckling. Equation (6.48) then leads to the n^{th} critical drag load:

$$\bar{p}_{xcn} = \frac{24n\pi}{l\left(3 + 4n^2\pi^2\right)}\sqrt{\left(\frac{4n^2\pi^2}{l^2}EI + H\right)\bar{\mu}_{scn}}, \tag{6.52}$$

from which, for $n = 1$, we obtain its smallest value:

$$\bar{p}_{xc1} = \frac{24\pi}{l\left(3 + 4\pi^2\right)}\sqrt{\left(\frac{4\pi^2}{l^2}EI + H\right)\bar{\mu}_{sc1}}. \tag{6.53}$$

Knowing $\bar{p}_{xc1}$, the critical wind velocity for lateral-torsional buckling can be obtained from Equation (6.26a).

Now, if both $\bar{p}_x$ and $\bar{\mu}_s$ are other than zero, from Equation (6.48) and recalling Equations (6.50) and (6.53) we obtain the following critical condition:

$$\frac{\bar{\mu}_s}{\bar{\mu}_{sc1}} = 1 - \left(\frac{\bar{p}_x}{\bar{p}_{xc1}}\right)^2. \tag{6.54}$$

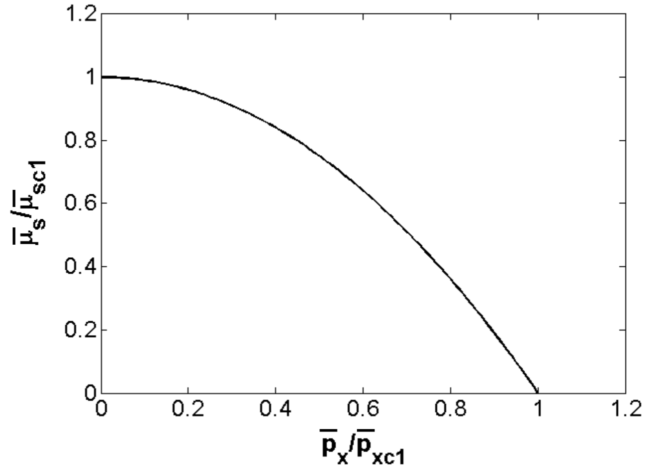

Figure 6.5 – Nondimensional moment vs. nondimensional drag ($\mu_g = I_\vartheta = 0,\ n = 1$).

Equation (6.54) represents a one-to-one relationship between $\overline{p}_x$ and $\overline{\mu}_s$ in a nondimensional form, describing the interaction between the distributed aerodynamic moment and the distributed drag load. A graphical representation of Equation (6.54) is provided in Figure 6.5: it gives us an idea about the influence of the drag on the critical moment for torsional divergence, showing that the latter is a decreasing function of the acting drag load.

Let us now consider the complete characteristic problem defined by Equation (6.42), which is expressed as follows:

$$\det\begin{bmatrix} \frac{4n^2\pi^2}{l^2}\left(\frac{4n^2\pi^2}{l^2}EI + H\right) - \omega^2\mu_g & -\frac{\overline{p}_x}{12}\left(3 + 4n^2\pi^2\right) \\ -\frac{\overline{p}_x}{12}\left(3 + 4n^2\pi^2\right) & \frac{4n^2\pi^2}{l^2}\left(\frac{4n^2\pi^2}{l^2}EI_\omega + GI_t + Hb^2\right) - \overline{\mu}_s - \omega^2 I_\vartheta \end{bmatrix} = 0. \tag{6.55}$$

For each value of *n*, varying $\overline{p}_x$ and $\overline{\mu}_s$ between zero and the corresponding critical values defined by Equations (6.52) and (6.49) respectively, we obtain the values of ω_v^2 and ω_ϑ^2 which satisfy Equation (6.55). This operation results in two surfaces (for each n), describing the dependence of the flexural and torsional frequencies on the aerodynamic drag and moment.

As an example, the characteristic surfaces corresponding to $n = 1$ are plotted in Figures 6.6 and 6.7 in a nondimensional form for an ideal suspension bridge. Figure 6.6 shows the nondimensional flexural frequency squared in terms of the nondimensional drag and moment loads, whereas Figure 6.7 shows the nondimensional torsional frequency squared in terms of the same quantities[11].

Before looking at the general case, let us consider some special cases. First, as can easily be seen in Figure 6.6, for $\omega_v = 0$ we return to the purely static problem examined before, finding the interaction curve between $\bar{p}_x$ and $\bar{\mu}_s$ (see Figure 6.5). Then, if $\bar{\mu}_s = 0$, Figure 6.6 shows that, when $\bar{p}_x$ is increased from zero (pure free vibration) up to the critical value $\bar{p}_{xc1}$ (pure lateral-torsional buckling), the

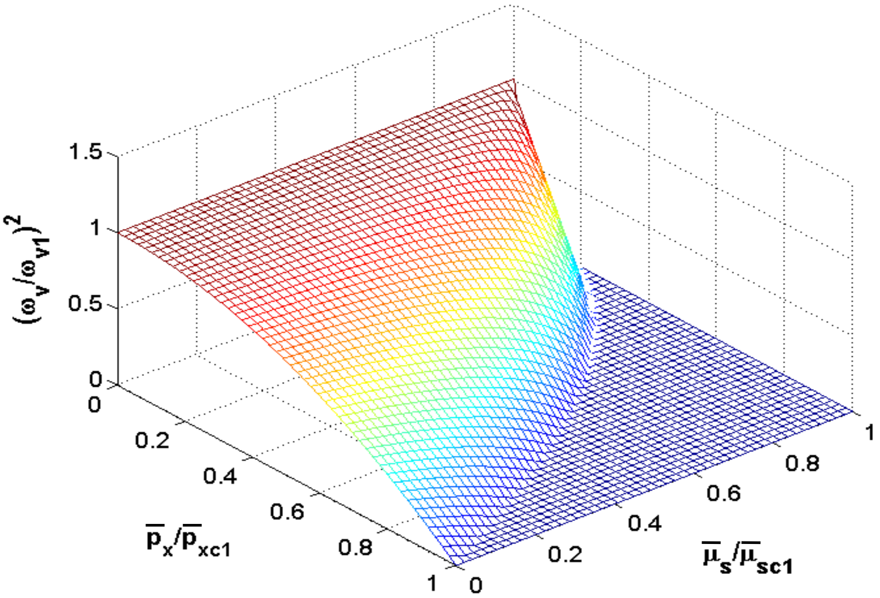

Figure 6.6 – Characteristic surface plotting the nondimensional flexural frequency squared in terms of the nondimensional drag and moment loads ($n = 1$).

---

[11] Both frequencies ω_v and ω_ϑ are nondimensionalized with respect to ω_{v1}.

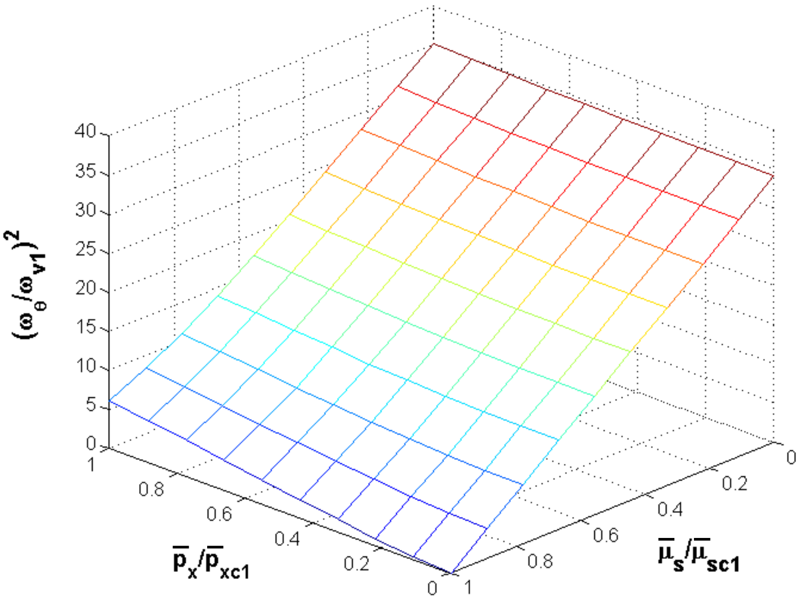

Figure 6.7 – Characteristic surface plotting the nondimensional torsional frequency squared in terms of the nondimensional drag and moment loads ($n = 1$).

frequency related to flexural oscillations decreases from ω_{v1} down to zero (Figure 6.8). Conversely, Figure 6.7 shows that, for the same case, the frequency related to torsional oscillations progressively increases from the value $\omega_{\vartheta 1}$ as $\overline{p}_x$ is increased (Figure 6.9). Finally, if $\overline{p}_x = 0$, Figure 6.6 clearly shows that the flexural frequency is always equal to ω_{v1} for all values of $\overline{\mu}_s$, consistently with the linearized theory of suspension bridges adopted here[12] (Figure 6.10). Conversely, still for $\overline{p}_x = 0$, Figure 6.7 shows that when $\overline{\mu}_s$ is increased from zero (pure free vibration) up to the critical value $\overline{\mu}_{sc1}$ (pure torsional divergence) the torsional

---

[12] If $\overline{p}_x = 0$, then the flexural and torsional oscillations of the bridge are uncoupled (see Equations (6.23a) and (6.23b)).

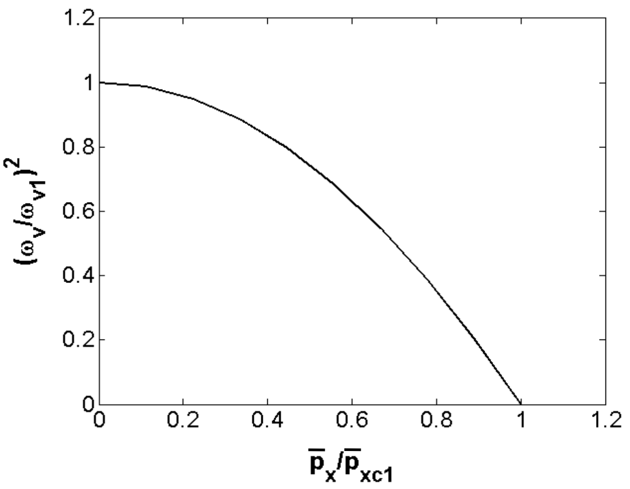

Figure 6.8 – Nondimensional flexural frequency squared vs. nondimensional drag for $\bar{\mu}_s = 0$ ($n = 1$).

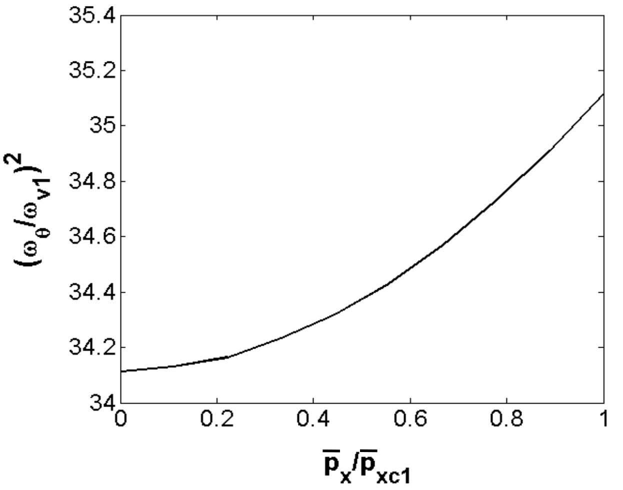

Figure 6.9 – Nondimensional torsional frequency squared vs. nondimensional drag for $\bar{\mu}_s = 0$ ($n = 1$).

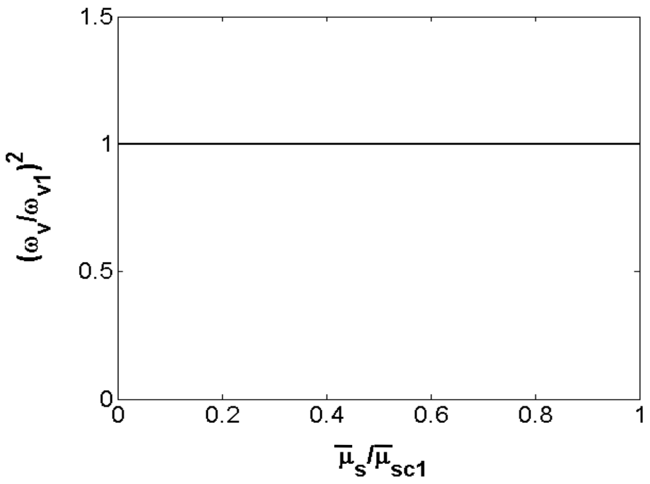

Figure 6.10 – Nondimensional flexural frequency squared vs. nondimensional moment for $\bar{p}_x = 0$ ($n = 1$).

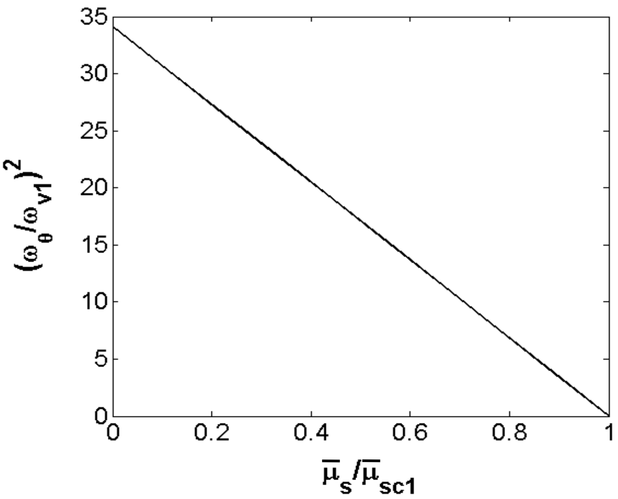

Figure 6.11 – Nondimensional torsional frequency squared vs. nondimensional moment for $\bar{p}_x = 0$ ($n = 1$).

frequency decreases from $\omega_{\vartheta 1}$ down to zero (Figure 6.11).

Now looking at the complete solution of the characteristic problem, Figure 6.6 shows that, as the moment $\bar{\mu}_s$ increases, the flexural frequency vanishes for increasingly smaller values of the drag $\bar{p}_x$. As a limit case, if $\bar{\mu}_s = \bar{\mu}_{sc1}$, then ω_v vanishes in correspondence of $\bar{p}_x = 0$. On the other hand, as pointed out before, the fundamental flexural frequency is always equal to ω_{v1} for all values of $\bar{\mu}_s$ (see Figure 6.10). The last two conclusions imply that the characteristic surface shown in Figure 6.6 must be discontinuous in correspondence of $\left(\bar{p}_x = 0, \bar{\mu}_s = \bar{\mu}_{sc1}\right)$: the vertical oscillation frequency, ω_v, tends to zero as $\bar{p}_x \to 0^+$ and $\bar{\mu}_s \to \bar{\mu}_{sc1}{}^-$, while is equal to ω_{v1} for $\bar{p}_x = 0$ and $\bar{\mu}_s = \bar{\mu}_{sc1}$.

Figure 6.7 shows that the fundamental torsional frequency, ω_ϑ, decreases as the moment $\bar{\mu}_s$ increases, still remaining an increasing function of the drag $\bar{p}_x$. In particular, for $\bar{p}_x = \text{cost.} \neq 0$ the dependence of the fundamental torsional frequency upon $\bar{\mu}_s$ is no longer linear.

Ultimately, the mechanical and geometrical properties of the bridge define the characteristic surfaces, whereas drag and moment depend upon the aerodynamic properties of the bridge cross-section. Thus, for a given wind speed, Equations (6.26a) and (6.29) can be used to calculate the aerodynamic loads $\bar{p}_x$ and $\bar{\mu}_s$, so that the natural frequencies of the bridge can be obtained by solving Equation (6.55).

6.4 Flutter Instability Analysis

Aeroelastic flutter is a dynamic instability phenomenon induced by self-excited forces that depend on motion. If a bridge deck immersed in a wind flow is given a small disturbance, its motion will either decay or diverge depending on whether the energy extracted from the flow is smaller or larger than the energy dissipated by mechanical damping. The theoretical line dividing decaying and diverging motions is called the critical wind velocity for flutter, or simply the flutter velocity, at which the motion of the bridge deck tends to grow exponentially. When flutter occurs, the oscillatory motion is characterized by a precise frequency called the flutter frequency. In a flutter analysis, only the onset instability condition is normally sought for the design of bridge structures.

The self-excited forces acting on a unit deck length are usually expressed as a function of the flutter derivatives (Scanlan and Tomko, 1971). Taking into account three force and displacement components (Figure 6.12), the general format of the self-excited forces written in matrix form for finite element analysis is (Namini et al., 1992):

$$\begin{Bmatrix} L_{se} \\ D_{se} \\ M_{se} \end{Bmatrix} = \frac{1}{2}\rho U^2 B \left(\begin{bmatrix} \dfrac{K^2 H_4^*}{B} & \dfrac{K^2 H_6^*}{B} & K^2 H_3^* \\ \dfrac{K^2 P_4^*}{B} & \dfrac{K^2 P_6^*}{B} & K^2 P_3^* \\ K^2 A_4^* & K^2 A_6^* & K^2 A_3^* B \end{bmatrix} \begin{Bmatrix} h \\ p \\ \alpha \end{Bmatrix} \right.$$

$$\left. + \begin{bmatrix} \dfrac{K H_1^*}{U} & \dfrac{K H_5^*}{U} & \dfrac{K H_2^* B}{U} \\ \dfrac{K P_1^*}{U} & \dfrac{K P_5^*}{U} & \dfrac{K P_2^* B}{U} \\ \dfrac{K A_1^* B}{U} & \dfrac{K A_5^* B}{U} & \dfrac{K A_2^* B^2}{U} \end{bmatrix} \begin{Bmatrix} \dot{h} \\ \dot{p} \\ \dot{\alpha} \end{Bmatrix} \right) \tag{6.56}$$

$$= \frac{1}{2}\rho U^2 \left(\left[F_d \right] \{q\} + \frac{1}{U} \left[F_v \right] \{\dot{q}\} \right),$$

where L_{se}, D_{se}, and M_{se} are the self-excited lift force, drag force, and pitch moment, respectively; h, p, and α are the displacements at the centre of the deck section in the directions corresponding to L_{se}, D_{se}, and M_{se}, respectively; ρ is the mass density of air; B is the deck width; H_i^*, P_i^* and A_i^* $(i = 1 \text{ to } 6)$ are the generalized flutter derivatives; $K = B\omega / U$ is the reduced frequency; ω is the oscillation circular frequency; U is the mean wind velocity; and $\left[F_d \right]$ and $\left[F_v \right]$ are the flutter derivative matrices corresponding to displacement and velocity, respectively.

In linear analyses, the general aeroelastic motion equations of bridge systems are expressed in terms of the generalized mode shape coordinates vector $\{\delta\}$:

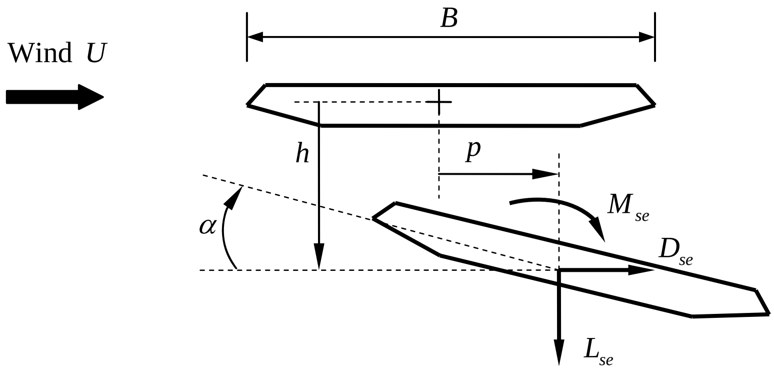

Figure 6.12 – Reference scheme for displacements and self-excited forces.

$$[M]\{\ddot{\delta}\}+\left([C]-\frac{1}{2}\rho U\left[C^*\right]\right)\{\dot{\delta}\}+\left([K]-\frac{1}{2}\rho U^2\left[K^*\right]\right)\{\delta\}=\{0\}, \qquad (6.57)$$

where $[M]$, $[C]$, and $[K]$ are the generalized mass, damping, and stiffness matrices, respectively, while $\left[C^*\right]$ and $\left[K^*\right]$ are the generalized aerodynamic damping and aerodynamic stiffness matrices, respectively. Matrices $[M]$, $[C]$, and $[K]$ are derived the same way as in the classical dynamic analysis. Matrices $\left[C^*\right]$ and $\left[K^*\right]$, corresponding to $[F_v]$ and $[F_d]$ in Equation (6.56), respectively, are assembled from aerodynamic element forces. It is noted that even the structural and dynamic matrices $[K]$, $[M]$, and $[C]$ are uncoupled between modes if $\{\delta\}$ represents the mode shape coordinates, the motion equation is always coupled due to the coupling of aerodynamic matrices $\left[K^*\right]$ and $\left[C^*\right]$.

By assuming harmonic oscillations in the form $\{\delta\}=\{\delta_0\}\mathrm{e}^{\mathrm{i}\omega t}$, the flutter velocity, U_{CF}, and the flutter frequency, ω_F, are obtained from the nontrivial solution of Equation (6.57) which is given by the following complex eigenproblem:

$$\det\left(-\omega^2\left[M\right]+\omega\left(\left[C\right]-\frac{1}{2}\rho U\left[C^*\right]\right)\mathrm{i}+\left[K\right]-\frac{1}{2}\rho U^2\left[K^*\right]\right)=0. \tag{6.58}$$

An examination of the flutter derivatives gives a preliminary judgment of the flutter behaviour of the section. Necessary section modifications should be made to eliminate the positive flutter derivatives, especially the A_2^* and H_1^*. The A_2^* controls the torsional flutter and the H_1^* controls the vertical flutter. It should be noted that for a coupled flutter, zero-damping is a sufficient but not a necessary condition.

Now, based on what we showed in Section 6.3, Equation (6.57) might be modified as follows:

$$\left[M\right]\left\{\ddot{\delta}\right\}+\left(\left[C\right]-\frac{1}{2}\rho U\left[C^*\right]\right)\left\{\dot{\delta}\right\}+\left(\left[K\right]-\frac{1}{2}\rho U^2\left[K_g\right]-\frac{1}{2}\rho U^2\left[K^*\right]\right)\left\{\delta\right\}=\left\{0\right\}, \tag{6.59}$$

where $\left[K_g\right]$ is the generalized geometric stiffness matrix. The matrix $\left[K_g\right]$ has to be obtained from the element geometric stiffness matrix. The latter must be derived considering the effects of the steady aerodynamic loads per unit deck length. In this way, the linear flutter equations would be modified to also take into account the effects of the motion-independent wind forces on the elastic stiffness of the bridge system.

Then, the flutter velocity, U_{CF}, and the flutter frequency, ω_F, can be obtained from the nontrivial solution of Equation (6.59) as:

$$\det\left(-\omega^2\left[M\right]+\omega\left(\left[C\right]-\frac{1}{2}\rho U\left[C^*\right]\right)\mathrm{i}+\left[K\right]-\frac{1}{2}\rho U^2\left[K_g\right]-\frac{1}{2}\rho U^2\left[K^*\right]\right)=0. \tag{6.60}$$

6.5 Concluding Remarks

In this chapter, we have presented a simplified analytical model through which we showed that the natural vibration frequencies of a suspension bridge deck are affected by the mean wind loading. In particular, we focused our analysis on the dependence of the fundamental antisymmetric flexural and torsional frequencies upon the aerodynamic drag and moment distributed along the deck: we found the corresponding characteristic surfaces by solving a generalized eigenvalue problem, in which the geometric stiffness matrix modifies the global stiffness of the system.

Based on the result that we have found, and given the strong dependence of the flutter velocity (and frequency) upon the stiffness parameters of the bridge structure, we suggest the possibility of modifying the classical flutter equations in order to take into account the effect of the motion-independent wind loads on flutter instability.

A first development of the study presented in the present chapter could be done by adding the self-excited aerodynamic lift and moment per unit length (see Equation (2.55)) into Equations (6.32a) and (6.32b), respectively. Finally, in order to describe the structural and geometrical properties of the bridge better, as well as to give a better description of the wind loading, the modified flutter analysis could be implemented in a finite element framework, as suggested by Equation (6.59).

Chapter 7

Conclusions

The thesis dealt with the interplay between dynamics and stability phenomena in elastic structures. The research has focused on the study of natural vibrations and instability of slender structures subjected to various types of actions (static loads, imposed displacements and aerodynamic actions) by means of experimental tests, numerical simulations and the development of an analytical model.

The experimental part of the research required the design, realization and set up of special equipment, the use of a non-invasive precision instrumentation, and particular attention in preparing specimens and the construction of models.

The research has addressed the following specific topics: (1) the fundamental frequency evolution in slender beams subjected to imposed displacements; (2) the effects of dead loads on natural vibration frequencies and mode shapes of slender space trusses; and (3) the influence of steady aerodynamic loads on the natural vibration frequencies of suspension bridge decks. With respect to the first topic, we found that a softening phase, where the fundamental frequency decreases with the axial load, is followed by a hardening one, where the trend is reversed. We observed that the geometric imperfection (initial curvature) reduces the negative slope of the softening branch, therefore anticipating the transition point and making this transition smother at the same time. These findings could find application in designing new structures as well as in monitoring existing ones. For example, the possibility to foresee the transition point, where the minimum frequency (minimum stiffness) is localized, could find application in monitoring in-service structures and components. Moreover, the possibility to reproduce the experimental results through numerical simulations allows a valid interpretation for in-situ measurements, or even to perform virtual laboratory tests. This approach could be used to interpret the behavior of more complicated structural systems subjected to imposed displacements or affected by subsidence of the external constraints.

Regarding the space trusses analyzed, we showed how, depending on the direction of the applied load, the stiffening effects due to the tensile may predominate the softening one due to the compression, or vice versa. While in the former case the consequence is an increase in the natural frequencies, in the latter they decrease. Moreover, we observed that in relation to the load magnitude, the frequency evolution may be monotonic, or could exhibit a trend reversal. Lastly, by comparing different geometrical configurations we found that the structure having the highest fundamental frequency does not necessarily have the highest buckling load at the same time. Such results may be of interest in designing, and specially in optimizing, slender space structures such as, for example, large truss roofs.

As regards to suspension bridges, we proposed an analytical model to study the free vibrations of the deck subjected to steady aerodynamic actions of drag force and pitching moment. In particular, we presented a generalized eigenvalue problem in which all the configurations intermediate between those of pure buckling (lateral-torsional or purely torsional) and pure free vibrations can be investigated. We showed through a simplified model how the considered actions affect the flexural and torsional vibration frequencies of the deck, revealing some possible implications in the analysis of more complex aeroelastic phenomena, such as flutter instability.

In all the analyzed cases, we found a relatively large influence of the applied loads on the natural vibration frequencies, emphasizing the importance of taking this aspect into account when analyzing the dynamic behaviour of slender structures.

References

Abramovich, H., Natural frequencies of Timoshenko beams under compressive axial loads, *Journal of Sound and Vibration*, **57**(1):183-189, 1992.

Addessi, D., Lacarbonara, W., and Paolone, A., On the linear normal modes of planar prestressed curved beams, *Journal of Sound and Vibration*, **284**:1075-1097, 2005a.

Addessi, D., Lacarbonara, W., and Paolone, A., Free in-plane vibrations of highly buckled beams carrying a lumped mass, *Acta Mechanica*, **180**:133-156, 2005b.

Anik'ev, I. I., Mikhailova, M. I., and Sushchenco, E. A., Nondestructive determination of the critical load of column-type structures, *International Applied Mechanics*, **30**(12), 1994.

Anik'ev, I. I., and Sushchenko, E. A., Experimental nondestructive determination of critical loads on thin-walled structures. *International Applied Mechanics*, **38**(4), 2002.

Arboleda-Monsalvea, L. G., Zapata-Medinab, D. G., and Aristizabal-Ochoa, J. D., Stability and natural frequencies of a weakened Timoshenko beam-column with generalized end conditions under constant axial load, *Journal of Sound and Vibration*, **307**:89-112, 2007.

Bathe, K. J., *Finite Element Procedures in Engineering Analysis*, Prentice-Hall Inc., Englewood Cliff, N.J., 1982.

Batra, R. C., Vidoli, S., and Vestroni, F., Plane wave solutions and modal analysis in higher order shear and normal deformable plate theories, *Journal of Sound and Vibration*, **257**(1): 63-88, 2002.

Bažant, Z. P., "Stability of elastic, anelastic, and disintegrating structures: a conspectus of main results", *ZAMM*, **80**(11-12), 709-732, 2000.

Bažant, Z. P., and Cedolin, L., *Stability of Structures: Elastic, Inelastic, Fracture and Damage Theories*, Dover, New York, 2003.

Belluzzi, O., On the vibration period of a structure in presence of compressive axial loads (in Italian), *Giornale del Genio Civile*, fasc. 4°, 1951a.

Belluzzi, O., On the experimental determination of the critical load through vibration tests (in Italian). *Ingegneri-Architetti-Costruttori*, n. 4, Bologna, 1951b.

Bigoni, D., Misseroni, D., Noselli, G., and Zaccaria, D., Effects of the constraint's curvature on structural instability: tensile buckling and multiple bifurcations, *Proceedings of the Royal Society A*, 2012, doi:10.1098/rspa.2011.0732.

Bisplinghoff, R. L., Ashley, H., and Halfman, R. L., *Aeroelasticity*, Dover, New York, 1996.

Bleich, H. H., *Die Berechnung verankerter Hängebrücken*, Julius Springer, Vienna, 1935.

Bokaian, A., Natural frequencies of beams under compressive axial loads, *Journal of Sound and Vibration*, **126**(1):49-65, 1988.

Bokaian, A., Natural frequencies of beams under tensile axial loads, *Journal of Sound and Vibration*, **142**(3):481-498, 1990.

Bolotin, V.V., *Nonconservative Problems of the Theory of Elastic Stability*, Pergamon Press, New York, 1963.

Bolotin, V. V., Dynamic stability of structures, in Kounadis, A. N., and and Kratzig, W. B., (Editors), *Nonlinear Stability of Structures: Theory and Computational Techniques*, pages 3-72, Springer, Wien, 1995.

Bowers, N. A., Tacoma Narrows Bridge Wrecked by Wind, *Engineering News Record*, Nov. 14, pp. 647 and 656, 1940.

Budiansky, B. and Hu, P. C., “The Lagrangian multiplier method for finding upper and lower limits to critical stresses of clamped plates”, NACA Report No. 848, Washington, DC, 1946.

Budiansky, B., Hu, P. C. and Connor, R. W., “Notes on the Lagrangian multiplier method in elastic-stability analysis”, NACA Technical Note No. 1558, Washington, DC, 1948.

Cai, C. S., and Montens, S., Wind Effects on Long-Span Bridges, in Chen, W. F., and Duan, L., (Editors), *Bridge Engineering Handbook*, CRC Press, Boca Raton, 2000.

Carpinteri, A., *Structural Mechanics: A Unified Approach*, Chapman & Hall, London, 1997.

Carpinteri, A., and Paggi, M., A theoretical approach to the interaction between buckling and resonance instabilities, *Journal of Engineering Mathematics*, Springer, pp. 36, 2013.

Carrera, E., A study of transverse normal stress effect on vibration of multilayered plates and shells, *Journal of Sound and* V*ibration*, **225**(5):803-829, 1999.

Chen, W. F., and Lui, E. M., *Structural Stability. Theory and Implementation*, PTR, Prentice-Hall, Englewood Cliffs, NJ, 1987.

Chen, L. W., and Shen, G. S., Vibration and buckling of initially stressed curved beams, *Journal of Sound and* V*ibration*, **215**(3):511-526, 1998.

Clough, R. W., and Penzien, J., *Dynamics of Structures*, 3rd Edition, Computers & Structures, Berkeley, 2003.

Cortinez, V. H., and Piovan, M. T., Vibration and buckling of composite thin-walled beams with shear deformability, *Journal of Sound and Vibration*, **258**(4):701-723, 2002.

de Silva, C. W., *Vibration: Fundamentals and Practice*, CRC Press, Boca Raton, 2000.

Dyrbye, C., and Hansen, S. O., *Wind Loads on Structures*, John Wiley, Chichester, 1997.

Dowell, E. H., (Editor), *A Modern Course in Aeroelasticity*, 4th Edition, Kluwer, Dordrecht, 2004.

El Naschie, M. S., *Stress, Stability, and Chaos in Structural Engineering: An Energy Approach*, McGraw-Hill, London, UK, 1990.

Farquarson, F. B., Aerodynamic Stability of Suspension Bridges with Special Reference to the Tacoma Narrows Bridge, University of Washington Engineering Experimental Station, Bulletin No. 116 (Sec. 3.2), 1654.

Feodos'ev, V. I., *Selected Problems and Questions in Resistance of Materials* (Izbrannye zadachi I voprosy po soprotivleniiu materialov), p. 165, Gostekhizdat, 1953.

Fridman, Y., and Abramovich,H., Enhanced structural behavior of flexible laminated composite beams, *Composite Structures*, **82**:140-154, 2008.

Fung, Y. C., *An Introduction to the Theory of Aeroelasticity*, Dover, New York, 2002.

Galambos, T. V., (Editor), *Guide to Stability Design Criteria for Metal Structures*, 4th Edition, Wiley, New York, 1988.

Gantmacher, F., *Lectures in Analytical Mechanics*, MIR Publishers, Moscow (Sec. 3.4), 1970.

Hallauer, W. L., and Ma, C., On the mechanical behaviour of slender, slightly curved, compressed microbridges, *Journal of Micromechanics and Microengineering*, **21**, 2011.

Holms, J. D., *Wind Loading of Structures*, 2nd Edition, Taylor & Francis, New York, 2007.

Huseyin, K., *Multiple Parameter Stability Theory and its Applications: Bifurcation, Catastrophes, Instabilities*, Clarendon, Oxford, 1986.

Hutchinson, J. W., "Postbifurcation behavior in the plastic range", *Journal of Mechanics and Physics of Solids*, **21**, 163-190, 1973a.

Hutchinson, J. W., "Imperfection–sensitivity in the plastic range", *Journal of Mechanics* *and Physics of Solids*, **21**, 191-204, 1973b.

Ishlinskii, A. Iu., Malashenko, S. V., and Temchenko, M. E., On the branching of stable positions of dynamic equilibrium of a mechanical system, *Izv. Akad. Nauk URSS*, OTN, No. 8, 1958.

Jun, L., and Hongxing, H., Free vibration analysis of axially loaded laminated composite beams based on higher-order shear deformation theory. *Meccanica*, **46**(6):1299-1317, 2011.

Jurado, J. A., Hernández, S., Nieto, F., and Mosquera, A., *Bridge Aeroelasticity. Sensitivity Analysis and Optimal Design*, WIT Press, Southampton, 2011.

Karnovsky, I., and Lebed, O. I., *Formulas for Structural Dynamics: Tables, Graphs, and Solutions*, McGraw-Hill, 2001.

Karnovsky, I., and Lebed, O. I., *Non-Classical Vibrations of Arches and Beams: Eigenvalues and Eigenfunctions*, McGraw-Hill, 2004.

Kim, S. M., Stability and dynamic response of Rayleigh beam–columns on an elastic foundation under moving loads of constant amplitude and harmonic variation, *Engineering Structures*, **27**:869-880, 2005.

Lacarbonara, W., Paolone, A., and Yabuno, H., Modeling of planar nonshallow prestressed beams towards asymptotic solutions, *Mechanics Research Communications*, **31**:301-310, 2004.

Langthjem, M. A., and Sugiyama, Y., Dynamic stability of columns subjected to follower loads: a survey, *Journal of Sound and Vibration*, **238**(5), 809-851, 2000.

Larsen, A., (Editor), *Aerodynamics of Large Bridges*, Balkema, 1992.

Larsen, A., and Esdahl, S., (Editors), *Bridge Aerodynamics*, Balkema, 1998.

Leonhardt, F., *Bridges*, Deutsche Verlag-Anstalt, Stuttgart, 1982.

Leipholz, H., *Stability theory*, 2nd Edition, Wiley, Chichester, 1987.

Li, C., Lim, C. W., Yu, J. L., and Zeng, Q. C., Analytical solutions for vibration of simply supported nonlocal nanobeams with an axial force, *International Journal of Structural Stability and Dynamics*, **11**(2):257-271, 2011.

Liapunov, A. M., *General Problem of Stability of Motion*, Kharkov (reproduced in Ann. Math. Studies 17, Princeton Univ. Press, Princeton 1949), 1892.

Librescu, L., and Song, O., *Thin-Walled Composite Beams: Theory and Application*, Springer, Dordrecht, 2006.

Matsunaga, H., Free vibration and stability of thin elastic beams subjected to axial forces, *Journal of Sound and Vibration*, **191**(5):917-933, 1996.

Matsunaga, H., Vibration and buckling of deep beam-columns on two-parameter elastic foundations, *Journal of Sound and Vibration*, **228**(2):359-376, 1999.

Melan, J., *Theorie der Eisernen Bogenbrücken und der Hängebrücken*, 2nd Edition, Leipzig, 1888.

Namini, A., Albrecht, P., and Bosh, H., Finite element-based flutter analysis of cable-suspended bridges, *J. Struct. Eng. ASCE*, **118**(6):1509-1529, 1992.

Nikolai, E. L., On the stability of the rectilinear form of equilibrium of a bar in compression and torsion, *Izv. Leningr. politekhn. in-ta*, **31**, 1928.

Nikolai, E. L., On the problem of the stability of a bar in torsion, *Vestn. prikl. matem. mekh.*, **1**, 1929.

Nikolai, E. L., *Studies in Mechanics*, Gostekhizdat, 1955.

Pflüger, A, *Stabilitätsproblem der Elastostatik*, p. 217, Springer-Verlag, Berlin, 1950.

Pignataro, M., Rizzi, N. L., and Luongo, A., *Stability, bifurcation and postcritical behaviour of elastic structures*, Amsterdam, Elsevier, 1991.

Reddy, J. N., *Energy Principles and Variational Methods in Applied Mechanics*, 2nd Edition, John Wiley, New York, 2002.

Scanlan, R. H., and Tomko, J.J., Airfoil and bridge deck flutter derivatives, *J. Eng. Mech. Div. Proc. ASCE*, **97**(6):1717-1737, 1971.

Simiu, E., and Scanlan, R. H., *Wind Effects on Structures: Fundamentals and Applications to Design*, 3rd Edition, Wiley, New York, 1996.

Seyranian, A. P., and Mailybaev, A. A., *Multiparameter Stability Theory with Mechanical Applications*, World Scientific Publishing Co. Pte. Ltd., 2003.

Timoshenko, S. P., and Gere, J. M., *Theory of Elastic Stability*, McGraw-Hill, New York, 1961.

Trahair, N. S., and Bradford, M. A., *The Behaviour and Design of Steel Structures*, Revised 2nd Edition, Chapman & Hall, London, UK, 1991.

Virgin, L. N., *Vibration of axially loaded structures*, Cambridge University Press, New York, 2007.

Vo, T. P., Lee, J., Lee, K., On triply coupled vibrations of axially loaded thin-walled composite beams, *Computers and Structures*, **88**:144-153, 2010.

von Kármán, T., Aerodynamic Stability of Suspension Bridges, *Engineering News Record*, 125(Nov.21):670 (Sec. 3.2), 1940.

Xie, Wei-Chau, *Dynamic Stability of Structures*, Cambridge, New York, 2006.

Wang, C. M., Wang, C. Y., and Reddy, J. N., *Exact solutions for buckling of structural members*, CRC Press, Boca Raton, 2005.

Weaver, W., Jr., Timoshenko, S. P., and Joung, D. H., *Vibration Problems in Engineering*, John Wiley & Sons, 5th Edition, Wiley, 1990.

Yang, J., Chen, Y., Xiang, Y., and Jia, X. L., Free and forced vibration of cracked inhomogeneous beams under an axial force and a moving load, *Journal of Sound and Vibration*, **312**:166-181, 2008.

Zaccaria, D., Bigoni, D., Noselli, G., and Misseroni, D., Structures buckling under tensile dead load, *Proceedings of the Royal Society A*, 2011, 467, 1686-1700.

Zhang, Y. Q., Lu, Y., Wang, S. L., and Liu, X., Vibration and buckling of a double-beam system under compressive axial loading, *Journal of Sound and Vibration*, 318:341-352, 2008.

Ziegler, H., *Principles of Structural Stability*, Blaisdell Publishing Company, Waltham, Mass. (Sec. 3.4), 1968.

Zienkiewicz, O. C., and Taylor, R. L., *The Finite Element Method for Solid and Structural Mechanics*, 6th Edition, Elsevier, Amsterdam, 2005.